

New Insights Into Amyloid Formation and Structure by Innovative Atomic Force Microscopy Methods

THÈSE N° 6597 (2015)

PRÉSENTÉE LE 1^{ER} MAI 2015

À LA FACULTÉ DES SCIENCES DE BASE
LABORATOIRE DE PHYSIQUE DE LA MATIÈRE VIVANTE
PROGRAMME DOCTORAL EN PHYSIQUE

ÉCOLE POLYTECHNIQUE FÉDÉRALE DE LAUSANNE

POUR L'OBTENTION DU GRADE DE DOCTEUR ÈS SCIENCES

PAR

Francesco Simone RUGGERI

acceptée sur proposition du jury:

Prof. A. Pautz, président du jury
Prof. G. Dietler, directeur de thèse
Dr T. Knowles, rapporteur
Prof. H. Lashuel, rapporteur
Prof. R. Mezzenga, rapporteur



ÉCOLE POLYTECHNIQUE
FÉDÉRALE DE LAUSANNE

Suisse
2015

To my Family

Acknowledgments

As I always like to remember: “I started a PhD on proteins aggregation by Atomic Force Microscopy without knowing nor what was a protein nor what was Atomic Force Microscopy”. I thought it would have been interesting and stimulating to work in such interdisciplinary field, in a beautiful environment as EPFL. Now, I am here happy for writing the first page of this thesis to describe last page of this intriguing adventure.

First, I would like to thank Giovanni (i.e. Prof. Dietler) who gave me the opportunity to start this journey in his laboratory. I am grateful for his kindness, advices, personal support and for how he had taught me to face *Research* with independent and curious full attitude. This is what actually makes me in love with science and makes me working hard to solve a problem. I also would like to thank Hilal (i.e. Prof. Lashuel) to bring me in so close contact with his research group. I would like to thank him to share all the high-level knowledge and expertise of his laboratory making me feeling always as a part of its group. Together with *some* biology and biochemistry, he had taught me the real meaning of sharing the scientific knowledge in order to solve a plague such as is neurodegenerative disorders. I would like to thank him also for his kind personal support. I am grateful to Annalisa, Sophie, Anne-Laure, Sean, Bilal, Bruno and all the people of the group of Hilal for the fundamental collaborations and scientific discussions that were fundamental for the success of my PhD.

I thank Andrzej (Dr. Kulik), who was always there to help and support me, to teach me really how an AFM works. I could never had so successful results without him bringing and pushing me to use the infrared nanospectroscopy system.

I would like also to thank Tuomas (Prof. Knowles) for the extremely interesting work we continue to conduct in collaboration and for gladly accepting my candidature to join his group in Cambridge. I thank him for his time and fundamental help in order to write my fellowship proposals (hopefully successful!).

I would like to thank Raffaele (Prof. Mezzenga) for the valuable work we have conducted together.

A special thank is reserved to all my colleagues, I had a great time at the Cubotron and I will always miss the beautiful atmosphere in our laboratory. I would like to thanks Gianni for teaching me the secrets of its nanomotion detector and all the personal support. I would also like to thank Sergey (Dr. Sekatskii) for all the nice work we conducted together. I am extremely grateful to Caroline and Carine for the invaluable scientific support in sample preparation. Furthermore, a particular thank goes to the people who make my every day work-life easier. I do not know how I could survive in Switzerland without the help of Christine. A thousands thanks to Michel for being so patient and kind in taking care in real-time (!) of my multiple operative systems crashing continuously. A special thank goes to Sandro and Sunny for all the help and the nice time spent in the office together, but also to all the past and present colleagues as Fabrizio, Dusan, Petar, Katya, Ewelina, Robert, Wojciech. Finally, in the last year, there was one person dealing with me patiently every day, making my work much and life easier in the last and hardest final period of my PhD, I would like to thank Ula for all the help, support and the nice time we spent together. I feel extremely lucky to have spent these four years at the Cubotron with these people, which have been more than colleagues and in particular good friends. I have not shared with all these people just work but also travels, beers, concert and parties. Between all of theme a special thanks goes to Andrea, for his faithful friendship.

During this journey, I had the privilege to meet wonderful people in Lausanne and several of them have become good friends. Contemporarily, my Friends in Catania were present as always and just waiting for me coming back home.

Finally, the deepest thank goes to my Family. I could use a lot of words to thank you them, but it is sufficient to say that I would never be the same person without what they taught me and everything I do is for them before than for myself.

Lausanne, 8th of April 2015

Simone

Abstract

Today, more than 40 million people worldwide are affected by dementia and neurodegenerative disorders. Onset of these and more than other fifty human diseases is associated at the molecular level with insoluble fibrillar protein aggregates, termed amyloids. The molecular origin and mechanistic link between amyloid formation and disease aetiology remain unclear and no disease modifying therapies are available for these disorders. Strong evidence links propensity of proteins to misfolding and aggregation to the pathological biology implicated in the onset of these diseases. Despite its importance, unraveling amyloids properties and formation still represents a formidable experimental challenge, mainly because of their nanoscale dimensions and their dynamic, heterogeneous and transient nature. Therefore, the investigation of the misfolding of monomers and oligomers into fibrils and their mechanical and structural properties is central to understand their stability, toxicity and mechanism of clearance in the body and to design new therapeutic strategies to the amyloid diseases problem.

The main objective of this PhD thesis is the biophysical investigation of amyloids structure and formation at the single scale aggregate. This objective was pursued mainly by the use of both conventional and innovative Atomic Force Microscopy (AFM) methodologies. AFM imaging emerged in the last decades as one of the most powerful and versatile single molecule techniques, because of the possibility to acquire with sub-nanometer resolution 3-D morphology maps of specimens on a surface. In the frame of this work, conventional AFM imaging and innovative AFM-based methods were assessed to resolve the complex and heterogeneous energy landscape of proteins aggregation providing direct information on the aggregation pathway and on the morphology, structure and mechanical properties of species forming during the process.

Initially, we used AFM imaging to compare quantitatively the kinetics of aggregation and the oligomeric and fibrillar morphological differences between wild type and mutated forms of huntingtin and α -synuclein proteins. In the first case, we focused on the effects of N-terminal post-translation modifications in the fibrillization of huntingtin. We demonstrated that a phosphorylated mutated form (pT3) of the protein fibrillates significantly slower than the wild type protein and that both forms aggregate below the polyglutamine length threshold for Huntington's onset. In the latter case, aggregation of wild type and H50Q mutated form of α -synuclein were investigated. This mutation was described in the case of patients with a familiar form of Parkinson's disease and dementia. Our study demonstrated the strict link between the

disease and the mutated form of the protein, which effectively enhanced α -synuclein aggregation. Successively, we investigated the early stages of α -synuclein fibrillization. We showed that the early stages of amyloid assembly proceed directly through the formation of single monomeric strands, which hierarchically assemble into intermediate prefibrillar structures and into the final mature fibrils. To investigate further the properties of these new prefibrillar species, we performed AFM force spectroscopy experiments, which confirmed the *non-mature* cross- β -sheet structure of this species and enabled studying their force of interaction with surfaces.

Successively, new AFM-based methodologies, such as peak force quantitative nanomechanical mapping (PF-QNM) and infrared nanospectroscopy (nanoIR), were successfully implemented to unravel amyloids mechanical and structural properties at the nanoscale. The PF-QNM method enabled investigating the evolution of mechanical properties of aggregates forming during fibrillization of A β 42 and α -synuclein. We demonstrated that β -sheet content is a major factor determining amyloid intrinsic stiffness. NanoIR, simultaneously exploiting AFM and infrared spectroscopy, was applied to investigate at the nanoscale the misfolding process and the structure of the amyloid species present during the aggregation process. A first proof of concept enabled distinguishing and structurally characterizing monomeric and aggregated forms of lysozyme μ -droplets. Successively, it proved to be ideal to characterize, *individually* and at the nanoscale, the oligomeric and fibrillar species formed during amyloid aggregation of the Josephin domain of ataxin-3. We described their secondary structure, monitoring at the nanoscale an α -to- β transition, and coupled these studies with an independent measurement of the evolution of their intrinsic stiffness. Consequently, for the first time at the nanoscale, we were able to link nanomechanical and structural properties of *individual* amyloidogenic species throughout their fibrillization.

Innovative AFM-based techniques correlated morphological, mechanical and structural properties of amyloid aggregates at the nanoscale. For this reason, they represent a future fruitful avenue to unravel the process of protein misfolding and to elucidate the molecular mechanisms of amyloid formation. The comprehension of these fundamental processes could allow the design of pharmacological approaches to contrast the onset of amyloid diseases.

Keywords: Neurodegenerative disorders; Amyloid; aggregation; fibrillization; Atomic Force microscopy; Single molecule Techniques; Nanoscale Infrared Spectroscopy; Secondary structure measurements; Nanomechanical Properties.

Abstract

Oggi giorno, più di 40 milioni di persone in tutto il mondo sono affette da demenza e da malattie neurodegenerative. L'insorgere di queste malattie e di oltre altre 50 patologie umane è strettamente connesso a livello biomolecolare con insolubili aggregati di proteine, denominati amiloidi. L'origine molecolare e la connessione meccanicistica tra la formazione degli amiloidi e l'insorgere della malattia non è stata ancora elucidata, inoltre non esistono ancora delle terapie capaci di modificare o interrompere lo sviluppo della malattia. Notevole evidenza correla la propensione delle proteine a misfoldarsi e aggregarsi con i processi biologici che causano l'insorgenza di queste malattie. Malgrado l'importanza, la possibilità di svelare le proprietà e la formazione degli amiloidi rappresenta ancora una formidabile sfida sperimentale, principalmente a causa delle loro dimensioni nanometriche e della loro natura dinamica, eterogenea e transiente. Lo studio del misfolding dei monomeri ed oligomeri per formare le fibre e le loro proprietà meccaniche e strutturali è fondamentale per comprendere la stabilità, la tossicità e il meccanismo di degradazione di queste strutture nel corpo umano e per conseguentemente ideare strategie per curare le malattie amiloidogeniche.

Il principale obiettivo di questa tesi è l'investigazione biofisica della struttura e formazione degli amiloidi su scala del singolo aggregato. Questo obiettivo è stato perseguito principalmente attraverso l'uso sia di convenzionali sia di innovative tecniche basate sulla Microscopia a Forza Atomica (AFM). L'AFM è emersa negli ultimi decenni come una delle più potenti tecniche capaci di investigare singole molecole, grazie alla possibilità di acquisire immagini morfologiche tridimensionali di un campione su una superficie, con risoluzione sub-nanometrica. Nell'ambito di questo lavoro, la realizzazione di immagini AFM e l'applicazione di nuove metodologie basate su questa tecnica sono state utilizzate per comprendere il complesso ed eterogeneo processo di aggregazione delle proteine e per fornire informazioni sul percorso di aggregazione e sulla morfologia, struttura e proprietà meccaniche delle specie formate durante il processo di aggregazione.

Inizialmente, la realizzazione di mappe morfologiche convenzionali è stata utilizzata per comparare quantitativamente la cinetica di aggregazione di forme standard e mutate dell'huntingtina e dell' α -synucleina. Nel primo caso, abbiamo focalizzato l'attenzione sull'effetto di mutazioni post-traslazionali nell' N-terminus della proteina nel modificare la sua dinamica di aggregazione. Questo, ci ha permesso di dimostrare che una forma fosforilata della proteina aggrega molto più lentamente che la forma non mutata. In particolare, entrambe le due

forme studiate hanno mostrato di essere capaci di fibrillare anche sotto la soglia genetica necessaria per l'insorgere della malattia. Nel secondo caso, abbiamo studiato la forma naturale e una forma mutata dell' α -synucleina, quest'ultima è legata all'insorgere genetico del morbo di Parkinson. Il nostro studio ha permesso di dimostrare che questa mutazione è strettamente legata alla malattia ed è capace di aumentare la sua propensione ad aggregarsi. Successivamente, abbiamo anche studiato nel dettaglio i momenti iniziali dell'aggregazione di questa proteina. Questo studio ci ha permesso di mostrare che l'aggregazione procede direttamente attraverso la formazione di catene di monomeri misfoldati. Per dimostrare che queste strutture non possiedono ancora una completa struttura amiloide, ne abbiamo anche investigato le loro proprietà meccaniche grazie alla spettroscopia a forza atomica.

Nella seconda parte di questo lavoro il mapping quantitativo delle proprietà nanomeccaniche (PF-QNM) e la spettroscopia ad infrarosso su scala nanometrica (nanoIR) sono state usate per svelare le proprietà meccaniche e strutturali degli amiloidi su scala del singolo aggregato. Il PF-QNM è stato utilizzato per monitorare l'evoluzione delle proprietà meccaniche e per dimostrare che il contenuto di struttura secondaria β è uno dei fattori principali nel determinare la loro elasticità. Il NanoIR è stato applicato per investigare su scala nanometrica le specie amiloidi presenti durante il processo di aggregazione. Un primo esperimento ha permesso di mostrare che lo strumento è in grado di discernere proteine nello stato monomero e proteine aggregate sotto forma di micro-gocce. Un secondo studio, ha dimostrato che la tecnica è capace di caratterizzare *single* specie amiloidi, durante il processo di aggregazione della proteina Josephina. Lo strumento ha permesso di studiare la struttura secondaria degli aggregati e, grazie a misure parallele di elasticità, di collegare direttamente per la prima volta su scala del singolo aggregato le proprietà meccaniche e strutturali delle specie amiloidi.

Le innovative tecniche usate in questo studio hanno permesso di collegare direttamente su scala nanometrica le proprietà morfologiche e ultrastrutturali degli amiloidi. Per tale ragione, rappresentano una interessante e fruttuosa strada per elucidare in dettaglio le proprietà e il meccanismo di formazione degli amiloidi. Queste informazioni sono fondamentali per trovare un rimedio all'insorgere delle malattie correlate alle malattie neurodegenerative.

Parole Chiave: Disordini Neurodegenerativi; Amiloidi; Aggregazione; Fibrillizzazione; Microscopio a Forza Atomica; Tecniche a singola molecola; Spettroscopia ad infrarosso; Misure di struttura secondaria; Proprietà nanomeccaniche.

List of Figures

Chapter 1

Figure 1.1 Amyloid fibrils, cross- β structure and related X-ray diffraction pattern.....	3
Figure 1.2 Influence of side chains on the amyloid structure.....	4
Figure 1.3 Fibrils self-assembly polymorphism.....	5
Figure 1.4. Schematic depiction of the nucleation dependent process of amyloid fibrils formation.....	6
Figure 1.5 Possible processes of amyloids nucleation.	7
Figure 1.6. Schematic representation of proteins conformational states bringing to amyloid formation.	8
Figure 1.7 α -synuclein structure	12
Figure 1.8 Human Huntingtin exon 1 sequence and major subdomains.	14
Figure 1.9 Structure of ataxin-3 e and its subdomains.	16
Figure 1.10 Circular dichroism signal for proteins with α -helical, random coil and β -sheet structure.....	20
Figure 1.11 Schematic depiction of Scanning Tunneling Microscopy and Atomic Force Microscopy.	23
Figure 1.12 Summary of the possible relevant Forces in AFM.....	25
Figure 1.13 AFM tip-sample potential energy representation and related AFM scanning modes.	26
Figure 1.14 Schematic depiction of AFM phase shift measurements.	27
Figure 1.15 AFM Schematic illustration of the convolution of the shape of the AFM tip with the shape of the feature or particle being scanned.....	29
Figure 1.16 Schematic depiction of a semi-flexible polymer and the parameter used to calculate its persistence length.....	29
Figure 1.17 Ideal force-displacement curve depiction.	31
Figure 1.18 AFM-based methods to investigate biomolecules and amyloid aggregates nanomechanical properties.....	32
Figure 1.19 Nanoindentation measurements.	32
Figure 1.20 Principle of operation of PF-QNM.	34
Figure 1.21 Schematic depiction of nanoscale infrared spectroscopy working principle.	35
Figure 1.22 NanoIR imaging and spectra acquisition of a bundle of collagen fibrils.	36

Chapter 2

Figure 2.1 Substrates used for AFM imaging.	43
Figure 2.2 Oligomerization and Fibrillization process of wild type and pT3 huntingtin.	45
Figure 2.3 AFM analysis of monomeric α -synuclein at a low concentration of deposition.	47
Figure 2.4 Aggregation process of wild type and mutated H50Q α -synuclein.	48
Figure 2.5 Morphology of fibrillar structures of WT and mutated H50Q.....	50
Figure 2.6 α -synuclein prefibrillar structures in-pathway of aggregation.....	51
Figure 2.7 <i>Fast</i> aggregation of α -synuclein at 45 μ M and pH 5.5 on APTES-mica.....	51
Figure 2.8 <i>Slow</i> aggregation of α -synuclein at pH 5.5 and 45 μ M on three different surfaces: mica, APTES-mica and HOPG.	52
Figure 2.9 Statistical analysis of early oligomeric species during the <i>slow</i> aggregation process of α -synuclein.	53
Figure 2.10 Statistical analysis of prefibrillar species on mica, APTES-mica and HOPG.	54
Figure 2.11 Polymorphism of α -synuclein protofilaments.	55
Figure 2.12 Comparison of the height of circular DNA and protofilaments.	56
Figure 2.13 Early aggregation model of α -synuclein.....	58

Chapter 3

Figure 3.1 Morphology of oligomeric and prefibrillar α -synuclein species.	65
Figure 3.2 Mechanical response as a function of oligomeric or prefibrillar species.	67
Figure 3.3 Force response of manipulated α -synuclein protofilaments.	68
Figure 3.4 Comparison of the lengths of α -synuclein protofilaments and lengths of plateaus events in the corresponding force curves.	69
Figure 3.5 Comparison of the lengths of plateaus events in the force curves.	70
Figure 3.6 Analysis of the constant force plateaus.	71
Figure 3.7 Comparison between the experimental data and the Monte Carlo simulations.	74
Figure 3.8 Model of single protofilaments pulling.	77

Chapter 4

Figure 4.1 Kinetics of amyloid fibrils formation and secondary structure measurements.	84
Figure 4.2 AFM imaging of α -synuclein and A β -42 fibrillization process.	85
Figure 4.3 Analysis of the morphology of α -synuclein oligomers and fibrils.	86
Figure 4.4 Analysis of the morphology of A β -42 oligomers, protofibrils and fibrils.	87
Figure 4.5 Young's modulus of α -synuclein oligomeric species.	88
Figure 4.6 Young's modulus of α -synuclein fibrillar species.	89
Figure 4.7 Stiffness of a α -synuclein bundle of fibrils.	90
Figure 4.8 Young's modulus evolution of A β -42 during fibrillization process.	91

Chapter 5

Figure 5.1 Droplets deposition on the prism for the Infrared Nanospectroscopy analysis.	98
Figure 5.2 Micrograph of droplet formation in a microfluidic device.	99
Figure 5.3 View of the aligned droplets.	101
Figure 5.4 Atomic force microscopy images of droplets dried under different conditions.	102
Figure 5.5 IR absorption maps of aggregated lysozyme.	103
Figure 5.6 IR Spectra from micro-droplets.	105
Figure 5.7 Spectra of monomeric and aggregated proteins with different method of deposition.	106

Chapter 6

Figure 6.1 Josephin's aggregation and fibrillization process.	115
Figure 6.2 Morphological analysis of the oligomerization process.	116
Figure 6.3 Young's modulus increases as a function of aggregation.	117
Figure 6.4 AFM-IR chemical map of Josephin proteins before incubation at 37 °C.	118
Figure 6.5 AFM-IR spectra of the oligomeric species before incubation.	119
Figure 6.6 nanoIR laser's power spectrum.	120
Figure 6.7 Average oligomeric IR spectrum and secondary structure de-convolution of amide I band.	121
Figure 6.8 Smallest detectable structures by infrared nanospectroscopy.	122
Figure 6.9 AFM and nanoIR analysis of oligomers at 2 days of incubation.	123
Figure 6.10 Morphological properties of aggregates after 7 days incubation.	124
Figure 6.11 Spectra of oligomeric and fibrillar structures after 7 days incubation.	124
Figure 6.12 PCA analysis.	126
Figure 6.13 Model of the link between nanomechanical and structural properties.	127

Table of Contents

Chapter 1. Introduction	1
1.1 Amyloids, Neurodegeneration and Nanotechnological Applications	1
1.1.1 Brief Early History	2
1.1.2 Amyloid Structure	3
1.1.3 Misfolding and Amyloid Aggregation	5
1.1.4 Misfolding diseases	9
1.1.5 Functional amyloids and Nanotechnology Applications.....	16
1.2 Biophysical Investigation of Amyloid Properties and Formation.....	19
1.2.1 Spectroscopic Bulk techniques.....	19
1.2.2 Single molecule investigation by Atomic Force Microscopy techniques	22
1.3 Objective of the Thesis.....	37
Chapter 2. AFM as a versatile tool to investigate pathway and kinetics of amyloids formation .	39
2.1 Introduction	40
2.2 Experimental Methods	42
2.3 Kinetics of Aggregation of Wild Type and Phosphorylated Huntingtin	44
2.4 Role of H50Q mutation in α -synuclein kinetics of aggregation and early stages of fibrillization	46
2.4.1 Comparison of the kinetics of aggregation of WT and H50Q mutated α -synuclein.....	46
2.4.2 Early aggregation pathway of wild type α -synuclein.....	50
2.5 Discussion	59
Chapter 3. Nanomechanical Manipulation of Amyloid Protofilaments of α-synuclein	61
3.1 Introduction	62
3.2 Experimental Methods	63
3.3 Results	64
3.3.1 AFM morphology studies of amyloid aggregates as a function of the incubation time	64
3.3.2 Force response as a function of the amyloidogenic species	66
3.3.3 Nanomechanical Manipulation of α -synuclein protofilaments	68
3.3.4 Elastic properties of α -synuclein prefibrillar species	72
3.3.5 Monte Carlo modeling of the process of protofilaments of α -synuclein unzipping from the surface	73
3.4 Discussion	75

Chapter 4. Content of β-sheet Controls Mechanical Properties of Aggregates during Amyloid Fibrillization	79
4.1 Introduction	80
4.2 Experimental Methods	81
4.3 Results	83
4.3.1 Aggregation process studies by conventional bulk techniques	83
4.3.2 Fibrillization investigation by conventional Atomic Force Microscopy	84
4.3.3 Peak-force Quantitative nanomechanical measurements of amyloid aggregate stiffness	87
4.4 Discussion	93
Chapter 5. Nanoscale spatially resolved infrared spectra from single microdroplets	95
5.1 Introduction	96
5.2 Experimental Methods	98
5.3 Results	101
5.3.1 Patterned micro-droplets	101
5.3.2 Infrared Nanospectroscopy Absorption Maps	103
5.3.3 Infrared Nanospectroscopy Spectra.....	104
5.3.3 Sensitivity and throughput of the method.....	107
5.4 Discussions.....	108
Chapter 6. Infrared nanoSpectroscopy Characterization of oligomeric and fibrillar Aggregates during amyloid Formation	109
6.1 Introduction	110
6.2 Experimental Methods	112
6.3 Results	114
6.3.1 Morphological properties of Josephin aggregates	116
6.3.2 Nanomechanical properties of Josephin aggregates	116
6.3.3 Infrared nanospectroscopy of Josephin amyloid species.....	117
6.3.4 Spectral signature of amyloid structure formation	125
6.3.5 Correlation between nanomechanical and structural properties	126
6.4 Discussion	128
Chapter 7. Conclusions and future perspectives	131
CURRICULUM VITAE - FRANCESCO SIMONE RUGGERI	137
Bibliography	141

Chapter 1. Introduction

This first introductory chapter consists of two main parts. The first one defines the amyloid state of proteins and it describes the state of the art of amyloid properties and formation, as it is known today. Besides, it relates the problem of protein aggregation to misfolding diseases and nanotechnological applications. The second part describes the experimental path followed in this thesis to bring new insights into the amyloid formation and ultrastructural properties. The used methodologies are strictly related to the biophysical investigation conducted in this thesis are presented. They are divided in two categories: spectroscopic bulk techniques and the single molecule atomic force microscopy (AFM) based methods. In particular, last part of the chapter presents the application of recently established innovative AFM-based techniques enabling to study at the nanoscale amyloid formation and properties.

1.1 Amyloids, Neurodegeneration and Nanotechnological Applications

Aging of the world population has increased the visibility of several human neurodegenerative disorders and diseases such as Parkinson's, Huntington's, Alzheimer's diseases, diabetes of type II and several forms of Ataxia.¹⁻³ The onset of these and of more than fifty further related pathologies is associated at the molecular level with the proliferation of insoluble fibrillar protein aggregates, termed amyloids⁴, formed from normally soluble cellular proteins. Despite their key role in human health disorders, amyloid fibrils are not only associated with pathology, and such structures have recently been discovered in many physiologically beneficial roles. These include bacterial coatings, catalytic scaffolds, adhesives and structures for the storage of peptide hormones,⁵⁻⁷ for which the term of *functional* amyloids has been cast. Amyloid fibrillar aggregates possess a universal cross β -sheet quaternary structure and are highly resistant to proteolytic degradation.⁸ Interestingly, despite the obvious differences in amino acid sequences and native structure, these amyloidogenic peptides all appear to share a common β -sheet conformation of their polypeptide backbone and it is likely that this characteristic confers the fibrillar, proteolytic resistant and insoluble features to all forms of amyloids. From a structural point of view, they are unbranched, several micrometer long fibrils, with a diameter of the order of 10 nm.^{8,9} Moreover, amyloidogenic structures exhibit remarkable mechanical properties with Young's moduli in the range of several GPa.¹⁰⁻¹²

1.1.1 Brief Early History

The term amyloid, meaning starch-like (*amylum* in latin) was coined initially by Virchow in the 19th century to describe structural bodies in human tissues, such as the iodine stained deposits seen in liver during *post-mortem* autopsy.¹³ He discovered that the macroscopic tissue abnormality stained pale blue on treatment with iodine, and violet upon the subsequent addition of sulfuric acid.¹⁴ For this reason, he concluded that the substance underlying the evident macroscopic abnormality was cellulose. At that time, the distinction between starch and cellulose was unclear and Virchow considered the amyloid substance to be starch. This hypothesis did not stand for long; indeed, few year later, Friedrich & Kekule demonstrated that proteins are the major component of amyloid deposits. Despite the demonstration of the proteinaceous nature, the name amyloid has endured.¹⁵ The initial method used to identify amyloid was that of iodine staining, introduced by Virchow. This method was soon replaced by one of the most important histological staining marker for amyloid, Congo red, which was introduced by Bennhold.¹⁶ In particular, the aggregates have a specific binding to the dye Congo Red which produced an apple green birefringence when examined between cross polarizers in a light microscope. Other staining methods have been successively developed and several of them are still used; the most important of these is probably Thioflavin T.^{17,18} The birefringence of polarized light suggested that amyloid was fibrillar in structure. We could affirm that the modern history of amyloidosis investigation have started with the discovery by Cohen and Calkins¹⁹ that amyloid are not amorphous, as contrarily suggested by light microscopy. Indeed, the two scientists showed by electron microscopy that amyloids have a characteristic fine fibrillar ultrastructure. This finding was confirmed in several other studies and pointed to a specific structural organization of the constituent proteins – an idea that at that time was a complete breakthrough. Finally, progress in biochemical and biophysical techniques enabled the isolation of amyloid fibrils from tissues and their X-ray fiber diffraction patterns allowed the interpretation of the nowadays universally accepted characteristic cross- β structure.²⁰ For a long time it was believed that all amyloids possess the same amino acid composition. Sequence analysis of the proteins comprising a range of ex vivo amyloid fibrils revealed that each amyloid disorder was associated with a particular protein or peptide. One of the first amyloidogenic protein to be isolated and analyzed was the A β peptide, which was discovered to be the main component forming the bulk of amyloid plaques in Alzheimer's diseased brain specimens.²¹ Together with the postulation of the “prion hypothesis” describing the possibility of infectious amyloid protein species and the discovery of its link with the Creutzfeldt-Jacob

disorders (spongiform encephalopathies),^{22,23} these findings enormously raised the interest of the scientific community in amyloids formation and properties. A new class of protein-related human diseases, due to not classical infectious agents as viruses and bacteria, was identified fuelling a new area of intense research.

1.1.2 Amyloid Structure

Amyloid fibrils appear at the atomic force microscopy or at the electron microscopy as unbranched elongated structures just few nanometers in diameter, but with several micrometers of length. As demonstrated by X-ray diffraction, amyloid characteristic fingerprint is the universal cross- β sheet quaternary structure.^{8,20} The repeating subunit of such structure consists of β -strands, forming continuous hydrogen-bonded β -sheets, which are oriented perpendicularly to the fibril axis.²⁴ The β -sheet ribbons are associated via side chain interactions that serve to stabilize the structure, which is closely packed and highly ordered.²⁵ The repeating cross- β motif gives rise to two characteristic X-ray diffraction patterns: 1) a meridional reflection at ~ 5 Å, corresponding to the inter β -strand spacing, 2) an equatorial reflection at ~ 10 Å corresponding to the distance between stacked β -sheets (**Fig. 1.1**).²⁴

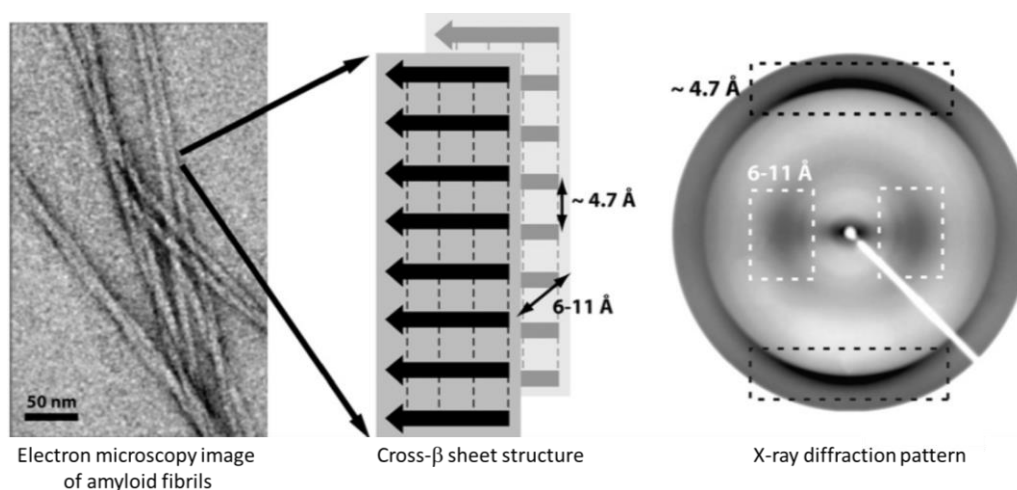


Figure 1.1 Amyloid fibrils, cross- β structure and related X-ray diffraction pattern. Adapted from Ref. 24.

Notably, there is not a clear similarity in the sequence, structure and functions of the group of amyloidogenic proteins. Indeed, the cross- β structure is largely independent of the sequence of the polypeptide chain of the precursor protein and a number of unrelated

polypeptide sequences have been observed to form fibrils with a very similar structure at atomic level.^{8,26} Moreover, notwithstanding that the amyloid state was identified in the context of human diseases, several studies have shown that a wide class of peptides and proteins can aggregate into amyloid fibrils with same characteristics as the ones related to diseases. These findings suggest that the amyloid structure could be adopted by any polypeptide chain.²⁷ To support this hypothesis, several experiments have been performed to show that homopolymers made up of only one type of amino acid can form the cross- β sheet structure.²⁸ Besides, several of the possible amyloid structures proposed, suggested that the amyloid core region is generally composed by two or four β -sheets interacting closely each other.^{4,29,30} Nevertheless, several observations have demonstrated that the details of the structure and its stability are highly dependent on the side chains of the aggregating sequence.¹¹ These details include the length of β -strand, the parallel or antiparallel arrangement of the β -sheets, the inter-sheet distance and the arrangement of all the other regions that are not part of the fibril core (**Fig. 1.2**).²⁸ All these results confirm the universality of the amyloid state, which is accessible to extremely different polypeptide chains independently of their sequence.^{31,32}

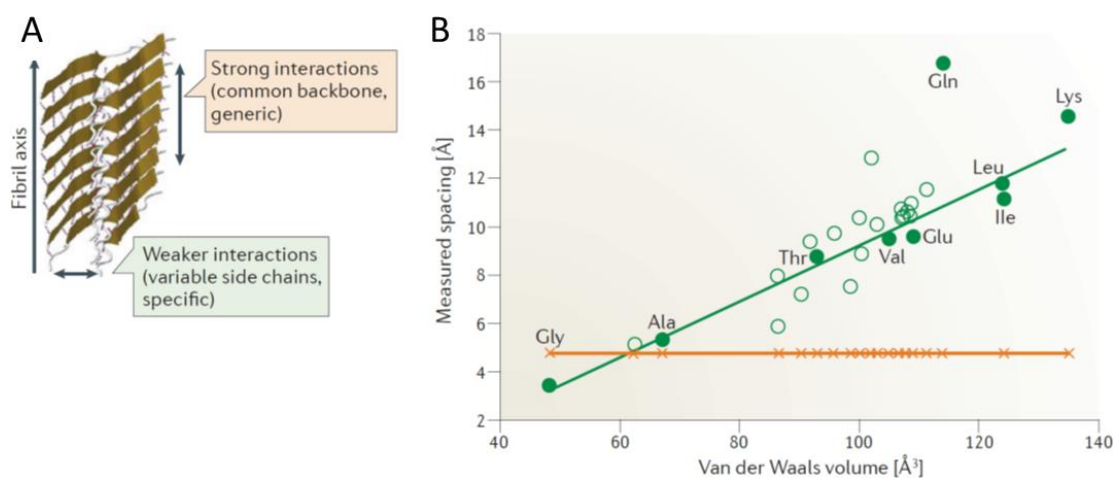


Figure 1.2 Influence of side chains on the amyloid structure.

(A) Schematic universal cross β -sheet structure. (B) β -strands spacing (orange) and β -sheets distance (green) as a function of the amino acid side chain van der Waals volume (filled green circles indicate homopolymers, open symbols heterogeneous sequences). Adapted from Ref. 27,28.

These investigations also confirmed the observation that mature amyloid fibrils are formed by the hierarchical self-assembly³³ of cross- β protofilaments, composed by a pair of β -sheets, twisting together through specific side chains interactions.²⁶ Although the basic structural arrangement of the cross- β structure is conserved for different fibrils, there are

different ways how protofilaments can pack into the three-dimensional fibril structure and causing a range of structurally different amyloid fibrils (**Fig. 1.3**).³⁴ Morphological different fibrils can diverge in the nature and number of component protofilaments, in their arrangement inside the fibrils and in several structural properties, such as the cross-sectional thickness, helical periodicity and chirality.³⁵⁻³⁹ This heterogeneity is termed *polymorphism* and it implies that, for the same peptide, fibril formation can lead to many different patterns of inter- or intra-residue interactions.^{34,36,40}

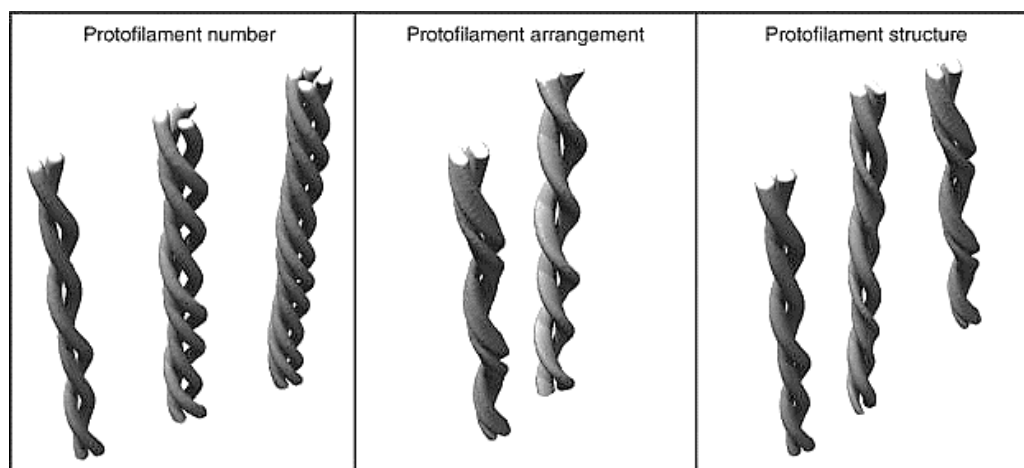


Figure 1.3 Fibrils self-assembly polymorphism.

Several examples of fibrils polymorphism are shown. In particular, polymorphism can be due to different number, arrangement and structure of protofilaments composing the fibril. From Ref. 34.

1.1.3 Misfolding and Amyloid Aggregation

The *native state* of a protein was initially associated with a compact globular conformation possessing a rigid and highly ordered structure. It was discovered that the structure of globular proteins is encoded in their amino acids sequences and that these proteins spontaneously fold following a diffusional search of a conformational free energy minimum, which corresponds to the native state.^{41,42} Later on, it has been discovered that certain proteins do not form a rigid globular structure and that in their native structure they are intrinsically disordered, even under physiological conditions. These proteins are still able to fulfill their specific functions and they are termed *intrinsically disordered* or *naturally unfolded* proteins.⁴³⁻⁴⁵ The existence of the disordered regions allows these proteins to interact with their numerous binding partners, which eventually led the protein to acquire a *partially folded* state.^{46,47} Such interactions are often accompanied by the formation of complexes that possess a more ordered structure than the

original components and lower free energy minima than the native state.^{43,47,48} This implies that proteins can acquire other biologically relevant conformational states different from their native one. Globular proteins can also adopt intermediate conformations simply as consequence of thermodynamical fluctuations, which correspond to local minima in their energy landscape.^{49,50} Some globular proteins are shown to have unstructured, highly dynamic fragments (termini, loops, etc.).^{51,52} Furthermore, partially unfolded states could retain a biological function as cellular trafficking and translocations through mitochondrial and nuclear membranes.⁵³⁻⁵⁵

The partially folded/unfolded states of a protein, independently of its globular or naturally unfolded conformation, are vulnerable to *misfolding* and to aggregation into amyloid structures.^{4,27,42,56-58} This condition is promoted by conditions that destabilize the native fold of the protein, such as high temperature, high pressure, low pH, organic solvents, natural or post-translational mutations.^{57,59,60} During their aggregation, proteins initially in their native monomeric forms undergo internal structural rearrangement, and misfold into conformations that are susceptible to form fibrils.⁸ Besides, several coexisting aggregate species are formed, giving rise to a highly heterogeneous reaction mixture. The fibrillation process typically takes the form of a nucleation-dependent polymerization reaction.^{27,61,62} This model supposes that the formation of oligomeric structures is necessary to nucleate the first protofibrillar structures, ultimately leading to the formation of the mature amyloid fibrils. This process is typically described by a sigmoidal reaction time course, commonly measured by ThT fluorescence and light scattering assays (**Fig. 1.4**).^{18,63}

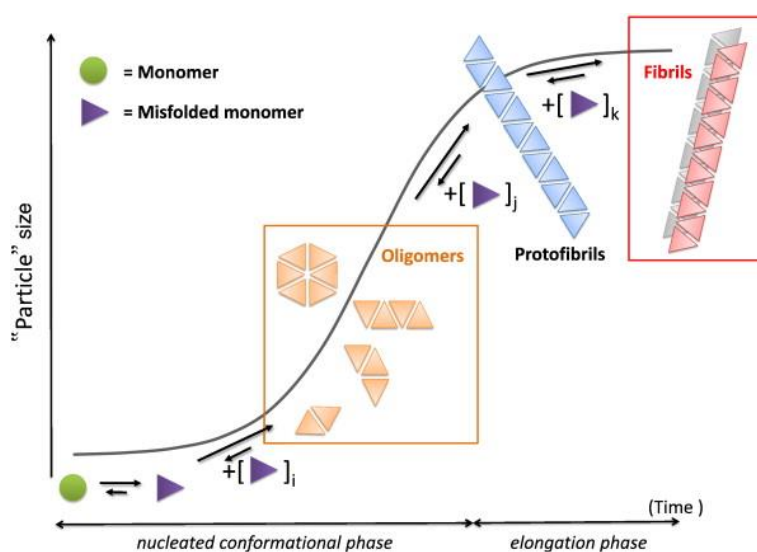


Figure 1.4 Schematic depiction of the nucleation dependent process of amyloid fibrils formation. From Ref. 64.

According to the classical nucleation process, a primary nucleation step is necessary for the formation of aggregates, but in the case of amyloid fibrils several secondary steps exist that can be involved.⁶⁵ In these secondary processes, the formation of the nuclei is catalyzed by fibrils fragmentation or surface catalyzed secondary nucleation (**Fig. 1.5**).²⁷ The availability of integrated laws describing protein aggregation allows to extrapolate the microscopic parameters determining amyloid fibrillization and to individuate if primary or secondary nucleation processes dominate.⁶⁵⁻⁶⁹

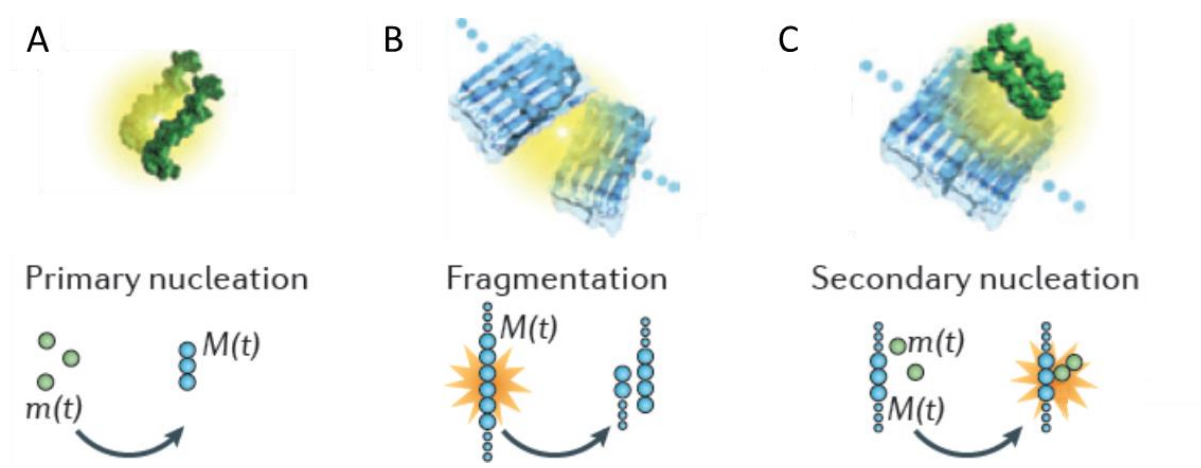


Figure 1.5 Possible processes of amyloids nucleation.

A) Primary nucleation, monomers interact to form an oligomeric nucleus. B) Fragmentation, a nucleus breaks forming two nuclei. C) Nuclei surface catalyze the aggregation. Adapted from Ref. 27.

The conventional “first-misfolding-then-aggregation” paradigm is the generally accepted process of amyloid formation, but several observations have shown that the misfolding process could take place after a first step in which native monomers aggregate (“first-aggregation-then-misfolding”).⁷⁰⁻⁷² These native oligomers undergo a structural misfolding to form the early cross- β sheets aggregate and the final amyloid fibrillar structures only in a second step. Despite the initial difference, both pathways are conceptually similar: a misfolded state, monomeric or oligomeric, is necessary to nucleate the formation of the universal amyloidogenic cross- β sheet structure.

Notwithstanding the great success of the kinetics descriptions of amyloid formation^{66,68,73-76}, the full elucidation of the process requires the identification of all the conformational and oligomeric states adopted by the protein and of its possible aggregates. Indeed, structural polymorphism can be encountered at all aggregation levels, and it originates as a consequence of the glassy, frustrated energy landscape that underlies misfolding and

aggregation.⁴⁰ Furthermore, oligomeric and protofibrillar structures can form both in-pathway and off-pathway of mature fibrils formation.⁷⁷⁻⁷⁹ In **Fig. 1.6**, we can observe a schematic depiction of the different conformational states populated by a protein leading to the formation of oligomeric and fibrillar structures, which can be either biologically functional or disease-related. All these conformational states are regulated in the cell's biological environment by molecular chaperones, degradatory systems and quality control systems.^{4,56,57,80-82}

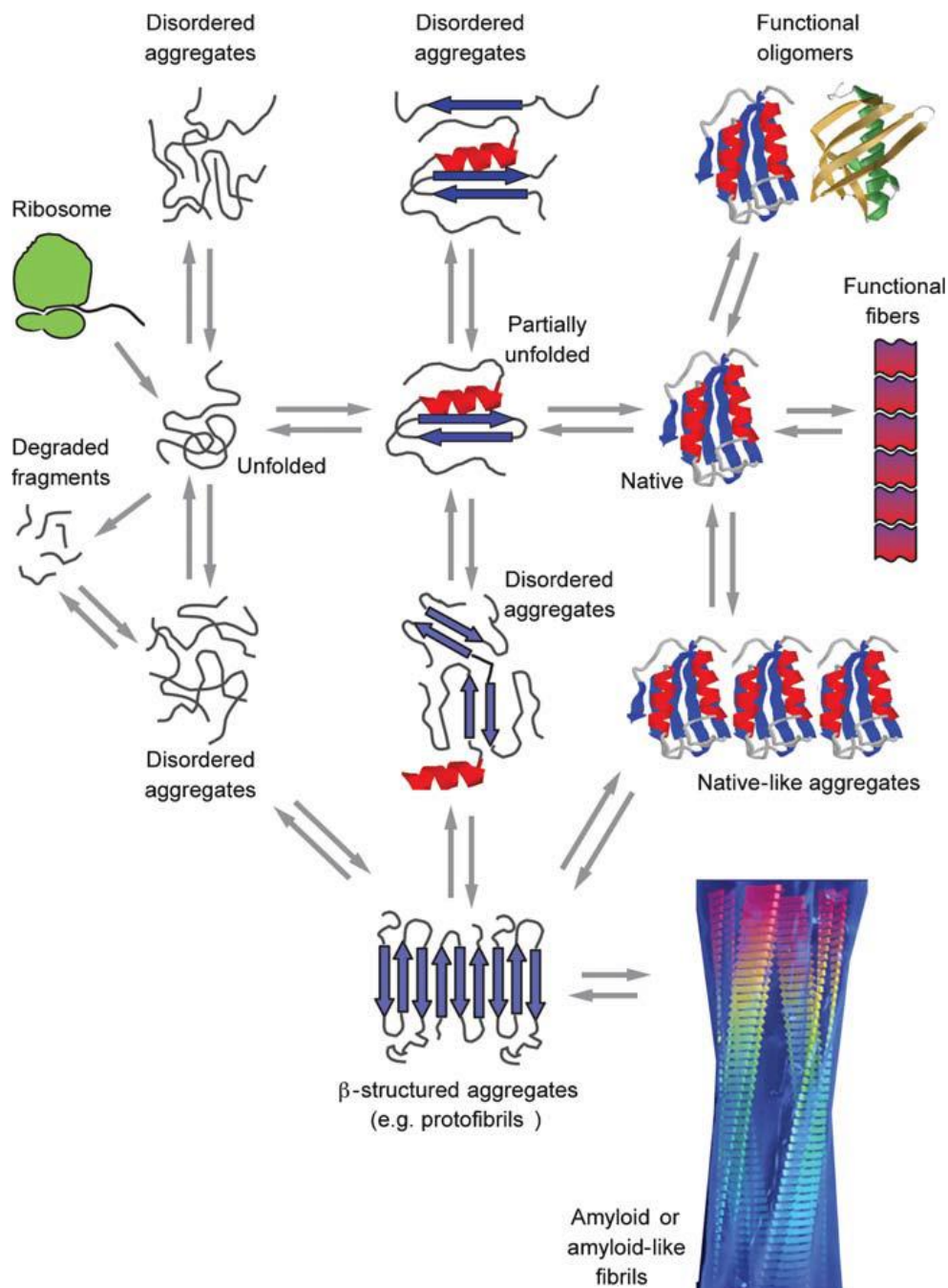


Figure 1.6 Schematic representation of proteins conformational states bringing to amyloid formation. From Ref. 4.

1.1.4 Misfolding diseases

A broad range of human diseases and neurodegenerative disorders is due to the failure of a specific peptide or protein to keep its native functional conformational state. This group of debilitating pathologies has received increasing visibility because of their link to the ageing of the world population in the last century. There are up to now approximately 50 illnesses associated with protein aggregation and formation of amyloid structures and they are generally indicated as *protein-misfolding diseases*. In **Table 1.1**,⁴ a selected list of amyloid-caused human diseases is shown. They can be divided in three classes: neurodegenerative diseases, including Parkinson's, Alzheimer's, the several forms of ataxias and the spongiform encephalopathies;⁸³ non-neuropathic systemic amyloidosis, such as lysozyme amyloidosis;⁸⁴ non-neuropathic localized amyloidosis, such as diabetes of type II, which is an endemic disease affecting approximately the 6% of human beings.⁸⁵⁻⁸⁷ The major part of these diseases are predominantly sporadic (85%), such as Parkinson's and Alzheimer's diseases, while others as lysozyme amyloidosis and Huntington's disease arise from genetic mutations and are hereditary (10%). In addition, spongiform encephalopathies (5%) are transmissible from animals to humans and are highly infectious.²³

Table 1.1 List of Misfolding Diseases. From Ref. 4.

Disease	Aggregating protein or peptide	Structure of protein or peptide
Neurodegenerative diseases		
Alzheimer's disease	Amyloid- β peptide	Intrinsically disordered
Spongiform encephalopathies	Prion protein or its fragments	Intrinsically disordered and α -helical
Parkinson's disease	α -synuclein	Intrinsically disordered
Amyotrophic lateral sclerosis	Superoxide dismutase 1	β -sheet and Ig-like
Huntington's disease	Huntingtin fragments	Mostly intrinsically disordered
Familial amyloidotic polyneuropathy	Transthyretin mutants	β -sheet
Non-neuropathic systemic amyloidosis		
Amyloid light chain (AL) amyloidosis	Immunoglobulin (Ig) light chains or its fragments	β -sheet and Ig-like
Amyloid A (AA) amyloidosis	Serum amyloid A1 protein fragments	α -helical and unknown fold
Senile systemic amyloidosis	Wild-type transthyretin	β -sheet
Haemodialysis-related amyloidosis	β_2 -microglobulin	β -sheet and Ig-like
Lysozyme amyloidosis	Lysozyme mutants	α -helical and β -sheet
Non-neuropathic localized amyloidosis		
Apolipoprotein A1 (Apo A-1) amyloidosis	Apo A-1 fragments	Intrinsically disordered
Type II diabetes	Amylin	Intrinsically disordered
Injection-localized amyloidosis	Insulin	α -helical and insulin-like

Despite the widespread association of amyloid formation with disease states, the mechanistic role of amyloids in cell death and disease onset has remained challenging to identify. In particular, the nature of the specific state of proteins that is most prone to cause cytotoxicity is not well established. It is clear, however, that aggregated rather than monomeric proteins are primarily implicated in the toxicity characteristic of protein misfolding diseases. Evidences for this hypothesis derive from: pathology, aggregates localize in the region of neuronal loss; biophysics, mutated proteins associated to the disease aggregate more rapidly.⁸⁸ Initially, the prevalence of fibrillar protein aggregates in the brains of patients suffering from neurodegenerative disorders led many authors to hypothesize that these structures themselves cause cell death. Indeed, in the case of systemic amyloidosis, it seems that the major cause of the disease onset is simply the presence of large quantities, in some cases even kilograms, of amyloid deposits in vital organs, including liver, spleen and kidney.²⁷ Instead, in the case of neurodegenerative disorders, several studies revealed only a weak correlation between the quantities of accumulated amyloid fibrils and the disease symptoms. In these cases, recent evidence has increasingly suggested that prefibrillar aggregates, such as oligomers and protofibrils, might be the toxic components, rather than the final mature fibrillar products.⁸⁸⁻⁹¹ The oligomeric toxicity could arise from their misfolded nature and at least by partial acquisition of the cross- β sheet structure. In fact, the structural rearrangements during the misfolding and/or aggregation could expose hydrophobic chemical groups, otherwise buried by the protein folding in the case of globular proteins or dispersed in the case of intrinsically disordered proteins, which normally are not accessible to the cellular environment. The non-native structure of misfolded oligomers could, finally, interfere with several cellular components and processes. Such events could bring to a malfunctioning of the cellular machinery and of its crucial aspects as membranes integrity and trafficking, oxidative stress, sequestration of essential proteins, ions balance causing finally the cell's death.^{4,27,58}

In the following sections, we briefly describe the details of the neurodegenerative diseases, together with the related proteins, mainly investigated in the frame of this thesis:

Alzheimer's disease: – Approximately 20 millions of people worldwide have dementia.⁹² The majority of these cases are due to Alzheimer's disease (AD). The most common early symptom of the illness is the short-term memory loss, followed then by other behavioral and cognitive problems. For this reason, the pathology represents a major public health concern and it has been identified as a research priority. The two main pathological hallmarks of Alzheimer's

disease are amyloid plaques and intracellular neurofibrillary tangles, formed by the aggregation of the amyloid β proteins ($A\beta$).^{21,93} This peptide has a molecular weight of 4 kDa and it has an intrinsically disordered structure in solution.^{94,95} The biological role of the $A\beta$ peptides is not yet clear, though it has been suggested that they could be part of the mechanism controlling the synaptic excitatory activity.^{96,97} $A\beta$ proteins are produced in the brain by a sequential proteolytic cleavage of the type I transmembrane amyloid precursor protein (APP) by β - and γ -secretases. As a function of the site of APP cleavage by the secretase, proteins of different chain lengths are generated. The *amyloid cascade hypothesis* suggests that aggregation and deposition of $A\beta$ triggers neuronal dysfunction and death in the brain.⁹⁸ In the original hypothesis, the neuronal dysfunction and death was thought to be a toxic effect of the total fibrillar load. However, several studies showed that the number and size of plaques in post mortem AD brains do not correlate with the severity of the pathology and that amyloid plaques were found in the cortex of cognitively normal elder people.^{99,100} As the knowledge of pathological effects of Alzheimer's disease has increased, research has been focused on the specific alterations in $A\beta$ processing, such as the cleavage of amyloid precursor protein (APP) into $A\beta$ peptides, the most abundant of which are the $A\beta_{1-40}$ (90%) and $A\beta_{1-42}$ (10%) in humans. Despite its minor abundance in human plasma and cerebrospinal fluid, the $A\beta_{1-42}$ peptide has higher aggregation propensity and toxicity than $A\beta_{1-40}$.¹⁰¹ The ratio of these two isoforms is influenced by the pattern of cleavage from APP by β and γ secretases and it is more critical than the total amount of $A\beta$ produced.^{102,103} *In vitro* and *in vivo* studies have shown that $A\beta$ oligomers reduce glutamatergic synaptic transmission strength and plasticity, posing them as the putative toxic species.¹⁰⁴⁻¹⁰⁶ Indeed, since the protein is normally expressed in the organism and many different events could cause fibrils formation and disease, similarly as Parkinson's disease, it is now generally accepted that the prefibrillar intermediates could be the triggering factor of the disease.^{107,108} However, the molecular mechanisms of the toxicity of different $A\beta$ amyloidogenic species is still under debate, the discussed evidences permit to conclude that fibrillar structures are not the only species causing the disease. Fibrillar aggregate formation could be even a protective mechanism by the organism to sequester intermediate aggregates, which could be toxic because of their misfolded nature.

Parkinson's disease – This illness is part of a group of neurodegenerative disorders termed Lewy Body diseases and it affects the central nervous system. Parkinson's (PD) causes numerous devastating motor and non-motor manifestations, such as thinking and behavioral problems.² The pathology affects millions of people worldwide and substantial evidence links

its onset to α -synuclein.¹⁰⁹ The pathogenic role of this protein is confirmed by genetic data, rare familial cases of PD are associated with four missense point mutations in α -synuclein (A30P, E46K, A53T and H50Q) or with the hyper-expression of the wild type protein due to its gene duplication/triplication.^{110,111} Furthermore, α -synuclein was identified as the major component of amyloid fibrils found in Lewy bodies and Lewy neurites, the characteristic proteinaceous deposits that are the diagnostic hallmarks of sporadic PD. The protein is normally present in high concentration at presynaptic terminals and it is found in both soluble and membrane-associated fractions of the brain. It is a naturally unfolded protein and composed of 140 residues. Structurally it can be divided into three regions with distinct characteristics.⁸⁹ The N-terminal domain, which encodes for a series of imperfect 11 amino acid repeats with a consensus motif of KTKEGV reminiscent of the lipid-binding domain of apolipoproteins. The central hydrophobic region having propensity to form fibrils with β -sheet structure. The acidic C-terminal tail contains mostly negatively charged residues and is largely unfolded. When isolated in solution, the protein is intrinsically disordered. Numerous studies have established that recombinant α -synuclein easily assembles into amyloid-like fibrils both *in vitro* and *in vivo*.^{79,112-114} In the presence of lipid surfaces, α -synuclein adopts a highly helical structure that is believed to mediate its normal function(s), which are still debated.¹¹⁵⁻¹¹⁷

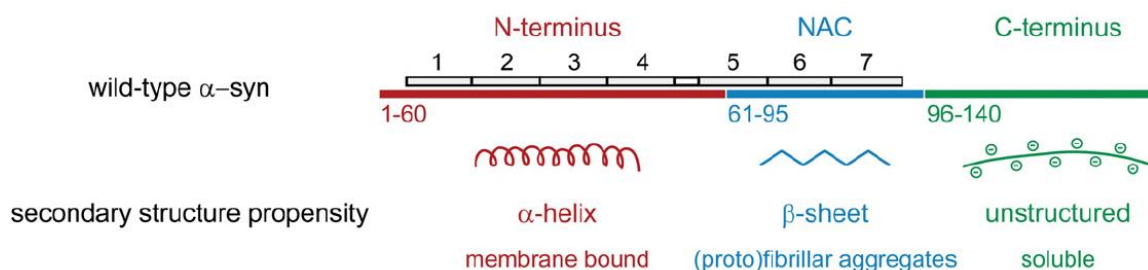


Figure 1.7 α -synuclein structure. From Ref. 118.

The role of α -Synuclein in cell death is unclear, as it is not known the form of the protein when it causes cell death. The bulk of the available evidence points to the aggregation of α -synuclein being essential for the pathological effects associated with PD. Moreover, the prevalence of fibrillar protein aggregates in PD brains has led many authors to hypothesize that they cause cell death. However, the survival of neurons with intracellular Lewy bodies shows that the presence of intracytoplasmic aggregates is not toxic to all cells and considerable evidence suggests that oligomers, formed as prefibrillar intermediates, may be the toxic

component.^{79,89} *In vitro* studies showed that annular oligomeric forms are able to destroy or permeabilize cellular and synthetic membranes, causing an increased flux of calcium in the cell.^{119,120} Oligomers could also cause toxicity by damaging mitochondria¹²¹, triggering lysosomal leakage¹²² or disrupting microtubules.^{123,124} Moreover, several studies suggest that the process of conversion of oligomers into fibrils is strictly connected to the disease onset. Indeed, mutations enhancing fibrillization also increase cytotoxicity, while mutations blocking oligomerization and fibrillization have a beneficial role.^{111,125} In addition, it was also showed that even if α -synuclein mutations enhance oligomerization, the loss of dopaminergic neurons is highly dependent on the ability of the protein to fibrillate.¹²⁶ Similarly as in the case of AD, this suggests that toxicity could be related to the progress of misfolding and aggregation or to the contemporary presence of oligomeric and fibrillar structures rather than only to the amyloid fibrils formation.

Polyglutamine diseases: Huntington's disease and Ataxia-3 – A growing number of neurodegenerative disorders, termed *polyglutamine diseases*, have been found to result from the expansion of an unstable CAG trinucleotide repeat coding for a polyglutamine (polyQ) tract in the respective protein.¹²⁷ Examples of such disorders are several forms of Ataxias and Huntington's disease.¹²⁸ Despite the lack of homology within the proteins involved in their onset, the pathologies all share fundamental common features: a severe neuronal dysfunction, an inverse correlation between age onset and length of the polyglutamine tract, a pathogenic threshold of the polyQ tract length, the presence of inclusion bodies constituted by the polyQ expanded protein.^{3,129}

Huntington's disease is an autosomal, dominant and strongly age-dependent neurodegenerative disorder. There are not sporadic forms of the pathology, which renders the disorder the most common inherited one.¹³⁰ The main symptoms are psychiatric disturbances, motor impairment and cognitive deficit. The disease is caused by a CAG expansion in the exon 1 of the IT-15 gene, which causes a consequent polyQ expansion of the encoded Huntingtin protein. The pathogenic threshold length for the disease onset is approximately 36-38 amino acids.^{131,132} Notably, CAG repeats in the exon 1 of the protein undergo expansion during transmission from one generation to the next. The severity of the pathology and the age of onset are directly linked to the length of the expanded polyQ tract.¹³¹ Huntingtin is a soluble and large protein of ~350 kDa. It has a folded structure with high α -helical content and the polyQ repeat domain starts at the residue 18. It has been difficult to establish the protein physiological

function, mainly because of its homology with other proteins and its ubiquitous expression. One of the main hypothesis suggested an anti-apoptotic role.^{133,134} The protein is subjected to several post-translational modifications, which are mainly clustered within the first 17 amino acids, and that are known to affect protein structure, aggregation and toxicity. Moreover, the protein undergoes several proteolytic cleavages, which lead to the formation of different N-terminal truncated fragments of the protein. In these shorter fragments, a polyQ expansion is more likely exposed.¹³⁵ Finally, the presence of diverse N-terminal huntingtin fragments in post-mortem brains affected by Huntington disease arouse the interest on their link to the disease. Strong evidences suggest that the N-terminal fragment 1-90, corresponding to huntingtin exon 1, is fundamental for the onset of the disorder. Indeed, if containing an expanded polyQ repeat, this fragment fibrillates into amyloid like fibrils and it is able to reproduce the neurological phenotype of the disease in animal models.^{136,137} Huntingtin exon 1 can be divided in five major subdomains: the 17 N-terminal amino acids (Nt17), the polyQ domain, two polyproline domains (polyP), a polyQ/P domain and the C-terminus.

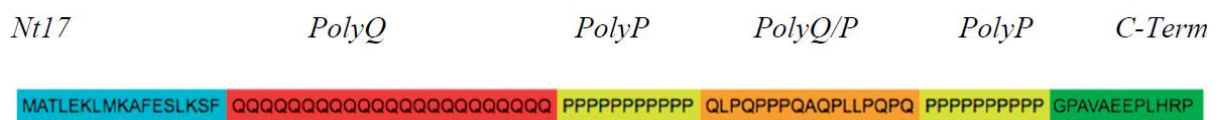


Figure 1.8 Human Huntingtin exon 1 sequence and major subdomains.

The polyQ and the Nt17 domains play a fundamental role in the aggregation of huntingtin exon 1. Initially, the aggregation of the protein was associated uniquely to the propensity of its polyQ domain to form a β -sheet core into the fibrillar structures when its length is larger than the pathogenic threshold.¹³⁸⁻¹⁴⁰ Several successive studies have shown that also the Nt17 terminus plays a critical role in promoting huntingtin aggregation.^{139,141} Indeed, huntingtin peptides lacking the Nt17 terminus have slower aggregation kinetics than the full-length counterpart. Additionally, it has been proposed that Nt17-mediated aggregation evolves through the formation of α -helical oligomeric intermediates, which could be the fundamental factor for the formation of the final cross- β sheet fibrillar structure.^{142,143} As previously described, it has been supposed that oligomers are the toxic species triggering the disease, however several contrasting evidences support both the hypothesis of a protective and toxic role of the protein inclusions in the brain.^{130,132,144-146} This discrepancy on the toxicity mechanism may be reconciled by taking into account the diversity of oligomeric and fibrillar forms of the expanded proteins. Indeed, morphology, composition and structure of polyQ

aggregates vary according to experimental conditions, subcellular localization, tissue environment, length of the polyQ and post translational modifications.¹⁴⁶ Regardless of the nature of the involved species, toxicity is likely associated with: the failure of the degradation system in the cells, as suggested by the presence in the inclusions of proteasome and chaperones subunits; the sequestration by the aggregates of heterologous proteins, making them unable to solve their function; with the cellular membrane permeabilization by pore-like intermediate species, as in the case of AD and PD.¹⁴⁴

Dominantly inherited spinocerebellar ataxias (SCA) are a group of neurodegenerative disorders characterized by a degeneration of the cerebellum, spinal tracts and the brain stem.¹²⁷ Spinocerebellar ataxia type 3 (SCA3) is the most frequent form among them and it is known as Machado-Joseph disease (MJD).¹⁴⁷ The bulk of the evidence links the onset of the disorder to CAG repeats expansion in the MJD1 gene, which results in an abnormal polyQ expanded region in the encoded ataxin-3 protein.^{3,128} The pathogenic threshold length for the disease onset is when the polyQ tract is longer than 48-52 glutamines. There is not a clear correlation between the onset and the CAG repeat length, which just accounts for the 50% of the total variability in the age of onset.¹⁴⁸ In particular, the aggregation of human ataxin-3 into amyloid fibrils and its neuronal inclusions, is responsible for the disease.¹⁴⁹ Ataxin-3 is a ubiquitously expressed deubiquitinating enzyme, with important functions in the proteasomal protein degradation pathway.¹⁵⁰ The protein has a variable molecular weight between 42–52 kDa and it is composed by a folded N-terminal domain (Josephin; residues 1–182), three ubiquitin interacting motifs (UIMs), a polyQ stretch of variable length and a C-terminal region.^{52,149} The polyQ region has been object of intense investigation, since it is insoluble in water and it has strong tendency to aggregate depending on the number of consecutive residues within polyQ stretches. However, it has been demonstrated that the Josephin domain of ataxin-3 strongly modulates the aggregation kinetics and aggregates into amyloid-like structures when isolated, suggesting that the full-length ataxin-3 aggregates with a two-stages mechanism.¹²⁹ The first stage involves interacting Josephin domains resulting in the formation of prefibrillar aggregates. The second stage consists of a polyQ aggregation step causing a subsequent misfolding event, and resulting in formation of insoluble fibrils.¹⁵¹ Thus, the two domains in ataxin-3, with an intrinsic ability to misfold, aggregate sequentially.¹⁵² Moreover, Josephine fibrillar structures have high similarity with the full-length ataxin-3 ones¹⁵³ implying that the Josephin domain has a strong influence on the aggregation pathway and on the shape and structure of ataxin-3 fibrils. It has been also shown that Josephin aggregation can be promoted by the exposition of hydrophobic

surfaces, otherwise buried in the native protein structure. This observation suggests that a structural rearrangement may not be necessary to induce aggregation and, as described above, that misfolding could be successive to the early aggregation process of the proteins.^{4,154}

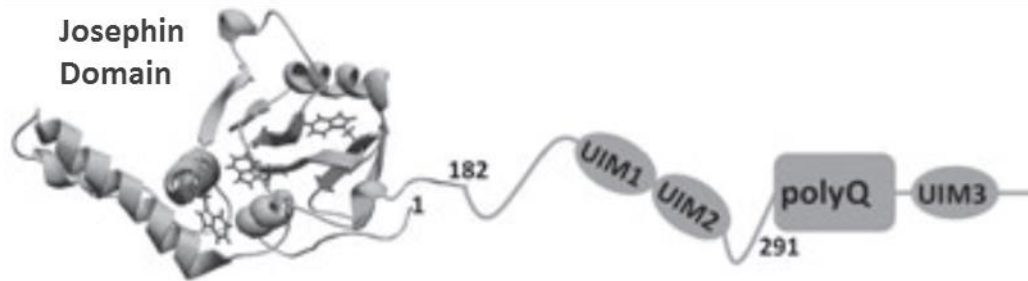


Figure 1.9 Structure of ataxin-3 e and its subdomains. Adapted from Ref. 52.

The expanded polyQ stretch in the C-terminus of ataxin-3 is thought to be the cause of the conformational changes of the protein aggregates, which may result in altered binding properties, loss of protein function, altered subcellular localization and proteolytic cleavage.¹⁵⁵ As suggested in the previously described disorders, intracellular ataxin-3 aggregates are probably not the main toxic entities in SCA3. The soluble protein fragments containing expanded polyQ, arising from proteolytic cleavage of ataxin-3 by caspases and calpains, are now considered fundamental in the pathogenesis.^{156,157} Moreover, recent evidence suggests potential involvement of a RNA toxicity component in SCA3 and other PolyQ expansion disorders, increasing the pathogenic complexity.¹⁵⁰ Notwithstanding the extensive research, as for the others polyQ diseases, the molecular mechanisms underlying the cellular toxicity deriving from expanded ataxin-3 is still unknown and there are not preventive treatments currently available.¹⁵⁰

1.1.5 Functional amyloids and Nanotechnology Applications

Since their discovery, amyloid fibrils were associated with a pathological state of living organisms. However, several amyloid structures having a functional physiological role in living organisms, such as bacteria, insects, invertebrates and humans were found. This biologically active state of proteins has been termed *functional amyloid* (**Table 1.2**).¹⁵⁸ The functional amyloid hypothesis states that living system have evolved to take advantage from the possibility that protein can form highly resistant to degradation and ordered fibrillar structures. Examples of such functional amyloids are bacterial coatings and adhesives, structures for the storage of

hormones and catalytic scaffolds.¹⁵⁸ An example of a functional amyloid in humans is fibrils formed by Pmel17 serving as template for the biosynthesis of melanin.¹⁵⁹ Moreover, it has been recently suggested that the $\alpha\beta$ peptides play a fundamental physiological role in hippocampal memory formation in humans.¹⁶⁰ Amyloid could be a powerful platform for the design of new biomaterials, since they are generally deriving from natural proteins and they could possess a low inflammatory and immunogenic response and high biocompatibility.^{161,162}

Table 1.2 Functional Amyloid exists in a wide variety of organisms. Adapted from Fowler et al.¹⁵⁸

Species	Organism	Protein	Function
Bacteria	Escherichia Coli, Salmonella, Streptomyces coelicolor	Curli Chaplins	Biofilm formation, host invasion, Modulation of water surface tension and development of aerial structures
	Podospora anserine	HET-s	Regulation of heterokaryon formation
Fungi	Saccharomyces cerevisiae	URE2p	Regulation of nitrogen catabolism
	S. cerevisiae, fungi	Sup35p, Hydrophobins	Regulation of stop-codon read-through, Fungal coat formation, modulation of adhesion and surface tension
Animalia	Insects and fish	Chorion proteins	Structural and protective functions in the eggshell
	Nephila clavipes	Spidroins	Structural (spider silk)
	Homo Sapiens	Pmel 17	Scaffolding and sequestration of toxic intermediates during melanin synthesis

A wide class of peptides and proteins, if thermodynamically destabilized *in vitro*, form artificial amyloid-like fibrillar materials possessing the characteristic cross- β structure. In particular, amyloid fibrillar structures are intriguing from a technological point of view because of their unique mechanical properties. They possess Young's modulus in the order of Giga Pascal and they are within the stiffer proteinaceous materials in nature, comparable even to inorganic materials as steel.^{10,12,163} The rigidity of amyloid is predominately due to weak non-covalent intermolecular chemical bonds (hydrogen bonds) involving polypeptide main chain. Their unique properties are sequence-independent and these structures form a generic class of stiff materials.^{11,163} Additional beneficial features for the use of fibrillar assembling as biomaterials are: the low cost of production, since they aggregate at room temperature and in aqueous solution without any external energy input; the *bottom-up* approach, in which few different molecular building blocks hierarchical assembly into several tunable polymorphic

structures with nanoscale dimensions,^{35,37} and the natural tendency of amyloids to form highly ordered structures can be used to template other materials otherwise disordered at the nanoscale.

Taking inspiration from functional amyloid and the properties described above, the self-assembly of these peptides has allowed the development of biomaterials for a broad spectrum of applications in medicine and nanotechnology.^{161,162,164,165} The power of amyloid as biomaterials has been shown in the fabrication of conductive nanowires, in the realization of biofilms,^{164,166} new surfaces coatings for cells adhesion¹⁶⁷ and in improving efficiency of organic solar cells.¹⁶¹ Several promising applications in medicine have been suggested. The conjugation of proteins with drugs could allow controlled long-lasting drug delivery. As proved in the case of the cancer therapy based on gonadotropin hormone, this could be achieved thanks to the administration of assembled amyloid structure with low dissociation rate compared to monomeric dissociation.¹⁶⁸ Another similar case is the antibody-derived candidacidal decapeptide, which has been shown to form amyloid fibrils spontaneously and in a reversible manner. Since the aggregated state is more resistant to proteolysis than monomers, it could be used as long-lasting delivery system.¹⁶⁹ Finally, the future integration of amyloid-based and carbon nanostructures could allow designing bio-inspired hybrids materials mimicking biological functions and including new properties such as conductivity, optical response and antiviral activity. This could lead to the development of tissues, biosensors and nanomedicine.^{165,170,171} Following this idea, for instance, β -lactoglobulin fibrils were integrated with graphene. Fibrils from this milk protein are not necessarily toxic, while graphene has exceptional mechanical and electronic properties, but unfortunately its high hydrophobicity is not biocompatible. The low cost integration of the two materials permits the creation of a new class of biodegradable composite materials with tunable properties. These materials could be successfully used as biosensor and biomedical devices.^{165,172}

1.2 Biophysical Investigation of Amyloid Properties and Formation

Biophysics is an extremely interdisciplinary science using methods and theories developed in the fields of physics, mathematics, and chemistry to study biological systems. One of the most significant achievement in biophysics remains the discovery in 1953 of the double-helix structure of Deoxyribonucleic acid (DNA) by Watson and Crick. Nowadays, biophysics scans all biological scales from atoms and molecules to cells, organisms, and environments. Experimental biophysics is based on the use of several methodologies, which can be divided in two categories: bulk and single molecule techniques. The first category includes techniques, such as nuclear magnetic resonance, circular dichroism, Thioflavin T fluorescence, dynamic light scattering, X-ray scattering and infrared spectroscopy that determine only average properties of biomolecules and living systems. On the other hand, single molecule techniques enable measuring single molecule properties. In particular, atomic force microscopy (AFM) has become one of the most powerful techniques available to investigate the structure of biomolecules, but also for their manipulation, at the single molecule scale. In the following paragraphs, the biophysical techniques involved in the frame of this thesis will be presented.

1.2.1 Spectroscopic Bulk techniques

Bulk techniques, applied to aggregating samples, provide important information and fundamental feedbacks on the state of the solution. For this motivation, throughout all my PhD work, bulk techniques have been used as control for all the single molecule scale measurements. In the following paragraphs, we will briefly describe them in relation to the experimental work done in my thesis:

Thioflavin T – The fluorescent benzathiole dye Thioflavin T (ThT) has become among the most widely used methods for selectively staining and identifying amyloid fibrils both *in vivo* and *in vitro*.¹⁷ Indeed, under the appropriate conditions, it selectively stains amyloid structures undergoing characteristic spectral alterations.¹⁷³ ThT fluorescence originates from the dye binding to cross- β sheet rich structures, which causes a dramatic enhancement of its fluorescence emission. When associated with amyloid fibrils, the dye displays a dramatic shift of its excitation maximum, from 385 nm to 450 nm, and of its emission maximum, from 445 nm to 480 nm.¹⁷⁴ Despite its widespread use, the structural basis for binding specificity and for the

changes to the photophysical properties of the dye remain poorly understood.¹⁷⁵ Unfortunately, ThT is not perfectly amyloid specific and it may not undergo a spectroscopic change upon binding to precursor monomers or small oligomers, even if with a high β -sheet content.¹⁷⁶ Moreover, some amyloid fibers as Huntingtin's ones do not affect Thioflavin T fluorescence, raising the prospect of false negative results and the necessity to couple studies based on this technique with other methodologies. However, as previously described in the paragraph 1.1.3 and depicted in **Fig. 1.4**, the method notably enables to investigate the kinetics of amyloid fibrils formation and other many histological and bio-imaging studies rely on this technique.^{17,18,69}

Circular Dichroism – Circular dichroism (CD) is the differential absorption of left- and right-handed circularly polarized light.¹⁷⁷ In the case of chiral biomolecules, the CD absorption of light in the far-UV (wavelength between 180-240 nm) derives from the peptide bond (amide bond) electronic transitions: $\pi \rightarrow \pi^*$ and $n \rightarrow \pi^*$ around 190 nm and 220 nm, respectively.¹⁷⁸ These transitions are highly sensitive to the molecule conformation and to its secondary structure. As we can observe in **Fig. 1.9**, when polarized light is absorbed by a protein, its electronic structure gives rise to characteristics bands in the far-UV.

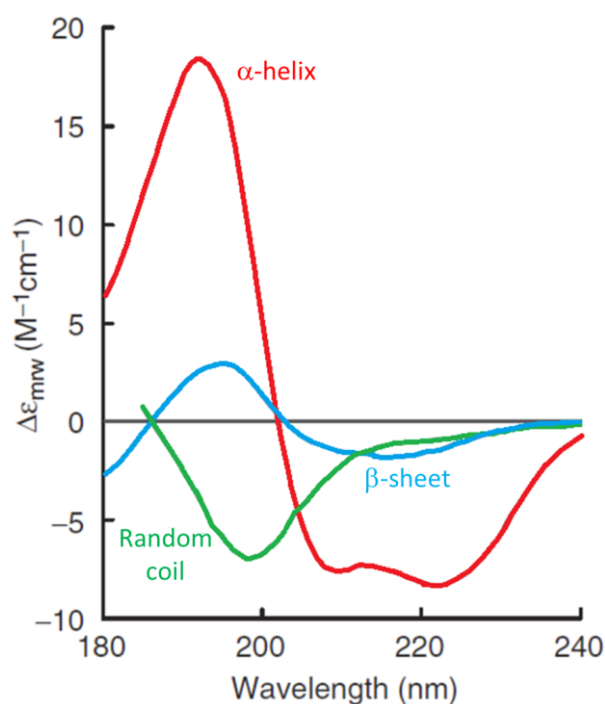


Figure 1.10 Circular dichroism signal for proteins with α -helical (red), random coil (green) and β -sheet (light blue) structure. Adapted from Ref. 177.

The dichroic signature corresponding to: β -sheet has $\pi\pi^*$ positive maximum near 195 nm and $n\pi^*$ negative maximum near 217 nm; random coil state a strong $\pi\pi^*$ negative maximum near 200 nm; and the α -helix structure has a strong maximum near 190 nm and a double negative maximum at approximately 208 nm and 222 nm.¹⁷⁹ The capacity of CD to give a representative structural signature makes it a powerful tool in modern biochemistry, especially for showing changes in conformation during the fibrillization of amyloidogenic proteins as a function of time, temperature or different solvent.^{31,52,71,180}

IR spectroscopy – Infrared spectroscopy is a general established tool for the determination of secondary structure of proteins.^{181,182} Moreover, the technique has been extensively used to observe the conformational transition from monomers to cross β -sheet amyloid structures during amyloid formation and to investigate the aggregates structural properties.^{63,64,183} IR spectroscopy is based on the molecular vibrations produced, under light exposition, by stretching, deformational motions, bending and rotations of chemical bonds. The amide I, amide II and amide III modes are the most commonly used to study the structural properties of polypeptides. The amide I mode arises mainly from backbone C=O stretching vibrations with frequencies at 1700-1600 cm^{-1} . The exact band position is determined by the backbone conformation and thus by the secondary structure of the protein.^{181,184} The amide II band reflects a combination of backbone N-H bending and C-N stretching and has frequencies within 1580-1510 cm^{-1} . The amide III band at 1350-1200 cm^{-1} reflects a combination of different modes such as C-N stretching, N-H bending, C-C stretching and C=O bending. We could associate the position of these two bands to the secondary structure of the protein, but the analysis is far from trivial because of the various contributions. The amide I band is thus the most frequently used to infer the secondary structure of peptides. From several studies, a consensus has emerged for the assignment of the secondary structure IR peaks in this spectral region.^{185,186} As shown in **Table 1.3**, there are several components concurring to the shape and position of the Amide I band: intermolecular antiparallel β -sheet are located within 1695-1680 cm^{-1} ; intramolecular β -turn within 1680-1665 cm^{-1} ; α -helical between 1660-1650 cm^{-1} ; random coil between 1645-1635 cm^{-1} ; intramolecular low density native β -sheet within 1635-1620 cm^{-1} ; intermolecular high density amyloid β -sheets within 1625-1610 cm^{-1} . In particular, several studies showed that amyloidogenic β -sheet are located at lower energy in the IR absorption spectrum than native β -sheet, reflecting likely the presence of stronger intermolecular hydrogen bonds in the cross- β structure than the intramolecular ones in the native globular protein.^{64,180,186,187} Finally, respect

to CD or Raman spectroscopies, in IR spectroscopy the β -sheet contribution has the highest absorption coefficient. Therefore, IR spectroscopy is a particularly suitable technique to analyze β -sheet-rich amyloid aggregates.¹⁸⁸

Table 1.3 Amide I band secondary structure components.

Amide I Structural assignment	Wavenumber (cm⁻¹)
Antiparallel β -sheets (Intermolecular)	1695-1680
β -turn (Intramolecular)	1680-1665
α -helix	1660-1650
Random coil	1645-1635
Low density Native β -sheets (Intramolecular)	1640-1625
High density Amyloid β -sheets (Intermolecular)	1625-1610

1.2.2 Single molecule investigation by Atomic Force Microscopy techniques

In this section, the principle of working of scanning probe techniques is presented. In particular, Atomic Force Microscopy will be presented in detail, its operational modes and ultimate resolution will be discussed. Successively, the force spectroscopy related modes able to investigate the nanomechanical properties of biomolecules at the nanoscale are shown. At the end, the principle of functioning of the innovative AFM-based infrared nanospectroscopy will be described.

Microscopy and Scanning Probe Techniques - A microscope is an instrument designed to produce magnified images of objects too small to be seen with naked eyes. The first idea that could come in mind in association with the word “microscope” is that the instrument manipulates light to obtain a magnified image of the object. Indeed, for a long time from its invention centuries ago, microscopy was normally based on a light source that emits photons that are used as probes directed onto or emitted from the specimen. Nowadays, there are different types of microscopes: optical, electron and scanning probe microscopy.

Optical and Electron microscopy are based on the scheme “source-specimen-detector-analyzer”, where particles are probes sent to the sample, then registered by a detector and subsequently analyzed bringing information on its morphology. The first technique uses photons as probes and it can reach a resolution r as small as approximately the half of the wavelength of the light interacting with the sample (~ 200 nm), as stated by Abbe’s principle $r = \lambda/2NA$, where NA is the numerical aperture of the microscope.¹⁸⁹ Electron microscopy, invented in the early 20th century, uses an accelerated electron beam to magnify and observe the specimen and, thanks to the much shorter wavelength of fast electrons, has a very significantly higher resolution than optical microscopy. A state-of-the-art electron microscope is capable of acquiring images with sub-angstrom resolution. The main limitation of this technique is that sample has to be conductive. Non-conductive samples, as biomolecules, must be coated with a conductive material, which could alter the sample or mask its properties.

In scanning probe microscopy (SPM), a sharp tip interacts with the sample and it scans its surface in a raster way. In other words, the probe interacts with the sample moving along sequential parallel lines. Every line is divided in pixels, which can record several types of signal as currents, voltages and forces. The first SPM technique invented was the scanning tunneling microscope (STM), which was awarded by the Nobel Prize.¹⁹⁰ This system is based on the quantum tunnel effect, which causes a current between two conductive objects posed close each other. First, a metallic tip is brought close to a conductive surface, causing an electronic current flow depending exponentially on the distance between the two elements. Successively, the tip scans the surface.

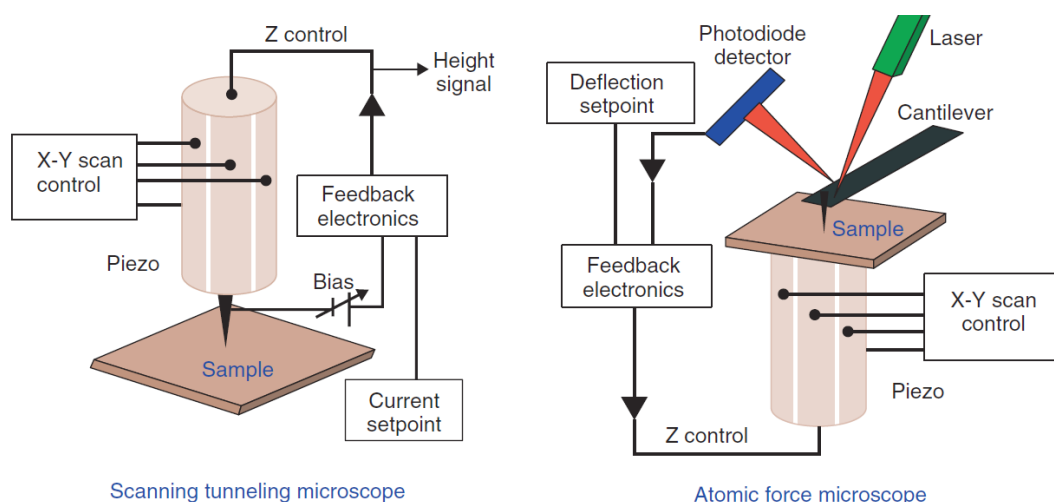


Figure 1.11 Schematic depiction of Scanning Tunneling Microscopy and Atomic Force Microscopy. From Ref. 191.

As depicted in **Fig. 1.10**, by means of a feedback system controlling piezoelectric elements that can move the sample respect to the tip, the system can keep tip-sample distance or electronic current constant. The signal from the feedback mechanism allows retrieving the topography of the sample with a resolution along the Z direction of approximately 0.01 nm and along the XY directions with sub-nanometer resolution. This was a conceptual revolution in the field of microscopy, but unfortunately, the limitation of the investigation to only conductive or semiconductive samples remained. For this reason, STM it is not suitable for biological samples.

Atomic Force Microscopy - In order to overcome the difficulties in investigating dielectric samples, in the 1986, Binnig et al. invented the atomic force microscope (AFM). They combined the principles at the base of the STM and of the so-called stylus profilometer. The probe of the AFM is a cantilever with a microfabricated sharp tip at its end, which is the sensing device. AFM probes are normally made of silicon or silicon nitride. The cantilevers have usually rectangular or triangular dimensions, typical length within 2-200 μm and they can be considered as springs with elastic constant k in the range of 0.01-100 N/m. The tips and the end of the lever typically have an apical radius between 1-50 nm. Similarly to STM, by means of a piezo-actuators system, the probe is kept at a distance in the order of the nanometer from the surface and it scans the surface in a raster way. In the easiest configuration, during the scanning, interaction forces between the tip and the sample produce a bending of the cantilever, which can be directly measured. There are several methods to measure the cantilever deformation. However, the most commonly used is the optical lever method, where a laser beam is focused on the back of the lever and the reflected beam is detected by a four-quadrant photodiode (**Fig. 1.10**). This configuration enables to measure vertical and lateral (torsion) deformations of the lever. Finally, the feedback electronics drives the piezoactuator in order to compensate the deviation of the lever deflection from the chosen setpoint and to keep a constant deformation of the cantilever. The bending Δx of the cantilever is proportional to the interaction force, as described by the Hook's law: $F = k \cdot \Delta x$, where k is the elastic constant of the lever.¹⁹² In a typical force microscope, cantilever deflection range from 0.1 nm to micrometers. This enable to routinely measure forces ranging from 10^{-13} to 10^{-4} N.¹⁹³

The forces relevant to AFM are ultimately of electromagnetic origin, which are due to the interaction between tip and sample atoms. However, different intermolecular, surface and macroscopic effects give rise to interactions with distinctive distance dependencies. In the

absence of external fields, the dominant forces are van der Waals interactions, short-range repulsive interactions, capillary and adhesive forces (**Fig. 1.11**).^{192,193} If the tip is in strong contact with the sample, elastic forces can occur. All the described forces can be divided roughly in two categories: repulsive and attractive. The former dominate at a close tip-sample distance, while the latter are long-range interactions. The sum of these forces is generally approximated by means of a Lennard-Jones potential, which combines short-range repulsive and long-range attractive forces, as represented in **Fig. 1.12**.

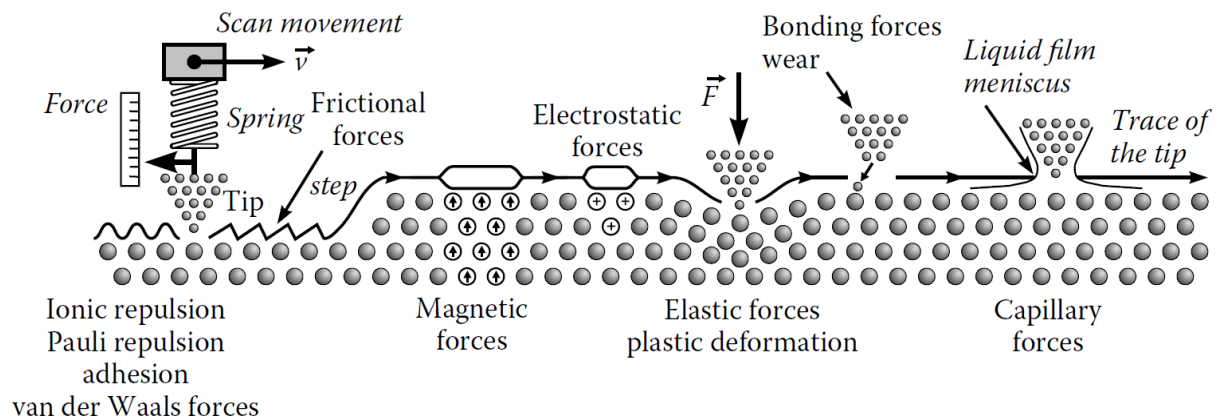


Figure 1.12 Summary of the possible relevant Forces in AFM. From Ref. 193.

Accordingly to the regime of interaction, there are two main operational modes of AFM: *static*, termed also contact mode, and *dynamic mode*. In contact mode, the tip is brought at close contact with the sample and scanned across the surface. In this modality, the tip-sample interaction is mainly due to strong repulsive forces ($\sim 1-10$ nN). As described above, the imaging of the sample is generally obtained by maintaining a constant deflection (force) of the lever during the scanning. This is possible through the extension or retraction of the piezoactuator along the z direction by the feedback electronics loop, which adjusts the tip-sample distance in order to have a constant deflection of the lever. The Δz adjustment of the piezo is used to display the sample height for each pixel of the XY plane, so retrieving a 3D map of the morphology of the sample (**Fig. 1.10**). Static mode was historically the first operational mode of AFM, it allows straightforwardly to obtain morphology images with atomic resolution. However, huge tip-sample lateral forces are present during scanning and they could introduce damage or artifacts into the specimen. For this reason, a dynamic mode was successively introduced. In this configuration, the tip is placed in oscillation, close or at resonance frequency of the cantilever, over the surface of the sample and typically at a distance from few to tens of nanometers. At

this distance, the tip-sample interaction is generally considered as mainly due to the much weaker attractive forces, such as Van der Waals and electrostatic interactions, which are typically below 1 nN. However, accordingly to the absolute value of amplitude oscillations and tip-sample separation, can have important contribution also the other of forces described above, such as repulsive, frictional and elastic deformation (**Fig. 1.11**). As shown in **Fig. 1.12**, two main dynamic regimes can be considered: the *tapping mode*, in which the equilibrium separation of the tip and sample is smaller than the amplitude of the cantilever oscillation, so the tip is periodically brought in contact with the sample; the *non-contact mode*, where there is not tip-sample mechanical contact, deformation and friction effects are eliminated, and the tip is mainly submitted to attractive forces.¹⁹⁴

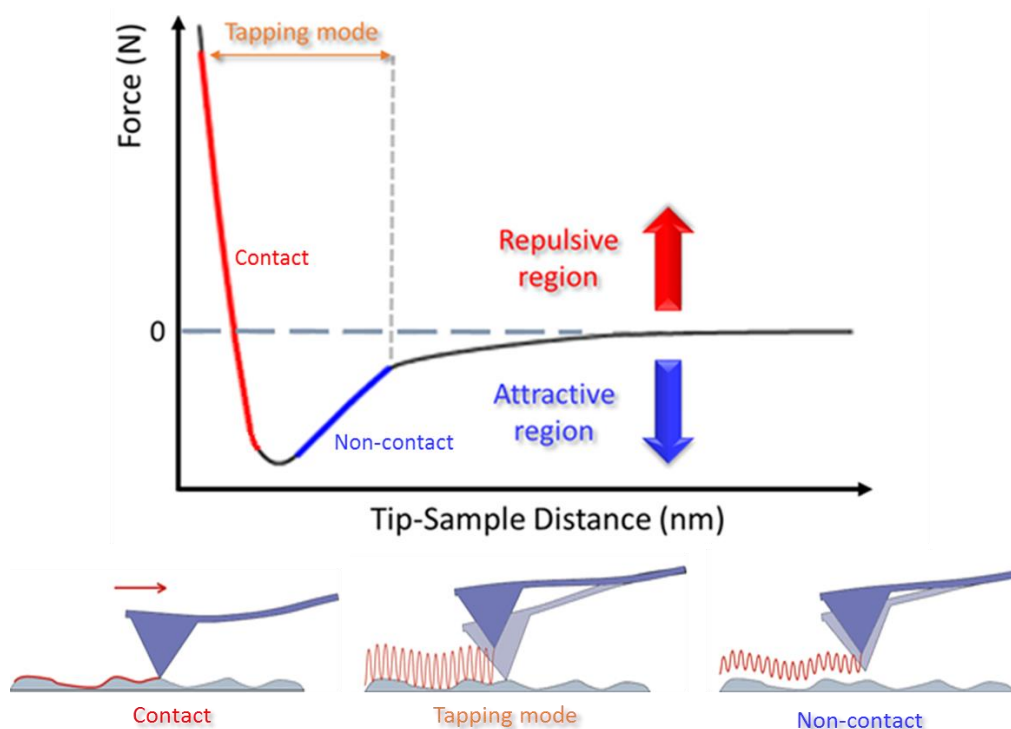


Figure 1.13 AFM tip-sample potential energy representation and related AFM scanning modes.

In both *dynamic* modes, when approached towards the sample, the parameters of the oscillation are influenced by the tip-sample interaction. The amplitude, the resonance frequency and the phase shift link the dynamics of the vibrating cantilever to the tip-surface force of interaction and they can be used as a feedback parameter to record the topography of the specimen. Two major AFM dynamic modes have been developed: amplitude modulation (AM-AFM) and frequency modulation atomic force microscopy (FM-AFM).^{193,194} In AM-AFM, the oscillation amplitude is used as a feedback parameter to measure the topography of the sample

surface. Indeed, when the tip approaches the surface the free oscillation amplitude is damped, the feedback loop will adjust the tip-sample distance in order to maintain amplitude constant and the measured difference is used to retrieve the topography. On the other hand, in frequency modulation the cantilever is kept oscillating with a fixed amplitude at its resonance frequency. This resonance frequency depends on the forces acting between tip and sample surface. The spatial dependence of the frequency shift Δf , the difference between the actual resonance frequency and that of the free lever, is the source of contrast. As in the case of amplitude modulation mode, a constant frequency shift can be chosen and an image is formed by profiling the surface topography maintaining Δf close to the reference value by means of the feedback system. FM-AFM has been implemented to reach atomic resolution in non-contact and in ultra-high vacuum environment, however the more complex feedback mechanisms and the low thermal stability of resonant cantilever frequency in air have limited its spreading for common applications. While, AM-AFM is generally used to perform robust measurements in liquid and in air, for these reasons it is the most commonly used modality to study biological specimen and it has been widely applied to investigate structures from the single protein to the cellular scale. Together with topography, in this operational mode, material properties variations could be mapped by recording the phase shift between the driving force and the tip oscillation.¹⁹³

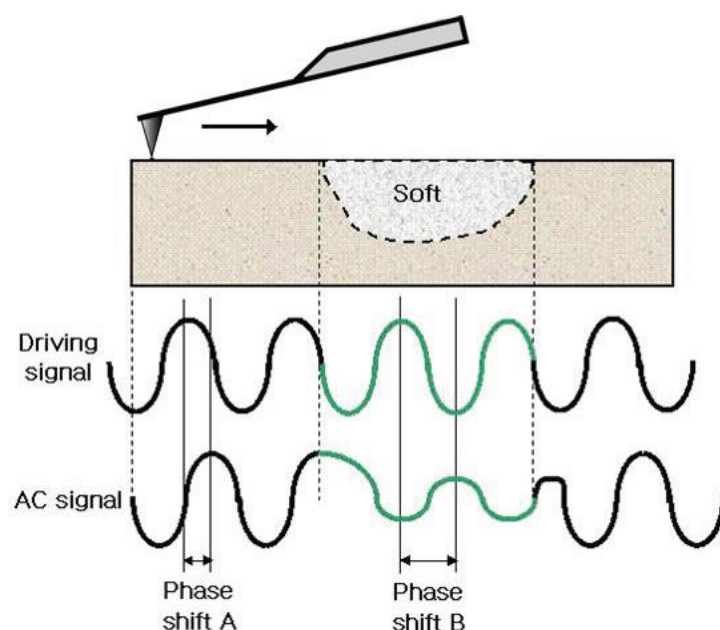


Figure 1.14 Schematic depiction of AFM phase shift measurements. Courtesy from Park System, South Korea.

As shown in **Fig. 1.13**, it is possible to demonstrate that the interaction of the tip with materials having different mechanical properties causes a phase shift of the cantilever oscillation.¹⁹⁴ Moreover, the phase change is strictly related with the phenomena of tip-sample energy dissipation during the scanning. In particular, it would be negligible if tip-sample interaction would be absent. Therefore, it can be concluded that the minimization of the phase changes enables to perform less invasive measurements, where dissipation is minimal.¹⁹⁴

Finally, the instrument resolution deserves a detailed discussion. AFM generates three-dimensional images of the sample surface. Although not always independent, two different resolutions should be distinguished: lateral and vertical. Vertical resolution is limited by both noise from the detection system and thermal fluctuations of the cantilever. In general, the thermal noise of the cantilever is the largest source of noise in AFM.^{194,195} Damping systems have become so effective that mechanical vibrations represent a negligible perturbation of the cantilever oscillation. For a cantilever with a force constant of 40 N/m, the thermal fluctuations of the cantilever are below 0.01 nm. Therefore, vertical resolution of AFM along the z directions is easily below sub-nanometer scale. A notable effect, especially in air conditions, is that AFM measurements of biomolecules report heights that are always smaller than their nominal values. Smaller heights are a consequence of different processes such as dehydration, sample deformation due to repulsive tip-sample forces and differential tip-surface-sample interaction. In the case of the lateral resolution, three main factors should be considered: the instrumental resolution, defined by the ratio between size and number of pixels of the image, the precision of the piezo along the XY direction, and the radius of the scanning tip. The instrumental resolution is generally sufficient, since it is possible to use an elevated number of pixels to scan and the piezoelectric system possesses sub-nanometric precision, while the geometrical shape of the tip is mainly determining the lateral resolution. If the apical radius of the tip is of the same order or bigger of the dimensions of the object under investigation, an effect of lateral broadening will be visible always in the AFM image (*convolution effect*). In Fig. 1.14, we can observe a depiction of the *convolution effect* in the case of scanning by tips with broad or sharp radius of curvature. Only if the tip has comparable dimensions with the object under investigation, the broadening effect will be minimum.¹⁹⁶

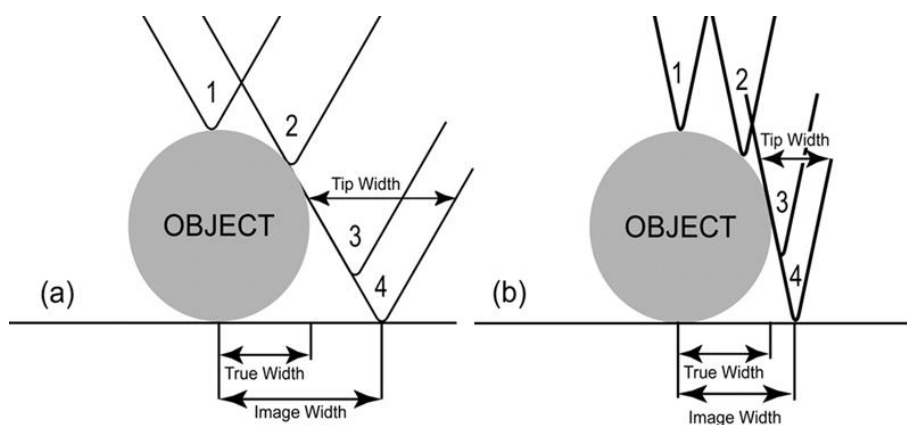


Figure 1.15 AFM Schematic illustration of the convolution of the shape of the AFM tip with the shape of the feature or particle being scanned. (a) Blunt tip, (b) sharp tip. From Ref. 196.

Statistical analysis of AFM Images – AFM morphology 3-D maps furnish a nanometer-resolution view of the structural and morphological characteristics of biomolecules aggregates, such as amyloid fibrils. From these maps is possible to retrieve several parameters regarding the structure of an amyloid fibril: height, width, contour length and periodicity.¹⁹⁷ Furthermore, AFM enables investigating the bending rigidity and persistence length of amyloid fibrillar structures, as successfully applied in the case of β -lactoglobulin fibrils.³⁶ The persistence length l_p is the length above which thermal fluctuations can bend a rod-like polymer and it is therefore a measure of its elastic properties.^{198,199} This quantity can be determined directly from AFM images, by means of the bond correlation function for semi-flexible polymers in a two-dimensional conformation:

$$\cos \Theta(s) \approx e^{-\frac{s}{2l_p}} \quad (1)$$

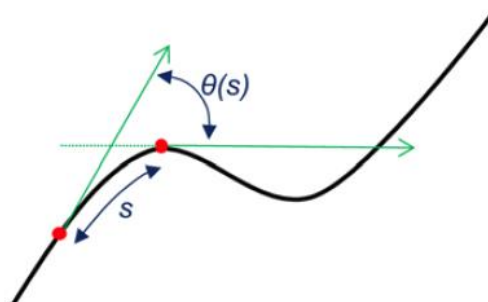


Figure 1.16 Schematic depiction of a semi-flexible polymer and the parameter used to calculate its persistence length.

As shown in **Fig. 1.15**, θ is the angle between the tangent vectors to the chain at two points separated by a contour distance s . The factor 2 is used to rescale the exponential decay in order to consider the two-dimensional nature of protein fibrils absorbed on a surface.¹⁹⁷ These fluctuations depend on the fundamental physical properties of the polymer, such as its bending rigidity.¹⁹⁹ The l_p can be used to calculate the elastic modulus E of a semi-flexible polymer, indeed these two physical quantities are directly linked by the following relationship:

$$l_p = \frac{EI}{k_b T} \quad (2)$$

Where I is the cross-sectional area moment of inertia of the polymer, T the temperature and k_b the Boltzmann constant. Therefore, the study of the statistical mechanics of such fluctuations is a valuable route towards understanding the nanoscale mechanics of polymers and other linear structures.

Force Spectroscopy Measurements and Peak Force Quantitative Nanomechanical Imaging –

A cantilever is an extremely precise and sensitive force sensor with piconewton resolution.¹⁹² Consequently, it can be used to measure mechanical properties of samples. The basic principle of this measurement relies on performing force-distance curves, in a trace-retrace manner, due to the vertical motion of the lever on the sample under investigation. A single force-distance curve is related to the plot of the tip-sample force versus the piezoelectric z displacement, as depicted in **Fig. 1.16**.¹⁹² The process can be illustrated by six fundamental regions.¹⁹² The 1-2 line represents the zero-extension line, when tip is approaching out of contact. Line 2-3 corresponds to the jump-in-contact, also called *snap-in*, which happens when gradient of attractive forces is higher than cantilever spring constant. The line 3-4 corresponds to the deflection of the cantilever in contact with the sample, in this region the lever passes from being bent downward, through the zero deflection, to being bent upward. This region is purely linear for perfectly elastic deformation, while is not linear in the case of plastic deformation. The line 4-5, indicates the beginning of the retracting and it should be ideally superimposed and with same slope of the corresponding approaching line 3-4. However, an eventual distance displacement and a different slope of the two curves is relate to the plastic indentation of the sample. Line 5-6 represents the moment of the loose of tip-sample contact, it is termed *snap-out*, and it is generally linked to adhesive forces. Finally, the line 6-7 represents the retracting out of contact. It is worth to underline that the instrument does not measure directly forces and

distances, but it measures directly the displacement of the piezo and the deflection of the laser by means of a photodiode. Therefore, in order to convert the read voltage by the photodiode into a distance, the photodiode sensitivity needs to be calibrated and this calibration is performed by relating the vertical movement of piezo relatively to the cantilever deflection on a stiff substrate. Successively, in order to convert the measured deflection into a force, the elastic constant of the lever is measured. A common method to perform this measurement is the thermal tuning.²⁰⁰

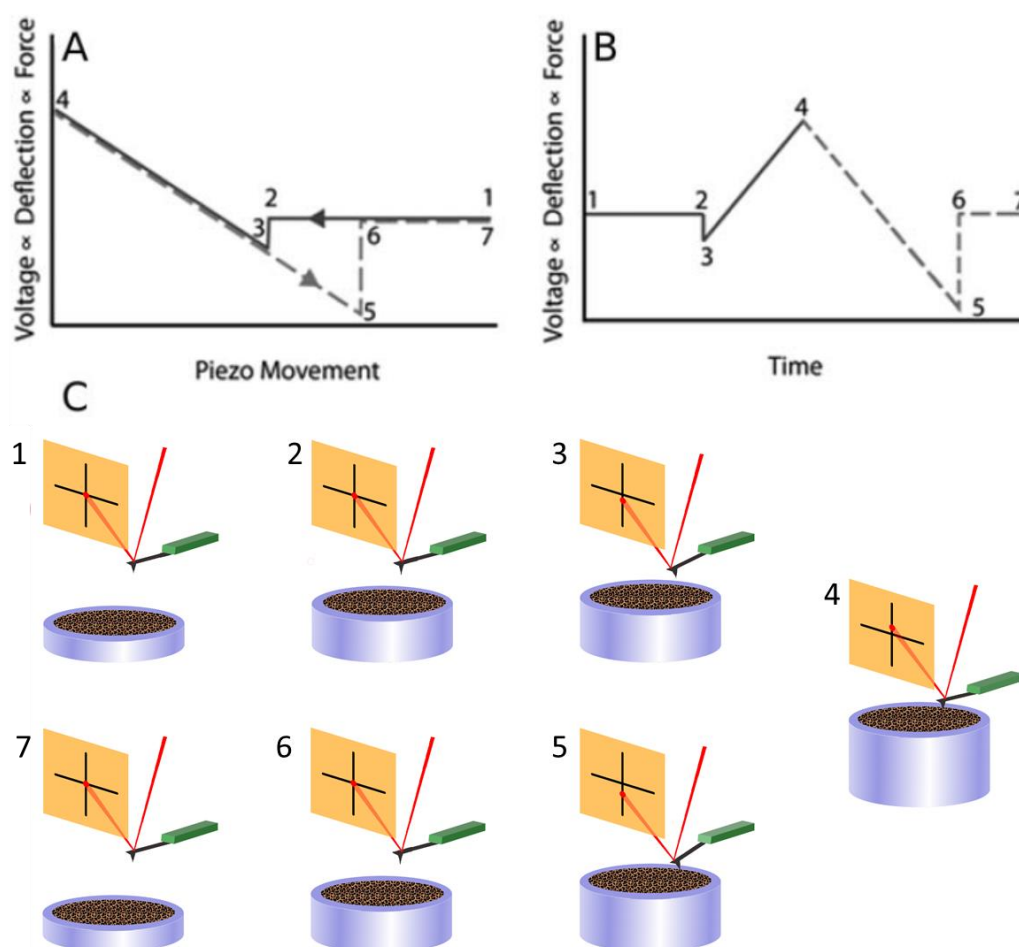


Figure 1.17 Ideal force-displacement curve depiction.

Ideal (A) force-distance and (B) force-time curves representation. From Ref. 201.

Once the force-distance curve is obtained, by means of its analysis, mechanical properties of the sample can be retrieved. Several methods have been implemented to study mechanical properties of biomolecules as amyloids. Nanoindentation, quantitative nanomechanical mapping and force spectroscopy pulling are part of this category (**Fig. 1.17**).^{197,198}

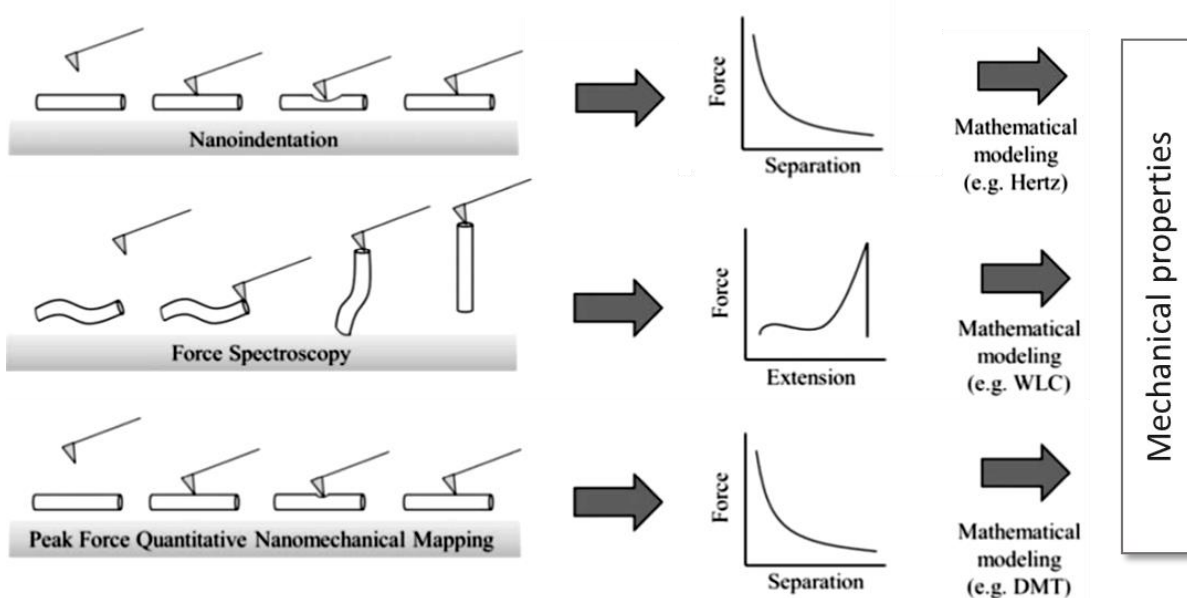


Figure 1.18 AFM-based methods to investigate biomolecules and amyloid aggregates nanomechanical properties. From Ref. 198.

Nanoindentation is one of the most common methodologies to retrieve the Young's modulus and hardness of a sample. Indeed, if the sample is soft relatively to the tip stiffness, during the approach the tip will indent the sample (**Fig. 1.18 A**). The subtraction of the force-distance curve obtained from an undeformable stiff substrate allows retrieving the indentation curve (**Fig. 1.18 B-C**). The fit of this curve, by means of a mechanical model¹⁹², enables to extract the intrinsic Young's modulus of the object. Nanoindentation measurements have been able to extensively measure the Young's modulus and stiffness of amyloid fibrils and to confirm its value in the range of GPa.^{198,202}

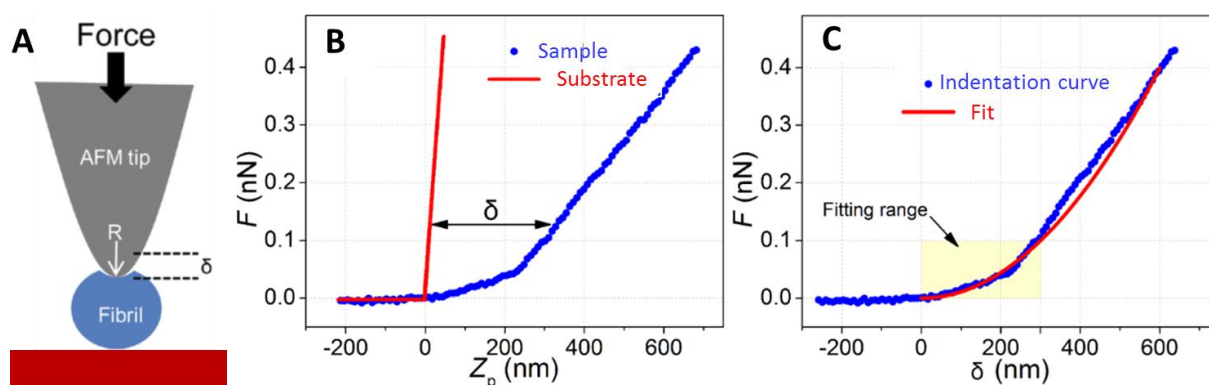


Figure 1.19 Nanoindentation measurements.

(A) Schematic depiction of the indentation mechanism, (B) force-displacement curves on the sample on an undeformable sample, (C) force-indentation curve and fit. (Adapted from Ref. 203).

In the frame of this thesis, we mainly concentrated on force spectroscopy nanomechanical manipulation and peak force quantitative nanomechanical mapping (PF-QNM) and of amyloid structures. In force spectroscopy measurements, the tip is able to adsorb and manipulate the macromolecule on the surface. In this configuration, upon retraction of the tip once a binding is created, it has been shown that amyloid molecules can be stretched or unzipped.²⁰⁴⁻²⁰⁶ The resultant force curves and the stretching behaviour can be analyzed by theoretical models, as the worm like chain (WLC). This model, which will be described in the 3rd chapter, enables to extract the persistence length of the stretched molecule. A further possible modality to perform nanoindentation studies is the *Force-Volume* mode, in which a map of force-distance curves is collected in a raster way over a selected area of the sample. However, a single force curve requires several tens of milliseconds to be completed, so a typical force volume image is characterized by long completion times (from several minutes to several hours) and low spatial resolution (32×32 or 64×64 pixel images are common). An improvement of the *force-volume* mapping is the *Quantitative Imaging*, implemented by *JPK Instruments*, which allows to acquire maps of mechanical properties of a sample with a resolution up to 512×512 pixel contemporarily with morphology maps.^{207,208} Finally, PF-QNM, a similar and relatively new technique is able to map mechanical properties with higher speed and spatial resolution. The methodology is based on a new tapping mode in which every tapping of the probe on the surface produces a force-distance curve. This technique uses the peak force value of the force-distance curve as imaging feedback, diversely than AM-AFM that uses the amplitude as feedback parameter. This mode can be used with standard tips and cantilevers, the drive frequency is notably below the resonance one and the typical amplitude oscillation is approximately 100 nm. In **Fig. 1.19 A**, it is represented the tip trajectory as a function of time over a tapping cycle. Initially (1), the tip is far from the surface and it is brought in contact with the sample (2). Successively, the tip indents the sample until the maximum peak force is reached (3). Then, it is pulled off until the adhesion force is maximum (4) and it finally recovers its original position (5). Using the maximum peak force for the feedback calculation, a force-distance curve is generated at every pixel. Since the Z position of the modulation and the deflection of the cantilever are controlled as a function of time, it is possible to eliminate the time variable, from **Fig. 1.19 A**, and a force-distance plot can be generated, as in **Fig. 1.19 B**. From those curves, the usually measured quantities by force spectroscopy can be measured: adhesion, dissipation and elastic modulus. This last parameter can be extrapolated by fitting the retraction curve by the Derjaguin-Mueller-Toporov (DMT) model.¹⁹² Since a force curve is obtained for each pixel, the resolution of channel is identical to the topography image. This

technique has been applied successfully, as it will be described in the 4th chapter, to measure the intrinsic elastic modulus of several amyloid fibrils.¹⁶³

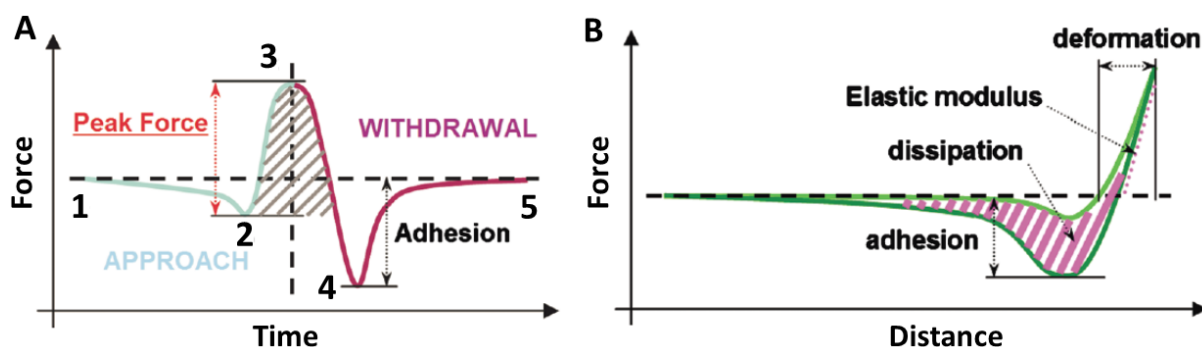


Figure 1.20 Principle of operation of PF-QNM.

(A) Principles of peak force tapping. (B) Force-distance curve and indicative representation of the calculated mechanical properties. From Ref. 208.

Infrared nanoscale spectroscopy – Invention of AFM was crucial to development of nanoscience. However, the study of macromolecules at nanoscale remains challenging, especially when truly quantitative information is required. The AFM-based local measuring methods that have developed until now have not brought wider field of applications. The main reason is that imaging, or in the best case mapping of a single property as stiffness and Young's modulus, is not sufficient when studying inhomogeneous and complex materials, such as aggregating proteins.

A real breakthrough was reached with the development of nanoscale Infrared (IR) Spectroscopy (nanoIR). Fourier transform infrared spectroscopy (FTIR) is a key method for studying conformational properties of proteins and their structural conversion during amyloid fibrillation.^{64,209} However, a significant factor, limiting the general applicability of FTIR and other bulk techniques for the study of protein aggregation, is that they are mainly able to give average information only on the ensemble of the species present in the heterogeneous aggregating solution. A new technique (nanoIR), exploiting the simultaneous use of AFM and IR, can be efficiently used to characterize at the nanoscale the structural properties of amyloids during their aggregation pathway (**Fig. 1.20**).²¹⁰

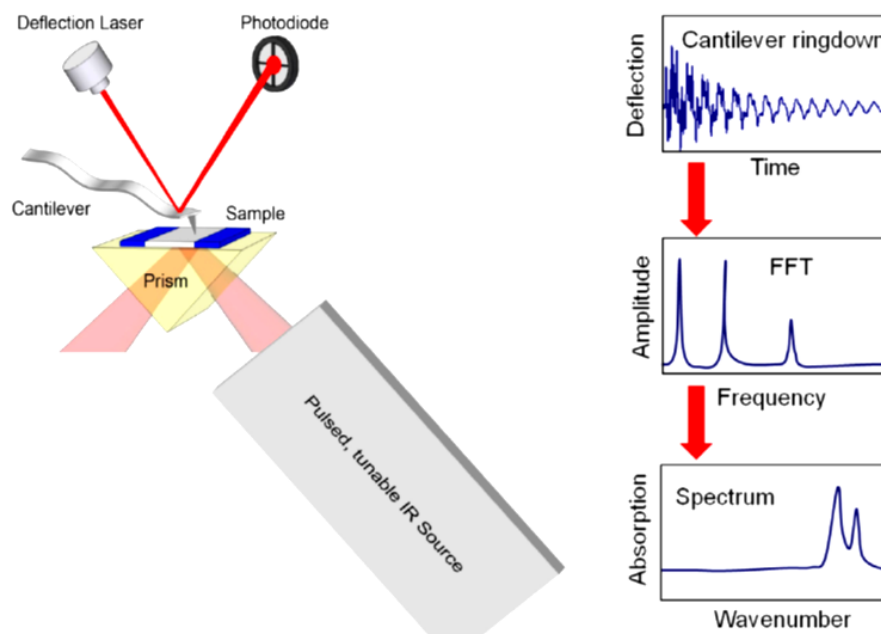


Figure 1.21 Schematic depiction of nanoscale infrared spectroscopy working principle.

The combination of AFM and IR spectroscopy is based on a photothermal induced resonance effect (PTIR).²¹¹ A pulsed, tunable laser beam passes through a ZnSe prism and undergoes total internal reflection from the upper face of the crystal (**Fig. 1.20**). An evanescent wave, with typical length of the order of the wavelength of incident light, interacts with the sample that is deposited on the ZnSe prism. If at a given wavelength, the IR pulse is absorbed by the sample, the local temperature rise leads to local thermal expansion. This deformation excites mechanical resonances in the AFM cantilever, which is in contact with the sample. The cantilever resonates with a ringdown shape containing several of its Eigen frequencies. If one mode is chosen, the peak-to-peak maximum and the Fourier transformed amplitude of its ringdown are directly proportional to IR absorption.²¹² Therefore, the AFM detection of the temporary expansion of the scanned region enables nanoscale resolution IR imaging and acquisition of local chemical spectra. The AFM–IR spectra generated from this technique contain the same information with respect to molecular structure as conventional IR spectroscopy measurements. Moreover, as illustrated in **Fig 1.21** in the case of collagen fibrils, simultaneously with the acquisition of IR-absorption and topography images, the system is able to obtain qualitative stiffness maps. Resolution of the instrument in the case of the morphology maps is determined by the usual parameters in standard AFM. While, the resolution of the IR, stiffness maps and spectra is unrelated with the topographic channel. The critical thickness (AFM height along the z direction) of the sample to acquire IR information is in the order of 50-100 nm and it is determined by the ultimate instrument sensitivity to the measurement of the

photo-thermal expansion.²¹² While, the lateral resolution for isolated objects is mainly determined by the geometrical shape of the tip. The instrument enables to acquire chemical information in a wide range of the infrared spectrum, more specifically between 3600-1000 cm^{-1} . However, it is worth to note that sensitivity of the instrument in the spectra region within 1610-1550 cm^{-1} is limited by the very low laser power in this region, which causes low signal-to-noise ratio. For this reason, in these region, the acquisition of chemical properties of objects with thickness close to the ultimate one (100 nm) is affected by high noise and signal fluctuations.

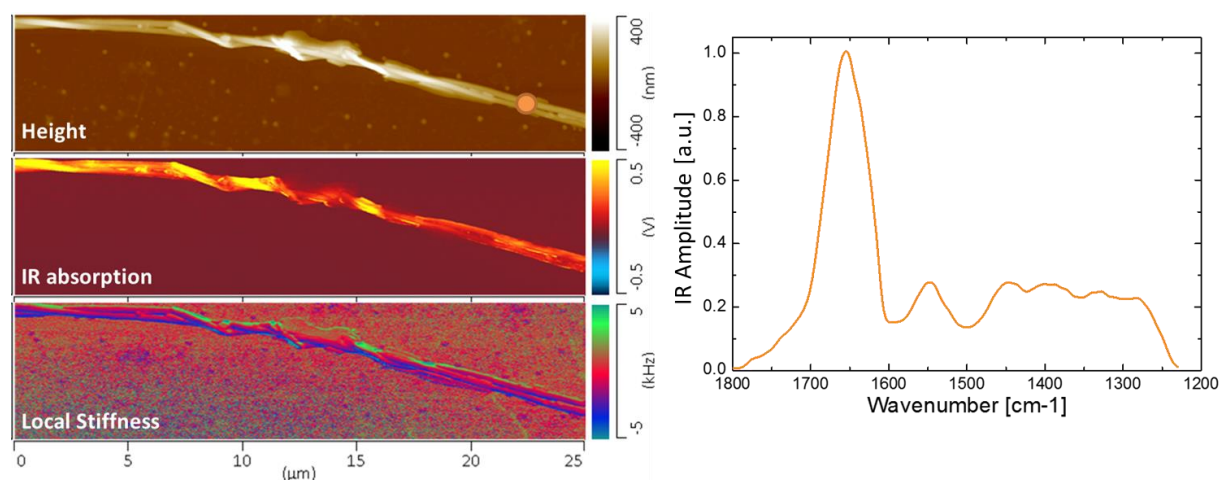


Figure 1.22 NanoIR imaging and spectra acquisition of a bundle of collagen fibrils.

In the figure are shown: the morphology, local stiffness and IR absorption maps; an IR spectrum in the proteins range (1800-1200 cm^{-1}) is acquired at a specific location of the maps (indicated by a circle).

One of greatest benefits of the nanoIR technique is the fact that chemical analysis can be performed at the submicron scale, with extremely tiny quantity of biological specimens. Purification and high throughput production of proteins is extremely expensive and time consuming; for this reason, reduction of sample quantity to perform routinely FTIR and secondary structure analysis is a problem of extreme importance which nanoIR can solve being able to measure thin and small samples. This is one of the main advantages of nanoIR compared to conventional IR techniques, which have spatial resolution limited by the smallest achievable IR spot size ($\sim 20 \mu\text{m}$)²¹³. NanoIR also requires very small quantities of biological specimens (less than picograms or sub-femtomoles is sufficient). This is a major advantage when working with biological materials whose production is expensive and time costly. Applications of this instrument have been shown in the case of several biological system, first applications in the field of amyloids will be shown in the 5th and 6th chapter of this thesis.²¹⁴

1.3 Objective of the Thesis

The main objective of this PhD thesis has been the elucidation of amyloids structure and formation at the single scale aggregate, mainly by means of AFM-based techniques. The use of AFM is essential to unravel the characteristic of these structures at the nanometer single molecule length scale. In particular, to address the challenge of understanding amyloids aggregation, single molecule measurements possess increased robustness than bulk measurements measuring heterogeneous populations. For this reason, the use of single molecule techniques as AFM is fundamental to resolve the complex and heterogeneous energy landscape of proteins aggregation. Moreover, the application of new AFM-based methodologies, such as the recently established PF-QNM and infrared nanospectroscopy, represents a fruitful avenue to unravel the process of monomer misfolding and to elucidate the molecular mechanisms of amyloid polymorphism and formation. Furthermore, the biophysical characterization of the properties of the intermediate structures during the fibrillization process is of fundamental importance to unravel their stability and gain insights into the potential toxicity of the intermediate aggregation species, information of crucial value in order to design new therapeutic strategies to prevent or delay the onset of neurodegenerative disorders. In parallel with this extensive research related to the field of human diseases, it is important to measure and quantify the structural and mechanical properties of amyloid fibrils as well as understand how they emerge from the fibrillization process in order to appreciate them fully as novel biomaterials.

During my experimental work, I focused on the biophysical investigation of the kinetics of amyloid fibril formation, of the early stages of aggregation and on the study of the mechanical and structural properties of the intermediate and final products of aggregation. These studies were performed by means of spectroscopic bulk techniques and both conventional and innovative single molecule techniques based on Atomic Force Microscopy. Bulk techniques as Thioflavin T, Circular Dichroism and Infrared Spectroscopy are powerful methods to investigate the properties of amyloid aggregation in solution. In particular, Thioflavin T enables following the kinetic of growth of fibrils, while Circular Dichroism and infrared spectroscopy give information on the conformational change and secondary structure of the forming structures. However, a significant factor, limiting the general applicability of these bulk techniques for the study of protein aggregation, is that they are able to give only average information only on the ensemble of the species present in the heterogeneous aggregating

solution. AFM allowed investigating at the single aggregate scale the oligomerization and fibrillization of wild type and mutated forms of several amyloidogenic proteins, such as α -synuclein and huntingtin, as mainly shown in the second chapter. Moreover, different implementations of the methodology, such as force spectroscopy, force volume mapping and the peak force quantitative nanomechanical mapping (PF-QNM) enable investigating the mechanical properties of fibrils and other species forming during the aggregation process. In particular, in the third chapter, an application of force spectroscopy in order to manipulate at the nanoscale and investigate the mechanical properties of α -synuclein prefibrillar structures is exposed. While, in the fourth chapter, the PF-QNM technique is implemented to study the evolution of the mechanical properties of amyloid aggregates. Notwithstanding the astonishing insight brought into the field of proteins aggregation by these techniques, until now the contemporary mechanical and structural characterization of amyloid aggregates has been limited by their nanoscale dimensions. A new AFM-based spectroscopic technique, termed infrared nanospectroscopy, has the potential to be used successfully to chemically and structurally investigate at the nanoscale the misfolding process and the structural properties of the oligomeric and fibrillar species present in the fibrillation pathway. This technique exploits the simultaneous use of AFM and IR. In the fifth chapter, it is exposed a first demonstration of the capability of this technique to distinguish and structurally characterize monomeric and aggregated forms of lysozyme micro-droplets. In the final chapter, for the first time at the nanoscale, the parallel application of AFM-based nanomechanical measurements and of the chemical investigation by infrared nanospectroscopy has allowed correlating amyloid elastic and structural properties during protein misfolding and aggregation of the Josephin domain of ataxin-3.

Chapter 2. AFM as a versatile tool to investigate pathway and kinetics of amyloids formation

This chapter contain part of the data of two scientific publications. The first published in Journal of Biological Chemistry with the following authors:

O. Khalaf¹, B. Fauvet¹, A. Oueslati¹, I. Dikiy², A. Mahul-Mellier¹, F. S. Ruggeri³, M. Mbefo¹, F. Vercruysse¹, G. Dietler³, S. Jae Lee⁴, D. Eliezer² and H. A. Lashuel¹

And the latter in Angewandte Chemie with the following authors:

A. Ansaloni¹, Z. M. Wang¹, Jae Sun Jeong³, F. S. Ruggeri³, G. Dietler³, and H. A. Lashuel¹

Affiliations:

¹Brain Mind Institute, EPFL, 1015 Lausanne, Switzerland.

²Department of Biochemistry, Weill Cornell Medical College, New York, 10065, USA.

³Laboratory of Physics of Living Matter, EPFL, 1015 Lausanne, Switzerland.

⁴Department of Biomedical Science and Technology, Konkuk University, Seoul, South Korea.

Abstract

Aging of the world population has increased the visibility of neurodegenerative disorders, such as Parkinson's and Huntington's diseases. These human illnesses are strictly linked with the aggregation towards amyloid fibrillar structures of α -synuclein and huntingtin proteins, respectively. The use of Atomic Force Microscopy is essential to unravel the characteristics of amyloid structures at the nanometer scale. The technique is able to provide direct information on the size and the morphology of the species present during the pathway of amyloids formation. In the present work, we show that the realization of consistent AFM measurements enable to study the aggregation pathway of these two proteins and to quantitatively compare the kinetics of fibrillization of wild type mutated forms of the proteins. First, we studied the role in the protein aggregation process of a post-translational mutation (pT3), in the N-terminus of the protein. We showed that phosphorylation of the protein conspicuously slowed the oligomerization and fibrillization process. Notably, the protein is fibrillating below the pathogenic threshold. Successively, we were able to unravel α -synuclein early aggregation pathway and to study the role of a new missense mutation (H50Q) in the process, in particular this mutation accelerated fibrillization *in vitro*. Elucidating the consequences of sequence mutations on the biochemical, structural and aggregation pathway of amyloidogenic proteins is essential for the unraveling of the molecular basis of their function in health and disease.

2.1 Introduction

The onset of Parkinson's (PD), Huntington's diseases (HD) and of more than fifty further related pathologies is associated at the molecular level with the proliferation of amyloid fibrillar aggregates, formed from normally soluble cellular proteins.^{2,131} During their aggregation, proteins initially in their monomeric forms undergo internal structural rearrangement, and misfold into conformations that are susceptible to form fibrils. During the aggregation process, several coexisting aggregate species are formed, giving rise to a highly heterogeneous reaction mixture. The fibrillation process typically takes the form of a nucleation-dependent polymerization reaction.²¹⁵ This model supposes that formation of oligomeric nuclei is necessary for the formation of the first protofibrillar structures, ultimately leading to the formation of the mature amyloid fibrils. Structural polymorphism can be encountered at all aggregation levels, and can be seen to originate as a consequence of the glassy, frustrated energy landscape that underlies misfolding and aggregation.⁴⁰

Atomic Force Microscopy (AFM) has emerged in the last decades as one of the most powerful and versatile single molecule techniques because of the possibility to acquire 3-dimensional morphology maps of specimens on a surface. This capability has been widely used in the field of protein aggregation and amyloid fibrils formation. Indeed, a simple AFM map provides extremely valuable information at the nanometer scale on the structure of amyloid fibrils, such as height, width, periodicity, flexibility and packing of single protofilaments inside mature fibrils.^{36,198} Furthermore, the possibility to analyze the morphology at several time points, during the process of amyloid aggregation, enables to shed light on the mechanisms of protein misfolding, on the pathway of aggregation and the hierarchical polymorphic process of assembly. In this chapter, AFM imaging is used to analyze in detail the early process of amyloid formation and to compare the kinetics of aggregation of different mutated forms of the same protein.

First, we investigated the effect of phosphorylation of the N-terminus of huntingtin protein. Despite constituting a small part of the total protein sequence (~3%), the overexpression of the N-terminal of the protein (residues 1-90, Httex1) is able to replicate the features of HD.¹⁴⁵ Within these residues, the first N-terminal 17 amino acids play a fundamental role in Httex1 structure, aggregation and function.¹³⁵ Increasing evidence suggests that specific N-terminal post-translation modifications of huntingtin play a role in the pathogenesis of the

illness.¹³¹ For this reason, here, we focused on the study of fibrillation differences between the wild type and a T3-phosphorylated forms of Httex1-23Q protein. For the first time, our AFM studies allowed to follow quantitatively the kinetic of amyloid fibrils formation and to show that the N-terminus phosphorylated (pT3) mutated form of the protein significantly slows the fibrillation process. Notably, the protein aggregate and fibrillate below the pathogenic polyQ stretch length for the onset of HD. This suggest that the crossing of the pathogenic threshold is not necessary for Httex1 formation of fibrillar structures. Afterwards, it was studied the aggregation process of wild type (WT) α -synuclein and it was compared to a mutated form of the protein containing a new missense mutation encoding a histidine-to-glutamine substitution (H50Q), which was described in patients with a familial form of PD and dementia.¹¹¹ During the last two decades, already three missense mutations were linked to familial forms of PD and they have been identified in the gene encoding α -synuclein: A30P, E46K and A53T.^{216,217} Several studies, *in vitro* and *in vivo*, revealed that these mutations influence α -synuclein physiological properties and enhance its oligomerization, fibril formation and toxicity. Here, we investigated the effects of the novel H50Q mutation on the biophysical properties of α -synuclein. Similarly to the previously discovered mutations, we demonstrated that it also enhances the oligomerization and fibrillization propensity. Moreover, in literature the aggregation process of α -synuclein was almost completely studied under the condition of shaking (*fast aggregation*). The process in absence of shaking (*slow aggregation*) is extremely slow, takes months, and it is particularly difficult to obtain and it has been studied poorly.¹¹³ Thus, we decided to investigate the pathway of *slow aggregation* process to understand if it is possible to resolve, with higher time resolution, the early moments in which monomers start aggregating. Through this approach, we were able to distinguish the moment when monomers started to assembly into the first prefibrillar structures.

The understanding of the mechanisms of amyloid fibrils formation and polymorphism can provide the basis for establishing approaches to the disease prevention, such as the inhibition of repression of the aggregation process *in vivo* or the stabilization of a specific non-toxic species rather than another causing cell death. Moreover, understanding the biophysical effects of mutations on the kinetics and pathway of aggregation is fundamental to unravel the role of these proteins both in physiological and disease-related conditions. Finally, from the opposite point of view, in order to appreciate the full potential of amyloid fibrils as biomaterials, it is fundamental to understand how they emerge from the fibrillization process and how their structure could be modulated by changing the aggregation conditions.

2.2 Experimental Methods

Expression and purification of α -synuclein

Recombinant wild type and mutated H50Q α -synuclein were synthesized by E. Coli and then purified by standard previously accepted protocols.^{111,218}

Production of Huntingtin Exon 1

A semisynthetic strategy was implemented for the site-specific introduction of post-translational modifications (PTMs) within the Nt17 domain of huntingtin exon 1 (Httex1) using expressed protein ligation (EPL). This strategy was used to produce untagged wild-type (WT), single phosphorylated T3-phosphorylated (pT3) Httex1 containing 23Q.¹³⁶

Amyloid In vitro fibrillization assays

Wild type and mutated H50Q monomeric filtrated through 100 kDa molecular weight cutoff filter (>95%) α -synuclein, in a 50 mM TRIS-buffer solution with 150 mM, were incubated at 37 °C and at a concentration of 45 μ M. Initial volume was 800 μ l and the solution was adjusted to both pH 5.5 and pH 7.5. Solutions were stored in a sealed Eppendorf tube, to avoid contamination and evaporation, under static and shaking conditions for a variable time up 365 days.

Huntingtin exon 1 proteins were dissolved in 500 μ L of 10 mM Tris-HCl, 75 mM NaCl pH 7.4 at a final concentrations of 30 μ M. The samples were filtered through 100 kDa molecular weight cutoff filter to remove any preformed aggregates prior to sample incubation. Protein concentration was initially determined by weight and adjusted using a UPLC methods and a set of standards of known concentrations. Equal protein concentrations were also verified by CD and SDS-PAGE. Fibrillization was performed by incubation of the proteins at 37 °C without agitation for 8 weeks.

Atomic Force Microscopy Imaging

Analysis by AFM was performed on three differently charged substrates, **Fig. 2.1**: negatively charged bare mica, positively functionalized mica (mica-APTES) and hydrophobic highly oriented pyrolytic graphite (HOPG),. In the last case after the cleaving, the mica substrate, was

incubated with a 10- μ l drop of 0.05% (v/v) APTES ((3-Aminopropyl)triethoxysilane, Fluka) in Milli-Q water for 1 minute at ambient temperature, rinsed with Milli-Q water and then dried by the passage of a gentle flow of gaseous nitrogen.

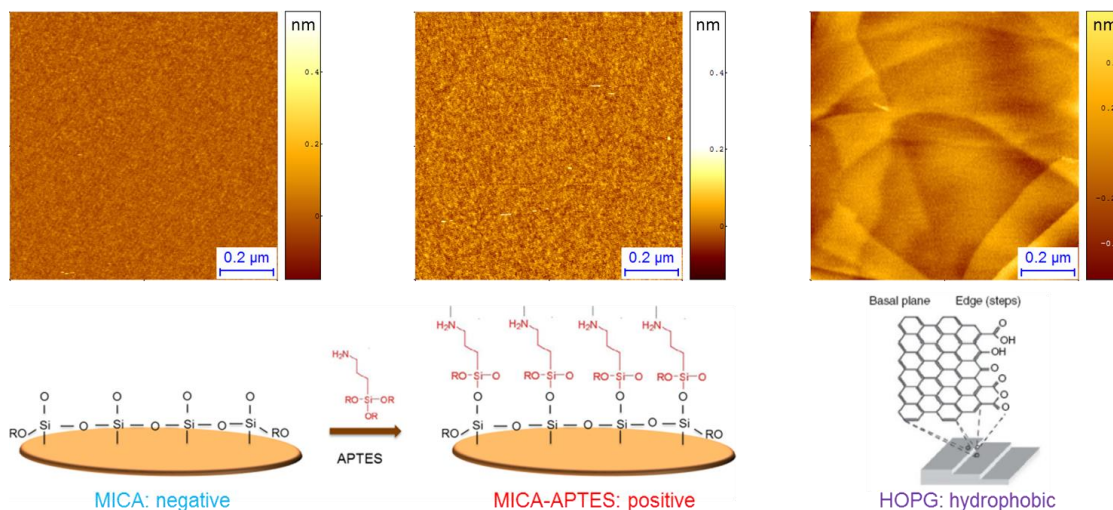


Figure 2.1 Substrates used for AFM imaging.

In the case of α -synuclein, samples were deposited on all surfaces at room temperature by deposition of a 10 μ l aliquot of solution, which was deposited at dilutions from full concentration (45 μ M) to 100 times dilution, with a deposition time in the range of 1-10 minutes. Successively, the sample was rinsed by water and dried by a gentle flow of Nitrogen. AFM images were made by means of two instruments in ambient condition: a Nanoscope IIIa by Bruker operating in tapping mode, equipped with a Silicon tip (Bruker, MPP-12120-10, 5 Nm^{-1}) with a nominal apex radius of 8 nm and a Park NX10 operating in true non-contact mode and equipped with a silicon tip (Nanosensor, PPP-NCHR, 40 Nm^{-1}) with a nominal apex radius of 7 nm. The first microscope was utilized for monitoring all the fibrillation process and in particular the early stages, while the second was used to compared consistently the morphology of wild type and H50Q fibrils after 6 days. Huntingtin samples were prepared on mica-APTES at room temperature by the deposition of 10 μ l aliquot of full concentrated solution. AFM was performed on a Park NX10 AFM system, which as described above was operated in the non-contact mode under ambient conditions, but using super sharp silicon tip with a nominal radius of 2 nm (Nanosensor, SSS-NCHR, 40 Nm^{-1}). AFM-images were flattened using the PARK built-in software and SPIP (Image metrology, Horsholm, Denmark). The statistical analysis of the images was conducted using SPIP software and the home-made software in our laboratory DNA-trace.²¹⁹

2.3 Kinetics of Aggregation of Wild Type and Phosphorylated Huntingtin

The aggregation of Huntingtin protein and its mutated forms is linked to the onset of Huntington's disease. Increasing evidence suggests that specific N-terminal post-translation modifications within the N-terminus of Huntingtin play a role in the pathogenesis of the illness. For this reason, we focused on the study of their fibrillation and on differences between wild type and a mutated form of this protein. Our AFM studies allowed following quantitatively the kinetic of amyloid fibrils formation and to show that the N-terminus phosphorylated (pT3) mutated form of the protein significantly slows the fibrillation process.

To assess the effect of phosphorylation at T3 on the aggregation properties of Httex1, we employed AFM, which allows the visualization and characterization of early aggregation events and the quantitative assessment of the size and morphological distribution of the aggregates. WT and pT3 Httex1, were incubated separately at 37 °C without agitation and aggregation was monitored using AFM for 14 days. The samples were filtered through 100 kDa molecular weight-cutoff filter to remove any preformed aggregates prior to sample incubation. In **Fig. 2.2 A**, we can follow the fibrillation process of wild type and pT3 Httex1. We imaged by Atomic force microscopy (AFM) our samples after 1 h, 7 days and 14 days of incubation time. Within the first few hours of incubation, **Fig. 2.2 B**, wild type proteins formed oligomers with a typical height of 1 nm and a broad distribution of diameter as big as 100 nm. While, pT3 proteins were still present as oligomers with a typical height of about 1 nm and with small diameter (< 20 nm). After 7 days, **Fig. 2.2 C**, the wild type Httex1 oligomers with big diameter disappeared and the present small oligomers had slightly increased height. Furthermore, now the AFM revealed fibrils with a broad distribution of average height within 4 nm and 6 nm (**Fig. 2.2 D**, blue bins in the histogram). Instead, after 7 days, pT3 Httex1 started to form oligomers with big diameter (ranging from 20 to 120 nm) and with slightly increasing height. At this point still no pT3 Httex1 fibrillar structures were formed. After 14 days, WT Httex1 formed extensive amounts of fibrils, whereas pT3 showed many elongated protofibrillar structures with an average height of approximately 2 nm, in addition to a small amount of mature fibrils with an average height of approximately 5 nm (**Fig. 2.2 D**, green bins in the histogram). The dimensions of pT3 fibrils were comparable with the dimensions of wild type Httex1 fibrils formed at 7 days. These results demonstrated that wild type Httex1 aggregated and formed fibrils more rapidly than pT3 Httex1. Notably, the study revealed that wild type Httex1 containing polyQ repeats below the pathogenic threshold exhibit high oligomerization and fibrillization

propensity as evidenced by the rapid formation of oligomers and fibrils both for the wild type and phosphorylated form of Httex1 proteins. Thus, suggesting that crossing the pathogenic threshold is not necessary to start amyloid aggregation.

Elucidating the consequences of sequence mutations on the biochemical, structural and aggregation pathway of amyloidogenic proteins is essential for the unraveling of the molecular basis of their function in health and disease.

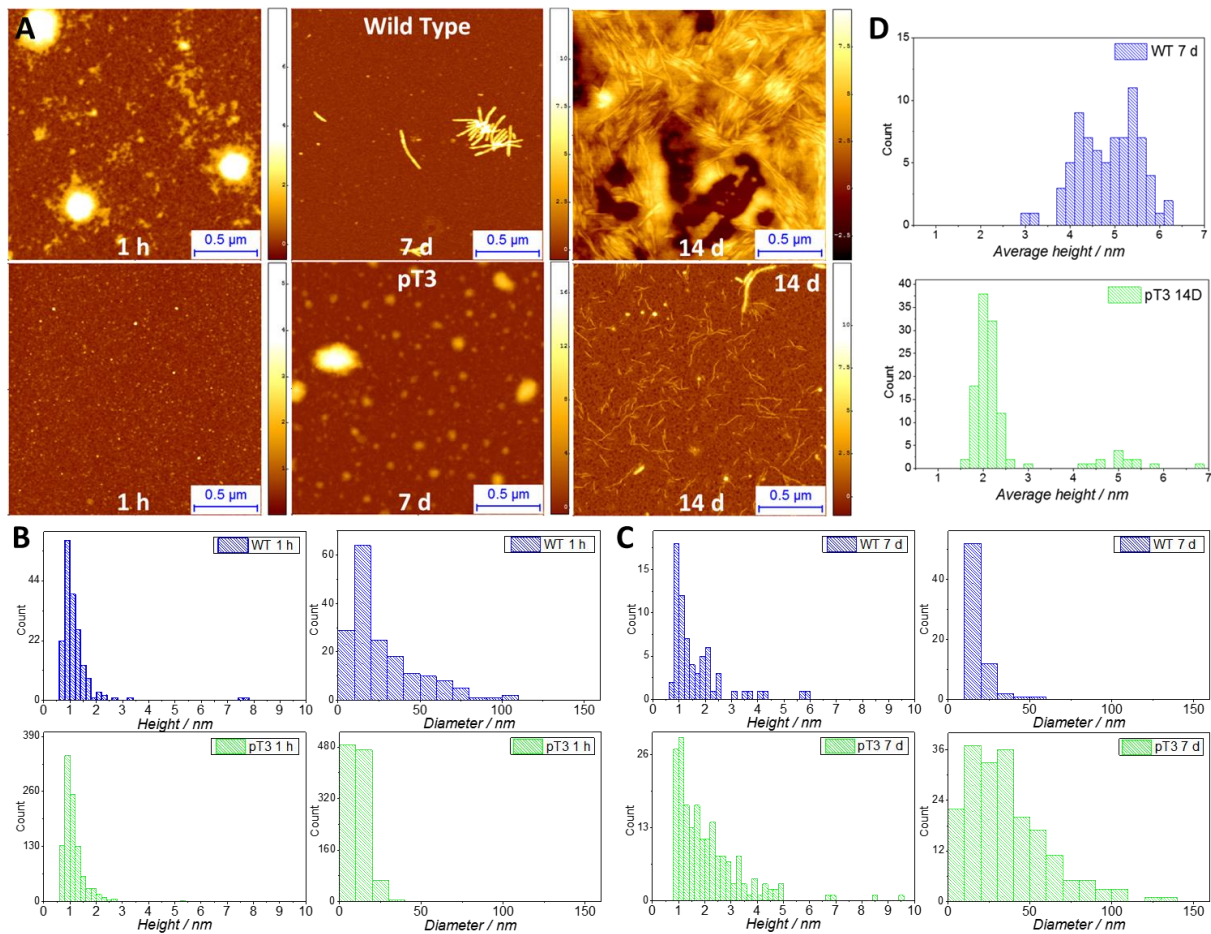


Figure 2.2 Oligomerization and Fibrillization process of wild type and pT3 huntingtin.

(A) Aggregation of wild type and mutated pT3 huntingtin followed by AFM. (B) Height and diameter distributions of mutated pT3 (green) and wild type oligomeric structures after 1 hour incubation. (C) Height and diameter distributions of mutated pT3 (green) and wild type oligomeric structures after 7 days incubation. (D) Height distribution of mutated pT3 (green) at 14 days and wild type protein at 7 days.

2.4 Role of H50Q mutation in α -synuclein kinetics of aggregation and early stages of fibrillization

The exact molecular mechanism underlying α -synuclein fibrillation it is not still fully understood and it is most likely determined by the experimental conditions used in the aggregation process. Fundamental parameters are: concentration, pH, salt content and shaking of the fibrillating solution. In particular, the shaking (*agitation*) is a strong accelerator of the fibril formation process: typically fibrillation of a 1 mg/mL concentrated solution of α -synuclein is completed within 3 days (*fast aggregation*), while without (*slow aggregation*) it needs a time of the order of months.

In the first part of this section, we will study and compare the *fast* aggregation of wild type and H50Q mutated α -synuclein. Usually, in literature, the study of amyloid fibrillization is conducted by the use of one substrate in which proteins are deposited and analyzed, in order to study separately the oligomerization and fibrillization process, we performed our analysis by depositing on differently charged surfaces the aggregated protein. In the second part, similarly, we will investigate the process of fibrillization in absence of shaking. In particular, it will be shown that it is possible to profit of the slowness of the reaction to follow with higher time-resolution the early moments of the aggregation process corresponding to the lag and growth phases.

2.4.1 Comparison of the kinetics of aggregation of WT and H50Q mutated α -synuclein

To determine the effect of H50Q mutation on α -synuclein early stages of oligomerization and on fibrillation, we compared the *fast* aggregation at 37 °C, at pH 7.5 and at 45 μ M of WT and H50Q proteins by AFM imaging. Since α -synuclein is negatively charged at physiological pH, it has high affinity towards positively charged surfaces, such APTES-mica. However, functionalization of mica causes a higher surface roughness (~0.1 nm) than the negative bare substrate, which possess low topographical roughness (~0.01 nm) allowing higher resolution imaging. Thus, both surfaces were used to image the aggregation of WT and mutated α -synuclein and to separately study the oligomerization and fibrillization process. At low concentration of deposition (0.5 μ M, i.e. low surface coverage) bare mica is suitable for the

visualization and statistical analysis of the single monomers and the early oligomerization process (**Fig. 2.2**). At the late aggregation stages, a high concentration of deposition ($45 \mu\text{M}$) on APTES-mica is more suitable for a statistical characterization of protofibrils and fibrils (**Fig. 2.4, 2.5**).

Freshly prepared WT and H50Q α -synuclein diluted to $0.5 \mu\text{M}$ and deposited on bare mica surfaces displayed a mixture of monomeric and dimeric species as well as some higher-order oligomers (**Fig. 2.3**).

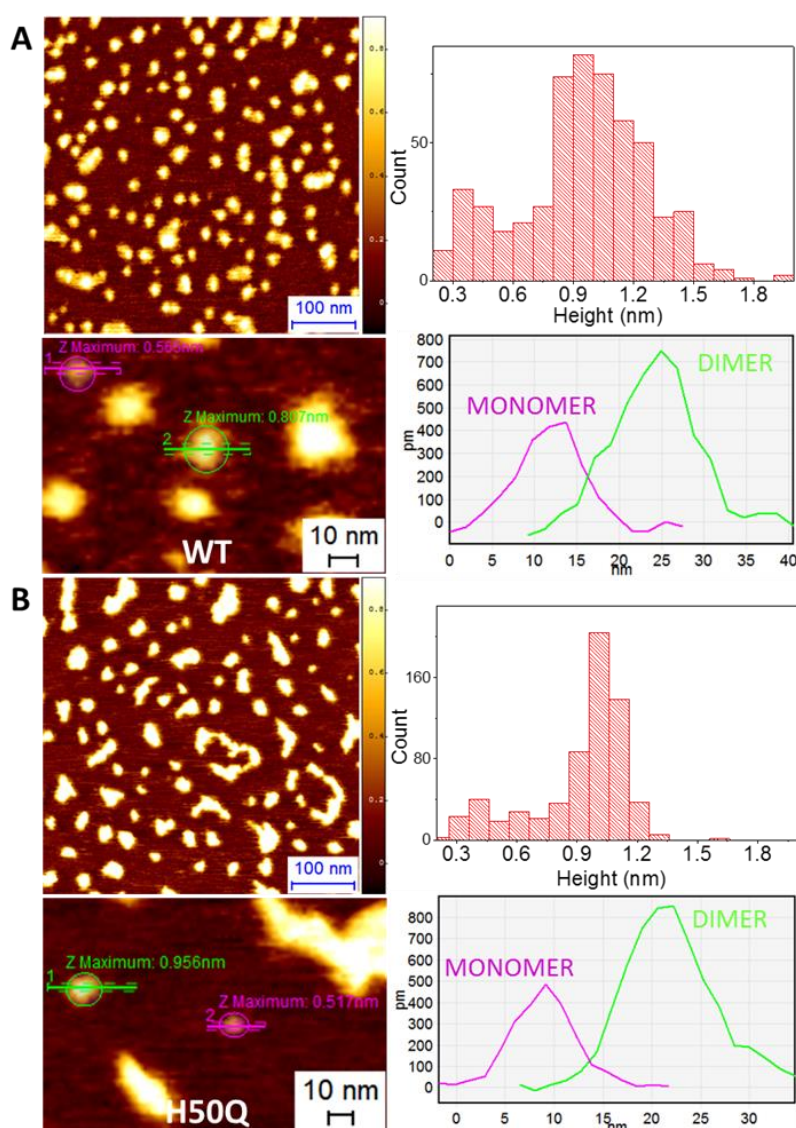


Figure 2.3 AFM analysis of monomeric α -synuclein at a low concentration of deposition.

Comparison of wild type (A) and mutated H50Q (B) α -synuclein. For both parts: top left panel, high resolution height map; bottom left panel, zoomed section of the above picture showing typical monomer and dimer particles top right panel, height distribution histogram; bottom right panel, cross-sectional analysis of a monomer (magenta line) and dimer (green line) particles from the bottom left picture.

Monomers and dimers from both α -synuclein variants displayed similar average diameters and heights, but H50Q α -synuclein showed more elongated oligomeric structures than WT α -synuclein. The height histograms show a first height population (monomers) with an average height of ~ 0.3 nm and a second population (dimers) composed with average height of ~ 0.9 nm. These dimers were always present for both WT and H50Q α -synuclein, with a higher proportion of dimers in H50Q compared to WT α -synuclein. Even though samples were filtered through 100 kDa membranes, these dimers quickly re-form after the filtration and might deposit more efficiently than the monomers on the mica surface. No larger species are detectable in significant proportions in **Fig. 2.3**, thus excluding the presence of large oligomers and/or protofibrils. Due to the limit of the AFM tip's lateral resolution, it is not possible to obtain reliable lateral diameter estimation of the particles. Thus, the larger structures seen with H50Q α -synuclein (Fig. 4B, b) correspond to closely-associated monomers and dimers in the x-y plane. Together with circular dichroism data,¹¹¹ these analysis suggested a faster rates of β -sheet-rich oligomer formation for H50Q α -synuclein compared with its WT counterpart.

In order to determine whether fibrillization pathway and structural properties of α -synuclein fibrils were affected by the H50Q mutation, a first comparison of the aggregation is showed in **Fig. 2.4**. Both proteins were deposited at full concentration on an APTES-mica substrate.

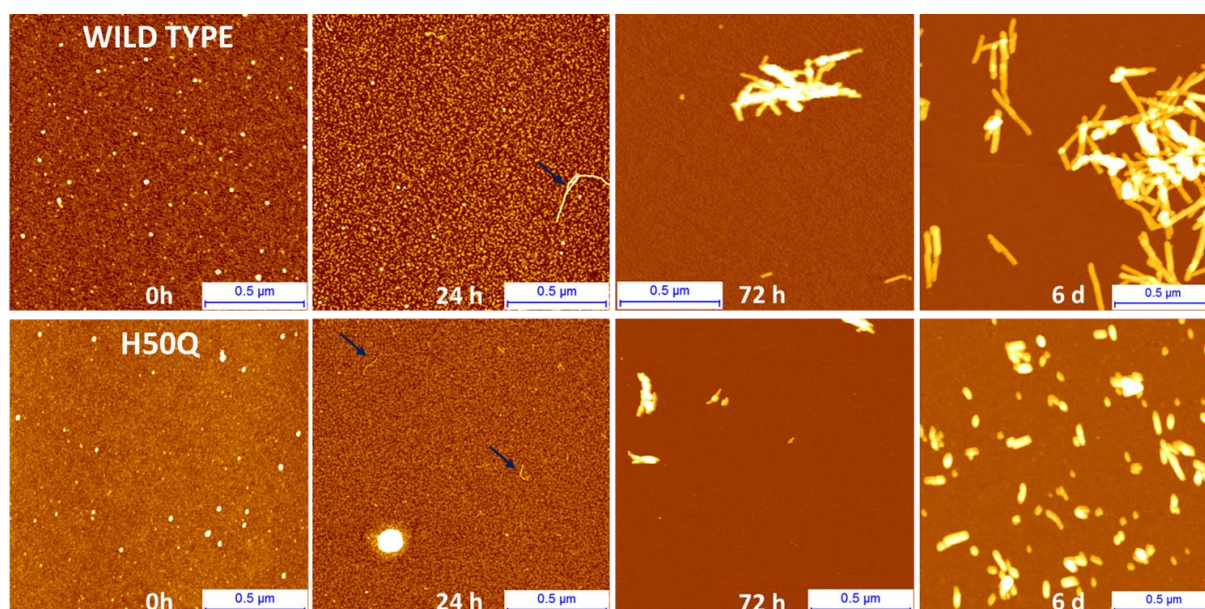


Figure 2.4 Aggregation process of wild type and mutated H50Q α -synuclein.

Deposition of proteins on APTES-mica at 0, 1, 3, 6 days. Top panel, aggregation of wild type protein. Down panel, aggregation of mutated H50Q protein. Arrows indicate small prefibrillar structures.

At a first glance, in both cases, it is possible to conclude that initially only oligomeric structures are present (0 hours), successively first prefibrillar structures form (24 hours) and at later points (72 hours, 6 days) protofibrillar and fibrillar structures are formed. Notably, the WT fibrillar structures are longer than H50Q ones. This easy comparison could bring to the conclusion that WT protein fibrillate faster than mutated H50Q.

A single aggregate statistical analysis of the fibrillar cross-sectional dimensions scale enabled to quantitatively retrieve a comparison of the kinetics of aggregation of the two different proteins and to conclude that previous affirmation is erroneous. In order to prove it, we performed the statistical analysis after 6 days incubation (**Fig. 2.5**). The detailed analysis of WT fibrillar structures and the measurement of their cross-sectional dimensions enabled to observe two different populations of structures with height of ~ 4 nm and $\sim 6-7$ nm (**Fig. 2.5 A,B**). While, the average height distribution showed an abundant population peaked at 4.8 ± 0.5 nm and a tail with bigger fibrils (**Fig. 2.5 C**). This means that we had abundant formation of protofibrils (typical height between 3-4 nm) and formation of mature fibrils (typical height between 6-9 nm), which are much rare, is still at the initial stage. The statistical analysis of the length of WT fibrils showed an average value of 150 ± 70 nm (**Fig. 2.5 D**). The same analysis was performed in the case of the mutated protein. High resolution images of H50Q fibrillar structures and measurement of their cross sectional dimensions revealed again two distinct fibrillar populations (**Fig. 2.5 E**). Moreover, in this case, the statistical analysis of the height distribution of these structures showed that both populations were abundant. The first one had an average height of 4 ± 0.4 nm and the second one of 6.2 ± 0.5 nm (**Fig. 2.5 F**). This means that H50Q formation of amyloid mature structures is in a more advanced stage than the WT proteins, notwithstanding the fact they have shorter than WT fibrils average length, of 80 ± 30 nm (**Fig. 2.5 G**). Considering that measurements of the two samples have been performed by the same AFM tip and in identical scanning conditions, we can affirm that: 1) H50Q protofibrils have smaller heights than WT ones. 2) H50Q fibrillar structures have smaller length than WT ones. 3) WT fibrillation is occurring more slowly than for H50Q.

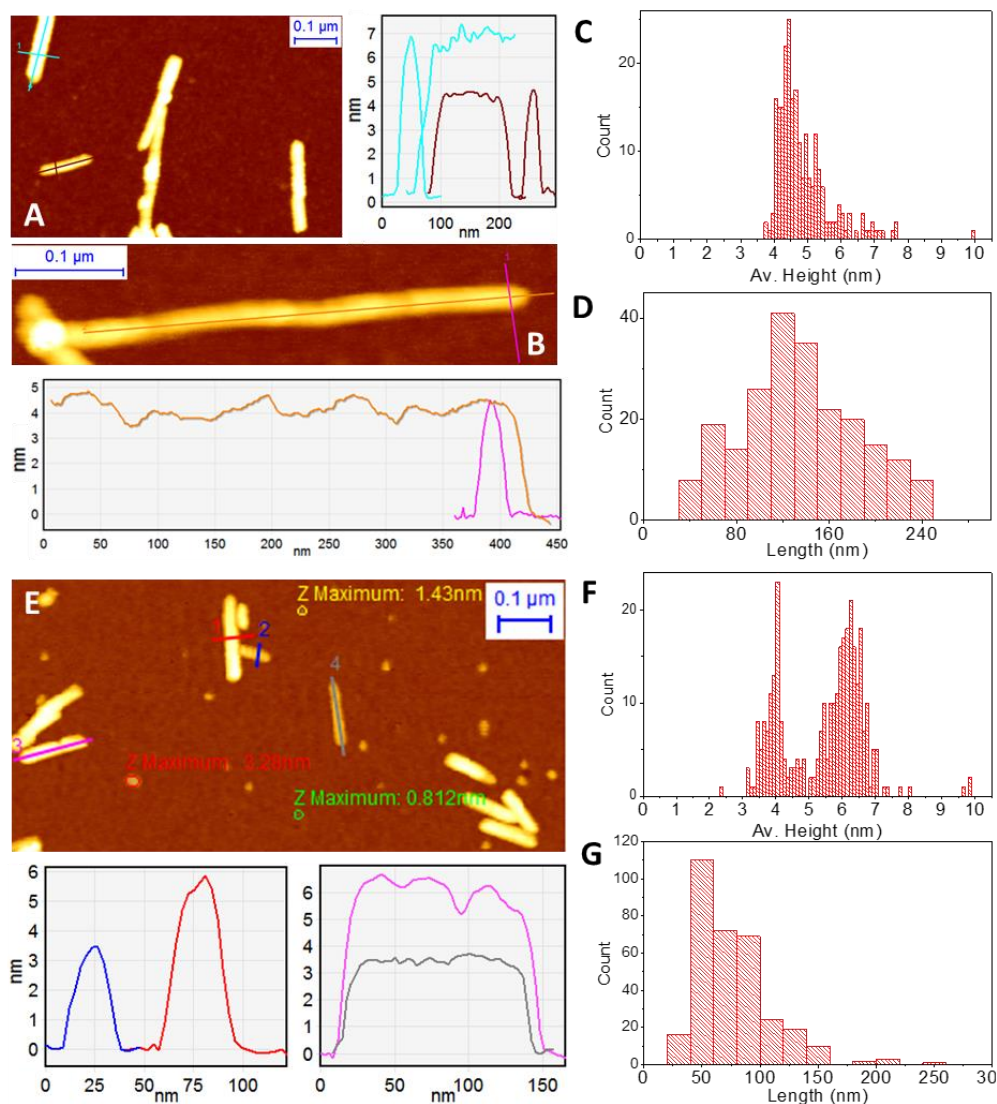


Figure 2.5 Morphology of fibrillar structures of WT (top panel) and mutated H50Q (low panel) α -synuclein after a 6 days incubation, high concentration deposition (45 μ M) on APTES-mica.

(A-B) Details of WT protofibrils and fibrils and cross-sectional dimensions. (C-D) Distribution of the average height and length of WT fibrillar structures. (E) Details of H50Q oligomers, protofibrils and fibrils and of their cross-sectional dimensions. (F-G) Distribution of the average height and length of H50Q fibrillar structures.

2.4.2 Early aggregation pathway of wild type α -synuclein.

As it is indicated by the blue arrows in **Fig. 2.4** and showed in detail in **Fig. 2.6**, *in-pathway* of the process of α -synuclein *fast* aggregation at pH 7.5, prefibrillar structures are already present after 24 hour of incubation for both mutated and wild type protein. Accordingly, at this time point, CD measurements showed the initial acquisition of β -sheet structure both for the mutated H50Q and the wild type protein.

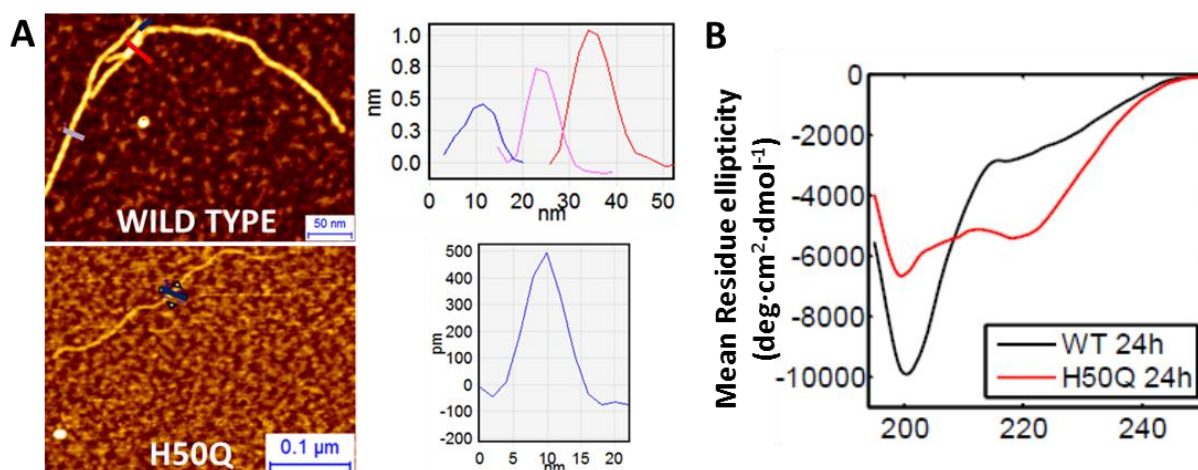


Figure 2.6 α -synuclein prefibrillar structures in-pathway of aggregation.

(A) Top: detail of wild type joining prefibrillar structures and cross-sectional dimensions. Down: detail of H50Q prefibrillar structure and relative cross-sectional dimension. (B) CD measurements.¹¹¹

As it is showed by the measurement of their height in **Fig. 2.6**, these prefibrillar structures have sub-nanometer apparent height at the AFM. Notably, their height and width are comparable to the monomeric and dimeric ones in **Fig. 2.3**. This strongly suggested for physical reasons that no more than a dimer could be packed inside such a small structure. Recently, it was again supposed that subfilaments with diameter of about 1 nm should be the constituents of final matures fibrils of α -synuclein, but so small prefibrillar species were never been isolated.²²⁰ Thus, we started to modify the parameters of aggregation in order to understand if these prefibrillar structures are always *in-pathway* of aggregation. We found that presence/absence of salt content in the aggregating solution did not affect their formation, while a decrease in pH enhanced their formation in the early stages of *fast* aggregation, **Fig. 2.7**.

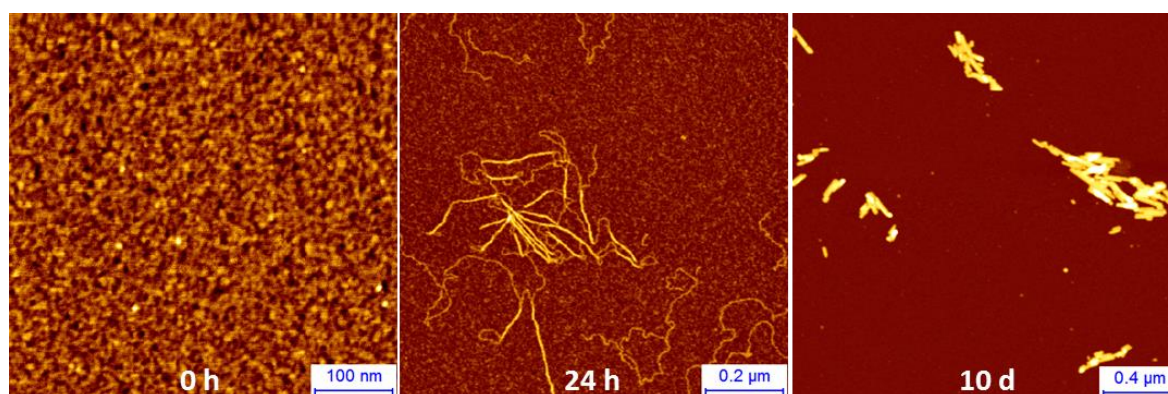


Figure 2.7 *Fast* aggregation of α -synuclein at 45 μ M and pH 5.5 on APTES-mica.

The transient nature of the observed prefibrillar species, together with the short time of formation during the *fast* aggregation process, did not allow to study in detail the pathway of their aggregation. Thus, in order to unravel the process of prefibrillar structures formation, we decided to investigate the static and *slow* aggregation of the protein solution in identical conditions than the *fast* process (**Fig. 2.8**). Moreover, we followed the fibrillation by depositing wild type α -synuclein on three different surfaces: negatively charged mica; positively functionalized mica (APTES-mica) and hydrophobic graphite (HOPG).

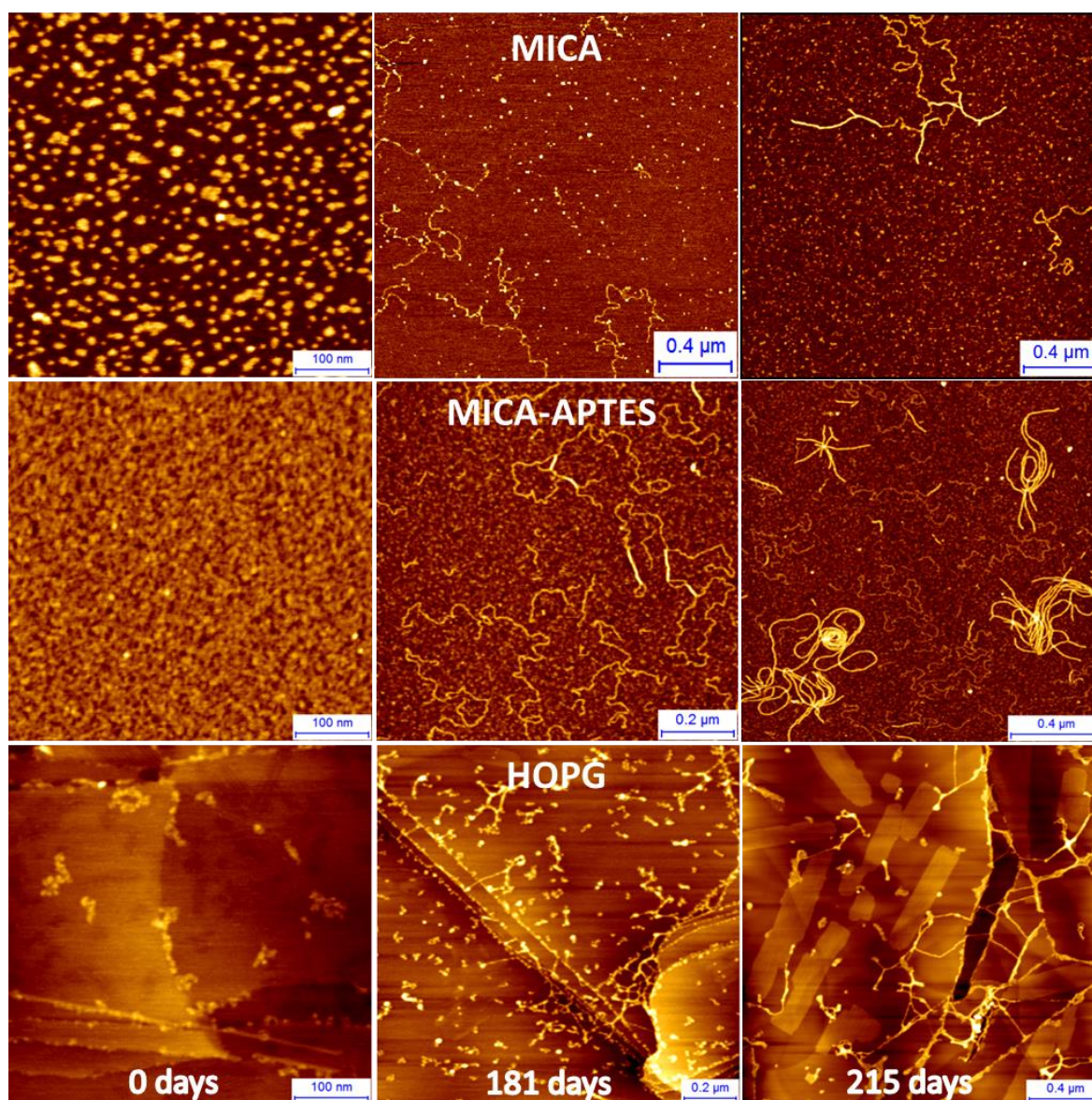


Figure 2.8 *Slow* aggregation of α -synuclein at pH 5.5 and 45 μ M on three different surfaces: mica, APTES-mica and HOPG.

Our idea was that, during the aggregation process and before of formation of fibrils, different structures are present in the heterogeneous, in *non-equilibrium*, incubated solution and that they can be selected by differential interaction with each surface. Before of incubation, we observed just oligomers on our surfaces. We performed an accurate statistical analysis of their cross sectional dimensions on the atomically flat mica surface (**Fig. 2.9 A**). Similarly to **Fig. 2.3**, at the initial stage of the aggregation two main height populations were found: first one were monomers and they have a height of ~ 0.4 nm, second one were dimers with height of ~ 0.8 nm (**Fig. 2.9 B**). These oligomeric species were present with constant cross-sectional dimensions all over the aggregation process (**Fig. 2.9 C**). The high abundance of monomers and dimers confirmed that the aggregation reaction even after months is still in its initial stage.

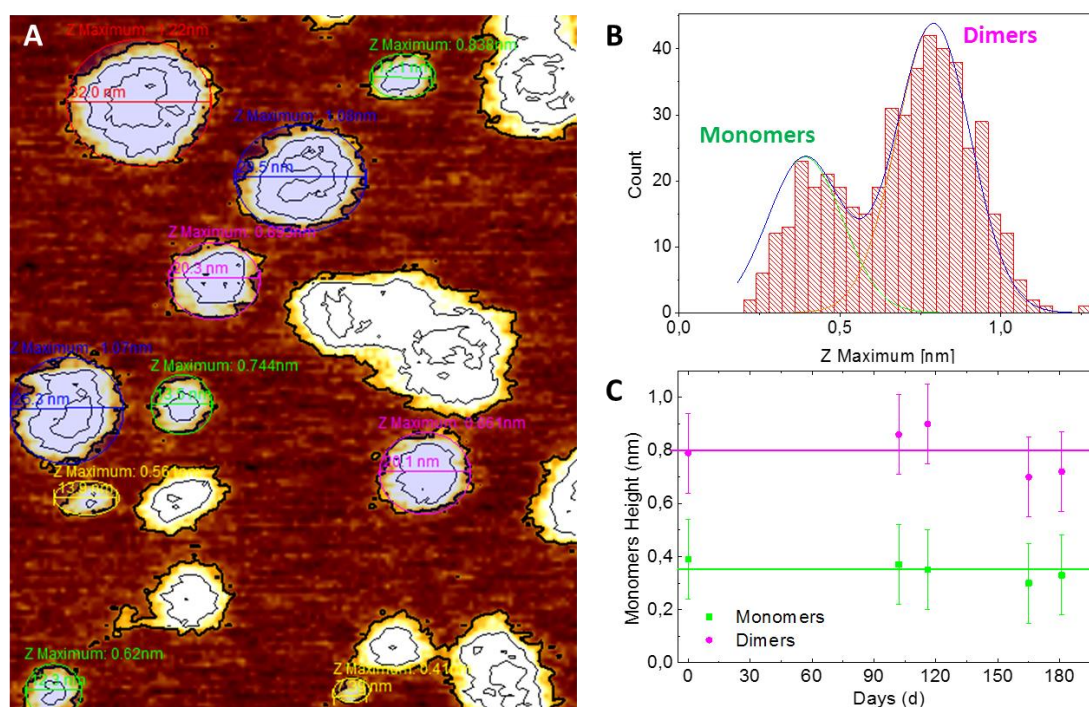


Figure 2.9 Statistical analysis of early oligomeric species during the *slow* aggregation process of α -synuclein.

(A) Oligomers at the initial stage of the aggregation (0 days). (B) Height distribution at 0 days of the more abundant populations: monomers (~ 0.4 nm) and dimers (~ 0.8 nm) and early oligomeric species (height > 1 nm). (C) Height of monomers and dimers during the aggregation process.

As expected, with increasing incubation time, elongated structures started to be present on all surfaces (**Fig. 2.10**). We termed these structures *protofilaments*. Furthermore, we found that protofilaments formation was independent from presence of salt, shaking and pH of the

solution. Together with the previous findings on *fast* aggregation, this suggested that protofilaments are a general feature of the aggregation process. We performed a statistical analysis of the height of protofilaments on all the three surfaces.²¹⁹ On charged substrates, we observed mainly two families of prefibrillar structures with height respectively of: ~ 0.4 nm and ~ 0.8 nm; instead on HOPG, after 181 days, we could also observe abundant formation of protofibrils with average height up to ~ 2 nm (**fig. 2.10 A-B**). A direct comparison of the monomeric and dimeric dimensions with the prefibrillar ones showed a perfect correspondence between their heights, similarly as in the case of the *fast* aggregation process. Therefore, we suggested that the first family of protofilaments is composed by a single monomeric layer and we termed it *single strand* protofilament. While second population had height corresponding to the one of dimers, thus we termed it *double strand* protofilaments because they form by association of *single strand* ones (**Fig. 2.10**).

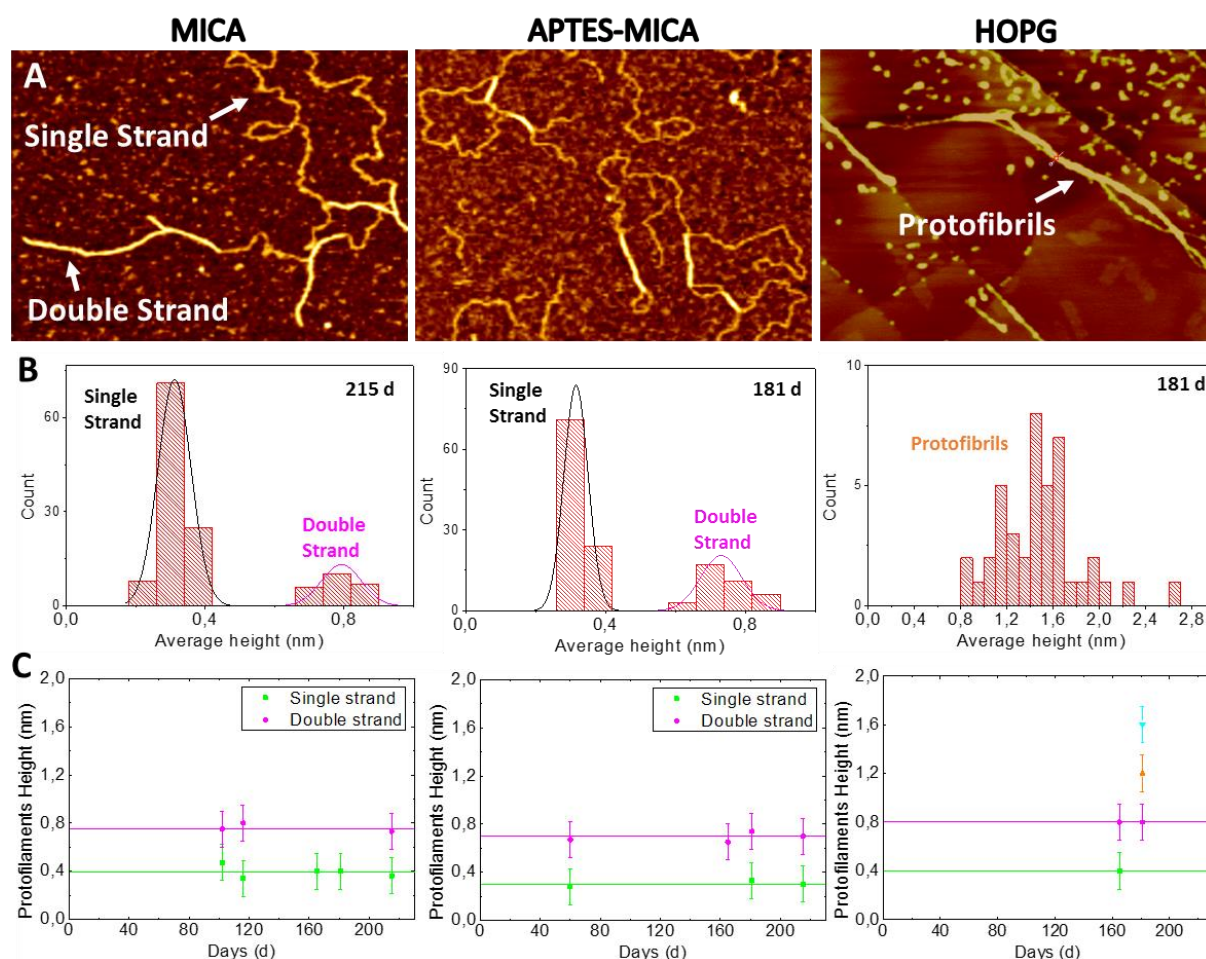


Figure 2.10 Statistical analysis of prefibrillar species on mica, APTES-mica and HOPG.

(A) Detail of the prefibrillar structures. (B) Height distribution at a time point. (C) Average value of height as a function of incubation time.

A further analysis of the persistence length and the periodicity of the prefibrillar structures enabled to study their polymorphism. *Single strand* protofilaments did not show any internal structure and they appeared in the images as semi flexible rod-like structures. By means of the bond correlation function for semi-flexible polymers in a two-dimensional conformation (**Equation (1)**, Chapter 1), we calculated a value of persistence length for *single strand* protofilaments of ~ 20 nm, which is the same for both the structures on mica and APTES mica. The analysis of this quantity for the protofilaments deposited on HOPG was not possible because of the notable surface effects, due to the ordering of the structures along the HOPG steps.

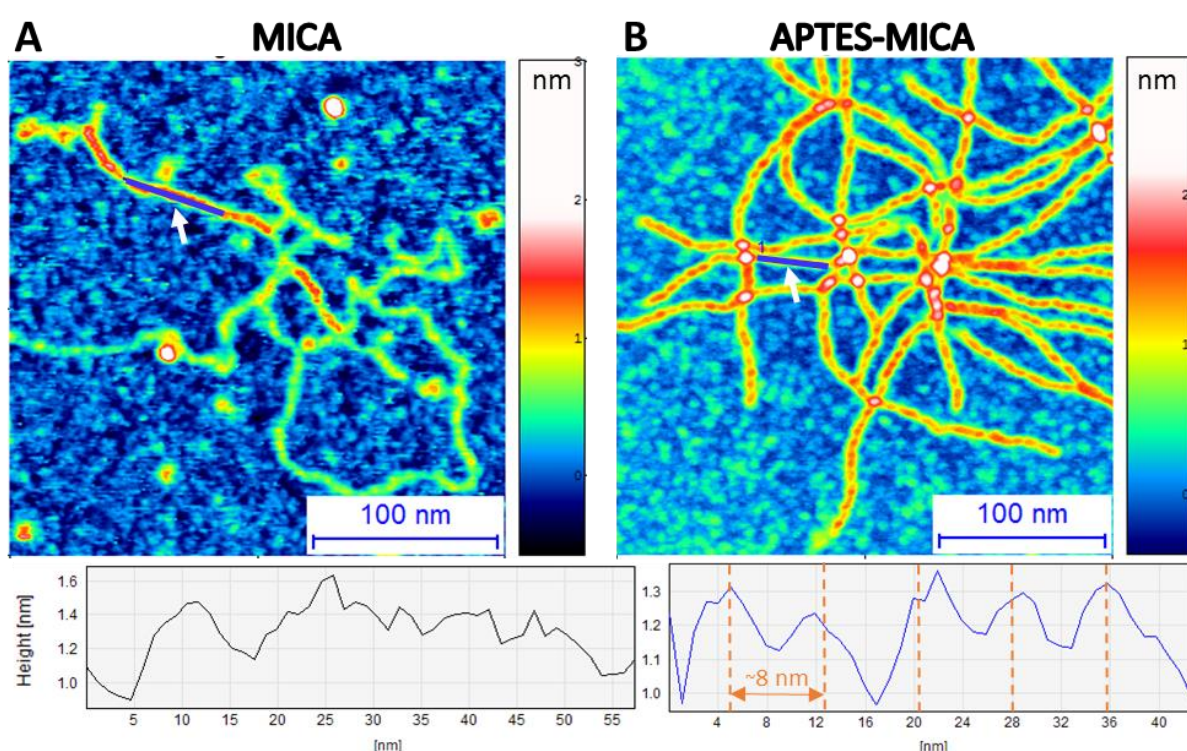


Figure 2.11 Polymorphism of α -synuclein protofilaments.

(A) Single strand and double strand protofilaments on mica and cross sectional irregular profile of a double strand protofilament. (B) Double strand protofilaments on APTES-mica clearly showing periodicity and cross-sectional profile of a protofilament. The structure has a periodicity of ~ 8 nm.

It is worth noticing that *double strand* protofilaments showed a small periodicity of < 10 nm on APTES-mica, but not on mica (**Fig. 2.11**). Moreover, periodic (twisted structure) *double strand* structures had a persistence length of ~ 150 nm, while laterally associated (ribbon-like) ones had a persistence length of ~ 250 nm. All together, these results suggested that two polymorphic *double strand* protofilaments exist: (i) first type deriving from the intertwining of

two *single strand* ones; (ii) second type deriving from two laterally associating *single strand* protofilaments.

The measurement of the persistence length l_p enabled extracting the Young's modulus E of the protofilaments, through the application of the relationship $E = l_p k_b T / I$. An important issue that aroused to measure the Young's modulus, it was calculating the protofilaments cross sectional moment of inertia I . If the fibril is formed by several filaments, it becomes necessary to propose a filament packing mechanism.^{11,36,221} Furthermore, the measurement of height by AFM, in air for a relaxed object on a surface less tall than 4 nm, is affected by a considerable underestimation. This is majorly due to dehydration effects, to the influence of the tip-substrate interaction in the measurement of the force between tip and sample and to the mechanical deformation and pushing of the sample by the tip.^{194,222} For this reason, the measured apparent heights at the AFM of the *single strand* population and of the oligomers (~0.4 nm) were much smaller than their "real" value.²²³ Thus, we deposited our prefibrillar structures together with circular DNA (**Fig. 2.12**) in order to use it as an *internal ruler* for the measurement of the "real" height of the prefibrillar structures, which is the fundamental parameter to calculate the cross sectional moment of inertia I . The structure of DNA has been extensively studied and it is universally accepted as a flexible double helix with ~2 nm diameter.²²⁴ *Single strand* structures possessed half of the height of DNA, while *double strand* ones had similar height as the DNA. Supposing that the structures have circular cross section, this means that the "real" diameter of first population is ~1 nm, while second one has a real diameter of ~2 nm.

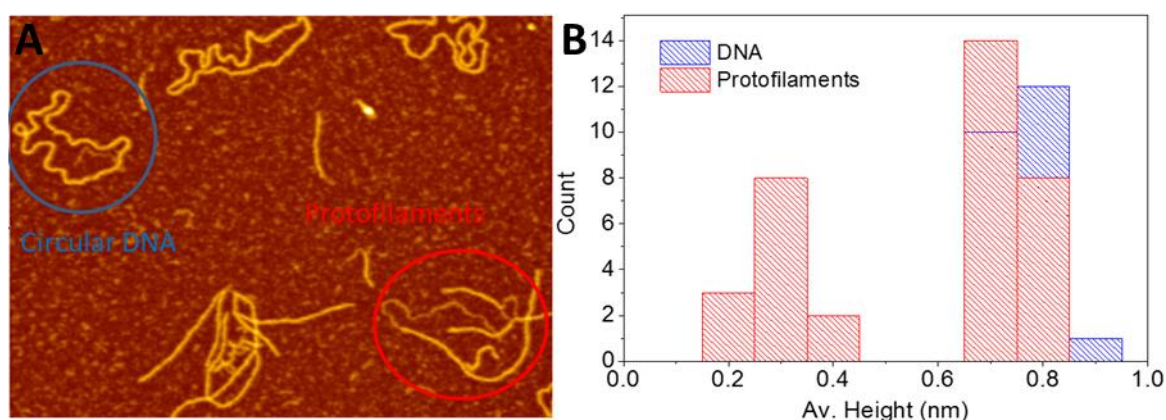


Figure 2.12 Comparison of the height of circular DNA and protofilaments.

(A) AFM image of protofilaments and circular DNA deposited on APTES-mica. (B) Height distribution of DNA and protofilaments.

Considering *single strand* protofilaments as a rod with circular cross section and moment of inertia of $I = \frac{1}{64}\pi d^4$, persistence length of 20 nm, diameter of $\approx 1-1.2$ nm for a measurement at 295 K, we were able to extract a Young's modulus of $E \approx 0.8-1.7$ GPa. This notable value confirms that protofilaments possess a rigid structure, likely because of the formation of the universal amyloid cross- β structure. Nevertheless, it is smaller than the typical value for a mature amyloid fibril (i.e. typical 2-4 GPa)¹⁶³, confirming the prefibrillar nature of these protofilaments. We extracted the value of Young's modulus also for the *double strand* protofilaments showing periodicity. We considered a twisted ribbon packing model³⁸ with $l_p = 150$ nm and $I = \frac{n}{64}\pi d^4 \sqrt{\frac{4}{3} - \frac{1}{n^2}}$, where $n=2$ is the number of component filaments. We obtained a value of Young's modulus of $E \approx 1.2-2.5$ GPa. Despite this is just a rough estimation, because of the indetermination in diameter, the value of stiffness is comparable to what obtained independently by PF-QNM for mature fibrils. This suggested that *single strand* structures had a *non-mature* amyloid structure, while *double strand* protofilaments possessed a more mature cross- β sheet structure stabilized by the numerous intermolecular hydrogen bonds, which determine the high value of intrinsic stiffness.

Finally, we can affirm that this new approach, based on differential surface-molecule interaction, allowed a more detailed study of amyloids aggregation process and polymorphism. Surfaces with different state of charge/hydrophobicity selected different amyloids species. All the three used substrates were able to adsorb *single strand* protofilaments, APTES-mica was able to select mainly intertwining *double strand* protofilaments, bare mica just laterally associated ones and HOPG was able to absorb the forming protofibrillar structures. Rarely, also on charged substrates we could observe *double strand* protofilaments branching to higher order structures. Recently, it was supposed that subfilaments with diameter of about 1 nm should be the constituents of final matures fibrils of α -synuclein.²²⁰ As it is extensively discussed in the third chapter of this thesis, the height of the *single strand* protofilaments is comparable to the height of proteins backbone, suggesting that they are formed from the direct assembly of monomers. According to the proposed model here, α -synuclein is not aggregating through oligomerization, but it is assembling to prefibrillar structures directly from monomers. As depicted in **Fig. 2.13**, protofibrils structures derive from the hierarchical assembly of the protofilaments and oligomerization is *off-pathway* of fibrillization. This picture is in fully agreement with the Hierarchical Assembling Process, proposed by Khurana as general trend for amyloids formation.³³ This model hypothesizes that the nascent protofilaments are formed by

non-native partially folded monomers assembling in small protofilaments, which successively assemble to form mature fibrils.

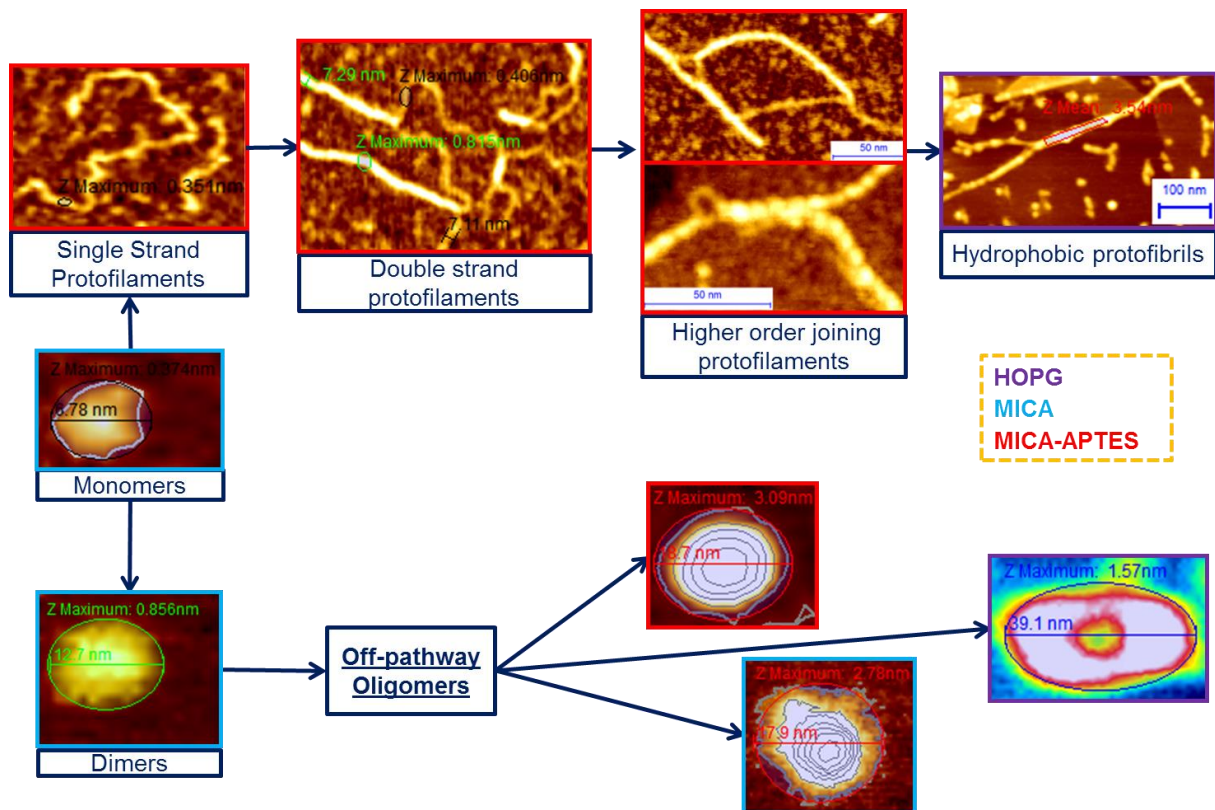


Figure 2.13 Early aggregation model of α -synuclein. By means of the application differential substrate-protein absorption, the aggregation process of α -synuclein is reconstructed. In particular, two separated process are shown: the first shows oligomerization process proceeding from monomers to dimers and larger oligomeric formation (down); the latter shows the hierarchical assembly of protofilaments towards protofibrillar structures.

2.4 Discussion

AFM is a versatile tool to follow the kinetic of amyloid aggregation process of amyloid proteins. Here, we compared the kinetics of aggregation of mutated and wild type forms of the same protein. Initially we showed that a N-terminus phosphorylated form of the huntingtin protein aggregates slower than the wild type protein. Successively, we presented a comparison of the speed of fibrillization and difference in morphology of WT and mutated H50Q fibrils. In particular, H50Q fibrillar structures showed smaller dimensions than wild type ones and they aggregated faster. The study of the effects of mutation on the aggregation of amyloidogenic proteins is of fundamental importance to shed light on their role in both physiological and diseases-associated role. Furthermore, AFM analyses are routinely limited to the use of only one substrate and this procedure produces just a partial depiction of the extremely heterogeneous aggregating solution. The use of three different surfaces of deposition with different state of charge (positive, negative, hydrophobic) enabled to overcome the problem of surface selectivity and to inquire deeply amyloids polymorphism and to have a complete representation of the heterogeneity of the sample. We were able to highlight that first stages of their formation comes from direct assembling of unfolded monomers into prefibrillar species. Remarkably, this behavior was independent on the agitation of the sample during incubation. This new mechanism of fibril formation and the studied monomeric prefibrillar species could be fundamentally linked to the process of disease onset. Indeed, these never observed species could be responsible for cytotoxicity. Therefore, a rational approach to avoid their formation could be the base for the development of pharmacological approaches to cure amyloid diseases.

Chapter 3. Nanomechanical Manipulation of Amyloid Protofilaments of α -synuclein

This chapter is based on an in revision paper in Journal of Biological Chemistry with the following authors:

Francesco Simone Ruggeri¹, Fabrizio Benedetti², Hilal Lashuel³, Sergey Sekatsky¹, Giovanni Dietler¹

Affiliations:

¹ *Laboratory of Physics of Living Matter, EPFL, 1015 Lausanne, Switzerland.*

² *Center for Integrative Genomics, University of Lausanne, 1015 Lausanne, Switzerland.*

³ *Brain Mind Institute, EPFL, 1015 Lausanne, Switzerland.*

Abstract

Amyloids are insoluble protein aggregates with a common cross β -sheet quaternary structure. Aggregation of α -Synuclein plays a central role in the onset of Parkinson's disease (PD). In our work, for the first time, prefibrillar structures of α -synuclein with nanometer scale dimensions were observed and mechanically manipulated at single molecule scale by Atomic Force Spectroscopy. The filamentous structures could be detached from a surface. This unzipping process was represented in the atomic force spectroscopy curves by constant force pulling events (plateaus). We were able to measure a fundamental value of interaction force within a single molecule and surface of 56 ± 5 pN. Moreover, the study of stretching events inside a plateau by means of the statistical theory of biopolymers allowed to investigate the internal mechanical properties of our prefibrillar structures and to confirm their direct assembling from unfolded monomers. We modeled the process of contemporary detachment of n filaments from a surface by a Monte Carlo simulation as the contemporary breaking of n parallel bonds. The model successfully reproduced the experimental values of the rupture forces necessary to unzip n protofilaments from the surface. The presented results highlighted the potential of force microscopy to unravel the driving forces of the fibrillization process at surfaces. A quantitative understanding of the mechanical properties of new prefibrillar α -synuclein aggregates is of fundamental importance for understanding their stability and mechanisms of clearance in the body. This would be central to design new therapeutic strategies for Parkinson's disease.

3.1 Introduction

The ability of proteins to assemble into functional complexes is one of the most fundamental processes in biology. One of these processes is the Amyloidosis, which is the aggregation of proteins in insoluble fibrous structures with a cross β -sheet quaternary structure, termed amyloids. Aggregation of α -synuclein towards amyloids quaternary β -sheet structures plays a central role in the neuropathology of Parkinson's disease (PD).^{2,89,110} Numerous studies have established that α -synuclein easily assembles into amyloid-like fibrils both in vitro and in vivo.^{33,112,113} In addition, α -synuclein can adopt a large variety of no-fibrillar oligomeric structures, the most commonly noted being the following: spheroidal, annular and chain-like aggregates with a broad range of variability of their dimensions. Moreover, α -synuclein fibrillation can take place in association with the cellular membrane surface⁹⁰. For these reasons, understanding of the mechanisms of formation of amyloid fibrils, of their intermediate products and of their deposition properties on surfaces is crucial for understanding the role of amyloid formation in the pathogenesis of PD.

Atomic Force Microscopy (AFM)-based single molecule force spectroscopy, similarly to AFM imaging, naturally poses itself as an important research tool in the field and can deliver information about mechanical and related structural properties of amyloid fibers at the single molecule scale. Force spectroscopy studies of different *mature* amyloid fibrils have been presented in the past by Kellermayer *et al.*^{204,205} These studies tried to quantify the interaction forces within β -sheet filaments inside a fibril of different fragments of A β 1–42, finding substantially smaller forces necessary to unzip subunit sheets of A β 1-42 *mature* fibrils in comparison with A β 1-40 ones. They well highlighted the importance of these works for understanding the details of amyloid formation and pointed out how single molecule manipulation methods allow to study mechanics and structural dynamics of amyloid formation. Such studies could be of special importance for initial and likely the most crucial stages of fibril formation. As an AFM study by Khurana showed, many amyloidogenic proteins follow a Hierarchical Assembling Model (HAM) in which a certain number of nanometer size protofilaments intertwine or laterally associate to form final amyloid polymorphic structures with typical diameter in the order of 10 nm; this was also the case of α -synuclein.³³ Others studies by X-ray diffraction and electron microscopy (EM) demonstrated that the final amyloid structures should be composed of protofilaments with nanometer size diameter.^{8,225} Moreover,

this has recently been explicitly proposed for α -synuclein by mean of an AFM mechanical study.²²⁰ Until this moment, nobody succeeded to isolate such small amyloidogenic precursors and researchers were constrained to explore their properties when already present inside a *mature* fibril. In the present work, we report first observations of protofilaments of α -synuclein having an apparent sub-nanometer diameter at the AFM height images. This observation enabled the possibility to nanomechanical manipulate the protofilaments by single molecule force spectroscopy studies. Thus, we could quantify the interaction force between of these amyloid protofilaments at the surface of deposition. Interaction forces at the surface could be of fundamental importance to unravel the driving forces of amyloid formation during the early assembling process and to understand their polymorphism. Finally, unraveling α -synuclein amyloid structure, mechanical properties, stability and driving force of fibrils formation would be of fundamental importance to design therapeutic strategy for Parkinson's disease.

3.2 Experimental Methods

Expression and purification of α -synuclein

Recombinant α -synuclein was synthesized by E. Coli and then purified by previously accepted protocols.²¹⁸

Amyloid fibrils preparation

A 45 μ M monomeric (>95%) α -synuclein filtrated solution in a 50 mM TRIS-buffer, NaCl 150 mM, and pH 5.5 was incubated at 37 °C, in an sealed Eppendorf tube to avoid contamination and evaporation, for 180 days.

Atomic Force Microscopy Imaging

The protein solution was diluted to a concentration of 0.25 μ M by means of TRIS-buffer at pH 5.5. AFM sample preparation was realized at room temperature on a positively functionalized mica surface. In order to functionalize the mica, after the cleavage, it was incubated with a 10- μ l drop of 0.05%(v/v) APTES ((3-Aminopropyl)triethoxysilane, Fluka) in Milli-Q water for 1 minute at ambient temperature, rinsed with Milli-Q water and dried by a gentle flow of gaseous nitrogen. Then, a droplet of 10 μ l of our sample was deposited on the APTES-mica surface for

one minute, it was rinsed with Milli-Q water and dried by a flow of gaseous nitrogen. AFM images were realized in ambient condition using a Nanoscope IIIa (Bruker Corp.) operating in tapping mode, the microscope was equipped with an Antimony n-doped Si tip (Bruker, MPP-12120-10, 5 Nm^{-1}) with a nominal radius of 8 nm.

Atomic force spectroscopy

The imaged dried samples were rehydrated with the same Tris-buffer at pH 5.5 for the force spectroscopy measurements. Force-extension curves of pulled and stretched amyloids fibrils were obtained by means of a Picoforce AFM Nanoscope IIIa, equipped with a Mikromash CSC38 n-type silicon tip with a nominal radius of 8 nm and elastic constant k determined by thermal fluctuation method and with value equal to 0.103 Nm^{-1} (nominal 0.09 Nm^{-1}).

Force curves analysis

We analyzed force curves by means of the built in Nanoscope (Bruker) program and by means of OriginPRO. In the case of non-linear mechanical response, we fitted the curves by the worm-like chain equation, see **eq. (2)** below. The average plateau forces were measured by means of HOOKE software²²⁶, as the difference between the average force of the step and the average force of the retracting baseline.

3.3 Results

3.3.1 AFM morphology studies of amyloid aggregates as a function of the incubation time

In this work, we considered the slow aggregation of α -synuclein (i.e. without shaking during the aggregation). Aggregates of α -synuclein showed different morphologies as a function of their incubation time. Immediately after the dissolution of the amyloidogenic proteins in buffer at 0 days, only monomers and oligomers were present on the surface and no fibrillar species were visible in our AFM scans (**Fig. 3.1 A**). After 180 days of incubation at 37 C° , we observed many flexible prefibrillar aggregates (**Fig. 3.1 B**). As shown in detail in the high-resolution AFM image in **Fig. 3.1 C**, they can be separated in two families accordingly to their height (Z direction in the AFM map). A statistical analysis of these prefibrillar species, **Fig. 3.1 D**,

showed that the type I had an average height of 0.3-0.4 nm, and type II had average height of 0.7-0.8 nm. Moreover, the type II family was much less frequent. We could observe that the type II species is formed by entangling of two Type I structures, as can be seen in **Fig. 3.1 C**. Finally, this was the first observation of such small intermediate prefibrillar aggregates of α -synuclein. These aggregates did not have the typical dimensions of mature amyloid fibrils (i.e. measured height by AFM of 6-9 nm), since their heights were lower than 1 nm and smaller than the typical dimensions of protofibrillar species (i.e. measured height by AFM of about 3-4 nm). For this reasons, as extensively illustrated in the previous chapter, we termed them *Protofilaments*.³³

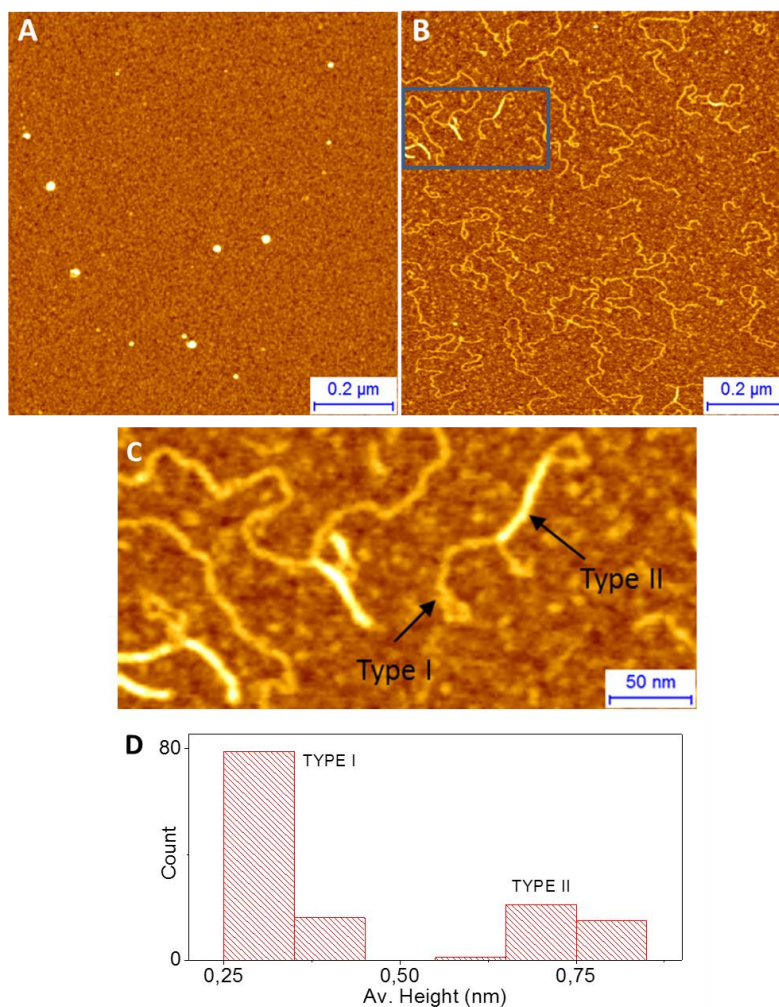


Figure 3.1 Morphology of oligomeric and prefibrillar α -synuclein species.

(A) AFM image of monomers and oligomers covering the surface at time 0 h. (B) AFM image of protofilaments after several days of incubation. (C) High resolution detail of entangling protofilaments. (D) Distribution of heights of Type I and II protofilaments.

A deeper analysis permitted to investigate the nature of these new intermediate amyloidogenic structures. The monomeric α -synuclein protein is naturally unfolded (14 kDa, 140 aa), it has a radius of gyration of about 3 nm and it could be represented at the scale of the AFM tip as a long flexible rod having the diameter of the carbon-nitrogen backbone.²²³ The average apparent height of type I protofilaments at AFM images was of 0.3 ± 0.1 nm, and we were able to measure a corresponding height of about 0.4 ± 0.1 nm for monomers.¹¹¹ Therefore, the height of protofilaments corresponded to that of monomers suggesting that the protofilaments are made from the assembly of a single layer of monomeric α -synuclein. Consistently with this model, previous STM studies of a slightly smaller protein (Cytochrome C, 12 kDa, 104 aa), showed a measured height of a protein on a surface ranging from 0.25 nm for the case of a totally unfolded structure to about 1 nm in the case of a partially folded state.²²⁷ The same conclusion was supported by the use of *ds* DNA as an internal standard (ruler) for AFM measurements (**Fig. 2.12**). The actual diameter of *ds* DNA molecule is 2 nm. It is well established that its apparent height in air, as measured by AFM, is always smaller.^{228,229} We measured, in the same scanning conditions as those characteristic for the experiments with protofilaments, an apparent height of *ds* DNA molecule of 0.8 ± 0.2 nm (**Fig. 2.12**). These results suggested that the apparent height of our protofilaments is nearly one-half of that measured for the *ds* DNA molecule. Thus, protofilaments real diameter is of the order of 1 nm. As already discussed, this value is even smaller than the radius of gyration of single monomer, thus excluding the possibility that more than one protein is present in the cross sectional dimension of the protofilament. Consequently, we could affirm that our type I protofilaments were chain of monomers without any other internal structure. We termed them *single-strand* protofilaments. We also showed, **Fig. 3.2 C**, that the type II protofilaments were formed by the intertwining of two monomeric chains. For this reason, we termed them *double strand* protofilaments.

3.3.2 Force response as a function of the amyloidogenic species

The tip of our AFM cantilever was approached against the functionalized mica substrate, where our aggregates and fibrils were deposited. Then, it was retracted and force extension curves were recorded. The investigation of the spectroscopic force response for oligomeric and prefibrillar species showed a remarkable difference. Before of incubation at 0 days, in the force spectra there was no presence of any complex or repeatable force response, except for few unfolding peaks due to the monomers and oligomers. Some capture events were occasionally

present, but they did not show any characteristic pattern, and the lengths of the corresponding force curves were never longer than approximately 50 nm (**Fig. 3.2 A**). This behavior could be associated with the capture and pulling of oligomers of α -synuclein. Diversely, after 181 days of incubation, multiple force plateaus (**Fig. 3.2 B**) forming a staircase-like picture were present in the corresponding force-distance curves.

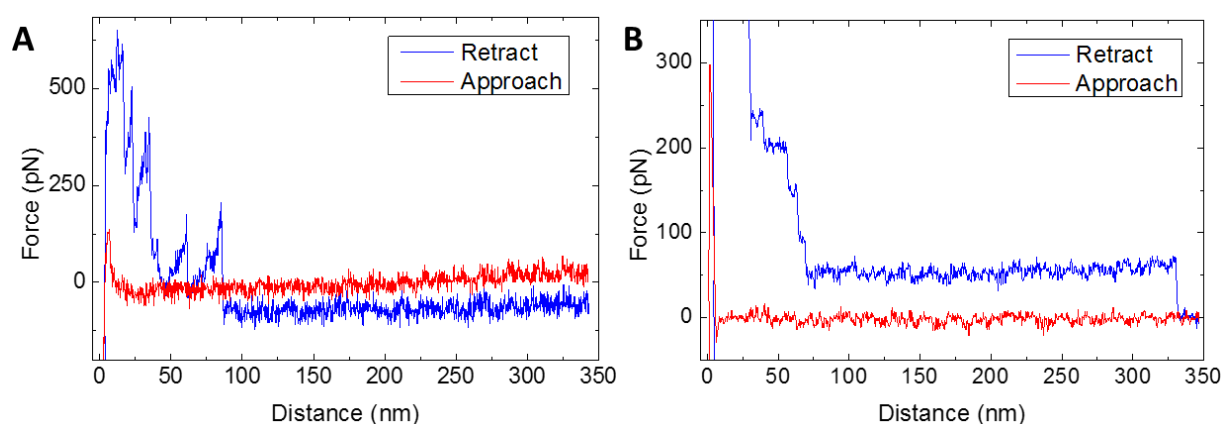


Figure 3.2 Mechanical response as a function of oligomeric or prefibrillar species.

(A) An example of an event of unfolding of oligomers at time 0 h. (B) Plateau event associated with the pulling of several protofilaments, present after prolonged incubation of the proteins.

Based on these considerations, we affirmed that force plateaus are due to the presence of the two families of protofilaments on our mica-APTES surface. Similarly to the previous mentioned works of Kellermayer *et al.*^{204,205}, we associated these constant force pulling events to an unzipping process and in particular to the unzipping of *single* and *double-strand* protofilaments from the surface. We could exclude any internal unzipping from the structure of protofibrillar or mature amyloid structures because *single-strand* protofilaments had cross-sectional dimensions just of the order of the carbon-nitrogen backbone of a single α -synuclein monomer. However, it was still possible the observation of some events corresponding to the unzipping of a *double-strand* protofilaments into the two intertwining *single-strand* protofilaments. However, the much lower abundance of these species and their much shorter length (**Fig. 3.1 B,C**) made such events rare. Thus, they could bring only rather insufficient broadening of the experimentally observed statistical distributions in this work. This evidences demonstrated that our force plateaus were mainly due to the pulling and detaching of the *single-strand* protofilaments from the substrate.

3.3.3 Nanomechanical Manipulation of α -synuclein protofilaments

In order to investigate the properties of the amyloidogenic protofilaments of α -synuclein, we analyzed the acquired force-distance curves in detail. Several kinds of mechanical responses were observed (**Fig. 3.3**).

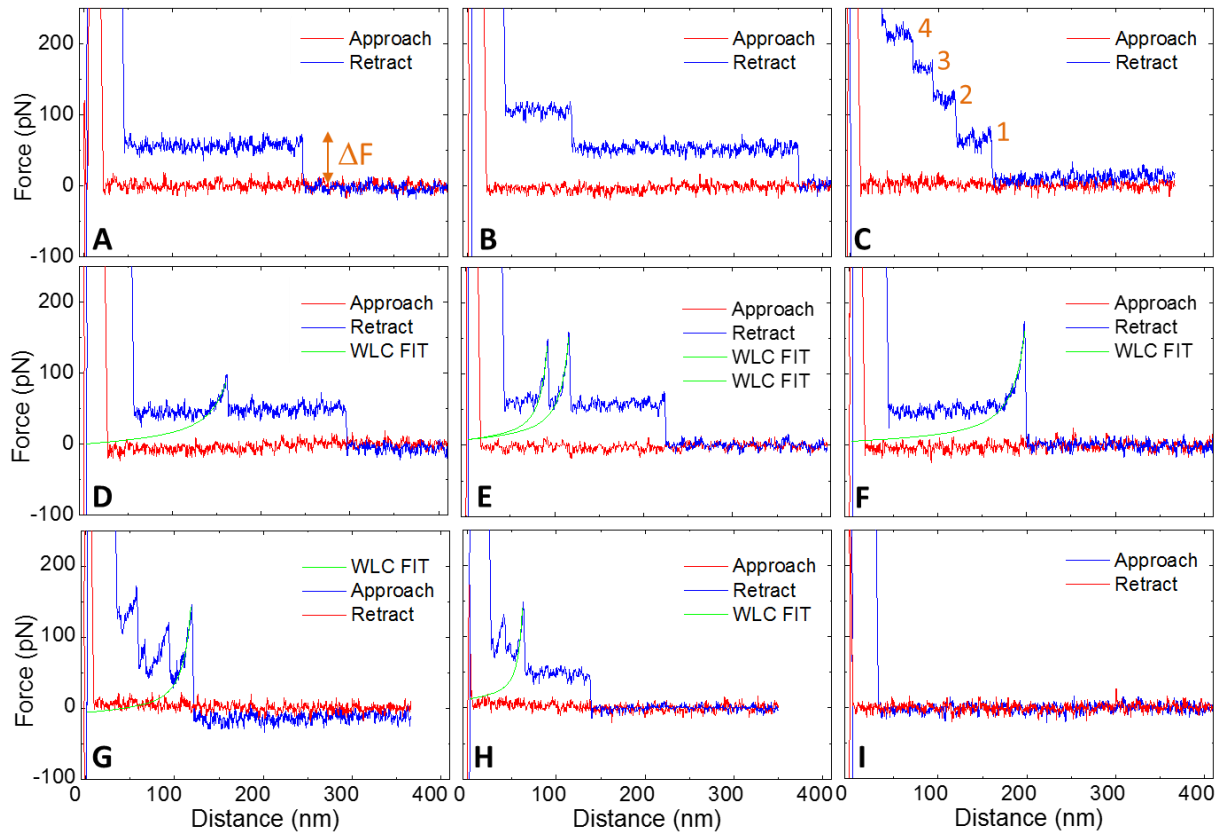


Figure 3.3 Force response of manipulated α -synuclein protofilaments.

(A) Single force plateau at 60 pN due to the pulling of one protofilament (B) Double plateau due to the pulling of 2 protofilaments with a force of 112 pN and 1 protofilament with a force of 57 pN. (C) Pulling of 4,3,2,1 protofilaments with force plateaus at 207, 160, 115, 56 pN. (D) Constant force plateau with a stretching event inside. Fitting by Worm Like Chain model (WLC, see below for details) gives a persistence length of 0.32 ± 0.05 nm. (E) Constant force plateau with two stretching events inside. Fitting by WLC gives a persistence length of 0.42 ± 0.06 nm and 0.44 ± 0.07 nm. (F) Force plateau preceded by a stretching event with a persistence length of 0.47 ± 0.04 nm. (G) Non-specific event due to oligomer unfolding, WLC fit gives a persistence length of 0.31 ± 0.03 nm. (H) An oligomeric unfolding, preceded by a constant force plateau, is fitted by WLC with a persistence length of 0.28 ± 0.05 nm. (I) No interaction is observed.

We could group the different force curves accordingly to their behaviour: (A) Single constant force plateau due to pulling and detaching of one protofilament from the surface. (B, C) Multiple constant force plateaus with a staircase shape due to detaching of several protofilaments from the surface. Constant force plateau with “stretching events” inside (D, E) or outside (F) the corresponding plateau regions. (G) Non-specific events linkable to pulling or unfolding of oligomers. (H) Plateaus mixed with non-specific events. (I) Flat curves due to approaching an empty area or picking up nothing. Similar combinations of plateau and stretching events were already observed previously.^{204,205} We collected in total 658 force curves, 64% of which showed pulling/unfolding events and the remaining 36% were just flat curves due to approaching and retracting on the bare surface or events with no interaction. From this 64%, 43% (282) of force curves recorded were plateaus, 8% (53) were plateaus mixed with stretching/defolding events inside or outside the corresponding plateau regions and unspecific behavior, 7.5% (50) were not specific events likely linked to oligomers pulling and unfolding. The remaining 3% (26) were curves with irregular retracting behavior.

A statistical analysis of the plateaus size showed that plateaus possessed average length of ~70 nm (**Fig. 3.4 A**). While, it was possible to observe that the fibrillar structures had a broad distribution of lengths with an average value of ~170 nm (**Fig. 3.5 B**). The statistical analysis confirmed that *single-strand* protofilaments were much longer than *double-strand* ones.

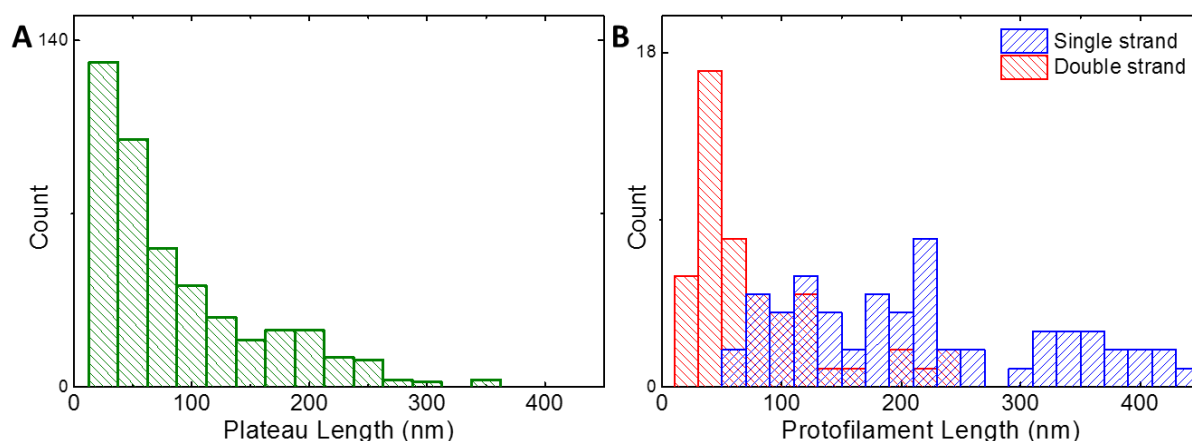


Figure 3.4 Comparison of the lengths of α -synuclein protofilaments and lengths of plateaus events in the corresponding force curves.

(A) Distribution of the lengths of constant force pulling events (plateaus). (B) Distribution of the lengths of Type I protofilaments and Type II protofilaments.

A comparison of the two distributions showed that the average length of protofilaments was double that of the observed plateau in the force-distance curves. This difference was likely due to the loosening of the tip-aggregate contact during the pulling of the protofilaments. A further statistical analysis showed that the length of the force plateau decreased exponentially as a function of the position of the plateau in the staircase (**Fig. 3.5 A**), and similarly it decreased as a function of the force of pulling (**Fig. 3.5 C**). This suggested that the probability to detach a high number of protofilaments, without any tip-protofilament contact break event, was smaller than the probability of pulling continuously just one of them.

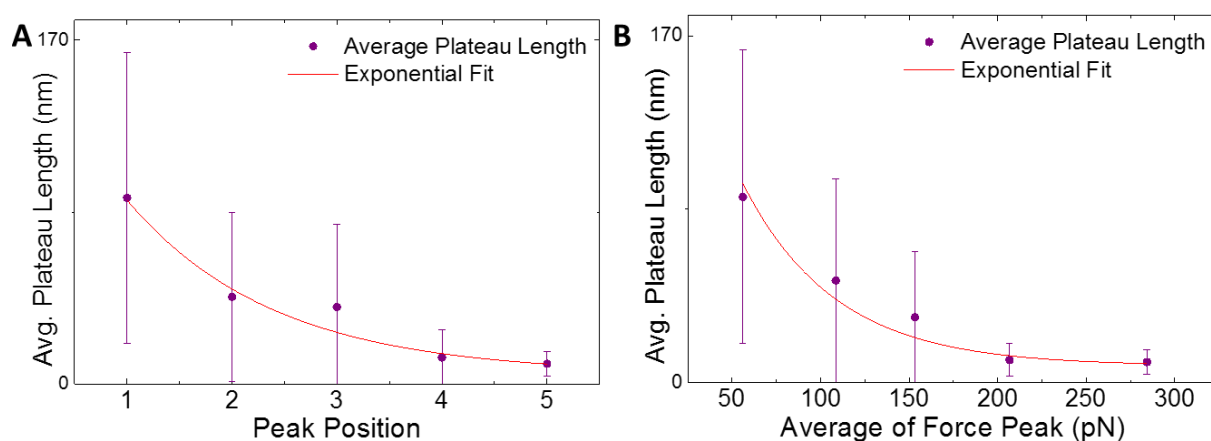


Figure 3.5 Comparison of the lengths of plateaus events in the force curves.

(A) Distribution of the lengths of plateaus according to their position in the force curve. (B) Distribution of the lengths of plateaus belonging to different families of force peaks.

Successively, we measured the force difference ΔF (**Fig.3.3 A**) between the average height of a plateau and the baseline in the force curve. The histogram of the force distribution is presented in **Fig. 3.6 A**. We observed a clear multimodal distribution with four peaks and some more rare higher force events, which we considered generically as the fifth peak. From the histogram, it was evident that the force peaks appeared at integer multiples of the “single detachment event” value of approximately 50 pN. This was in full agreement with the idea that our tip could pick up a different number of similar protofilaments. In order to justify the relative occurrence of the different force-peaks, it is worth to note that the size of our tip was of the order of 10-20 nm and thus comparable with the lateral cross-section of a single protofilament. Hence, the most probable case is the one in which the tip is able to catch just one protofilament. Then, it would be able to detach the protofilament from the surface with a characteristic force, which we measured to be about 50 pN. Furthermore, it could be also possible (but much less

probable) that the tip could land exactly on a crossing of two protofilaments, so that the first force plateau would be observed at 110 pN. Finally, it is quite probable, as it is possible to observe from the morphology of the sample in **Fig. 3.2B-C**, that certain single protofilament, which has been catch, actually crosses with another protofilament(s). Hence, it should be quite common to detach an increasing number of protofilaments one after another.

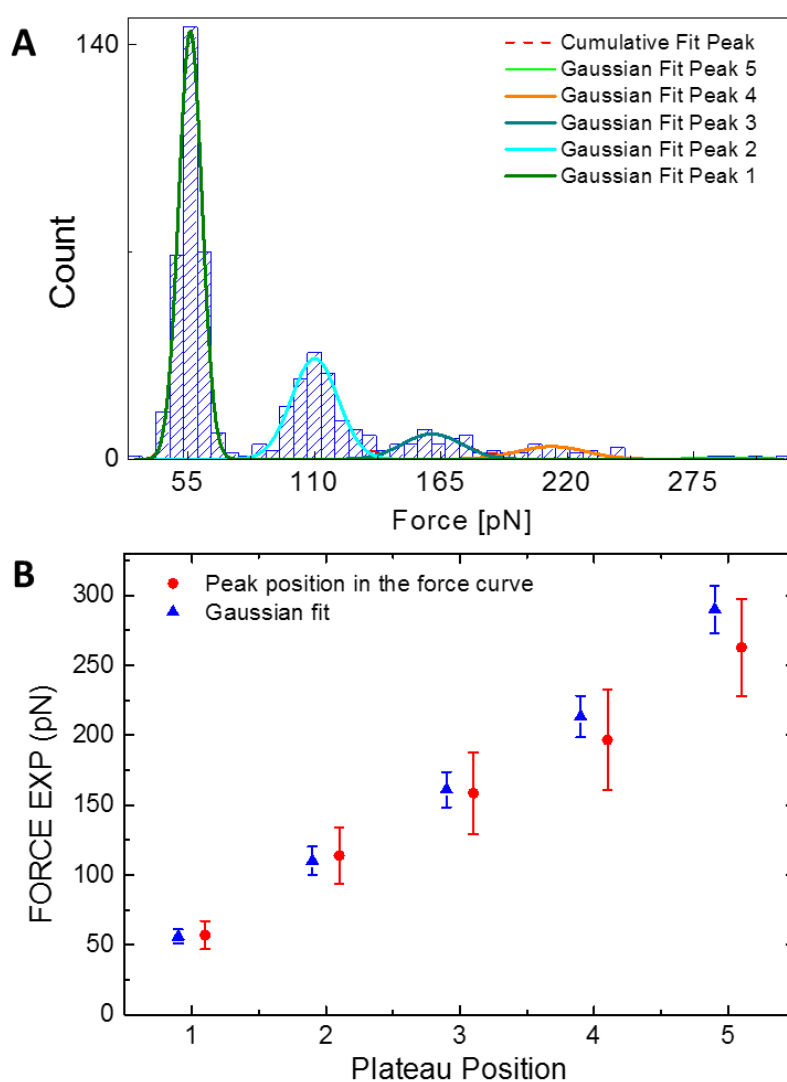


Figure 3.6 Analysis of the constant force plateaus.

(A) Histogram of the distribution of the average detachment forces. (B) Average force as a function of its position in the force curve (red), average value of the histogram maxima as a function of its position in the histogram by Gaussian fit (blue).

In order to quantify the process and obtain an experimental estimation of the detachment forces, we performed two types of analysis of our data: 1) we first numbered the force plateaus according to their position in the force curve, see the curve in **Fig. 3.3 C** as an example, and

then we averaged the values of the detachment force disregarding its number. 2) we fitted the peaks of the histogram of the distribution of the average detachment forces by a Gaussian curve, **Fig. 3.6A**. First method averaged all the values appearing as the first plateau in the force curve, independently of the fact that sometime the first force plateau could be a double force plateau because of the contemporary pulling of two protofilaments. This model gave back a good estimation of our “quantized” detachment forces, but it returned only a rough estimation of the statistical error. Instead, the second method, excluded the double pulling events and it gave back a better estimation of the experimental value of the interaction force of amyloid protofilaments with the surface as well as its error. However, it was not able to evaluate properly the last peak. As expected, both methods of analysis gave similar results and they allowed extracting a fundamental value of detachment force of 57 ± 10 pN and of 56 ± 5 pN, respectively. The results from these two methods of analysis are shown in **Fig. 4 B**, where the average force of the plateau is represented as a function of its position in the force curve. The force of pulling increases linearly with the position of the plateau in the force curve. This demonstrates that the force of pulling is proportional to the number of protofilaments that are detached from the surface.

3.3.4 Elastic properties of α -synuclein prefibrillar species

The stretching events present inside or at the border of a plateau were linked to the stretching and unfolding of the carbon-nitrogen backbone of the protofilaments. For this reason, the study of these events by means of the statistical theory of biopolymers allowed to investigate the internal mechanical properties of these prefibrillar structures. In particular, by means of fitting the stretching event with a worm-like chain model (WLC, see eq. 2), it was possible to determine the persistence length of the structures. We were able to extrapolate an average persistence length of 0.29 ± 0.16 nm (calculated from totally 33 events). This value was fully consistent with the persistence length of an unfolded protein.²³⁰ Indeed demonstrating that our protofilaments were early species of amyloids aggregation composed by unfolded monomers and with a much less complex and stiff structure than a mature amyloid fibril.

3.3.5 Monte Carlo modeling of the process of protofilaments of α -synuclein unzipping from the surface

The aforementioned characteristic features of our experiments were modeled through a Monte Carlo method. The observed cases of double-, triple- and even larger detachment events, were modeled to reveal a connection between the different values of detachment forces (“plateau levels”), which were characteristic for events with different numbers of protofilaments interacting with the support surface. In doing so, we were inspired by our recent work²³¹ where a connection between characteristic defolding forces observed for subsequent defolding events of individual modules constituting a (GB1)₈ homopolymer molecules (multimodular protein constructs) with 8 modules, has been established. Certainly, in this work we had the case where a number of similar α -synuclein protofilaments were connected *in parallel* rather than the case of a number of identical modules connected in series. Therefore, the previous approach²³¹ was properly modified.

We first considered only one protofilament of α -synuclein detaching from the surface. We considered this event as a single receptor–ligand bond breaking event occurring at the force loading rate of $\dot{f} = 53.3 \text{ nN/s}$. Successively, we used the standard formula to describe the dependence of the probability of the bond rupture on the force f : (see e.g.²³²)

$$p(f) = k_{off} \exp\left(\frac{f\Delta x}{k_B T}\right) \exp\left(\frac{k_B T k_{off}}{\dot{f}\Delta x} \left(1 - \exp\left(\frac{f\Delta x}{k_B T}\right)\right)\right) \quad (1)$$

By applying a bootstrap statistical modeling approach, we searched for such values of k_{off} (so called bond break rate at no force conditions) and barrier thickness Δx which approximated more accurately possible the experimentally observed distribution of the detachment forces. This enable to extrapolate the following values: $k_{off} = 0.048 \pm 0.030 \text{ s}^{-1}$ and $\Delta x = 0.91 \pm 0.05 \text{ nm}$.

The next step of our modeling was the Monte Carlo simulation of the breaking of n equivalent parallel “molecules” stretched between an AFM cantilever and support surfaces. Each of these molecules possessed exactly the aforementioned interaction kinetic parameters, describing the breaking probability, and the following elastic parameters: contour length $L=1 \text{ nm}$ and persistence length $A=0.3 \text{ nm}$. These molecules were thought to behave as worm-like

chain (WLC)²³⁰ polymers upon stretching in the experimental conditions characterized by the pulling speed equal to 969 nm/s, temperature T=300 K and cantilever spring constant of 0.11 N/m:

$$f(z) = \frac{k_B T}{A} \left(\frac{z}{L} + \frac{1}{4(1-z/L)^2} - \frac{1}{4} \right) \quad (2)$$

Where z is end-to-end distance of the stretched polymer molecule.²³³ The procedure exploited for Monte Carlo simulation of the dynamic force spectroscopy experiment using above parameters was similar to the protocol reported in literature²³⁴ and used earlier in the work of Rief *et al.*²³¹. The time-step of the simulation procedure was set in such a way that for each increase of the complex end-to-end distance equal to 5 pm (at any loading rate) we controlled the probability to dissociate (to be detached) the protofilament from the surface.

The results of the Monte Carlo simulation are presented in **Fig. 3.7**. The above proposed approach captured and it explained the small but observable and statistically significant differences between the plateau heights characteristic for n protofilaments of α -synuclein detached from the surface (n “parallel bonds” in above terminology) and the values of “ n times the plateau height characteristic for single protofilament of α -synuclein detached” (**Fig. 3.7A**).²³¹ The difference between experimental and modeled results for the fifth peak was simply due to the extremely poor statistics for this peak. Moreover, the values of standard deviations for each force plateau were also quite reliably predicted, **Fig. 3.7B**.

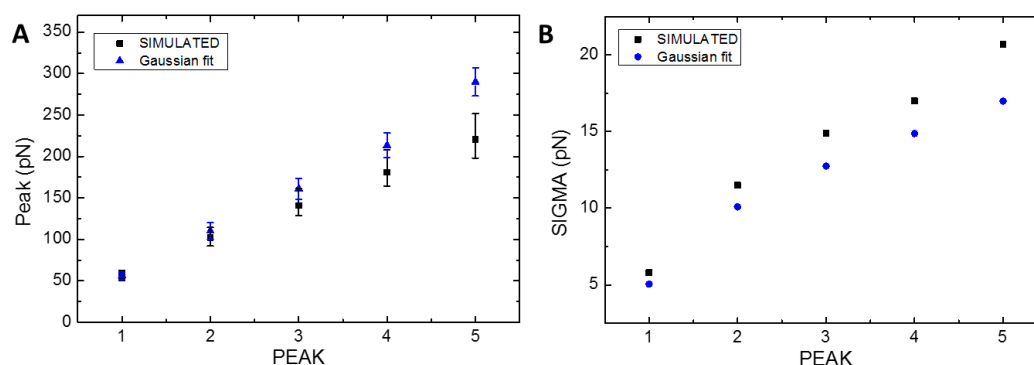


Figure 3.7 Comparison between the experimental data and the Monte Carlo simulations.

(A) Comparison of maxima of the peaks. (B) Comparison of standard deviations of the peaks. The simulated error bar is calculated using as maximum values of the kinetic parameters $\Delta x = 0.96$ nm and $k_{off} = 0.078$ s⁻¹; and as minimum values of the kinetic parameters $\Delta x = 0.86$ nm and $k_{off} = 0.018$ s⁻¹.

3.4 Discussion

In summary, the presented work illustrated the manipulation at nanometric scale of prefibrillar amyloid precursors of α -synuclein. We could quantify their mechanical properties, as persistence length, when subjected to stretching and their force of interaction with a silyanized substrate. We modeled one of the possible unzipping events of a protofilament from the surface (**Fig. 3.8**): 1) AFM tip approaches towards a protofilament and it is brought in contact with it. 2) The strong contact force (nN) breaks the polymer and it creates a tip-protein contact. As already measured in the case of mature amyloid structures, ~ 500 pN are sufficient to break by indentation an amyloid fibrils.¹⁰ Then, the retracting of the tip detaches the protofilament from the substrate and allows measuring the related “quantized” unzipping force. 3) Tip-protofilament contact is lost. 4) Tip returns to the initial position before approaching.

The measured quantum of interaction force within a single prefibrillar amyloid protofilament and the surface was 56 ± 5 pN. The quantized values of unzipping force obeyed to a linear law, implying that multiple plateaus were linked to the multiple unzipping of protofilaments from the surface. Monte Carlo simulation of the process, performed using rather simple model of breaking of n parallel bonds from the surface, quite well explained the nuances of this quantization. Moreover, the fundamental value of interaction force measured was substantially larger than the values of forces needed to unzip an individual A β subunit sheet from a mature fibril in a previous experiment (about 33 pN for A β 1–40 fibrils and about 23 pN for A β 1–42 ones²⁰⁴); though, the force curves recorded in the present work and those presented in the previous studies^{204,205} are rather similar in appearance. Does this similarity suggest that the interpretation of results of the force spectroscopy experiments with mature amyloid fibrils given in the aforementioned studies^{204,205}, explained as an observation of unzip of some subunit sheets from the fibrils, albeit plausible, is insufficient? In our opinion, also the possibility of an observation of detachment of mature fibrils from the *support surface* cannot be completely excluded. In fact, the authors based their previous works on the hypothesis of the impossibility to unzip fibrils from a silane-functionalized surface.^{204,205} In our work, we shed new light to these questions and we demonstrated clearly that this is possible to detach amyloid fibrillar structure from a surface with a similar chemistry of functionalization. We believe that a reversible observation of plateau events, as that presented in Fig. 3f of Ref. 205, where exactly the same force curve is reproduced when AFM tip moves forward/backward, cannot always be explained as the re-assembling of an earlier unzipped β -sheet to its maternal fibril. The latter

process would require a very precise reproducibility of all relevant positions during AFM tip movement. Instead, re-attachment/attachment of the earlier detached fibril (resting onto the tip surface after its detachment) onto the support surface (may be at some new position there), seems also quite probable and it would well explain the aforementioned experimental observations.

Furthermore, when subject to an elastic stretching, protofilaments showed an average persistence length of 0.29 ± 0.16 nm, which was in full agreement with the elastic properties of a polymer chain composed of unstructured monomers of α -synuclein, as supposed by their cross sectional dimensions. Indeed, it was already measured by force spectroscopy that mature amyloid fibrils formed by the glucagon peptide have an average persistence length of 0.70 ± 0.15 nm. This value is twice bigger than our protofilaments, suggesting that they possess prefibrillar structural nature. This was the first observation for α -synuclein of direct assembling from monomers into simple prefibrillar structures. Even if it was already supposed that protofilaments structures form the mature amyloid fibrils, their mechanical properties were never singularly studied.^{33,220}

Recent evidence has increasingly suggested that prefibrillar intermediates might be the toxic component causing the onset of misfolding diseases, rather than the fully fibrillar end-products.¹²⁴ This study poses the basis for new fundamental experiments to investigate and compare the interaction forces of different amyloid structure on different surfaces, such as hydrophobic ones. Unraveling these forces is central for the comprehension of the fibrillation process and its link to the disease onset. In fact, the obtained values of interaction force could be linked to the driving force within interacting protofilaments during the early hierarchical amyloid assembling process and could be central to unravel fibrillation process at surfaces, such as cell membranes. Moreover, the investigation of formation and of the mechanical properties of new prefibrillar species *in-pathway* of fibrillization in *physiological-like* conditions could be central to study their eventual toxicity, clearance mechanism in the body and to develop new therapeutic approaches to contrast amyloid diseases.

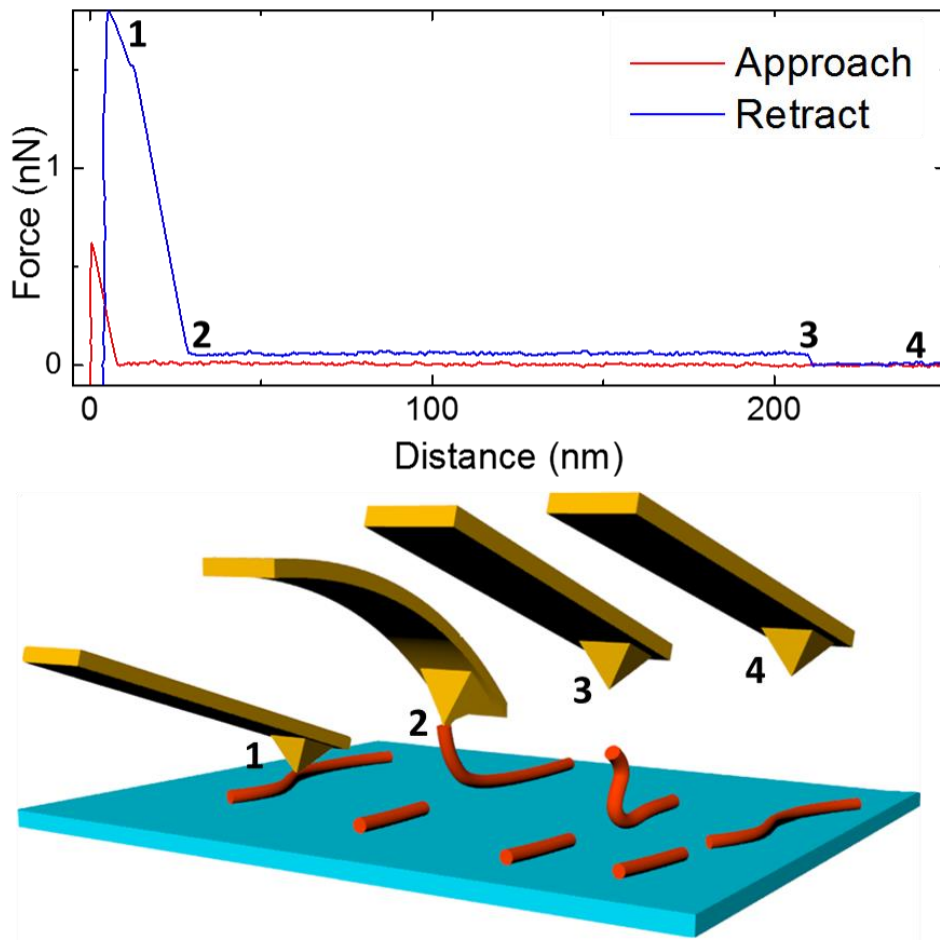


Figure 3.8 Model of single protofilaments pulling.

1) After approaching, AFM tip is strongly pressed against a protofilament (force of about 2 nN). 2) The strong pressure by the tip causes polymer breaking and a constant force plateau due its unzipping from the surface. 3) Tip-filament contact is lost during the pulling. 4) Tip returns to the initial position preceding the approaching to the polymer.

Chapter 4. Content of β -sheet Controls Mechanical Properties of Aggregates during Amyloid Fibrillization

This chapter is based on a paper published in Angewandte Chemie with the following authors:

+Francesco Simone Ruggeri¹, +Jozef Adamcik², Jae Sun Jeong¹, Hilal A. Lashuel³, Raffaele Mezzenga², Giovanni Dietler

+ The authors equally contributed to the work.

Affiliations:

¹ Laboratory of Physics of Living Matter, EPFL, 1015 Lausanne, Switzerland.

² Department of Health Sciences & Technology, ETH Zürich.

³ Brain Mind Institute, EPFL, 1015 Lausanne, Switzerland.

Abstract

Amyloid fibrils associated with neurodegenerative diseases such as Parkinson's and Alzheimer's consist of insoluble aggregates of α -synuclein and A β -42 proteins with high β -sheet content. The aggregation of both proteins proceeds from monomers misfolding, through formation of oligomeric and protofibrillar species, to the final fibrillar cross β -sheet structure. The morphological and mechanical properties of oligomers, protofibrils and fibrils formed during fibrillization process, investigated by Thioflavin T Fluorescence and Circular Dichroism techniques and combined with AFM peak force quantitative nanomechanical technique, reveal an increase of the Young's moduli from oligomers to mature fibrils inferring that the difference in their mechanical properties is due to an internal structural change from random coil to an increase of β -sheet content.

4.1 Introduction

Amyloid fibrils as highly ordered insoluble protein aggregates are most often related to human diseases, including numerous neurodegenerative disorders such as Parkinson's, Alzheimer's Creutzfeldt-Jakob disease, type II diabetes and bovine spongiform encephalopathy.^{4,42,235} However, amyloid fibrils are not only associated with diseases since they were also discovered in many physiologically beneficial roles including bacterial coatings, catalytic scaffolds, adhesives and structures for the storage of peptide hormones,⁵⁻⁷ from which the term of functional amyloids has been cast. A characteristic fingerprint of amyloid fibrils is the core cross- β -sheet structure in which β -strands contained within the β -sheets are oriented perpendicular to the fibril axis. From the morphological point of view, amyloid fibrils are unbranched, several micrometer long fibrils, consisting of 2-6 protofilaments associated laterally or twisted together.^{8,9,236,237} Moreover, amyloid fibrils exhibit remarkable mechanical properties with Young's moduli in the range of several GPa.¹⁰⁻¹² Taking inspiration from functional amyloid and the self-assembly of non-toxic proteins and peptides *in vitro* into highly ordered structures with unique mechanical properties, has allowed the development of biomaterials for a broad spectrum of applications in medicine, food and nanotechnology.^{164,197}

Experimental techniques such as Atomic Force Microscopy (AFM) and computational simulations have been widely utilized in order to quantify the mechanical properties of amyloid fibrils. AFM represents one of the most suitable method for quantitative measurements of local elasticity of amyloid fibrils. AFM single molecule imaging features combined to a statistical analysis of AFM images,^{11,36} together with the possibility to impose and measure forces,^{10,197} ideally makes AFM as an important research tool to deliver important information about the mechanical and related structural properties of amyloid fibrils at the single molecule scale. Atomistic simulations performed by Buehler and his co-workers have provided theoretical values of the Young's moduli of amyloid fibrils in the order of several GPa.²³⁸⁻²⁴¹ Moreover, the results obtained by both AFM and simulations, suggest that the intermolecular interactions (e.g. hydrogen bonds) between β -sheet layers are responsible for the remarkable mechanical properties of amyloid fibrils. Recently, a relatively new AFM technique, called peak force quantitative nanomechanical (PF-QNM), has been used to estimate the values of the Young's moduli of different classes of mature amyloid fibrils including β -lactoglobulin, α -synuclein, A β (1-42), bovine serum albumin, insulin, lysozyme, ovalbumin, and Tau protein in GPa

range,^{163,202,208,237} which are consistent with the values of the Young's moduli obtained by statistical analysis of AFM images.¹¹

In order to appreciate the full potential of amyloid fibrils as biomaterials, it is important to understand the mechanism of fibrillization process and to measure and quantify the mechanical properties of amyloid fibrils. Moreover, the understanding of the mechanical properties and of the intermediate structures during the fibrillization process is of fundamental importance to unravel their stability, toxicity and mechanism of clearance in order to design new therapeutic strategies to the onset of neurodegenerative disorders. For this reason, in this work, we set out to study the evolution of both the mechanical and structural properties of the amyloidogenic structures all over the fibrillization process of α -synuclein and A β (1–42) (A β –42).

4.2 Experimental Methods

Fibrillization assay

WT α -synuclein was incubated in an Eppendorf tube at concentration of 45 μ M in an initial volume of 800 μ L, under constant agitation at 400 rpm for 21 days at 37 °C. WT A β -42 was incubated in an Eppendorf tube at concentration of 20 μ M, without agitation for one week at 37 °C.

Thioflavin T

ThT fluorescence reading was measured for α -synuclein at 45 μ M, diluted at 1.5 μ M with a ThT concentration of 10 μ M, in a 70 μ L solution with pH 8.5 buffer containing 50 mM glycine (Sigma-Aldrich). ThT fluorescence reading was measured for a 70- μ L aliquot of A β -42 sample at 20 μ M with 20 μ L of 100 μ M ThT and 10 μ L of 500 mM glycine (pH 8.5) (Sigma-Aldrich). A Bucher Analyst AD plate reader was used to measure ThT fluorescence at an excitation wavelength of 450 nm and an emission wavelength of 485 nm. Aliquots taken at different time points were measured in triplicate.

Circular Dichroism

Samples were analyzed at room temperature (RT) using a Jasco J-815 CD spectrometer. An average of 10 spectra was collected in the range of 190–250 nm using a 1.0-mm-optical-pathlength quartz cuvette. Data points were acquired every 0.2 nm in the continuous scanning mode at a speed of 50 nm/min with a digital integration time of 2 s and a bandwidth of 1 nm. Processed spectra were obtained by subtracting the baseline signal due to the water and cell contribution from the protein spectra.

Atomic force microscopy samples preparation

Analysis by AFM was performed on three differently charged substrates: hydrophobic HOPG, negatively charged mica and positively functionalized mica. In the last case after the cleaving, the mica substrate, was incubated with a 10- μ l drop of 0.05%(v/v) APTES ((3-Aminopropyl)triethoxysilane, Fluka) in Milli-Q water for 1 minute at ambient temperature, rinsed with Milli-Q water and then dried by the passage of a gentle flow of gaseous nitrogen. AFM samples preparation was realized at room temperature by deposition of a 10 μ l aliquot of full concentrated 45 μ M solution for 10 minutes in the case of mica and 100 times diluted solution for 1 minute in the case of HOPG.

Atomic force microscopy Imaging and PF-QNM measurements

AFM images were realized by means of a Park NX10 operating in true non-contact mode and equipped with a silicon tip (Nanosensor, PPP-NCHR, 40 Nm^{-1}) with a nominal radius of 7 nm. Images flattening and analysis was performed by SPIP (Image metrology) software. PF-QNM measurements were performed by using a MultiMode VIII Scanning Probe Microscope (Bruker, USA) operated in intermittent mode under ambient conditions at a scan rate of 1 Hz. The microscope was covered with an acoustic hood to minimize vibrational noise. The AFM cantilevers (Bruker, USA) were calibrated on the calibration samples (Bruker, USA), -typically low-density polyethylene and polystyrene- covering the following ranges of Young's moduli: from 100 MPa to 2 GPa (for low-density polyethylene) and from 1 to 20 GPa (for polystyrene). The analysis of the Derjaguin–Mueller–Toporov (DMT) modulus was performed by the software Nanoscope Analysis.

4.3 Results

4.3.1 Aggregation process studies by conventional bulk techniques

Two of the most typical methods used to study the kinetics of amyloid fibrillization and to investigate the structural change that the proteins undergo during the fibrillization process are Thioflavin T (ThT) fluorescence¹¹³ and Circular Dichroism (CD),¹⁸⁰ respectively. Figure 1 displays the results of ThT and CD measurements of the fibrillization process of α -synuclein (Figure 4.1A and C) and A β -42 (Figure 4.1B and D).

The amyloid fibril formation monitored by ThT is generally characterized by a sigmoidal curve representing three main steps of the fibrillization process: starting with an initial lag phase, where monomers misfold and oligomeric nuclei form; continuing with a fast exponential growth, due to a fast formation/elongation of protofibrillar and fibrillar structures; and finishing with a plateau indicating a dynamic equilibrium within the final mature amyloid fibrils. The fibrillization processes of both α -synuclein and A β -42 amyloid fibrils followed the usually described sigmoid curve attributed to a nucleation-dependent polymerization process. (Figure 4.1A and B).^{65,242} The fibrillization process of α -synuclein was slower compared to A β -42 because even after 24 days of incubation the ThT signal did not reach the plateau phase and was increasing as a function of time after the exponential phase (Figure 4.1A) suggesting that the fibrils were still forming/elongating. In the case of A β -42 fibrillization process, the ThT signal reached the plateau region already after 30 hours and fibrils formation was in the stationary dynamical equilibrium (Figure 4.1B).

CD spectra of α -synuclein fibrillization displayed in Figure 1c show that at 0 hours the peak minimum was detected at 203 nm corresponding to a random coil structure while after 48 hours of incubation the peak minimum was shifted to 220 nm indicating the formation of β -sheet structure. The intensity of CD signal at 220 nm increased as a function of time and, according to the ThT signal, of fibrils formation. CD spectra of A β -42fibrillization are displayed in Figure 1d showing that the peak minimum at 0 hours was detected at 195 nm indicating a random coil structure while after 24 hours of incubation the peak minimum was shifted to 218 nm indicating the presence of the β -sheet structure. In this case the intensity of CD signal at 218 nm was decreasing as a function of time. Since the kinetic of A β -42 fibrils formation was already in its stationary regime after 30 hours of incubation according to ThT

results (Figure 1b) and amyloid are insoluble aggregates, sedimentation that is occurring during the measurements, can explain the decrease of the intensity of the CD signal as evidenced by the turbidity of the solution. This trend, together with the slow aggregation kinetics leading to coexistence of unfolded oligomers with growing fibrils, complicates the evaluation of the exact composition of β -sheet in the protofibrils during fibrillization, although it is evident from Figure 1 that both systems evolve towards an overall increase of β -sheet during aggregation.

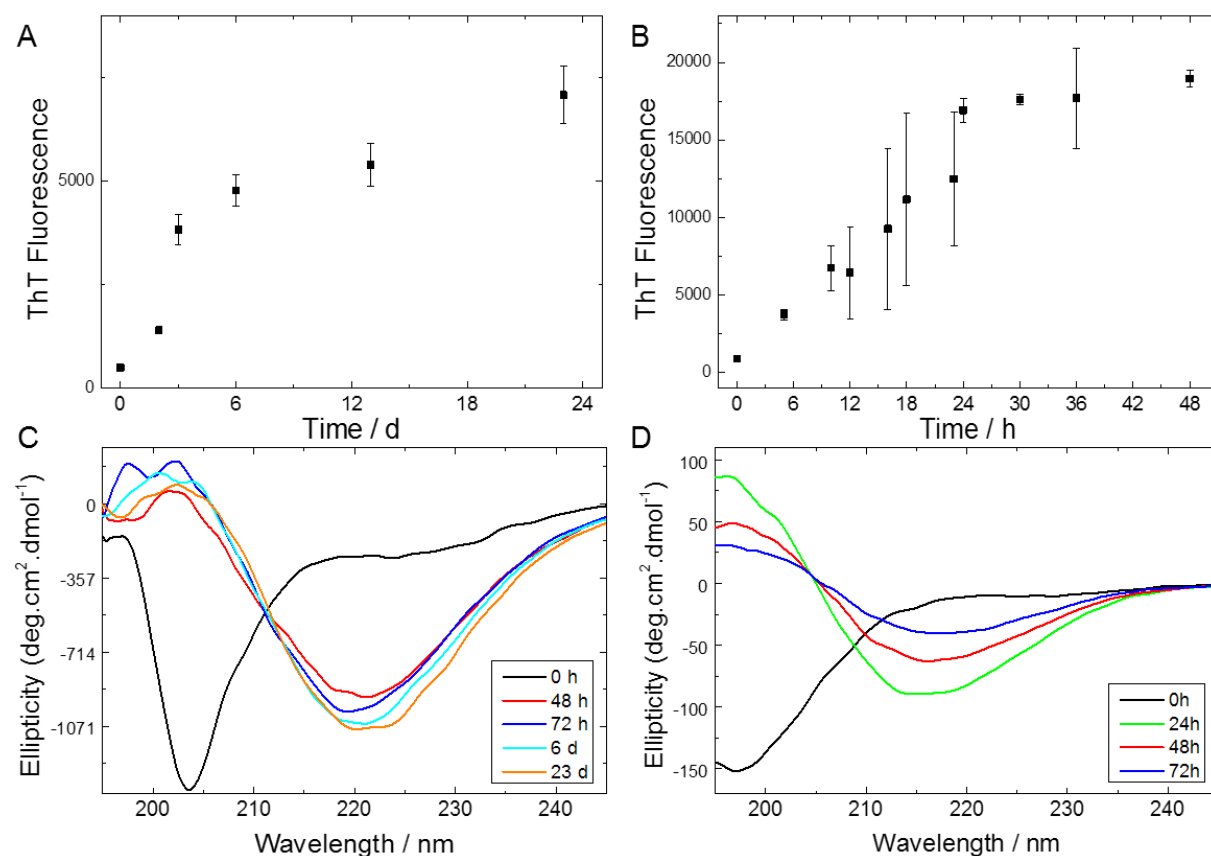


Figure 4.1 Kinetics of amyloid fibrils formation and secondary structure measurements.

Thioflavin T fluorescence of A) α -synuclein and B) $A\beta$ -42. Circular dichroism measurements of C) α -synuclein and D) $A\beta$ -42. Measurements were conducted at 45 μ M for α -synuclein and 20 μ M for $A\beta$ -42. (Please refer to section 4.3.1 for experimental details).

4.3.2 Fibrillization investigation by conventional Atomic Force Microscopy

Amyloid fibrillization is a complex process which proceeds through multiple pathways and several polymorphic amyloid species are contemporarily present in the heterogeneous aggregating solution.⁴⁰ For this reason, bulk techniques such as ThT and CD just give average information of this ensemble. In other words, if for example fibrils and oligomers are

contemporary present in the solution, the β -sheet signal for both bulk techniques is an average measurement of both structures.

A single molecule technique, such as AFM, allows gaining information on the fibrillization process and on individual protein structural transition.^{11,36} **Figure 4.2** displays the fibrillization process of α -synuclein and A β -42 by means of AFM imaging after deposition of the proteins on a positively functionalize APTES-mica substrate.

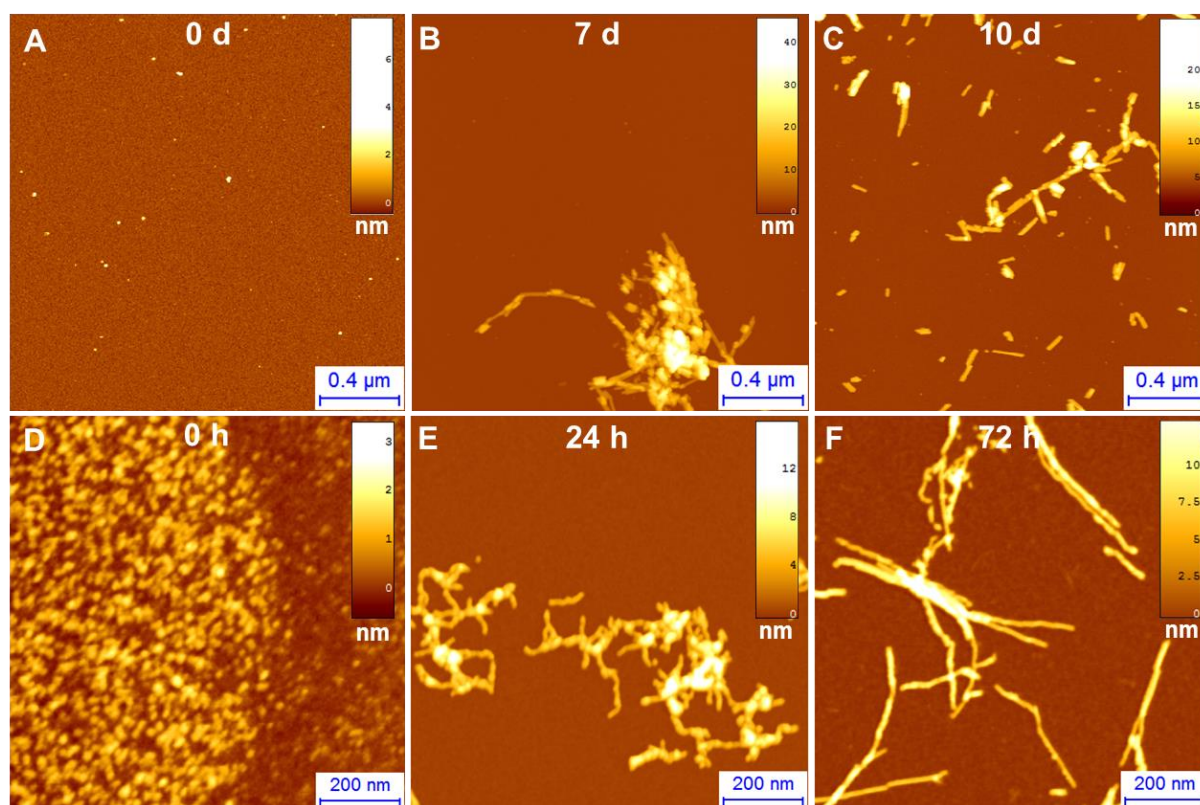


Figure 4.2 AFM imaging of α -synuclein and A β -42 fibrillization process.

Incubation times of: A) 0 days, B) 7 days, C) 10 days for α -synuclein; and D) 0 hours, E) 24 hours, F) 72 hours for A β -42.

At 0 hours, α -synuclein was mainly in the monomeric form, since the CD signal shows the typical random coil signal of intrinsically disordered proteins and just few early oligomers are present in AFM morphology images (**Figure 4.1C**, **4.2A** and **4.3A-C**). Already at 24 hours of incubation, the increase of number of bigger oligomers with height of 2-6 nm (**Figure 4.3D-F**) was detected. After 7 days of incubation the fibrillar structures started to assemble (**Figure 4.2B**) continuing to form mature amyloid fibrils (**Figure 4.2C**) with height of 6-7 nm (**Figure**

4.3G-I at 10 days of incubation. Similarly to the case of α -synuclein, at 0 hours, $A\beta$ -42 was in monomeric and early oligomeric structures (**Figure 4.1D** and **4.2D**) with height of 0.5-3 nm (**Figure 4.4A-C**). After 24 hours of incubation, abundant curly protofibrillar structures (**Figure 4.2E**) with the height of 3-4 nm (**Figure 4.5D-F**) were observed. Finally, at 72 hours of incubation, mature amyloid fibrils (**Figure 4.5F**) with the height of 4-6 nm (**Figure 4.5G-I**) were formed. Thus, in the case of both proteins the classical oligomerization process of aggregation was observed.^{242,243} This means for both proteins that formation of oligomeric nuclei is necessary for the formation of the first protofibrillar structures, ultimately leading to the formation of the mature amyloid fibrils.

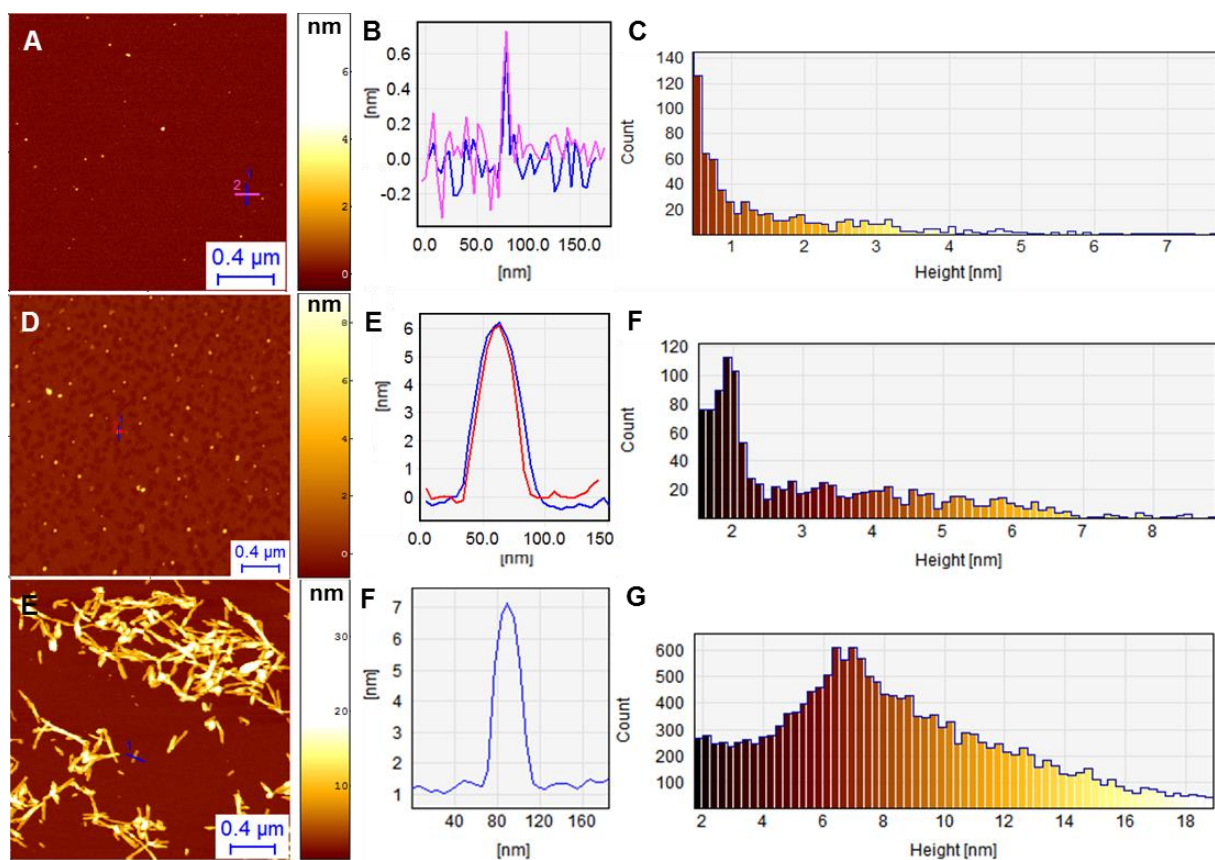


Figure 4.3 Analysis of the morphology of α -synuclein oligomers and fibrils.

Oligomers at 0 days: A) AFM image. B) Cross sectional dimensions of an aggregate. C) Distribution of height. Oligomers at 24 h: D) AFM image. E) Cross sectional dimensions of an aggregate. F) Distribution of height. Fibrils at 72 days: G) AFM image detail of fibrils. H) Cross sectional dimension of a fibril. I) Distribution of height.

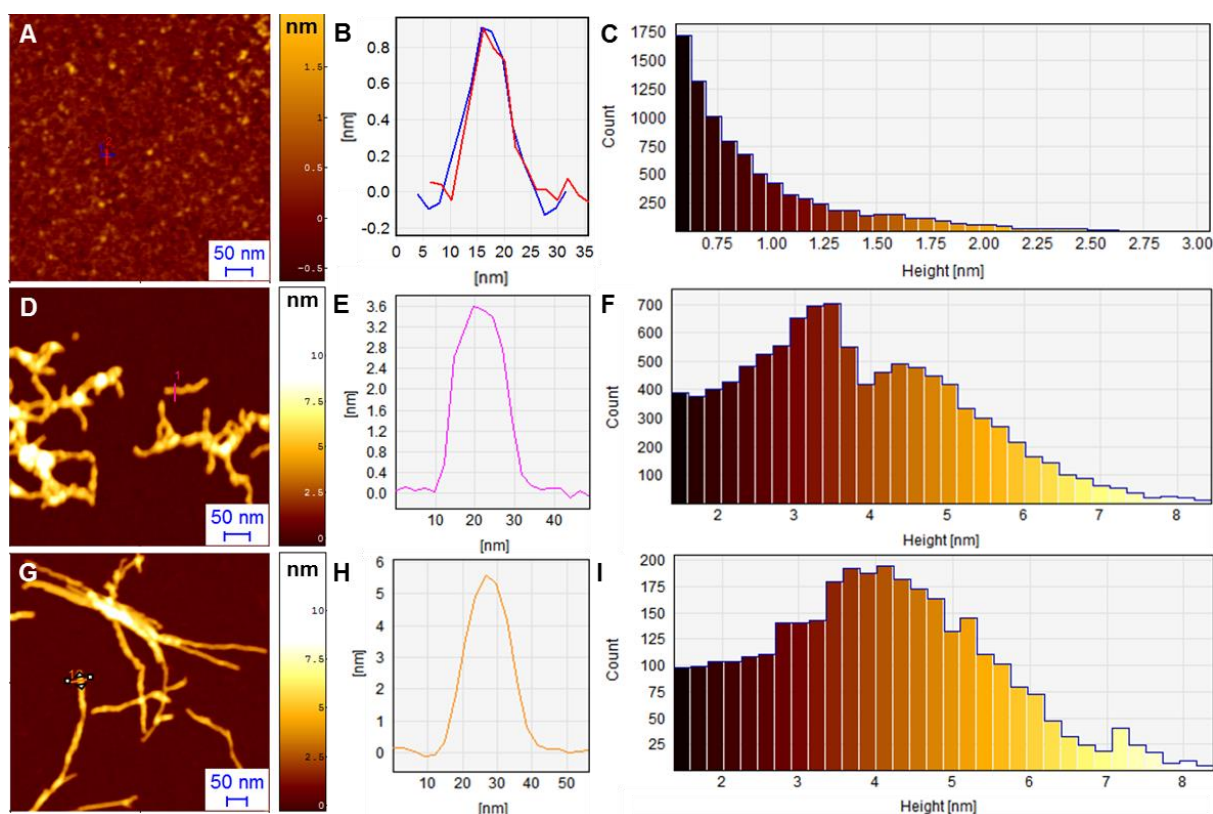


Figure 4.4 Analysis of the morphology of A β -42 oligomers, protofibrils and fibrils.

Oligomers at 0 days: A) AFM image. B) Cross sectional dimensions of an aggregate. C) Distribution of height. Protofibrils at 24 h: D) AFM image. E) Cross sectional dimensions of an aggregate. F) Distribution of height. Fibrils at 72 hours: G) AFM image detail of fibrils. H) Cross sectional dimension of a fibril. I) Distribution of height.

4.3.4 Peak-force Quantitative nanomechanical measurements of amyloid aggregate stiffness

In order to characterize the mechanical properties of the different species forming during the fibrillization process, PF-QNM measurements were performed. As starting point, the mechanical properties of early oligomeric structure of α -synuclein formed after 24 hours and deposited on a positively functionalize APTES-mica substrate, (**Figure 4.5**) were investigated. In the case of the oligomeric structures, the measurements revealed that they possessed already a notable value of Young's modulus in the order of the GPa and more specifically of 1.5 ± 0.5 GPa (**Figure 4.5B-C**).

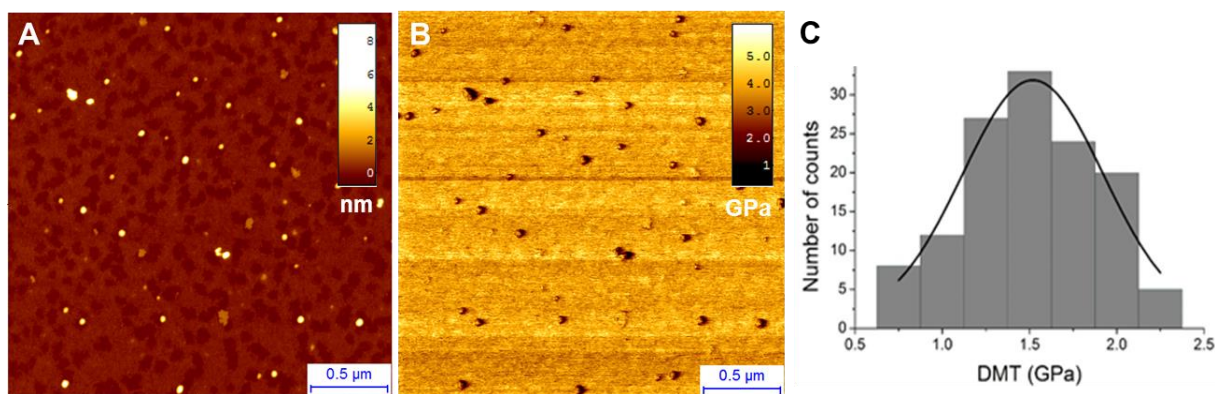


Figure 4.5 Young's modulus of α -synuclein oligomeric species.

A) AFM morphology image and B) AFM *Derjaguin–Mueller–Toporov* (DMT) modulus image of oligomers on APTES-mica with incubation times of 24 h. C) Distribution of Young's modulus of oligomers.

The same measurements were performed on the α -synuclein mature fibrillar structures, as confirmed by CD (**Figure 4.1C**), formed at 10 days incubation at 37 °C and deposited on three different substrates: positively functionalized APTES-mica substrate, negative bare mica and hydrophobic HOPG (**Figure 4.6A-C**). The reported a value of the Young's modulus was identical, inside the experimental error, on all the three substrates (**Figure 4.6D-I**). These result is in agreement to previously reported values of stiffness, available for mature fibrils only.^{163,202} The measurement of stiffness of the fibrillar structures of α -synuclein was realized on the three different substrates, described above, in order to rule out the surface effect on the estimation of the Young's modulus and to give more significance to the slight difference of the value of stiffness respect to the one of the oligomeric species. In all cases, the value of Young's modulus of fibrils adsorbed on these two substrates was 2.2 ± 0.6 GPa (**Figure 4.6G-I**), thus demonstrating that PF-QNM measurements are independent from surface influences.

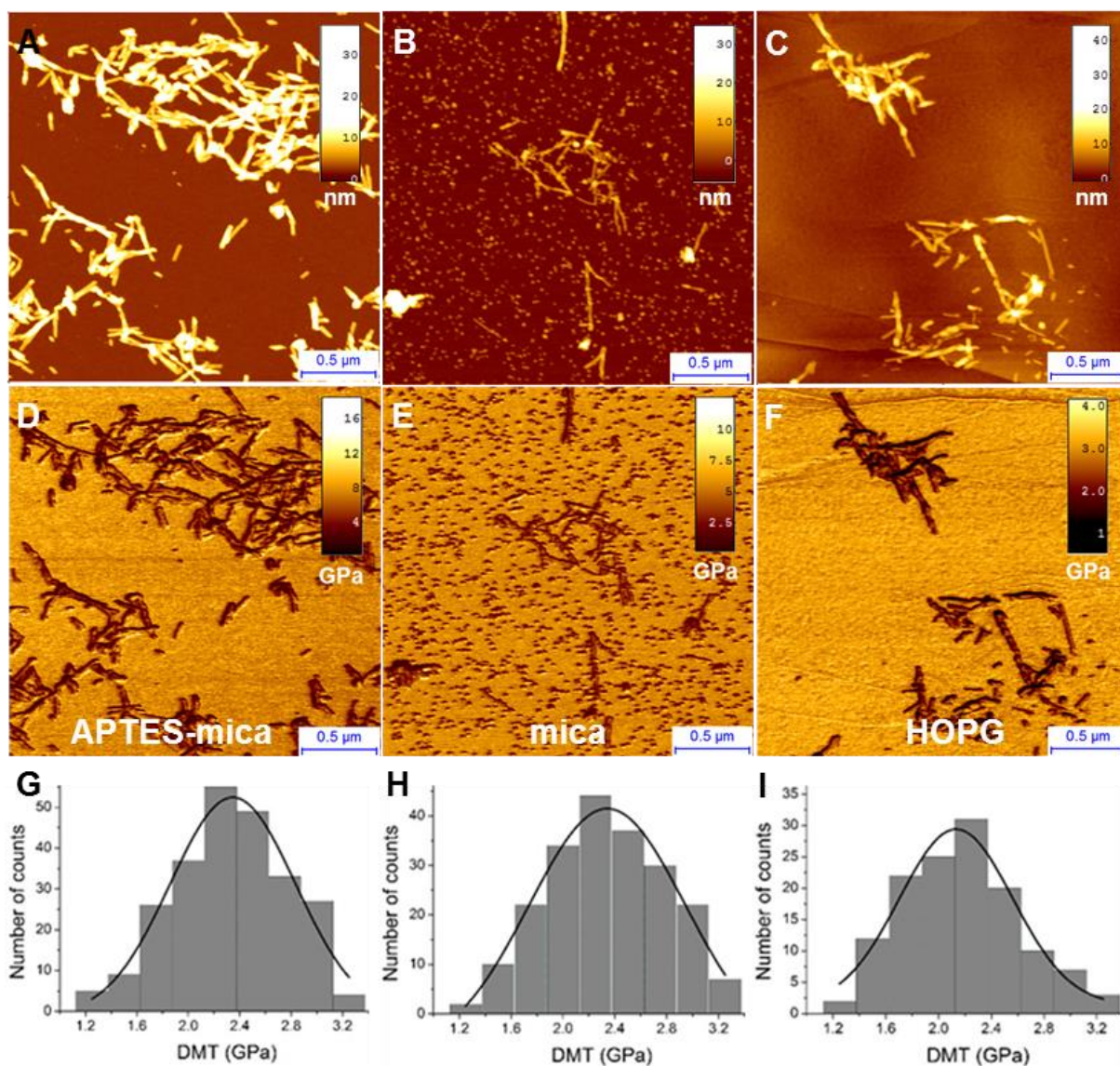


Figure 4.6 Young's modulus of α -synuclein fibrillar species.

A-B-C) AFM morphology images and D-E-F) AFM *Derjaguin–Mueller–Toporov* (DMT) maps of fibrils on APTES-mica, mica and HOPG. G-H-I) Histogram distributions of the Young's modulus of the fibrillar structures on each substrate.

Similarly, in order to eliminate the possibility of errors deriving from the nanoscale nature of the AFM tip and sample dimensions, the nanoindentation measurements were validated on thick aggregates of alpha-synuclein (AFM height ~ 50 nm, **Figure 4.7A-C**). In these conditions both substrate and cantilever tip radii corrections become irrelevant. These measurements yielded results identical to single fibril indentation, within experimental error, and to a value of stiffness of 2.3 ± 0.8 GPa (**Figure 4.7 D-E**). Finally, all together these results revealed that oligomers possess a lower elastic modulus than mature fibrils, but still in the order of GPa.

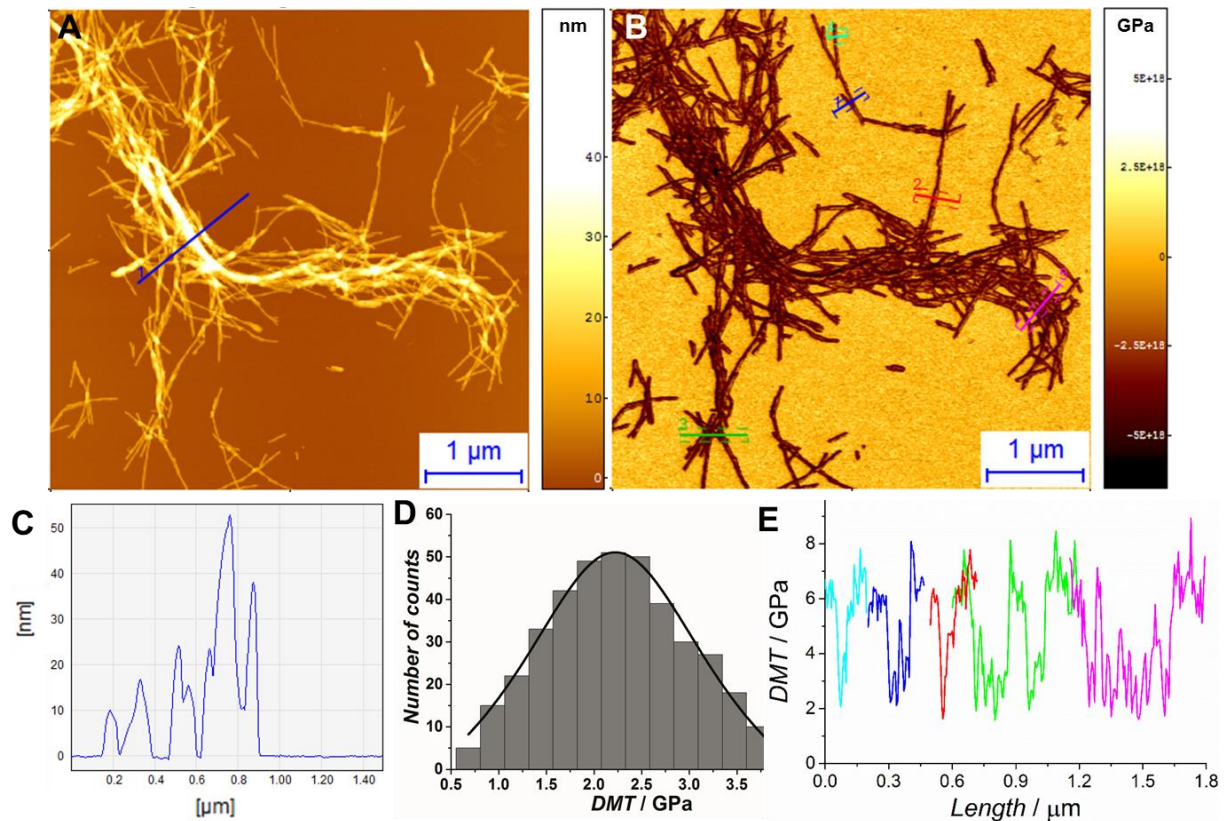


Figure 4.7 Stiffness of a α -synuclein bundle of fibrils.

A) AFM height image, B) AFM DMT modulus images, C) Cross section of the height of a bundle, D) Histogram of Young's modulus of the bundle of fibrils. E) Cross sections of AFM DMT images. Single fibrils and bundles of fibrils show similar values of Young's Modulus.

To generalize these results, PF-QNM measurements for A β -42 fibrillization were also performed (**Figure 4.8**). The Young's modulus of the oligomers at 0 hours (**Figure 4A**), of protofibrils at 24 hours (**Figure 4B**) and of mature fibrils at 72 hours (**Figure 4C**) was evaluated accordingly. In the same way as in the case of α -synuclein, the value of the Young's modulus increased from a value of 1.2 ± 0.5 GPa for oligomers (**Figure 4D**), through 2.1 ± 0.6 GPa for protofibrils (**Figure 4E**), to a final value of 3.3 ± 0.8 GPa for mature fibrils (**Figure 4F**). Once again, oligomers and protofibrils showed an increasing and high value of intrinsic stiffness in the order of GPa, but still lower than mature fibrils. Indeed, we can suggest the generality of this result since, as we previously measured, several mature amyloid fibrils range their stiffness value between 2-4 GPa (**Table 1**).

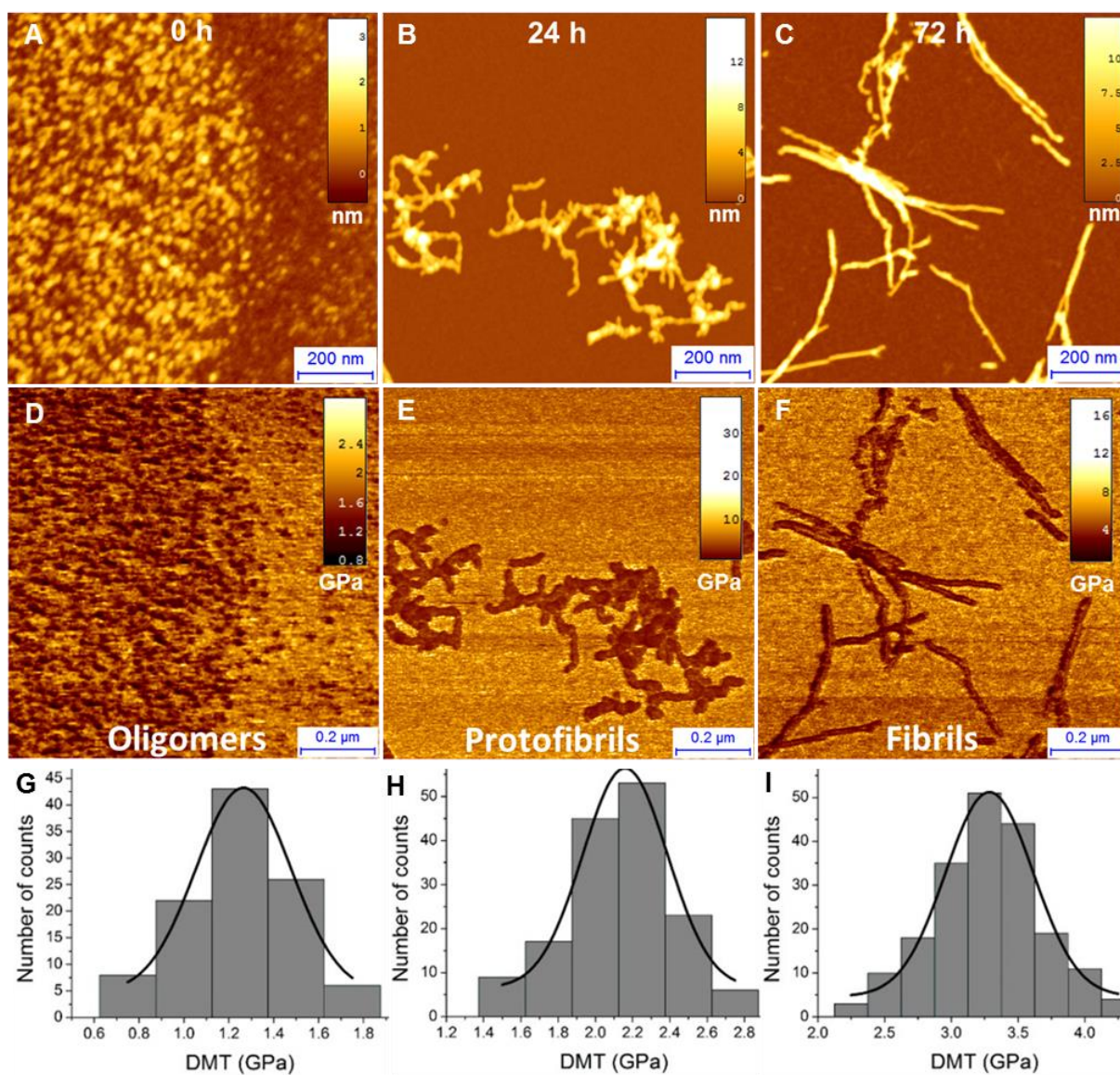


Figure 4.8 Young's modulus evolution of Aβ-42 during fibrillization process.

AFM morphology maps A) 0h, oligomers, B) 48 h, protofibrils, C) 72 h, fibrils. *Derjaguin–Mueller–Toporov* (DMT) modulus images of D) 0h, oligomers, E) 48 h, protofibrils, F) 72 h, fibrils. Distribution of the measured Young's modulus for G) oligomers, H) protofibrils and I) fibrils.

Table 4.1 Young's Modulus of Amyloid fibrils.¹⁶³

Amyloid fibrils	Young's modulus
CH ₃ CONH- β A β AKLVFF-CONH ₂	2.3 \pm 0.6 GPa
Insulin	3.2 \pm 0.6 GPa
β -Lactoglobulin	3.7 \pm 0.8 GPa
Lysozyme	2.8 \pm 0.9 GPa
Bovine serum albumin	3.0 \pm 0.6 GPa
Ovalbumin	2.7 \pm 0.8 GPa
Tau protein	3.4 \pm 0.7 GPa
A β (1-42)	3.2 \pm 0.8 GPa
α -Synuclein	2.2 \pm 0.6 GPa

It was mentioned above that the hydrogen bonds between β -sheets play a key role in the mechanical properties of amyloid fibrils and the presence of β -sheets is a characteristic feature of amyloid fibrils. It has also been reported that during the aggregation process, oligomers or eventually present protofibrils contain partial β -sheet conformations.⁷⁹ This suggests that the content of β -sheets in the assembled structures during fibrillization process is an important parameter affecting the mechanical properties of these structures. The presented results just confirm these predictions. Indeed, although mature fibrils were initially not observed by AFM, CD spectra indicated the presence of β -sheet structures already at 48 hours for α -synuclein (**Figure 4.1C**) and 24 hours for A β -42 (**Figure 4.1D**), and the measured values of the Young's moduli of the corresponding assembled structures (oligomers and protofibrillar structures) were already in the order of the GPa (**Figure 4.5** and **Figure 4.8**).

4.4 Discussion

PF-QNM allowed us to investigate at the single molecule level the nanomechanical properties of different products of amyloids aggregation process. In particular, we were able to measure the evolution of Young's modulus during fibrillation of α -synuclein and A β 42. As resumed in Table 1, their elastic modulus evolved monotonically during the process of aggregation as a function of the maturity of the fibrillation process. In fact, oligomers and protofibrils showed an increasing value of the intrinsic stiffness in the order of GPa. These results, as proved by CD and ThT bulk measurements (**Figure 4.1**) and other previous studies,⁷⁹ are explained by the fact that early oligomeric and protofibrillar structures have already a partial and increasing β -sheet content. Furthermore, we previously demonstrated that: PF-QNM technique measures Young's modulus of amyloid fibrils independently of the polymorphic state and cross-sectional structural details; their high value (GPa) of the elastic modulus is mainly due to the tight β -sheet ordering in the forming amyloid structure. For this reasons, it is natural that intermediate products of aggregation with partial β -sheet conformation possess a high value of the intrinsic Young's modulus, but still consequently lower than the one of mature fibrils with complete cross β -sheets structure.²⁴⁴ As demonstrated by previous studies²⁴⁵, even if DMT-QNM technique could overestimate by about a factor of two the value of Young's modulus, the measured values would still be in the order of GPa and the measured monotonically increasing behavior would not be modified. Finally, increase in the Young's modulus during amyloid fibrillization can be interpreted as the result of the internal structural rearrangement of monomers from their intrinsically disordered structure towards aggregated structures with an increasing content of β -sheet conformation. This work allows, for the first time, a quantitative understanding of the structural and mechanical properties of α -synuclein and A β -42 aggregate snapshots during the fibrillization process, which can be of significant importance for the understanding of the cytotoxicity mechanisms and the design of new therapeutic strategies for Parkinson's and Alzheimer's diseases.

Table 4.2. Young's Modulus of amyloidogenic structures.

	Oligomers	Protofibrils	Fibrils
α -synuclein	1.5 \pm 0.5 GPa	-	2.2 \pm 0.6 GPa
A β -42	1.2 \pm 0.5 GPa	2.1 \pm 0.6 GPa	3.3 \pm 0.8 GPa

Chapter 5. Nanoscale spatially resolved infrared spectra from single microdroplets

This chapter is based on a paper published in the journal Lab on a Chip with the following authors:

⁺Thomas Müller¹, ⁺Francesco Simone Ruggeri², Andrzej J. Kulik², Ulyana Shimanovich¹, Thomas O. Mason¹, Tuomas P. J. Knowles¹ and Giovanni Dietler² (+ These authors contributed equally to the manuscript)

Affiliations:

¹ *Department of Chemistry, University of Cambridge, Cambridge, UK.*

² *Laboratory of Physics of Living Matter, EPFL, 1015 Lausanne, Switzerland.*

Abstract

Atomic force microscopy (AFM) has enabled gaining notable insights into the formation and properties of amyloid structures. Despite capable of unraveling morphological and mechanical properties at the nanoscale, AFM is not able to investigate the structural and chemical properties of these structures. Inversely, infrared spectroscopy (IR) is a key method for studying conformational properties of proteins and their structural conversion during amyloid fibrillation. However, it is able to give average information only on the ensemble of the species present in the heterogeneous aggregating solution. In this chapter, it is shown that a new system, exploiting the simultaneous use of AFM and IR (nanoIR), can be efficaciously used to characterize at the nanoscale the structural properties of amyloids during their aggregation. In this first proof of concept, the system was used to analyze proteins deposited as patterned μ -droplets by means of a microfluidic system. Droplet microfluidics has emerged as a powerful platform allowing reactions to be carried out in spatially distinct micro-compartments. The compartmentalisation of biomolecules into monodisperse, micrometer-sized droplets allows for quantitative and high-throughput biochemical studies on amyloid formation. Due to their small size, however, the spectroscopic characterization of species encapsulated in such systems remains challenging. Infrared nanospectroscopy is able to acquire infrared spectra from single μ -droplets containing aggregation-prone proteins. The technique is capable of investigate structural differences in the amide bands of the spectra of monomeric and aggregated lysozyme from single microdroplets with picolitre volume. In particular, the shift of the amide I band toward lower wavenumbers allowed identifying an α -to- β structure transition associated with amyloid formation.

5.1 Introduction

Lab on a chip technologies offer a range of unique opportunities for preparation and manipulation of molecular species. In particular, the compartmentalisation of biomolecules into monodisperse, micrometer-sized droplets allows for quantitative, high-throughput biochemical studies such as directed evolution,²⁴⁶⁻²⁴⁸ screening for reagents, reaction conditions or cells,²⁴⁹⁻²⁵¹ as well as for the fabrication of designer emulsions and microgels.^{252,253} Microdroplets can also allow the study of rare events, such as nucleation, and have thus enabled studies of the nucleation step of A β aggregation²⁵⁴ as well as insulin amyloid growth.²⁵⁵ With the rapid development of microfluidic technologies, the need of ultra-sensitive detection methods becomes ever more pressing. A large fraction of present-day experiments rely on optical detection,²⁵⁶⁻²⁵⁸ with alternative strategies including, for instance, electrochemistry,^{259,260} mass spectrometry²⁶¹⁻²⁶³ or Raman spectroscopy.^{264,265} Also, infrared (IR) spectroscopy techniques have been utilized to monitor the contents of microfluidic flows.^{266,267}

Here, we demonstrate an approach for performing IR spectroscopy on the contents of single microdroplets with sub-micrometer spatial resolution. Infrared spectroscopy (IR) is a key method for studying conformational properties of proteins and in particular for inferring their secondary structure.^{182,209} Exposed to IR radiation, chemical bonds undergo vibrations such as stretching, bending and rotating. In the case of proteins, this leads to a spectrum characterized by a set of absorption features in the amide bands.¹⁸⁵ Thereby, the modes most commonly used to study the structural properties of polypeptides are the amide I, amide II and amide III bands. Amide I arises mainly from C=O stretching vibrations and is generally localized within 1690–1600 cm⁻¹; the exact band position is determined by the backbone conformation – in other words by the secondary structure of the protein. In contrast, amide II originates from a combination of N–H bending and C–N stretching and is localized around 1580–1510 cm⁻¹. It is still possible to associate the position of the band to the protein's secondary structure, but the fact that this band stems from a combination of two different modes makes this analysis less straightforward. Finally, the amide III band is a combination of many modes such as C–N stretching, N–H in-plane bending, C–C stretching as well as C=O bending and occurs in the range of 1300–1200 cm⁻¹. In practice, α -helical structures have this band centered around 1654 cm⁻¹, random coil proteins show a maximum between 1635–45 cm⁻¹, and β -sheet-rich amyloidic aggregates exhibit an amide I maximum within 1610–1630 cm⁻¹.⁶⁴

To achieve sub-micron spatial resolution for protein IR spectroscopy experiments, we utilized a thermomechanical detection technique based on atomic force microscopy (AFM): if an IR pulse at a given wavelength is absorbed by a sample, the local temperature rise leads to local thermal expansion.^{211,268,269} This deformation excites a mechanical resonance in the AFM cantilever which is in contact with the analyte. AFM detection of this temporary expansion of the scanned region therefore allows nanoscale resolution IR imaging and acquisition of local chemical spectra. Simultaneously with the IR-absorption image, the system is able to scan topography (with conventional contact mode) and sample stiffness (related to the frequency of the cantilever oscillations).

The capability of studying the contents of single microdroplets individually with a high-precision method paves the way for a wide range of experiments harnessing the advantages of microfluidics. For instance, combination with on-chip selection techniques²⁷⁰⁻²⁷⁴ that pre-screen for a predefined species within droplets could allow for specific in-depth investigation of analytes in the context of protein aggregation as well as directed evolution. In addition, it should be emphasized that the technique of aligning individual microfluidic droplets off-chip offers further possibilities for systematic *ex situ* assays beyond IR spectroscopy or AFM. In order to be able to reliably locate and distinguish the protein contents of individual microdroplets for performing nanoscale IR spectroscopy as well as to provide for an enormous amount of statistics, the droplets are aligned on a ZnSe prism using a pre-patterned polymer stamp and dried overnight, as shown schematically in **Fig. 5.1A–C**. Thereafter, spectra of single dried microdroplets containing monomeric, aggregating and aggregated lysozyme protein are acquired. The ability to easily differentiate between these different species demonstrates the efficacy of the presented approach to study amyloid properties. In particular, this experiment represents the first step towards the application of infrared nanospectroscopy in order to unravel the process of protein misfolding and aggregation at the nanoscale.

5.2 Experimental Methods

In brief, micrometer-sized droplets of protein solutions in fluorinated oil are generated via a microfluidic droplet maker and deposited on a ZnSe prism (**Fig. 5.1A**). These droplets are then aligned on a grid using a patterned stamp of polydimethylsiloxane (PDMS) as shown in **Fig. 5.1B** and dried overnight in a desiccator at room temperature or in an oven at 65 °C. To measure the IR spectrum, the dried protein is heated locally using a laser and the resulting thermal expansion is determined using an AFM tip, which is sketched in **Fig. 5.1C**. In the following, these steps are described in more detail.

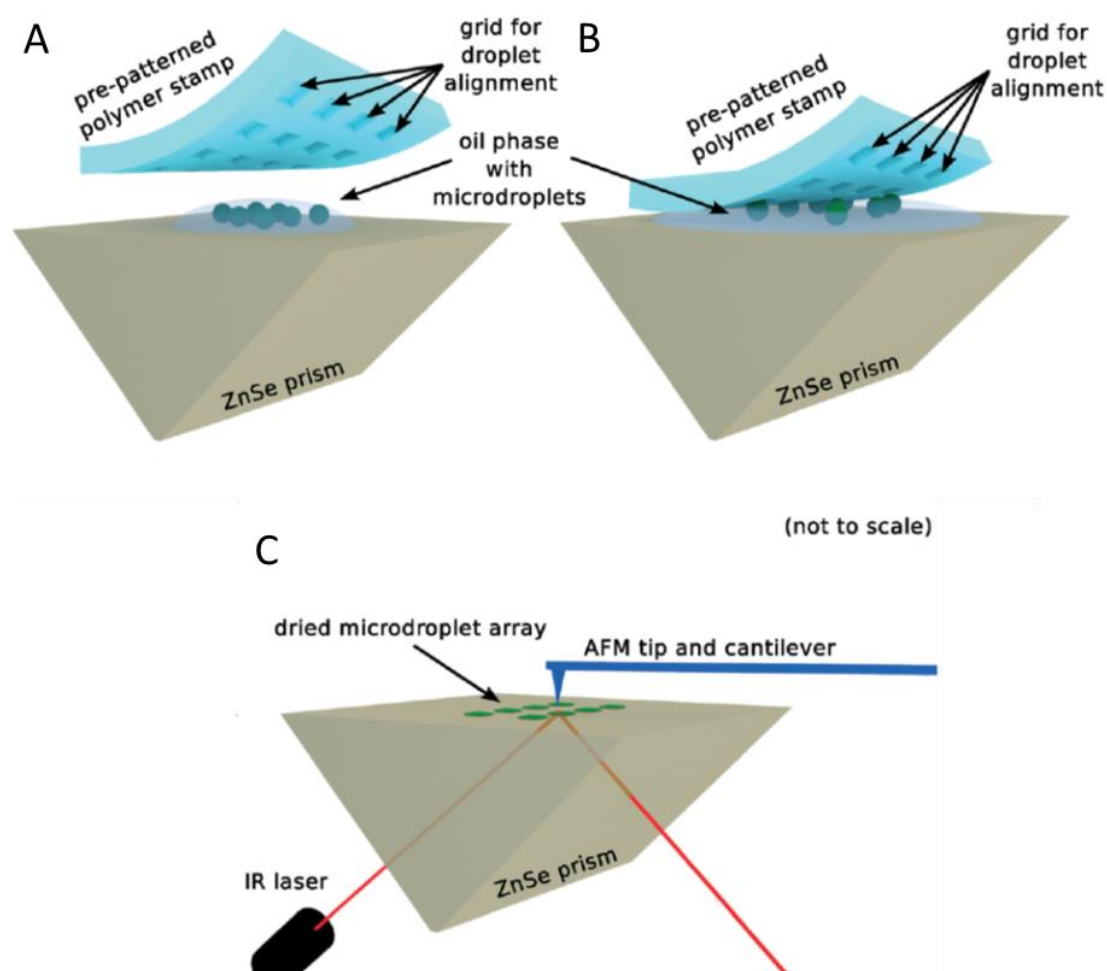


Figure 5.1 Droplets deposition on the prism for the Infrared Nanospectroscopy analysis.

(A) Schematic representation of the droplets deposited on a ZnSe prism and the pre-patterned polymer stamp. The indents on the grid are $20\ \mu\text{m} \times 20\ \mu\text{m} \times 25\ \mu\text{m}$, separated by $200\ \mu\text{m}$ in each direction. (B) Alignment of the droplets on a grid by pressing the polymer onto the solution. (C) Pictogram of a laser locally heating the dried protein contents of single droplets, with an atomic force microscope measuring the resulting thermal expansion.

Protein solutions

For the monomeric solution, lysozyme from chicken egg white (Sigma-Aldrich, #62970) is dissolved in deionized water at a concentration of 6 mg ml^{-1} . Aggregates are formed by mixing 60 mg lysozyme with 1% Sodium Azide, 200 μl of 1M HCl, 600 μl of 10 mM HCl, 200 μl of 2 M NaCl and 5 μl of a preformed seed-fibril solution, filtering through 0.45 μm pores, followed by incubation at 65 °C for 24 h. This approach yields approximately micrometer-sized fibrils that form a gel-like structure when encapsulated as an aqueous droplet.

Droplet generation

As depicted in **Fig. 5.2**, droplets are generated using a microfluidic junction with a cross-section of $25 \mu\text{m} \times 25 \mu\text{m}$, fabricated through a standard soft lithography approach.²⁷⁵ The protein solution is injected through the central arm at a flow rate of $50 \mu\text{l h}^{-1}$, whereas fluorinated oil (Fluorinert FC40, Sigma-Aldrich, #F9755) containing 2% w/v surfactant (N, Nbis(n-propyl)polyethylene oxide-bis(2-trifluoromethyl polyper fluoroethylene oxide) amide) is pumped through the side channels at $100 \mu\text{l h}^{-1}$. These settings result in droplets with a diameter of approximately 25 μm which are collected in a microcentrifuge tube.

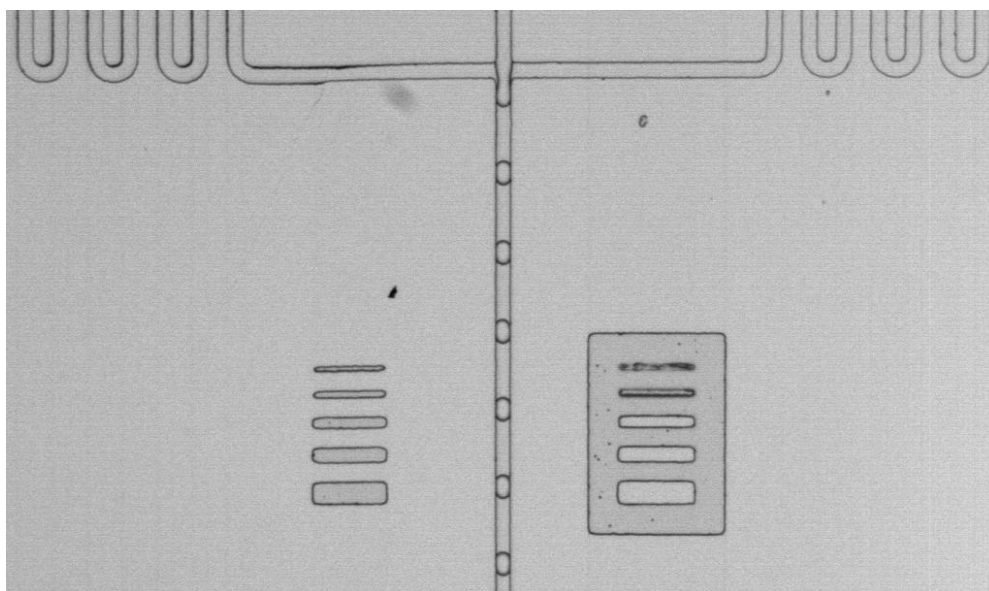


Figure 5. 2 Micrograph of droplet formation in a microfluidic device.

The aqueous solution containing the protein is pushed through the central channel and encapsulated in fluorinated oil streaming in from both sides.

Droplet alignment and drying

One ml of solution with droplets from either monomeric or aggregated protein, respectively, are pipetted onto opposite ends of the surface of an attenuated total internal reflection element prism made out of ZnSe monocrystals. Thereafter, a pre-patterned PDMS stamp is pressed onto each drop of liquid in order to align the droplets to its imprinted grid. The grid consists of $20\ \mu\text{m} \times 20\ \mu\text{m} \times 25\ \mu\text{m}$ indents to capture individual droplets, with a spacing of $200\ \mu\text{m}$, and is imprinted into PDMS by soft lithography.²⁷⁵ This process is illustrated in **Fig. 5.1A** and **B**; for simplicity, only one instance of droplet solution is shown. The prism – including the alignment polymer – is then stored for 15 h in a desiccator. Alternatively, the devices can be dried at elevated temperatures – for instance, in an oven at $65\ ^\circ\text{C}$ at ambient pressures for 15 h. This, however, will lead to further aggregation inside the droplets upon drying. Careful removal of the PDMS slab yields a regular pattern of the dried contents of single microdroplets – in the present case protein – as shown in **Fig. 5.3A-B**.

Spatially resolved infrared spectroscopy

Samples were scanned by a commercial nano-IR microscopy system (Anasys Instruments), with a line rate between $0.02\text{--}0.08\ \text{Hz}$ in contact mode. We used a silicon cantilever (AppNano) with a nominal radius of $10\ \text{nm}$ and a nominal spring constant of $0.5\ \text{N m}^{-1}$. All images have a resolution of 512×256 pixels. Spectra were collected with a step width of $1\ \text{cm}^{-1}$ within the range of $1200\text{--}1800\ \text{cm}^{-1}$ at 40% of the instrument's maximal laser power. All measurements were performed at room temperature.

5.3 Results

5.3.1 Patterned micro-droplets

Our results demonstrate that using the approach presented here, it is feasible to align tens to hundreds – if desired even thousands – of microdroplets, as shown in **Fig. 5.3A-B**.

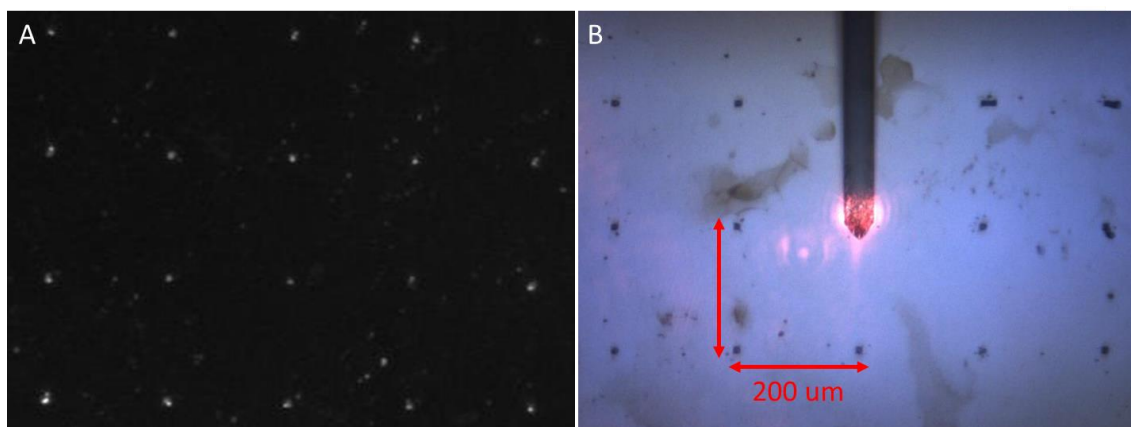


Figure 5.3 View of the aligned droplets.

(a) Photograph of the aligned and dried droplets after removing the polymer slab. Each bright spot is the protein content of a microdroplet. (b) Optical image during AFM imaging, each black dot is a microdroplet. The smears in the background stem from the fluorinated oil which has been found to not affect the IR measurements.

Such a regular deposition allows for reliable, systematic off-line assays including ultra-high precision analytical tools as, for instance, the nanoscale IR spectroscopy utilized in this work. Our droplets were aligned at the corners of squares with a side of 200 μm .

Several conditions for drying and analyzing the droplets were investigated. We have deposited microdroplets on pure ZnSe prisms and SiO₂-coated ZnSe prisms. As mentioned above, drying was effected by either placing the prisms under vacuum at room temperature or in an oven at 65 °C at ambient pressure for a time span of 15 h. The resulting morphologies varied significantly, as summarized in **Fig. 5.4**. Most importantly, droplets that have been heated overnight (G-J) exhibit a smaller size, which may well be caused by the protein becoming more attached to the PDMS stamp and therefore being removed when detaching the stamp.

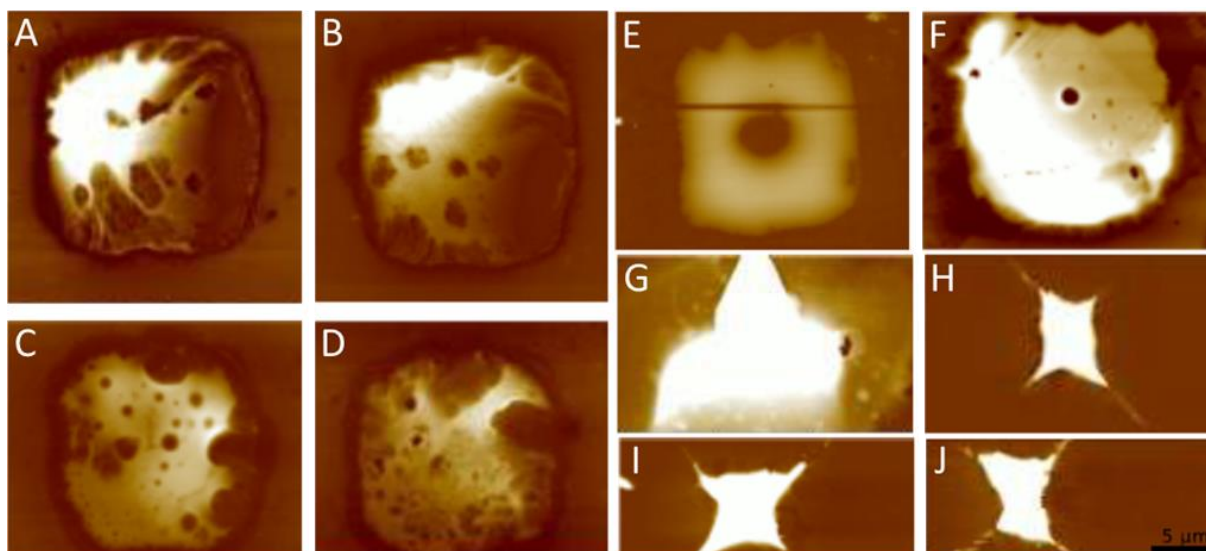


Figure 5.4 Atomic force microscopy images of droplets dried under different conditions.

(A) Aggregated lysozyme, deposited on a ZnSe prism and dried for 15 h at room temperature under vacuum. Scale height is ± 250 nm. (B) Same as (A), for a different droplet. Scale height is ± 500 nm. (C) Aggregate lysozyme, deposited on a SiO₂-coated ZnSe prism and dried for 15 h at room temperature under vacuum. Scale height is ± 500 nm. (D) Same as (C) but for a different droplet. Scale height is ± 500 nm. (E) Monomeric lysozyme, deposited on a ZnSe prism and dried for 15 h at room temperature under vacuum. Scale height is ± 150 nm. (F) Monomeric lysozyme, deposited on a SiO₂-coated ZnSe prism and dried for 15 h at room temperature under vacuum. Scale height is ± 250 nm. (G) Aggregated lysozyme, deposited on a ZnSe prism and dried for 15 h at 65 °C at ambient pressure. Scale height is ± 300 nm. (H) Monomeric lysozyme, deposited on a ZnSe prism and dried for 15 h at 65 °C at ambient pressure. Scale height is ± 300 nm. (I) Same as (H), but for a different droplet. Scale height is ± 300 nm. (J) Same as (H), but for a different droplet. Scale height is ± 300 nm.

5.3.2 Infrared Nanospectroscopy Absorption Maps

The nanoIR system, contemporarily to conventional IR maps **Fig. 5A**, allows to measure sub-micron IR absorption maps of our droplets. **Fig. 5.5B–D** shows how the aggregated lysozyme from an individual microdroplet can be analyzed accurately.

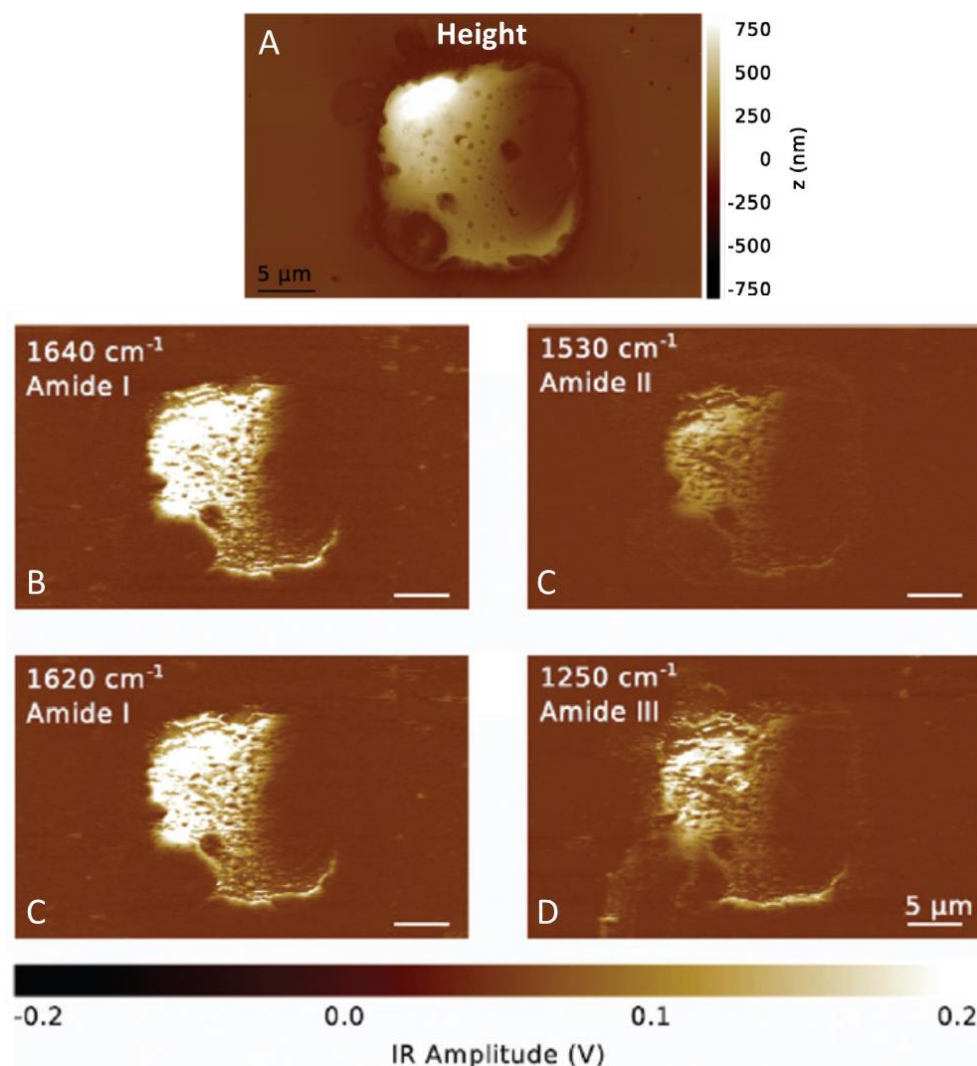


Figure 5.5 IR absorption maps of aggregated lysozyme.

(A) AFM morphology and (B-D) IR maps from a microdroplet on a ZnSe prism at different excitation wavelengths corresponding to the amide I, II and III bands.

Presented is the spatially resolved absorption of infrared radiation, determined via thermal expansion as measured by an AFM tip. The wavenumbers are fixed at 1640 cm^{-1} (A), 1620 cm^{-1} (B), 1530 cm^{-1} (C), 1250 cm^{-1} (D), corresponding to two instances from the amide I band, one from the amide II band, and one from the amide III band, respectively. While all

the four plots share their topographical features, it is readily apparent that absorption is higher in the amide I band than the amide II and III bands. Moreover, the absorption in the amide III band exhibits a stronger spatial dependence. This could be linked to the fact that this band is sensitive to different vibrational modes and therefore is influenced by local conformational changes accompanying the transition of protein from its monomeric form into aggregates.⁴² Thus, it is possible to investigate the IR absorption behaviour of the contents of individual droplets locally. Furthermore, the correlation with the height measurement from the AFM scan in **Fig. 5.5(A)** emphasizes that the recorded absorption originates from the contents of a single microdroplet.

5.3.3 Infrared Nanospectroscopy Spectra

The complete spectrum of the lysozyme aggregates in this droplet – averaged over 12 spectra recorded at different locations and smoothed by a Savitzky–Golay filter – is given by the dashed blue line in **Fig. 5.6**. As expected from the spatially resolved data, the nearly constant absorption observed in the amide I band – lightly peaked at approximately 1640 cm^{-1} – is higher than in the amide II and III bands. Remarkably, when comparing with a spectrum taken from a droplet containing only monomeric protein (the solid red line is the smoothed average over 15 individual spectra), striking differences are apparent. First and foremost, the monomeric protein exhibits a sharp peak at around 1655 cm^{-1} , due to the high α -helical content of lysozyme, and a shoulder at 1640 cm^{-1} originating from random coils and β -sheets – all in good agreement with the structure of lysozyme.²⁷⁶ Secondly, the amide II band seems slightly shifted towards higher energies for the monomer, and thirdly, absorption in the amide III band is significantly higher in monomeric than in aggregated protein. The shift of the amide I peak as well as the dramatic increase of absorption at 1620 cm^{-1} are the typical signatures of the formation of amyloid-like cross- β structure and have been studied extensively for the case of lysozyme.¹⁸³ Notably, our spectra from dried lysozyme correspond very well to measurements obtained in bulk solution.¹⁸³ In fact, even if monomers already contain β -sheet domains their spectra differ from the amyloidic β -sheets and can be distinguished by the change in the location of the amide I peak.²⁷⁷ Similarly, the position of the amide II band is expected to shift towards lower wavenumbers if the secondary structure changes from predominantly α -helical to β -sheet.²⁰⁹ As the amide III band has a significantly more complex origin, the differences in the monomeric and aggregated spectra are less directly explainable, but strong deviations are reasonable bearing in mind the extensive structural modification proteins undergo during aggregation.

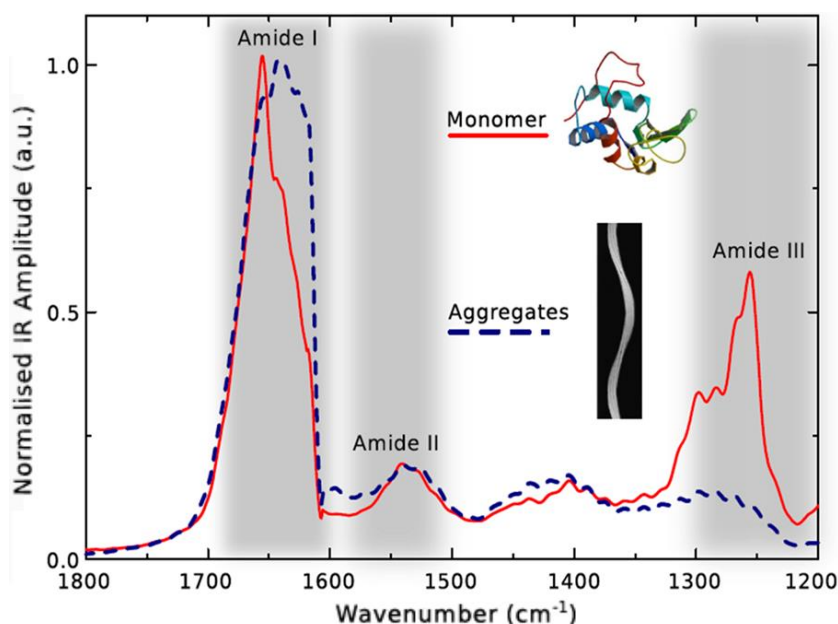


Figure 5.6 IR Spectra from micro-droplets.

Spectra of monomeric (solid red line) and aggregated (dashed blue line) Lysozyme on the ZnSe prism. Insets for the structures of monomer and lysozyme amyloid are adapted from ref. ²⁷⁸ and ²⁷⁹, respectively.

To demonstrate the repeatability of our approach, we present spectra of droplets containing monomeric and aggregated lysozyme dried under the described different conditions in **Fig. 5.7A-B**, respectively. Specifically, we investigated two different types of infrared-transparent prisms (ZnSe and SiO₂-coated ZnSe) and dried the droplets either at room temperature under vacuum or at 65 °C at ambient pressure. For the monomeric protein, the vacuum-dried droplets on either substrate exhibit a distinct peak around 1655 cm⁻¹ as well as a sharp feature in the amide III band which is pronounced more strongly for the plain ZnSe prism. Heating the droplets for 15 h to evaporate all solvents lead to a drastic increase of the absorption in the amide I band (see black ellipse in **Fig. 5.7A**) that corresponds very well to the spectra observed for aggregated protein. Furthermore, in the case of the heated, SiO₂-coated prism the peak in the amide III band also vanishes. Considering the original approach for forming the aggregates, it is highly plausible that the conditions for drying the droplets at elevated temperatures are sufficient to cause at least partial aggregation of the initially monomeric protein in particular since the evaporation of water continuously increases the protein concentration. The spectra of the droplets containing aggregated protein presented in **Fig. 5.7B** are very similar for all conditions and demonstrate the reliability of our approach. The most notable difference is that with the additional layer of SiO₂ on the surface of the prism the absorption at the high-energy side of the amide I band is increased relatively to the rest of the

spectrum. The peak positions, however, are unchanged. Also, the spectra from three droplets on the same substrate (solid, dashed and dotted blue lines) indicate the quantitative variability between individual droplets with nominally the same contents.

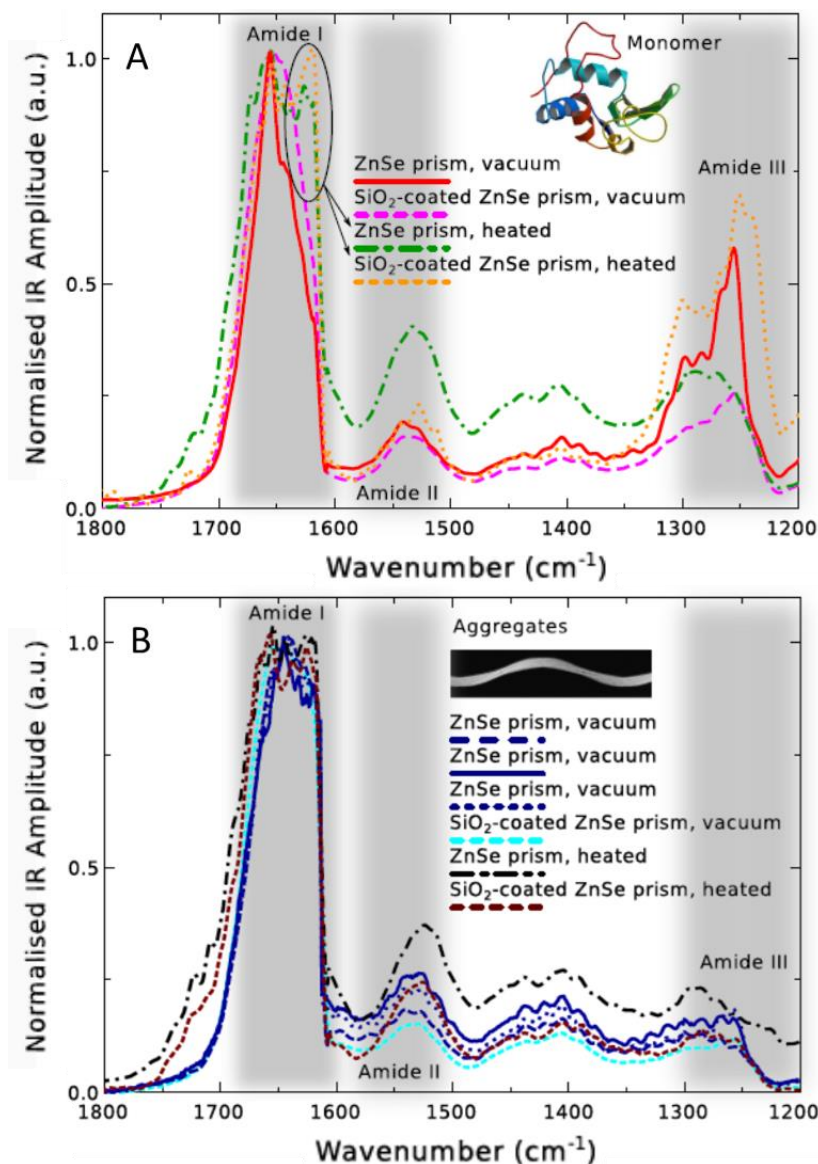


Figure 5.7 Spectra of monomeric and aggregated proteins with different method of deposition.

(A) Spectra of dried droplets containing initially monomeric protein. Shown are droplets dried in vacuum at room temperature during 15 h, deposited on a ZnSe prism (solid red line; same curve as in main text) or a SiO₂-coated ZnSe prism (dotted orange line), as well as dried at ambient pressure at a temperature of 65 °C on a ZnSe prism (dash-dotted green line; same curve as in main text) or on a SiO₂-coated ZnSe prism (dashed magenta line). The black ellipse marks the appearance of a shoulder in the amide I band for the heated droplets. (B) Same as in (A) but for aggregated protein. For the vacuum-dried ZnSe prism spectra of three different droplets are presented (dashed, solid and dotted blue lines).

In both cases - that is monomeric and aggregated protein - some of the differences between the spectra from ZnSe prisms and SiO₂-coated ZnSe prisms may be explained by the different absorption behaviour on different substrates. Indeed, in all instances of the coated prisms we observe stronger absorption towards higher wavenumbers. Therefore, if protein aggregation from microdroplets is investigated, it is highly recommended to effect the drying under vacuum instead of at elevated temperature. Furthermore, we find that our spectra exhibit sharper features on the pure ZnSe prisms. Finally, comparison to a spectrum from a droplet containing initially monomeric protein that was dried at 65 °C and ambient pressure for 15 h – such that aggregation can occur within the droplet – reveals that the monomeric features of the amide I and III bands are lost upon fibrillation (dash-dotted green line; average over 21 spectra). Note that due to the normalization of the spectra to 1, the amide II band seems more pronounced. Nevertheless, the relative amplitudes of the amide II and III bands correspond very well to the spectra from the aggregates. For a ZnSe prism that was covered with SiO₂ and heated with droplets containing monomeric lysozyme, we observed a similar increase of absorption in the amide I band but the peak in the amide III band did not vanish, which may be an indication of partial aggregation.

5.3.3 Sensitivity and throughput of the method

Given a droplet diameter of 25 μm, the molar weight of lysozyme (14.3 kDa) and the concentration we have used for the monomers (6 mg/ml ~ 400 μM), each droplet contains as little as 50 pg or 3 fmol of protein. We can estimate the sensitivity of this approach via the minimal sample thickness (recommended is 0.1 μm, but we have obtained spectra from samples down to $h \approx 60$ nm height) of our Anasys nanoIR platform. Let evaluate the amount of analyte deposited on a square with length l to a height h using the inverse density of lysozyme ($v = 0.7$ ml/g). This yields to:

$$C_{min} = \frac{V_{sample}/v}{V_{droplet}} \sim \frac{h/v}{l} \quad (1)$$

and with l being maximally of the order of 300 μm the minimal concentration is around 0.2 mg/ml ~ 20 μM. While standard optical techniques may detect much smaller concentrations, nanoIR provides a quite different set of information: the nanometer spatially resolved IR spectra from picograms or sub-femtomoles of protein material.

Finally, the time required to obtain a spectrum of a single droplet is typically of the order of a few minutes. Performing spatially resolved measurements may take much longer. Therefore, nanoIR can by no means be considered a high-throughput technique. NanoIR can provide information on the contents of the droplets that it is not accessible using traditional techniques. It should rather be regarded as a method complimentary to on-line high-throughput techniques where measurements can be taken at kHz rates at concentrations as low as tens of nM.^{280,281}

5.4 Discussions

A technique for deposition and alignment of individual micrometer-sized droplets for their precise analysis using nanoscale spatially resolved IR spectroscopy was presented. Off-stream alignment on a grid was achieved by means of a stamp with a patterned indentation on its surface. Drying overnight fixes their content, which is accessible upon removal of the polymer grid. Subsequent high-precision measurement of local IR absorption demonstrates the power of this approach to probe structural transitions in ultra-small volumes. Spectra from droplets containing monomeric, aggregated and aggregating lysozyme were obtained and found to be readily distinguishable. In particular, the shift in the amide I band allowed us to identify an α -to- β secondary structure transition which is associated with amyloid formation. Therefore, nanoscale IR spectroscopy represents a valuable analytic technique for the investigation of the amyloids. Once its robustness in differentiating diverse amyloidogenic species has been proved, the method could be successively applied to study the formation and properties of individual forming amyloidogenic aggregates at the nanoscale.

Chapter 6. INFRARED NANOSPECTROSCOPY

CHARACTERIZATION OF OLIGOMERIC AND FIBRILLAR AGGREGATES DURING AMYLOID FORMATION

This chapter is based on a paper in revision in the journal “Nature communications” with the following authors:

Francesco Simone Ruggeri¹, Giovanni Longo², Serena Faggiano², Ewelina Lipiec³, Annalisa Pastore² and Giovanni Dietler¹

Affiliations:

¹*Laboratory of Physics of Living Matter, EPFL, 1015 Lausanne, Switzerland.*

²*Department of Clinical Neuroscience, King’s college, London (United Kingdom)*

³*The Henryk Niewodniczanski Institute of Nuclear Physics, PAN, Krakow (Poland)*

Abstract

Amyloids are insoluble protein fibrillar aggregates. The importance of characterizing their aggregation has steadily increased because of their link to human diseases and material science applications. In particular, misfolding and aggregation of Josephin domain of ataxin-3 is implicated in spinocerebellar ataxia-3. Infrared nanospectroscopy, simultaneously exploiting Atomic Force Microscopy and Infrared Spectroscopy, can characterize at the nanoscale the conformational rearrangements of proteins during their aggregation. Here, we demonstrate that we can *individually* characterize the oligomeric and fibrillar species formed along the amyloid aggregation. We described their secondary structure, monitoring at the nanoscale an α -to- β transition, and coupled these studies with an independent measurement of the evolution of their intrinsic stiffness. These results allowed suggesting that the aggregation of Josephin proceeds from the monomer state to the formation of spheroidal intermediates with a native structure. Only successively, these intermediates evolve into misfolded aggregates and into the final fibrils.

6.1 Introduction

Aging of the world population has increased the visibility of several neurodegenerative disorders such as Parkinson's, Huntington's, Alzheimer's diseases and that of several forms of Ataxia.¹ The onset of these and of more than other twenty pathologies is connected with fibrillar aggregates, termed amyloids.⁴ However, these structures are not only associated with diseases since they were also discovered in many physiologically beneficial roles (*functional* amyloids) including bacterial coatings, adhesives and structures for the storage of peptide hormones.⁵⁻⁷ During their aggregation, these proteins, which are initially monomeric and soluble, undergo internal structural rearrangements leading to the formation of fibrils with a universal cross β -sheet quaternary structure.⁸ This is independent of the monomeric initial structure and is the fingerprint of amyloids. During the fibrillization process, several coexisting amyloidogenic species are formed.⁴⁰ The aggregation pathway typically proceeds through the formation of oligomers and protofibrils, which eventually lead to the mature fibrils. Strong evidence indicates that the intermediate stages of fibrillization rather than the ending point are associated to cytotoxicity, posing the problem of investigating these early stages of fibrillization and the inter-conversion of monomers and oligomers into amyloid fibrils.²⁴ However, the investigation of these processes and of the chemical, mechanical and structural properties of amyloid structures represents a formidable experimental challenge, in large part due to the dynamic and transient nature of the intermediate aggregation products.

To assist this challenging endeavor, development of new methodologies capable to capture shapes, size, chemical and structural properties of the aggregation species is of primary importance. In this work, we have employed an innovative technique able of monitoring the aggregation process of proteins at the nanoscale. This instrument (nanoIR, Anasys) exploits the combination of Atomic Force Microscopy (AFM) and infrared (IR) spectroscopy. AFM can provide direct information on the size, morphology and mechanical properties of amyloid species along the aggregation pathway.^{36,197,163} While, IR is widely used to describe the conformational changes in secondary structure of a protein through the process of aggregation.^{209,277,180,64} Separately, these conventional techniques do not tell us if and at which time point misfolding occurs, nor what is the secondary structure of the individual species. Indeed, AFM can only give morphological and nanomechanical description of the species formed during the aggregation pathway. While, as other bulk spectroscopic techniques, IR is just able to provide average structural information of the several amyloidogenic species, present

contemporarily in the heterogeneous aggregating solution, because it has limited the smallest practical IR spot size to 20 μm .²¹³ We, thus, used the new AFM-IR technique to structurally characterize the amyloid species at the nanoscale.²¹² This means that the system allows to overcome the diffraction limit and to map and characterize the chemical properties of biological specimens at the nanoscale.²⁸²

This new technique is of primary significance when studying non homogeneous samples such as amyloids and it requires only tiny quantities of biological (smaller than pico-kilograms) specimens²⁸², that is a major advantage when working with biological material whose production is expensive and time costly.

In a preliminary work, we used nanoIR to analyze proteins deposited as patterned microdroplets by a microfluidic system. We acquired spectra from droplets containing monomeric and aggregated lysozyme, which were readily distinguishable. A shift in the amide I band allowed us to identify a α -to- β structure transition associated with amyloid formation.²⁸² In the present work, we show how we are able to measure sub-micron maps and IR spectra along the whole aggregation pathway of the Josephin domain of ataxin-3. This human protein is of interest because responsible for spinocerebellar ataxia of type 3, an incurable neurodegenerative disease caused by misfolding and aggregation of this protein. The process is triggered by expansion of a polyglutamine tract present at the C-terminus but strongly modulated by the N-terminal Josephin domain which is itself highly prone to aggregation.^{283,77,152,151} By means of a combination of size exclusion chromatography and circular dichroism spectroscopy, we previously suggested that Josephin retains its native-like structure at the initial states of aggregation, while eventually undergoing a β -enriched structure.¹⁵³ However, with the techniques available at the time, we could not determine when the conformational transition occurs or characterize structurally the aggregate intermediate species.

We demonstrate here that nanoIR allows distinction in the same AFM map of structurally different objects by means of their different IR light absorption and chemical spectra. We could simultaneously detect the standard AFM morphology imaging and a description of the structural properties of Josephin protein and its aggregates. This allowed to structurally describe both oligomeric and fibrillar properties almost at the nanoscale providing new and powerful information on the aggregation pathway. We could also detect directly the conversion of monomers into amyloid β -sheet aggregates and demonstrate that this occurs only after the first events of aggregation. Understanding the aggregation pathway of Josephin may provide

essential information on the role of this protein, which could ultimately be correlated to the mechanism that induces neurodegeneration.

Our results provide convincing evidence that AFM-IR is a powerful methodology of general validity, which allows the study of the heterogeneous and polymorphic aggregation pathway of proteins. Its application to understand the structural bases of protein aggregation and misfolding holds a concrete promise towards a deeper comprehension of this field.

6.2 Experimental Methods

Sample preparation

The N-terminal Josephin domain of ataxin-3 (residues 1-182) was produced as reported previously.¹⁵⁴ Josephin was incubated at 37 °C to follow the aggregation pathway. Aliquots of 10 µl were taken before 2 and 7 days after incubation.

Quantitative imaging AFM

We performed all the Force Volume investigations using JPK Nanowizard III microscope (JPK Instruments AG, Berlin, Germany). The AFM head is working on a commercial inverted optical microscope (Axio Observer.A1, Carl Zeiss, Göttingen, Germany). Analyses were performed using Bruker DNP-10 cantilevers (Bruker probes, Berlin, Germany), choosing the ones with a nominal spring constant of 0.35 N/m. Before each experiment, we calibrated the mechanical properties of the tip using the JPK software. All images were obtained by working in the quantitative imaging (QI) modality, an evolution of the force-volume mode in which the AFM tip is placed in fast oscillation over the sample and the deformation of the cantilever is recorded to reconstruct an image formed by a large number of force distance (FD) curves. Typical images contain up to 256x256 pixels and, for every pixel, 2048 points per FD curves were collected. The length of the curves was 300 nm and the imaging speed ranged from 0.1 to 3 lines per second. The tip-sample interaction was limited to a maximum cantilever deflection of 3 nm (i.e. 1 nN). The data files were recorded on at least 5 different areas per sample and on minimally 20 different molecules per area. In total, the average values were calculated over more than 100 individual molecules. Depending on the size and on the resolution of the image, the stiffness of each molecule was measured on a minimum of 5 points. Processing was done in a semi-

automated way with the JPK data processing software assuming that the cantilever behaved accordingly to the Hook law (i.e., the deflection of the cantilever is directly proportional to the vertical component of the force applied on the tip). In this case, the FD curves collected on the sample can be subtracted from the FD curves obtained on the hard substrate, resulting in indentation curves. For calculations, we assumed a pyramidal tip model with a 35° opening angle. The shape of each indentation curve is then used to calculate the mechanical properties of the sample and specifically the stiffness. Measures of the average stiffness values for each condition (monomers, oligomers, fibrils) are expressed in MegaPascals (MPa) or GigaPascals (GPa) as the mean \pm standard deviation (SD).

NanoIR measurements

For all the nanoscale IR measurements, we used a nanoIR platform (Anasys, CA- USA), which combines high resolution and low noise AFM with a tunable IR laser. This instrument allows nanoscale measurements of IR absorption as a function of wavenumber to characterize specimens at spatial resolutions not previously achievable. This approach has been made possible by the photothermal induced resonance effect (PTIR), also referred to as AFM-IR. More details regarding the AFM-IR experiment can be found elsewhere²⁸⁴⁻²⁸⁶.

The aliquot samples, diluted at 1 μ M, were deposited at the surface of the attenuated total internal reflection element prism made of ZnSe monocrystals and dried. Then, they were scanned by the nanoIR microscopy system, with a rate line within 0.08-0.04 Hz and in contact mode. We used a silicon (AppNano, CA - USA) cantilever with a nominal radius of 10 nm and an elastic constant of about 0.5 N/m. All images have a resolution of at least 1024x512 pixels per line. The AFM images were treated using SPIP software. The height and IR amplitude images were first order flattened. The spectra were collected with a sampling of 1 cm^{-1} and 256 co-averages, within the range 1200-1800 cm^{-1} and with a spectral resolution of 8 cm^{-1} . Spectra were averaged from at least 10 measurements. They were normalized using the microscope's built-in Anasys software (Analysis Studio) and OriginPRO. Successively, they were smoothed with a Savitzky-Golay filter (2nd order, 9 points).

All measurements were performed at room temperature. The ultimate resolution of the instrument allows detecting objects with thickness of 50-100 nm and with a lateral resolution as small as the radius of the AFM tip. This minimal measurable thickness is defined by the minimal detectable photo-thermal expansion of the sample. On the other hand, the lateral

resolution of an isolated object is only limited by the sharpness of the AFM lever. In the case of non-isolated objects, thermal diffusion can limit lateral spatial resolution.

Principal Component Analysis

We performed the Principal Components Analysis (PCA) by means of the Non-linear Iterative Partial Least Squares (NIPALS) algorithm with *cross validation* and mean centered data, using Unscrambler 9.2 software (CAMO Norway). Analysis was performed on underivatized spectra and second derivatives. Second derivatives were calculated with Unscrambler 9.2 software using Savitzky–Golay algorithm for smoothing (2nd order, 9 smoothing points). The amide II region (1620 cm⁻¹–1480 cm⁻¹) was excluded from the analysis because of low signal to noise ratio in this spectral range, as mentioned earlier.

6.3 Results

6.3.1 Morphological properties of Josephin aggregates

First, we followed the amyloid aggregation of the Josephin by AFM at 0 days, 2 and 7 days of incubation at 37°, **Figure 6**, to set the scenario for further observations. At 0 days, spheroidal oligomeric species were present, with varying diameters from 3 to several hundreds of nanometers (**Figure 6.1A**). After 2 days, we could still observe a similar picture, but the oligomers lost their spheroidal shape (**Figure 6.1B**). At 7 days, there was massive formation of fibrillar aggregates (**Figure 6.1C**). The images showed fibrils entangling and forming supra-molecular rod-like aggregates of progressively increasing height and width (**Figure 6.1D-F**). Moreover, a quantitative analysis indicated a linear relationship between the height and the convoluted width of the fibrillar structures. This suggested that the supra-molecular rod-shaped aggregates derive from the association of the single amyloid fibrils with height of 10-15 nm.²⁸⁷

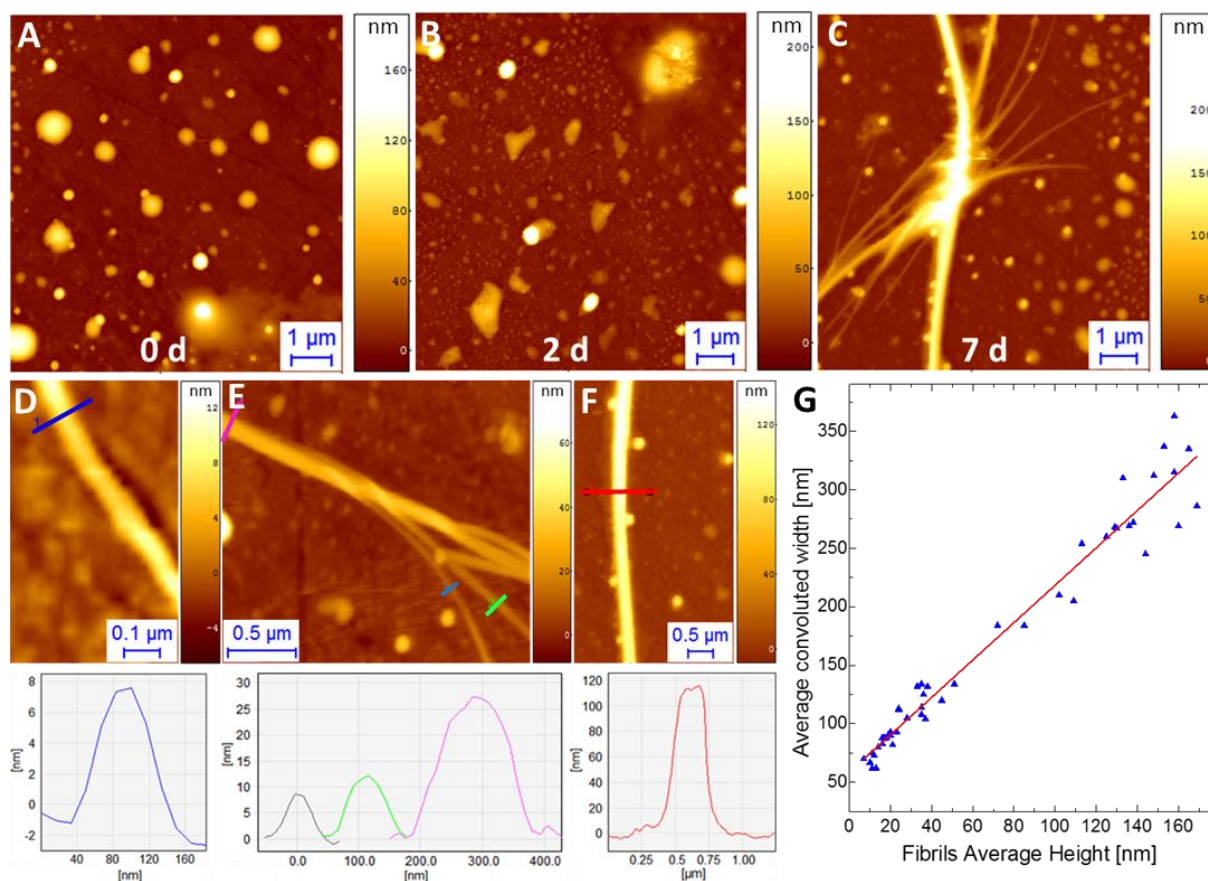


Figure 6.1 Josephin's aggregation and fibrillization process.

AFM morphology at A) 0 days, B) 2 days, C) 7 days of incubation at 37 °C. D) Smaller observable fibrils with height in the order of 10-15 nm. E) Entangling fibrils with different growing height. F) Supra-molecular aggregate with height of approximately 115 nm. G) Analysis of fibrillar morphology: fibrils average convoluted (see first chapter, **Fig. 1.14**) width as a function of height.

The smaller oligomeric species have an average height of 3-6 nm at 0 days (**Figure 6.2A**), of approximately 10 nm at 2 days (**Figure 6.2B**) and between 10-15 nm at 7 days (**Figure 6.2C**). A statistical analysis of the height of the smaller oligomeric species in the AFM maps confirmed that this parameter is increasing as a function of the incubation time (**Figure 6.2C-E**). Correspondingly, the smaller population of fibrils have an average height of ~10-15 nm (**Figure 6.2G**). In other words, at 7 days, the height of fibrillar structures corresponds to that of the oligomers, indicating that aggregation is following the usual process of oligomerization, in agreement with previous studies.¹⁵³

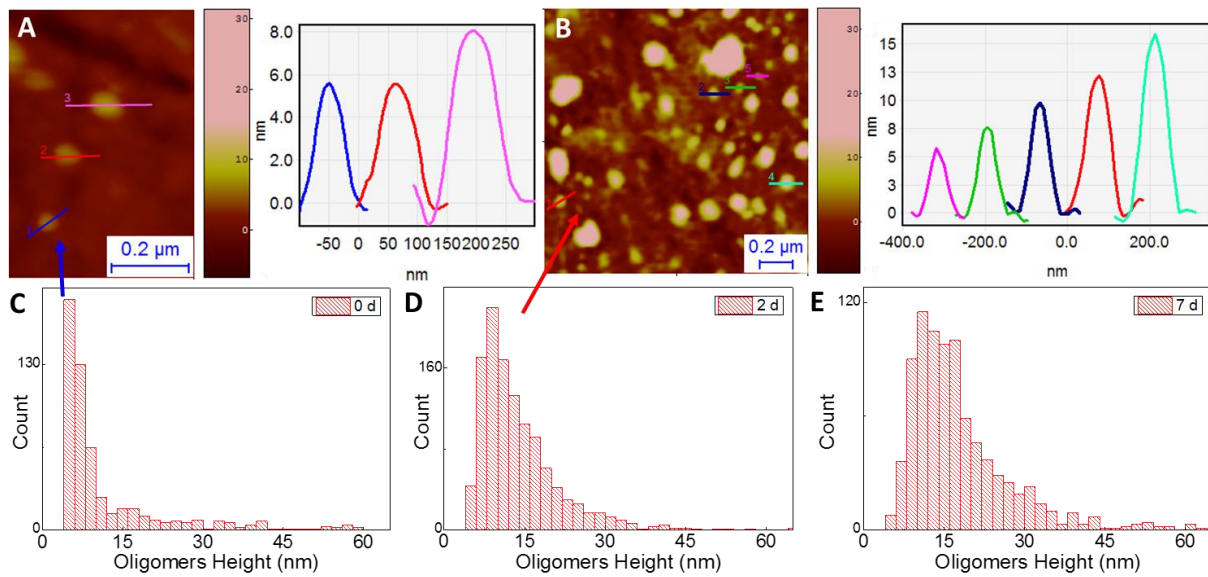


Figure 6.2 Morphological analysis of the oligomerization process.

A) AFM detail of the smaller oligomeric species at 0 days and relative cross-sectional dimensions. B) AFM detail of the smaller oligomeric species after 2 days of incubation and relative cross-sectional dimensions. C) Histogram distribution of the population of the smaller oligomers measured at 0 days, typical value of about 3-6 nm. D) Histogram of the height of the oligomers at 2 days, the typical value is about 10 nm. E) Histogram of the height of the oligomers at 7 days, the oligomeric population stabilized to approximately 10-15 nm height.

6.3.2 Nanomechanical properties of Josephin aggregates

To map the evolution of the nanomechanical properties of the Josephin aggregates, we used a fast force-volume system (Quantitative-Imaging - QI). We produced QI maps of the oligomeric (**Figure 6.3A,B**) and fibrillar (**Figure 6.3C**) structures. Before incubation, the spheroidal oligomers have a uniform Young's modulus of 450 ± 200 MPa (**Figure 6.3D**). This value is appreciably smaller than what expected for an amyloid structure.^{10,12,163} After 2 days of incubation, the sample did not have uniform mechanical properties any longer and two different populations were observed. The first showed stiffness similar to the previous time point (550 ± 170 MPa), while the latter showed a larger Young's modulus of 1.1 ± 0.5 GPa (**Figure 6.3E**), a value consistent with formation of a β -rich structure due to misfolding.^{46,288} The final fibrillar structures, after 7 days of incubation, had uniform stiffness of 1.9 ± 0.4 GPa (**Figure 6.3F**), in good agreement with the generally accepted value of stiffness of a mature and complete amyloid cross β -sheet structure.^{10,12,163}

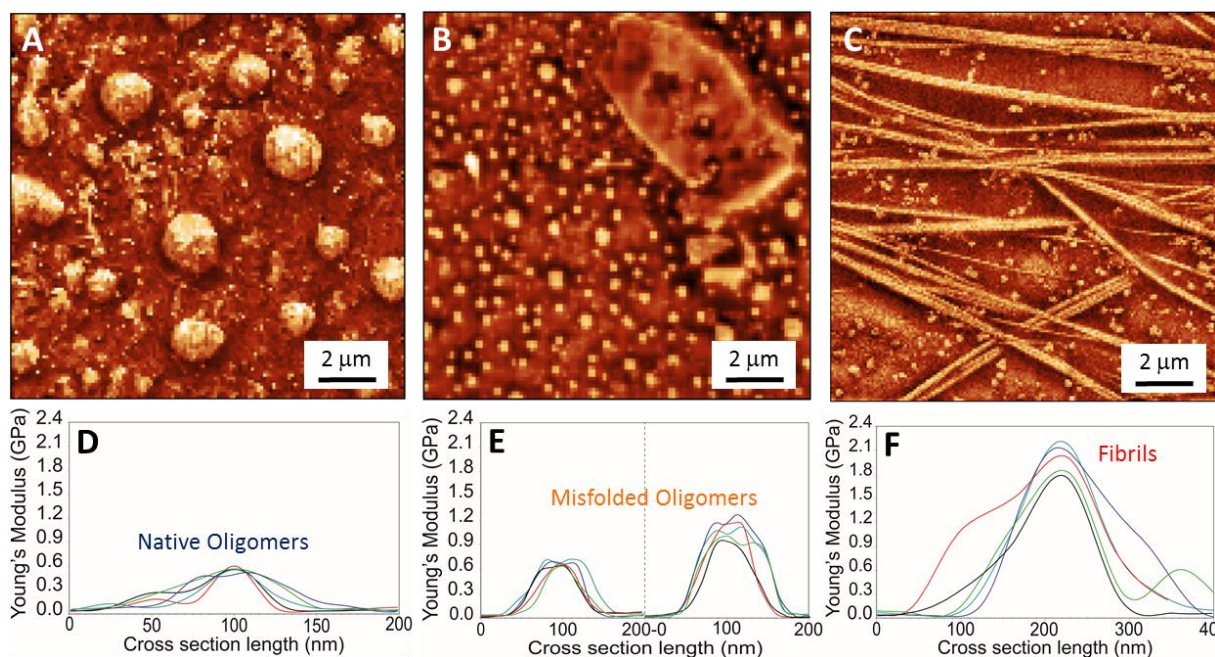


Figure 6.3 Young's modulus increases as a function of aggregation.

AFM Quantitative imaging of: A) Oligomeric proteins at 0 days, B) Oligomers after 2 days, C) Fibrillar structure after 7 days of incubation at 37 °C. Stiffness cross sections of D) oligomers at 0 days, E) oligomers at 2 days, F) fibrillar structures.

6.3.3 Infrared nanospectroscopy of Josephin amyloid species

AFM can only provide a morphologic description of the species formed during the aggregation pathway but does not tell us if/at which time point misfolding occurs nor what is the structure of the *individual* species. We thus used nanoIR to characterize further the aggregation pathway. This technique is of particular value when studying non homogeneous samples, such as amyloid aggregates, offering an important advancement as compared to conventional IR techniques which, like most spectroscopies, averages the structural information over the highly heterogeneous aggregating solution.

Native Oligomeric Species before incubation

We investigated the structural properties of Josephin, before incubation at 37 °C (**Figure 6.4 and 6.5**). The images show the morphology (**Figure 6.4 A**) and the absorption of IR light in the amide I (1700 cm^{-1} and 1655 cm^{-1} , **Figure 6.4 B,C**) and amide III (1300 cm^{-1} , **Figure 6.4D**) bands. From the comparison of the absorption maps and considering the components of

amide I band related to proteins secondary structure,¹⁸⁴ we can infer that the oligomers adsorb mainly IR radiation in the spectral region of the amide I band, related to α -helical and random coil conformations. These chemical absorption maps clearly indicated that the instrument could detect oligomeric structures with minimal average heights of approximately 50-100 nm.²⁸²

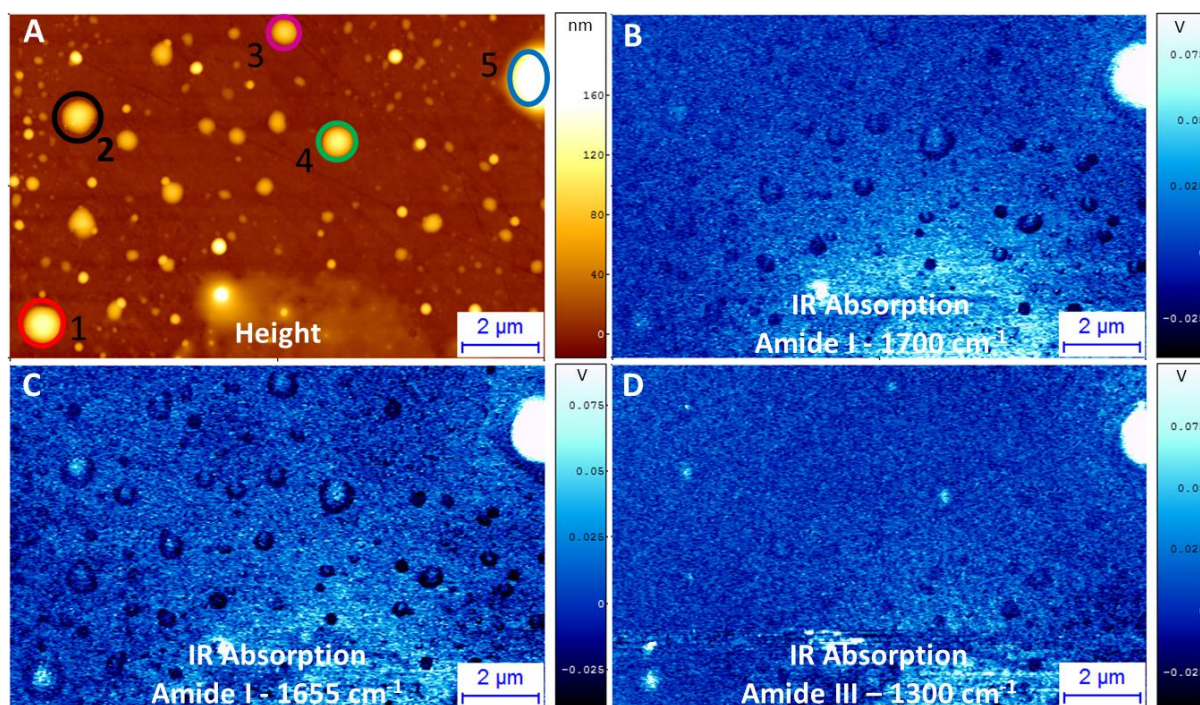


Figure 6.4 AFM-IR chemical map of Josephin proteins before incubation at 37 °C (0 days).

A) AFM height image. IR absorption map at: B) 1700 cm^{-1} (amide I). C) 1655 cm^{-1} (amide I). D) 1300 cm^{-1} (amide III).

To confirm quantitatively the trend of absorption shown by IR, we acquired spectra of *individual* oligomeric aggregates present on the surface (**Figure 6.5**). The spectra range investigated was between 1800-1200 cm^{-1} , where the amide band I, II and III of proteins are present. The nanoscale spectra acquisition was possible by positioning the AFM tip on each structure and collecting several spectra (minimum 10) inside their area, which is indicated in **Figure 6.4 A** by coloured circles. System sensitivity to the photothermal expansion allowed to acquire spectra of objects with thickness (height in the AFM map) as small as approximately 100 nm.^{210,211}

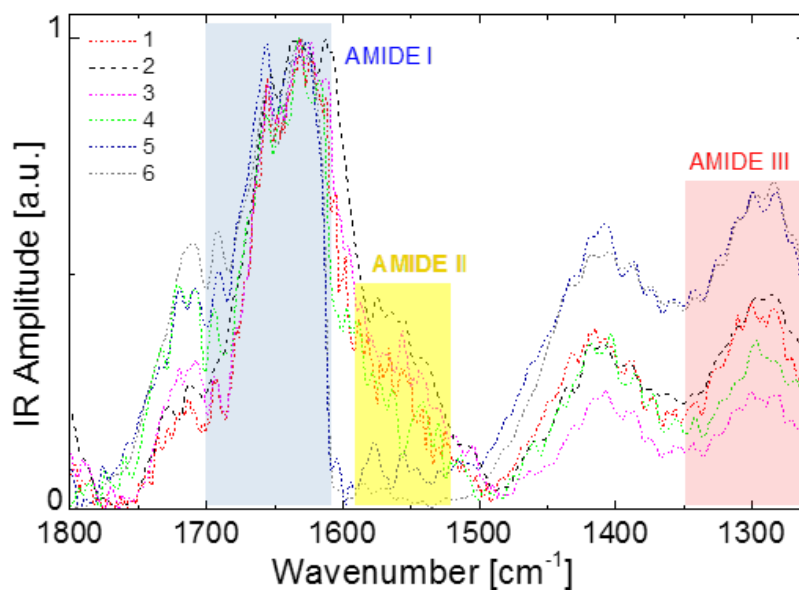


Figure 6.5 AFM-IR spectra of the oligomeric species before incubation.

Numbers in the caption correspond to the oligomers indicated in Figure 6.4. Spectrum number 6 derives from the measurement of an aggregate out of the presented image.

The comparison of these spectra shows that they have similar peak amplitudes and positions. The amide I band is approximately within 1655 cm^{-1} (α -helix) and 1620 cm^{-1} (β -sheet) and centred at $\sim 1630\text{-}1640\text{ cm}^{-1}$ (random coil) with a shoulder within $1720\text{-}1680\text{ cm}^{-1}$ (antiparallel β -sheets, β -turns and side chains vibrations). The position of the amide II band is approximately within $1590\text{-}1560\text{ cm}^{-1}$. However, it is worth to note that sensitivity of the instrument in the spectra region within $1610\text{-}1550\text{ cm}^{-1}$ is limited by the extremely low power and higher instability of the laser in this region, which causes signal instability and low signal-to-noise ratio (**Figure 6.6**). For this reason, in these region, the acquisition of chemical properties of objects with thickness close to the ultimate one (100 nm)^{210,211} is affected by noise and spectra deformation. The amide III band, centred at 1300 cm^{-1} , appeared to be coupled with a second peak, which is visible at $1410\text{-}1400\text{ cm}^{-1}$. This was already observed in our studies on lysozyme, where we observed a change of the relative ratio of the amplitude of this peak and the amide III band during the process of aggregation.²⁸² This peak can be attributed to a combination of COO^- , C-N, C-C stretching vibration, C-H and N-H bending, in plane O-H bending. A weaker contribution derives from the vibration of the glutamine (1410 cm^{-1}), glutamic acid (1404 cm^{-1}) and aspartic acid (1402 cm^{-1}) side chains.^{182,289}

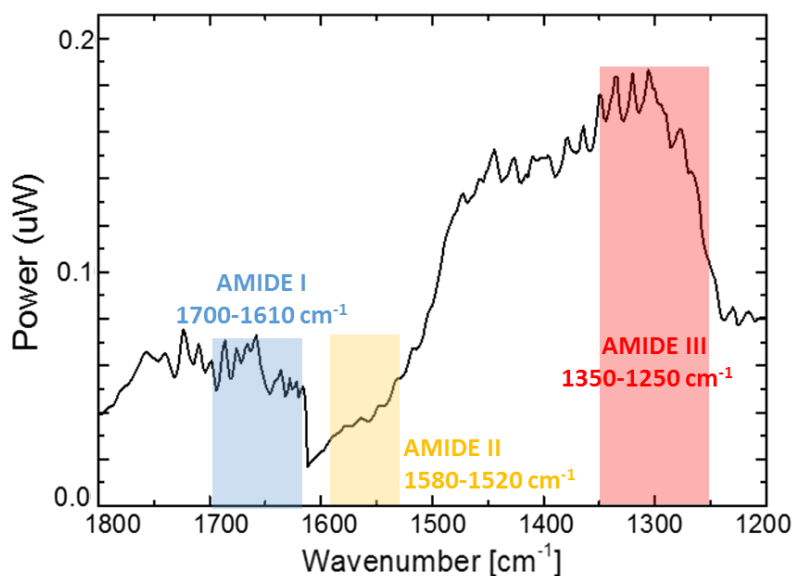


Figure 6.6 nanoIR laser's power spectrum.

Effective power of the laser at each wavenumber. The spectra are normalized in order to have constant laser power along all the investigated spectral region.

We estimated the secondary structure content of our Josephin uniform spheroidal intermediates before incubation at 37 °C by de-convolution of the amide I band of the spectrum of the uniform protein aggregates before incubation (**Figure 6.7**). The analysis was performed by XPSPEAK and a χ -squared of at least 0.001 was reached for the statistical significance of the fit. The shoulder of the spectrum around 1715-1725 cm^{-1} was fitted by considering the IR absorption peaks of the side chain vibrations of aspartic and glutamic acids.²⁹⁰ The addition of this band in the fit is easily explicable considering that these amino acids are relatively abundant in the Josephin structure (~15% of total composition, ~30% more abundant than in the average protein composition). Moreover, these residues have stronger absorbance coefficients than the average side chains absorption and they are not superimposed to any other secondary structure component of amide I band. Although the shape of the band is affected by the high noise between 1610 cm^{-1} and 1550 cm^{-1} , we could estimate a secondary structure content of 33% α -helix, 29% random coil, 23% β -sheet and 15% β -turn. These values are in excellent agreement with the monomeric structure of Josephin (35% α -helix, 29% random coil, 19% β -turn and 16% β -sheet).²⁸³ Thus, before incubation, proteins retain a native structure.

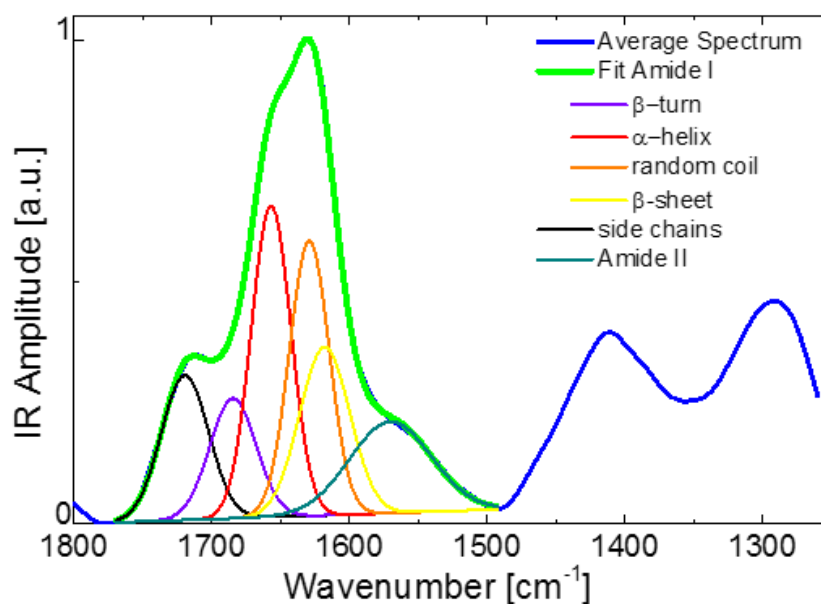


Figure 6.7 Average oligomeric IR spectrum and secondary structure de-convolution of amide I band.

As mentioned above, the ultimate resolution for spectra acquisition was a sample thickness of approximately 100 nm. Even if we could not acquire the IR spectra of objects with smaller height than 100 nm, the division of IR maps by the corresponding AFM height map allowed enhancing the visualization of differential response of the structures to different IR light excitation. In **Figure 6.8 A,B**, we focus our attention on several spheroidal oligomers with typical height of approximately 50-60 nm. Besides, we can observe the ratio maps resulting from the division of the IR absorption maps at 1655 cm^{-1} (**Figure 6.8 C**) and at 1300 cm^{-1} (**Figure 6.8 D**) by the corresponding morphology map (**Figure 6.8 A**). The comparison of the two ratio maps showed that it is possible to retrieve the spectroscopic behaviour of oligomeric species as small as 50-60 nm in height (for example oligomers 1 and 2 in **Figure 6.8 A,B**). Indeed, it is possible to observe that the spheroidal intermediates have higher absorption in the amide band I than in the amide band III, as already measured for the oligomeric species with bigger volume. This means that even if a full IR spectrum is not acquirable for such small objects, by functional imaging we can still retrieve the spectroscopic properties of objects as small as 50-60 nm in height.

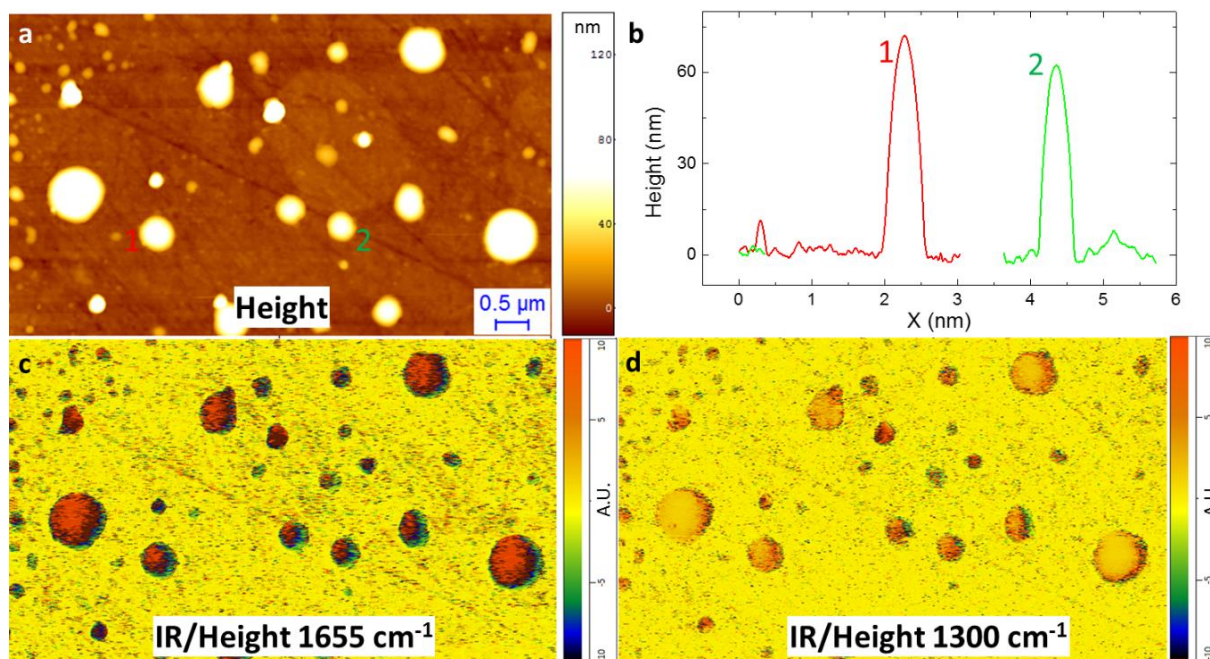


Figure 6.8 Smallest detectable structures by infrared nanospectroscopy.

AFM height. b) Height cross sections. IR absorption at c) 1655 cm^{-1} divided by height and at d) 1300 cm^{-1} divided by height.

Misfolded oligomeric species

We repeated the measurements after incubation for two days (**Figure 6.9**). As for the 0-day case, we collected the AFM morphology (**Figure 6.9 A**) and the IR absorption maps (**Figure 6.9 B,C**). At this time point, the IR absorption in the amide I spectral region, between 1700 cm^{-1} and 1655 cm^{-1} , remained approximately unchanged. Thus, we focused on the spheroidal structures present on the surface and acquired full IR spectrum (**Figure 6.9 D,E**). We could distinguish two different families of oligomeric structures. The amide I band of the first oligomeric species resonates at frequencies ($1655\text{-}1620\text{ cm}^{-1}$) similar to the values observed for the spheroidal oligomers observed before incubation. However, the band shows an increased absorption around 1700 cm^{-1} , which is consistent with an increased content of antiparallel β -sheet and β -strand. The shift of the amide I band is more dramatic for the second species, which shows two bands with maxima at 1700 cm^{-1} and 1640 cm^{-1} respectively, indicating the disappearance of the α -helical component and the increase of the antiparallel β -sheet content, as also supported by an inversion of the amplitude ratio between amide III band and the one at 1410 cm^{-1} .

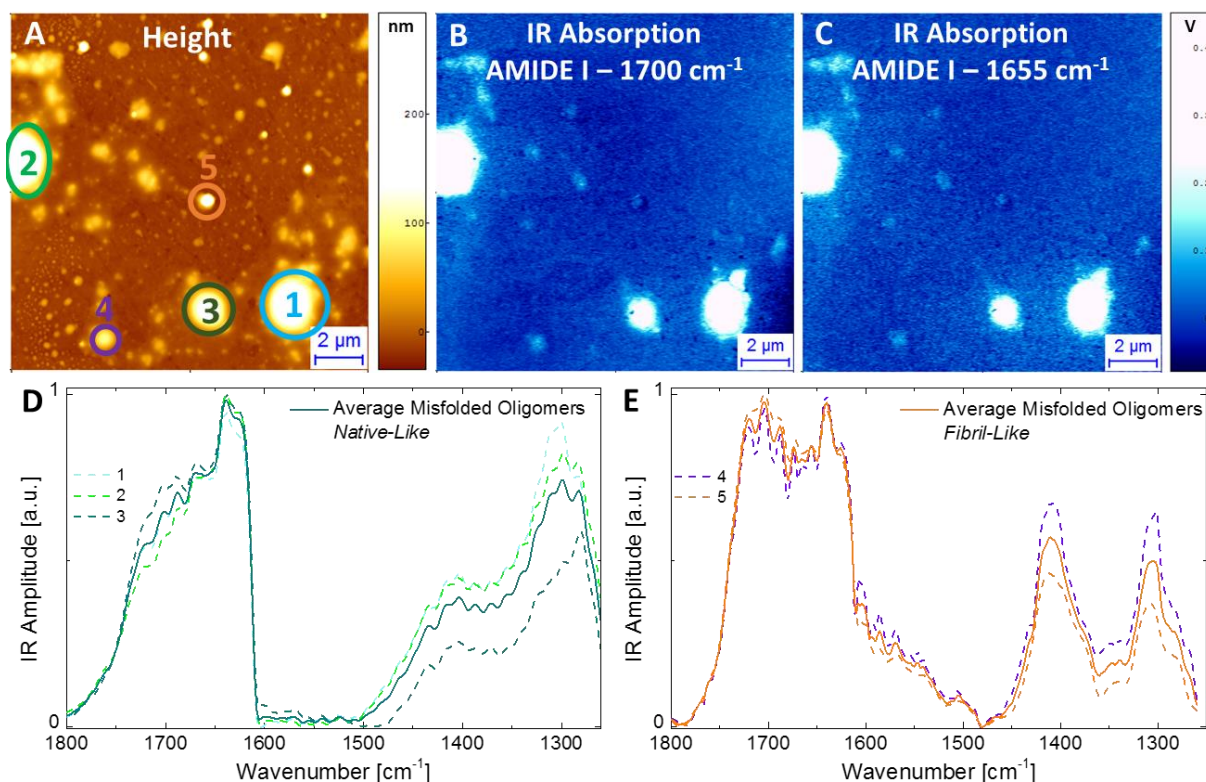


Figure 6.9 AFM and nanoIR analysis of oligomers at 2 days of incubation..

A) AFM height image. IR absorption in amide I band at B) 1700 cm^{-1} C) 1655 cm^{-1} . D) Spectra of misfolded oligomers, which are *monomers-like* with amide I similar to the monomeric structures. E) Spectra of misfolded oligomers, *fibrils-like* showing a conformational switch towards β -sheet structure.

Oligomeric and mature fibrillar species

After 7 days incubation, both oligomers and fibrils are present in the AFM images (**Figure 6.10 A**) with typical heights of 100-150 nm (**Figure 6.10 B**). Comparison of the absorption maps collected at the amide I band (**Figure 6.11 A,B**) and at the band around 1430 cm^{-1} (**Figure 6.11 C**), shows a clear difference between oligomers and fibrils. The first species has higher absorption in the α -helix component of the amide I band (1655 cm^{-1}). The latter have higher absorption close to the β -sheet and β -turn components (1700-1680 cm^{-1}) and at 1430 cm^{-1} . In other words, by performing absorption maps at different wavenumbers, we can clearly distinguish the structure of oligomers from that of fibrils through their different secondary structure content, which is causing differential response to IR light exposure. To prove the behaviour shown by the IR maps, we acquired spectra of *individual* oligomeric and fibrillar aggregates (**Figure 6.11 E,F**). Overall, the spectra of the fibrils are different from those of oligomers: they show a shift of the maximum of the amide I band at 1700 cm^{-1} and an inversion

of the amplitude ratio within the amide III band and the band around 1400 cm^{-1} , which has also a net shift towards higher wavenumbers ($\sim 1430\text{ cm}^{-1}$). This measurements showed that it is possible to distinguish structurally different amyloid species within the same AFM map.

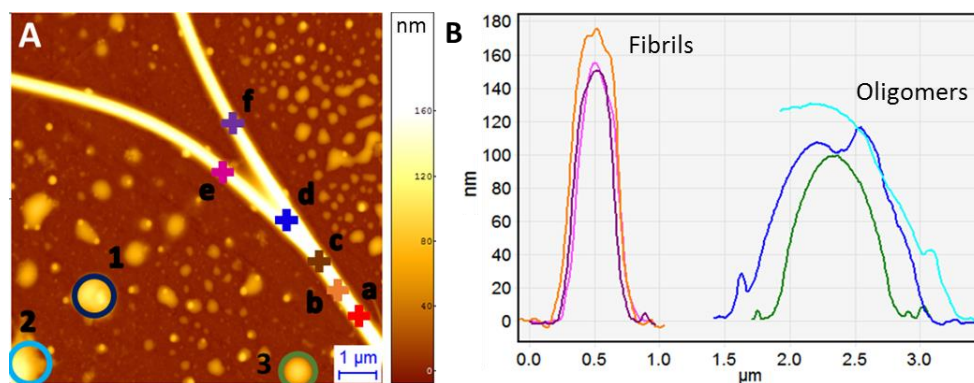


Figure 6.10 Morphological properties of aggregates after 7 days incubation.

A) AFM height. B) Height cross sections.

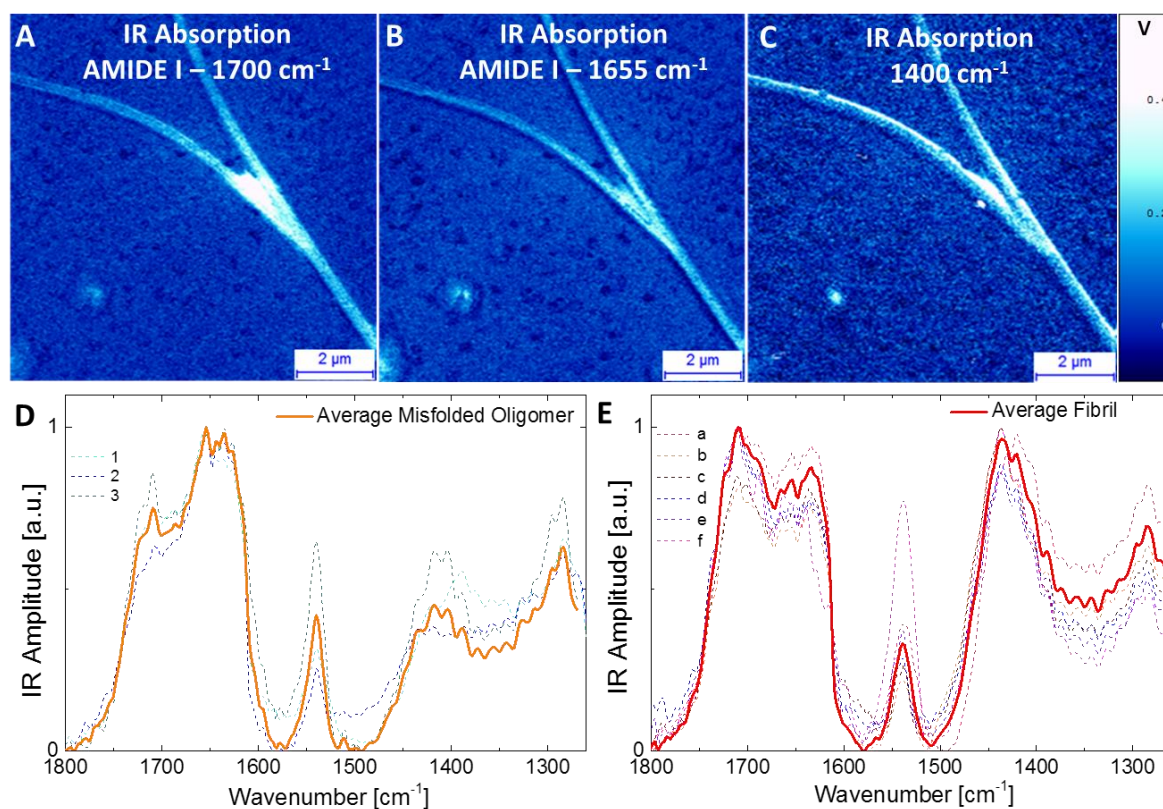


Figure 6.11 Spectra of oligomeric and fibrillar structures after 7 days incubation.

IR absorption maps at: A) 1700 cm^{-1} (amide I), B) 1655 cm^{-1} , (amide I) C) 1430 cm^{-1} . Spectra of amyloid structures: D) Misfolded oligomers (corresponding structures to the spectra are indicated by numbers in Figure 6.10), E) Fibrils (corresponding structures to the spectra are indicated by letters in Figure 6.10).

6.3.4 Spectral signature of amyloid structure formation

Finally, we performed Principal Components Analysis (PCA) to prove that the spectral differences measured between the different populations are statistically significant and to extract the spectral fingerprint of amyloid formation. PCA allowed noise reduction, resolution of subtle differences and detection of sub-groupings within the spectra. The most important results of PCA are the *Scores Plots* and the *Loadings Plots*. The *Scores Plots* represent the spectra in the multidimensional space of Principal Components, which represent the degree of variability within the ensemble of spectra. The *Loadings Plots* show which variables are responsible in the data set for the greatest degree of separation inside this spectra ensemble. The spectral differences are presented in the *Loadings Plots*. These determine clustering of spectra in the multidimensional *Scores Plots*. For the raw data, the maximum (minimum) of loading is related to the position of a particular vibrational motion, which is typical of the spectra clustered on the positive (negative) values of corresponding *Principal Component* (PC) on the *Scores Plot*.

The collected spectra are placed in the new space of the *Principal Components* (PCs). Thus, we can distinguish three distinct clusters, corresponding to three groups of aggregates: native oligomers, misfolded oligomers and amyloid fibrils (**Figure 6.12 A**). PC-1, which explains 50% of total variance within the ensemble of spectra (black in **Figure 6.12 B**), is positively correlated with the wavenumbers attributed to the amide I in spectral range from 1710 cm^{-1} to 1680 cm^{-1} , to the COO^- vibration around 1430 cm^{-1} and to the amide III at 1285 cm^{-1} (**Figure 6.12 B**). The *Scores Plot* shows that these three bands are positively correlated with the PC-1 scores for fibrils and, partially, for misfolded oligomers and negatively correlated with the PC-1 scores for native oligomers and partially for misfolded oligomers (**Figure 6.12 B**). This shows that the amide I band between 1655-1620 cm^{-1} and the amide III band at 1308 cm^{-1} are typical of these species. The PC-3, representing 10% of the total variance, clearly indicates a shift of the COO^- band. The PC-3 is positively correlated with the COO^- band at 1430 cm^{-1} (fibrils and partially misfolded oligomers) and negatively correlated with the band at 1412 cm^{-1} (native oligomers and partially misfolded oligomers).

This analysis confirms statistically that the shift of the amide I band from 1655-1620 cm^{-1} to 1710-1680 cm^{-1} , the peak at 1430 cm^{-1} and the shift of amide III band from 1308 cm^{-1} to 1295 cm^{-1} are markers (arrows in the *Loadings Plot*, **Figure 6.12B**) of the conformational transitions

from the random coil/ α -helical structure in native oligomers to β -turn/antiparallel β -sheet conformations in misfolded oligomers and final amyloids fibrils.

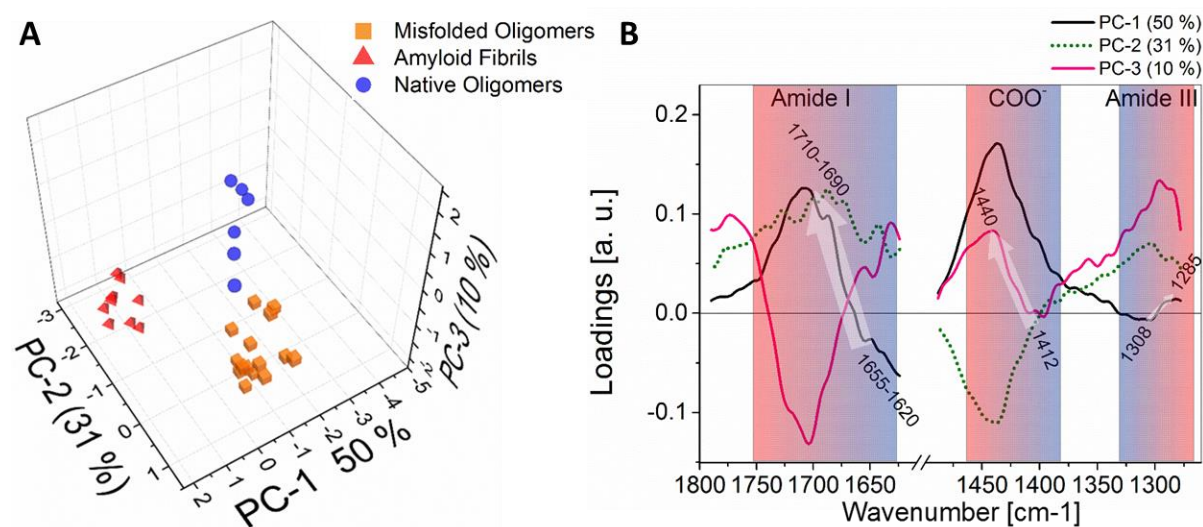


Figure 6.12 PCA analysis.

The results of PCA analysis in the spectral range $1800\text{ cm}^{-1} - 1270\text{ cm}^{-1}$ (excluding $1620\text{ cm}^{-1} - 1480\text{ cm}^{-1}$) applied to three groups of spectra: native oligomers, misfolded oligomers and fibrils. a) 3-D Scores Plot. b) Loadings Plot. The arrows indicate the fingerprint of the conformational changes during amyloid formation.

6.3.5 Correlation between nanomechanical and structural properties

The aggregation pathway of Josephin comprises species of large heterogeneity, as we confirmed by using different AFM based techniques. Morphology measurements showed that fibrillization follows the usual nucleation process of oligomerization. QI force volume indicated that the intrinsic stiffness of amyloidogenic species increases as a function of fibrillation maturity (**Figure 6.13 A**). A more direct answer on the structural changes that individual amyloid species undergo during aggregation was provided by coupling these results with infrared nanospectroscopy. The initial uniformity of the sample before incubation and the presence of two structurally different oligomeric species at 2 days are well in agreement with intrinsic stiffness measurements performed by QI. For both techniques, we observed two families of misfolded oligomers (**Figure 6.3 and 6.9**). The first has nanomechanical and structural properties similar to those of native oligomers, and we have denominated it *native-like*. The latter shows an increased stiffness and β -sheet content, and we called it *fibril-like*.

Finally, the system evolves into a uniform group of fibrillar structures exhibiting the stiffness values and β -sheet content typical of amyloids (Fig. 6.13 A,B).

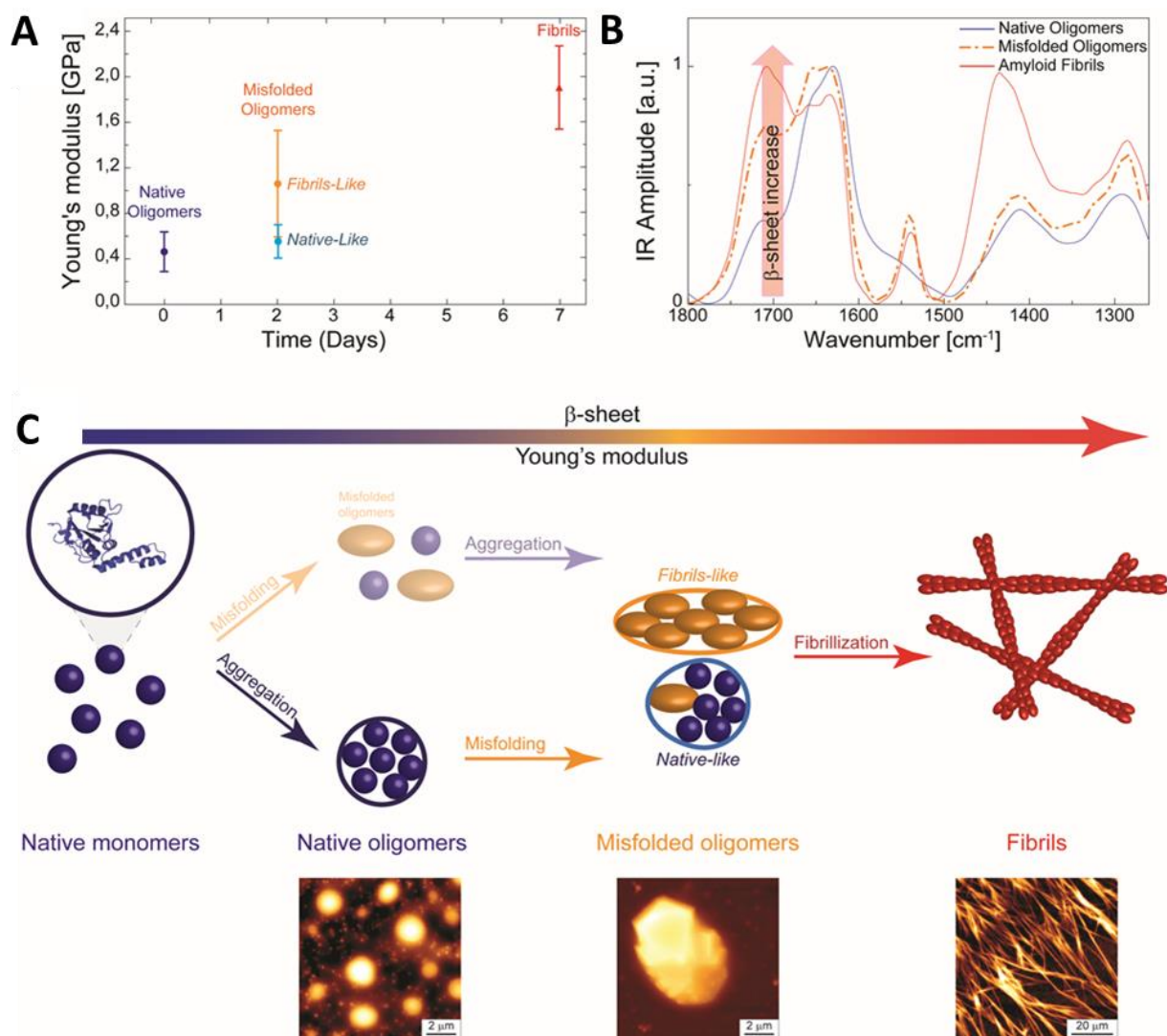


Figure 6.13 Model of the link between nanomechanical and structural properties.

A) Young's modulus increases as a function of fibrillization maturity. B) Spectra of native oligomers at 0 days (blue), misfolded oligomers at 7 days (orange) and amyloid fibrils at 7 days (red). The red arrow indicates the increase of content of β -sheets secondary structure. c) Model of the possible pathways of Josephin aggregation: the transparent model refers to the generally accepted model "first-misfolding-then-aggregation", the solid one depicts the model we suggest in this work, "first-aggregation-then-misfolding". In the lower part of the panel, to illustrate the steps of the fibrillization, we show representative AFM images collected at 0, 2 and 7 days.

6.4 Discussion

Characterization of all the species formed along the aggregation pathway of a protein is essential in view of the role that protein aggregation has in human health and in material science. In this work, we have investigated, for the first time at the nanoscale, the aggregation pathway of the Josephin domain of ataxin-3, a protein known to be highly fibrillogenic. We could observe directly the conformational transition from native spheroidal oligomers, through misfolded oligomers, to the final amyloid fibrils. We probed the secondary structure of the aggregates down to 50 nm and demonstrated that, before incubation, the secondary structure of Josephin inside the spheroidal oligomers is clearly native, while misfolding occurs only later, when a conformational transition towards β -enriched structure occurs. This indicates the intermediate nature of the oligomers, some sharing the structural properties of native monomers (*monomer-like*), the others being more similar to fibrils (*fibril-like*). The *fibril-like* oligomers form mature fibrils, which have a β -rich structure and mechanical properties typical of amyloids. This means that we can identify the spectral fingerprint of the α -to- β transition that native proteins undergo during fibrillization at the nanoscale.

In this way, we correlated the secondary structure of amyloid intermediates and final aggregates to their nanomechanical properties. Indeed, it is central to measure and quantify the ultrastructural properties of amyloid fibrils in order to appreciate their full potential as biomaterials. It was already suggested that the content of β -sheets in the aggregates during fibrillization process is an important parameter affecting the nanomechanical properties of these structures. AFM measurements and simulations suggested that the intermolecular interactions (e.g. hydrogen bonds) between β -sheet layers are responsible for the notable mechanical properties of amyloid fibrils.²³⁸⁻²⁴¹ Our results directly demonstrated, together with the nanomechanical measurements of amyloid structures showed in the fourth chapter,²⁹¹ for the first time at the *individual* amyloid species scale, that the increase of β -sheet content is a fundamental parameter determining the growth of amyloids intrinsic stiffness. Moreover, our evidence strongly suggests that Josephin aggregation precedes misfolding, indicating this protein as an example in which the assumption of ‘first-misfolding-and-then-aggregation’ may not be true.²⁹² This possibility is often assumed implicitly or explicitly, mainly because of the observation that misfolding of many globular proteins occurs only upon destabilization of the native fold. Such misfolding allows exposure of fibrillogenic sequences otherwise protected in the hydrophobic core. On the other hand, a different pathway to amyloid formation (‘first-

aggregation-and-then-misfolding') has been more recently identified, in which aggregation of normally globular proteins has been suggested to start from conformational states close to native ones, with no need of transitions across the major energy barrier for unfolding.²⁹³ Our conclusions agree with the evidence that Josephin aggregation is promoted by exposed hydrophobic patches, which have evolved to allow interaction with the non-pathologic cellular partner ubiquitin.

Infrared nanospectroscopy proved to be ideal for this study and to characterize *individually* the species formed along the aggregation pathway, which comprises species of large heterogeneity. We were able to reconstruct the aggregation process and to link nanomechanical and structural properties of *individual* amyloidogenic species throughout their fibrillization pathway. Conventional methods could not have provided this information with the same clarity. This is promising for the development of biomaterials for a broad spectrum of applications in food, nanotechnology and in medicine. Under this perspective, the use of nanoIR can have terrific applications and provide a unique tool to study the aggregation pathway of proteins and help us to design molecules that could interfere with amyloid aggregation.

Chapter 7. Conclusions and future perspectives

A key reason for the longstanding and widespread interest in the biophysical and biochemistry studies of amyloids fibrillation is the strict link with several human illnesses and neurodegenerative diseases. Despite its fundamental role in biological function and malfunction, the mechanism of protein aggregation and the fundamental origins of the connection between the aggregation process and cellular toxicity have remained challenging to elucidate in molecular detail. Strong evidence intimately correlated the physical and structural properties of intermediate and final forms of amyloids to the biochemistry of neurodegeneration. However, the molecular origins of the process of neurodegeneration and its connection with amyloid formation remain unclear and there is no cure to the related diseases. Therefore, the unraveling of the mechanisms of amyloid formation and polymorphism, as well as the mechanical and structural properties of the products of their aggregation is fundamental to understand their stability, toxicity and mechanism of clearance in the body. This is central in order to design new therapeutic strategies to the diseases problem. Furthermore, it has been recently found that it exists an always-bigger class of *functional* amyloids occurring naturally in several disease-unrelated biological processes and that many artificial peptides can form amyloid-like structures *in-vitro*. For this reason, in order to appreciate the full potential of amyloid fibrils also as biomaterials for future biomedical and nanotechnology applications, it is important to measure and quantify the structural and mechanical properties of amyloid fibrils and understand how they emerge from the fibrillization process.

In the frame of this PhD thesis, we have been able to bring new insight into the nanoscale investigation of several specific aspects of the amyloid fibrillation process and of the structural properties of the products of the aggregation. We challenged this problem by the use of single molecule AFM-based methodologies. Together with conventional AFM imaging, we reported the successful application of nanomechanical mapping (PF-QNM) to inquire the nature of the notable intrinsic stiffness of amyloids and we reported the first application of infrared nanospectroscopy to elucidate proteins misfolding and amyloid species ultrastructural properties at the single aggregate scale. These studies led to new insights into the problem of biophysical investigation of amyloid formation and structure, which enabled us formulating the following conclusions:

- **Proteins mutations can enhance/inhibit the kinetics of oligomerization and fibrillization.**

A statistical analysis of oligomeric, protofibrillar and fibrillar cross-sectional dimensions has been successfully applied to compare the kinetics of wild type and mutated forms of α -synuclein and huntingtin proteins. In the first case, it was demonstrated the link between a sequence mutation (H50Q) in α -synuclein, enhancing aggregation propensity, and Parkinson's disease onset. In the latter, it was investigated the effects of post-translational mutations, and in particular of the N-terminus phosphorylation, in the fibrillization kinetics of the huntingtin protein. We showed that phosphorylation of the protein conspicuously slowed down the oligomerization and fibrillization process. Elucidating the role of mutations is fundamental to investigate both physiological and disease related functions of proteins.

- **The early stages of α -synuclein aggregation proceed directly through the assembly of monomers into single monomeric strands amyloid species.**

Scanning probe analyses are routinely limited to the use of only one substrate and this procedure produces just a partial depiction of the extremely heterogeneous aggregating solution. In our work, the use of three different surfaces of deposition with different state of charge (positive, negative, hydrophobic) allowed to overcome the problem of surface selectivity, to inquire deeply amyloids polymorphism and to have a complete representation of the heterogeneity of the aggregating amyloid solution. Thus, we investigated the *slow* and *fast* aggregation process of α -synuclein by means of the differential surface-protein absorption method. We showed that their early aggregation stages did not follow the classical oligomers-nucleated process. More specifically, we were able to highlight that the first stages of amyloid formation comes from direct assembling of unfolded monomers into prefibrillar species, which further hierarchically assembly into the mature fibrils. Remarkably, this behavior is independent on pH and the agitation of the sample during incubation. This new mechanism of fibril formation might bring new insights to the problem of neurodegeneration. Indeed the discovered new monomeric prefibrillar species could be the species ascribed to toxicity.

- **The β -sheet content determines the mechanical properties of amyloid species during aggregation.**

We observed a monotonic evolution of the elastic modulus of amyloid species of α -synuclein and A β 42, as a function of sample fibrillization and incubation maturity, by means of the innovative PF-QNM method. Coupling this study with secondary structure bulk measurements, we could conclude that the increase of stiffness is strictly linked to the improving of β -sheet structural ordering and of intermolecular hydrogen bonds into aggregates during the process of aggregation. Notably, the different elastic modulus between monomeric, protofibrillar and fibrillar structure could be strictly linked to their toxicity. Finally, the understanding of amyloid mechanical properties would be fundamental for the development of new amyloid bioengineered materials.

- **Infrared nanospectroscopy allows studying amyloid misfolding and structure at the nanoscale.**

AFM-based infrared spectroscopy allowed studying amyloids ultrastructural properties at the nanoscale with astonishing resolution. The obtained results promise notable advances for the comprehension of the pathway of fibrils formation and for the studying of amyloid polymorphism. Initially, as proof of concept, the technique was applied to investigate structural differences in the IR spectra of monomeric and aggregated lysozyme from single μ -droplets with picolitre volume. In particular, the shift of the amide I band toward lower wavenumbers allowed identifying an α -to- β structure transition associated with amyloid formation. Successively, we applied nanoIR to measure the properties of the several species present in the heterogeneous aggregation solution at the nanoscale. We could reconstruct the conformational changes that the Josephin domain of ataxin-3 undergoes during aggregation. In particular, coupling these studies with parallel nanomechanical measurements, we could link mechanical and structural properties of oligomers and fibrils at the *individual* nanoscale aggregate scale. Furthermore, the recent improvements in the nanoIR technique could allow measuring directly at single molecule scale the misfolding of monomers and the conformational changes of proteins during their aggregation.

These specific studies and conclusions brought new insights into the problem of protein self-assembling. Notwithstanding the usefulness of this information, several general scientific questions, whose answer is fundamental to address successfully the problem of misfolding diseases, are still open:

- a) *Which is the main pathway of fibrillation process? Do amyloid fibrils generally form directly from naturally unfolded monomers association? Could oligomers be always off-pathway with respect to the formation of mature fibrils?*
- b) *Would it be possible to have direct information at the single molecule level on the link between elastic and structural properties of amyloids at the single molecule scale?*
- c) *Which are the structural properties of the different amyloidogenic structures?*

In order to answer these questions, we believe the idea that bridging together bulk and single molecule techniques has central importance. Consequently, we have already planned some future studies to inquire these questions. First, an extensive application, for different amyloid proteins, of differential surface-protein absorption effect in combination with bulk techniques, such as ThioflavinT and Circular Dichroism, and an advanced application of statistical theory of biopolymers could bring new information to understand the general pathway of amyloid formation. The possibility of successfully measuring at the single molecule scale the secondary structure of amyloid species has been achieved by exploiting quantum cascade lasers, which have allowed a 10-fold improvement in the sensitivity of infrared spectroscopy (nanoIR2, Anasys Instruments) , allowing measurements of IR spectra of single molecules. Preliminary measurements already enabled to inquire the secondary structure of single amyloid fibrils. Furthermore, the ability to study spectroscopically the contents of single microdroplets individually with a high-precision method opens up the possibility for a wide range of experiments benefiting from the unique advantages of microfluidics. We would like to pursue in the future two key experiments. In the first, we aim to combine nanoIR with microfluidic on-chip selection techniques and pre-screening for a predefined species within droplets for a high-throughput investigation of protein aggregation evolution. In the latter, we would apply nanoIR to investigate directly liquid phase separation in concentrated protein solutions and its effect on amyloid formation. Together with mechanical and structural analysis

of the micro-gel, this could bring direct information between mechanical and structural properties of amyloids.

We believe that the development of new biophysical methodologies, which are able to bridge together the investigation of morphological and ultrastructural properties of amyloid at the nanoscale, represents a fruitful avenue to address the challenge of solving the problem of protein self-assembly, to unravel monomer misfolding and to elucidate the molecular mechanisms of amyloid polymorphism and formation. Such a molecular level understanding of the key pathogenic processes is crucial in order to provide the basis to answer the proposed above scientific questions. Their elucidation would be fundamental for establishing rational approaches to the prevention and to the design of pharmacological approaches to combat amyloid-related diseases.

CURRICULUM VITAE - FRANCESCO SIMONE RUGGERI

Swiss Federal Institute of Technology (EPFL), Laboratory of the Physics of Living Matter, CH-1015, Lausanne

Telephone +41 21 69 30461, +41787969574

E-mail **simone.ruggeri@epfl.ch**

Nationality Italian

EDUCATION AND RESEARCH EXPERIENCE

- Title **PhD in Physics (ongoing)**
- Institute **Swiss Federal Institute of Technology of Lausanne (EPFL)**
- Dates *2011- Nowadays*
- Subject of the Thesis The thesis is focused on the biophysical characterization of proteins aggregation towards amyloids fibrillar structures. This process is central in the onset of several human diseases as Parkinson's and Alzheimer's. The use of AFM is essential to unravel the morphological properties of amyloids. While a new scanning probe technique (nanoIR), combination of AFM and Infrared Spectroscopy, is used for chemical characterization of amyloids at the nanometer single aggregate scale. This work is supervised by Prof. Giovanni Dietler.
- Collaborations The Project is conducted in collaboration with several groups of research, held by: Prof. H. Lashuel (EPFL, Lausanne), Prof. R. Mezzenga (ETH, Zurich), Prof. Annalisa Pastore (King's College, London), Prof. Tuomas Knowles (University of Cambridge) and Prof. Yves Jacquot (École normale supérieure, Paris).
- Publications **Ruggeri FS***, Adamcik J, Jeong JS, Lashuel HA, Mezzenga R, Dietler G (2015) Influence of the beta-Sheet Content on the Mechanical Properties of Aggregates during Amyloid Fibrillization. *Angewandte Chemie International Edition*. DOI: 10.1002/anie.201409050
Ruggeri FS*, Byrne C, Khemtouri L, Ducouret G, Dietler G, Jacquot Y (2015) Concentration-dependent and surface-assisted self-assembly properties of a bioactive estrogen receptor alpha-derived peptide. *Journal of peptide science*. 21: 95-104
Muller T*, **Ruggeri FS***, Kulik AJ, Shimanovich U, Mason TO, Knowles TPJ, Dietler G (2014) Nanoscale spatially resolved infrared spectra from single microdroplets. *Lab on a Chip* 14: 1315-1319 (Muller T and Ruggeri FS equally contributed to this work.)

- Kasas S, **Ruggeri FS***, Benadiba C, Maillard C, Stupar P, Tournu H, Dietler G, Longo G (2015) Detecting nanoscale vibrations as signature of life. *Proceedings of the National Academy of Sciences of the United States of America* 112: 378-381
- Ansaloni A, Wang Z-M, Jeong JS, **Ruggeri FS***, Dietler G, Lashuel HA (2014) One-Pot Semisynthesis of Exon 1 of the Huntingtin Protein: New Tools for Elucidating the Role of Posttranslational Modifications in the Pathogenesis of Huntington's Disease. *Angewandte Chemie-International Edition* 53: 1928-1933
- Khalaf O, Fauvet B, Oueslati A, Dikiy I, Mahul-Mellier AL, **Ruggeri FS***, Mbefo MK, Vercruysse F, Dietler G, Lee SJ, Eliezer D, Lashuel HA (2014) The H50Q mutation enhances alpha-synuclein aggregation, secretion, and toxicity. *Journal Biological Chemistry* 289: 21856-21876
- Adamcik J, Lara C, Usov I, Jeong JS, **Ruggeri FS***, Dietler G, Lashuel HA, Hamley IW, Mezzenga R (2012) Measurement of intrinsic properties of amyloid fibrils by the peak force QNM method. *Nanoscale* 4: 4426
- Crupi I, **Ruggeri FS***, Grasso A, Ruffino F, Catania G, Piro AM, Di Marco S, Mirabella S, Simone F, Priolo F (2012) Influence of the electro-optical properties of an α -Si:H single layer on the performances of a pin solar cell. *Thin Solid Films* 520: 4036-4040
- Publications Submitted/ In Submission
 - F S Ruggeri***, S Faggio, E Lipiec, A Pastore, G Dietler, *Nano-IR as a new tool to follow the aggregation pathway of proteins: A nanoscale Structural analysis of the Josephin domain aggregation.* In revision in *Nature Communications*.
 - F. S. Ruggeri***, F. Benedetti , Hilal Lashuel , S. Sekatsky, G. Dietler, *Nanomechanical Manipulation of Amyloid Protofilaments of α -synuclein and Measuring of their Interaction Force with Surface.* In revision in *Journal of Biological Chemistry*.
 - Awards
 - Best Poster Presentation Award at the Swiss Physical Society, 2014.
 - Title
 - Master Degree in Physics, 110/110 summa cum laude.**
 - Institute
 - University of Catania, Italy.**
 - Dates
 - 2007-2010
 - Principal subjects
 - Solid State Physics. The degree focused on properties of condensed matter and Material Science, with special attention to: Semiconductors, Nanostructures and Photovoltaic Technology.
 - Thesis
 - "Hydrogenated amorphous silicon characterization for thin film solar cells optimization"*. The electrical and optical properties of the material and the related improvement in the quantum efficiency of a diode pin solar cell were extensively studied. This work was supervised by Prof. F. Priolo and
 - Collaboration
 - This work has been made in collaboration with ST Microelectronics.

- Publications I. Crupi, **F. S. Ruggeri**, A. Grasso, F. Ruffino, G. Catania, A. M. Piro, S. Di Marco, S. Mirabella, F. Simone, F. Priolo, *Influence of the electro-optical properties of an α -Si:H single layer on the performances of a pin solar cell*, *Thin Solid Films*, **2012**, 520, 4036-4040.
 - Title **Bachelor Degree in Physics, 110/110 summa cum Laude.**
 - Institute **University of Catania, Italy.**
 - Dates 2004-2007
 - Thesis “The lower limit of photon mass and its implications”. A study of the Proca theory on the electromagnetic field. The theory is based on the hypothesis that photons have mass. The several consequences of the theory, as dispersion of light in vacuum and reformulation of the second principle of relativity, were explored. This work was supervised by Prof. Giuseppe Russo.
 - Experimental Work Characterization of the response of a dosimetry film for radiotherapy applications.
 - Dates and Place 06-07/2009, University of Catania, Italy.
 - Experimental Work Ion Implantation on Silicon and Germanium. Analysis of doping profiles as a function of the energy of incident ion by Rutherford Backscattering technique.
 - Dates and Place 02-05/2009, University of Catania, Italy.
-

RELEVANT SKILLS

- LANGUAGES** Italian: Mother Tongue, English: Fluent, French: Good oral skills.
- EXPERIMENTAL METHODS AND TECHNIQUES** Expert in the use of the following techniques: Atomic Force Microscopy Imaging, Force spectroscopy and Infrared Spectroscopy combined technique (nanoIR); Circular Dichroism; Dynamic Light Scattering; Fluorescence microscopy; UV-vis spectroscopy; Electrical characterization of thin films; nanomechanical oscillator systems to characterize biological living samples as cells and bacteria; *In Vitro* fibrillation assays of proteins; surfaces and tip chemical functionalization.
- SOFTWARE AND PROGRAMMING SKILLS** Advanced user of images processing programs as SPIP (Image Metrology), ImageJ, Gwiddion and Dnatrace. Advanced user of C language. Advanced competences with data analysis software like Origin Pro, Matlab, Mathematica and Fitpeak. Good knowledge of Photoshop, CorelDraw and Blender.
- TEACHING** Teaching assistant, both in French and English, at the EPFL of: General Physics for Students of Biology and Chemistry; Thermodynamics for students of Physics.

ORGANIZATIONAL AND ADMINISTRATIVE	Treasurer of the association of students for the promotion of Italian culture in Switzerland, "Italaus". Co-founder of the theatre group of the EPFL " <i>Pourquoi Pas?</i> ". Representative of the students during High school.
OTHERS: SPORT	National level athlete in 400 meters with hurdles for 14 years.

CONFERENCES

- 07-2014, **oral contribution**, Protein Folding Conference, Punta Cana (Dominican Republic): "**Amyloid nanoscale chemical analysis by AFM Infrared Spectroscopy**".
- 07-2014, Poster Contribution, Swiss Physical Society, Fribourg (Switzerland): "AFM nanoscale Infrared spectroscopy: Chemical Characterization at single molecule amyloid Scale".
- 05-2014, **oral contribution**, 11th Annual International Workshop on Nanomechanical Sensing, Madrid (Spain): "**Characterizing neuroblastomas Cells exposed to α -synuclein amyloids**".
- 02-2014, poster contribution, Biophysical Conference, San Francisco (USA): "AFM nanoscale Infrared spectroscopy: Bridging to Amyloid Single Molecule Chemical Characterization".
- 09-2013, poster contribution, Soft Matter Conference, Rome (Italy): "Study of In-vitro Amyloid Fibrils, oligomers and monomeric state of α -synuclein by Single Molecule Statistical Analysis".
- 03-2013, **oral contribution**, Swiss Soft day, Zurich (Switzerland): "**Study of the early stage of amyloids fibrils formation in α -synuclein by AFM Single Molecule Statistical Analysis**".
- 02-2013, **oral contribution**, Advances in single molecule research for biology and nanoscience, Linz (Austria): "**Study of the early stage of amyloids fibrils formation in α -synuclein by AFM Single Molecule Statistical Analysis**".
- 01-2013, Winter School, From Fundamentals to Applications in Life Science, Kandersteg (Switzerland).
- 02-2012, Winter School, Advances in single molecule research for biology and nanoscience, Linz (Austria).
- 01-2012, Winter School, Cellular Biophysics: Molecules, Membranes and Mechanics, Ascona, (Switzerland).
- 08-2011, Conference, Amyloid Fibrils, Prions and Precursors: Molecules for Targeted Intervention, Halle (Germany).

Bibliography

- 1 Hardy, J. & Selkoe, D. J. The amyloid hypothesis of Alzheimer's disease: progress and problems on the road to therapeutics. *Science* **297**, 353-356, doi:10.1126/science.1072994 (2002).
- 2 Goedert, M. Familial Parkinson's disease. The awakening of alpha-synuclein. *Nature* **388**, 232-233 (1997).
- 3 Zoghbi, H. Y. & Orr, H. T. Glutamine repeats and neurodegeneration. *Annu Rev Neurosci* **23**, 217-247, doi:10.1146/annurev.neuro.23.1.217 (2000).
- 4 Chiti, F. & Dobson, C. M. Protein misfolding, functional amyloid, and human disease. *Annual review of biochemistry* **75**, 333-366 (2006).
- 5 Chapman, M. R. *et al.* Role of Escherichia coli Curli Operons in Directing Amyloid Fiber Formation. *Science* **295**, 851-855 (2002).
- 6 Fowler, D. M., Koulov, A. V., Balch, W. E. & Kelly, J. W. Functional amyloid – from bacteria to humans. *Trends in Biochemical Sciences* **32**, 217-224, doi:10.1016/j.tibs.2007.03.003 (2007).
- 7 Shewmaker, F., McGlinchey, R. P. & Wickner, R. B. Structural Insights into Functional and Pathological Amyloid. *Journal of Biological Chemistry*, doi:10.1074/jbc.R111.227108 (2011).
- 8 Sunde, M. *et al.* Common core structure of amyloid fibrils by synchrotron X-ray diffraction. *Journal of Molecular Biology* **273**, 729-739, doi:<http://dx.doi.org/10.1006/jmbi.1997.1348> (1997).
- 9 Fitzpatrick, A. W. *et al.* Atomic structure and hierarchical assembly of a cross-beta amyloid fibril. *Proc Natl Acad Sci USA* **110**, 5468-5473, doi:10.1073/pnas.1219476110 (2013).
- 10 Smith, J. F., Knowles, T. P., Dobson, C. M., MacPhee, C. E. & Welland, M. E. Characterization of the nanoscale properties of individual amyloid fibrils. *Proceedings of the National Academy of Sciences* **103**, 15806-15811 (2006).
- 11 Knowles, T. P. *et al.* Role of Intermolecular Forces in Defining Material Properties of Protein Nanofibrils. *Science* **318**, 1900-1903 (2007).
- 12 Knowles, T. P. & Buehler, M. J. Nanomechanics of functional and pathological amyloid materials. *Nat Nanotechnol* **6**, 469-479, doi:10.1038/nnano.2011.102 (2011).
- 13 Rambaran, R. N. & Serpell, L. C. Amyloid fibrils: Abnormal protein assembly. *Prion* **2**, 112-117 (2008).
- 14 Sipe, J. D. & Cohen, A. S. Review: history of the amyloid fibril. *J Struct Biol* **130**, 88-98, doi:10.1006/jsbi.2000.4221 (2000).
- 15 Sipe, J. D. Amyloidosis. *Annu Rev Biochem* **61**, 947-975, doi:10.1146/annurev.bi.61.070192.004503 (1992).
- 16 Elghetany, M. T., Saleem, A. & Barr, K. The congo red stain revisited. *Annals of clinical and laboratory science* **19**, 190-195 (1989).
- 17 Rogers, D. R. SCREENING FOR AMYLOID WITH THIOFLAVIN-T FLUORESCENT METHOD. *American Journal of Clinical Pathology* **44**, 59-& (1965).
- 18 Levine, H. THIOFLAVINE-T INTERACTION WITH SYNTHETIC ALZHEIMERS-DISEASE BETA-AMYLOID PEPTIDES - DETECTION OF AMYLOID AGGREGATION IN SOLUTION. *Protein Science* **2**, 404-410 (1993).
- 19 Cohen, A. S. & Calkins, E. ELECTRON MICROSCOPIC OBSERVATIONS ON A FIBROUS COMPONENT IN AMYLOID OF DIVERSE ORIGINS. *Nature* **183**, 1202-1203, doi:10.1038/1831202a0 (1959).
- 20 Eanes, E. D. & Glenner, G. G. X-RAY DIFFRACTION STUDIES ON AMYLOID FILAMENTS. *J. Histochem. Cytochem.* **16**, 673-& (1968).
- 21 Glenner, G. G. & Wong, C. W. ALZHEIMERS-DISEASE - INITIAL REPORT OF THE PURIFICATION AND CHARACTERIZATION OF A NOVEL CEREBROVASCULAR AMYLOID PROTEIN. *Biochemical*

- and *Biophysical Research Communications* **120**, 885-890, doi:10.1016/s0006-291x(84)80190-4 (1984).
- 22 Prusiner, S. B. NOVEL PROTEINACEOUS INFECTIOUS PARTICLES CAUSE SCRAPIE. *Science* **216**, 136-144, doi:10.1126/science.6801762 (1982).
- 23 Prusiner, S. B. Prions. *Proceedings of the National Academy of Sciences of the United States of America* **95**, 13363-13383, doi:10.1073/pnas.95.23.13363 (1998).
- 24 Greenwald, J., Rol, Riek & Riek, R. Biology of Amyloid: Structure, Function, and Regulation. *Structure* **18**, 1244-1260 (2010).
- 25 Makin, O. S., Atkins, E., Sikorski, P., Johansson, J. & Serpell, L. C. Molecular basis for amyloid fibril formation and stability. *Proc Natl Acad Sci U S A* **102**, 315-320, doi:10.1073/pnas.0406847102 (2005).
- 26 Fändrich, M. On the structural definition of amyloid fibrils and other polypeptide aggregates. *Cell. Mol. Life Sci.* **64**, 2066-2078, doi:10.1007/s00018-007-7110-2 (2007).
- 27 Knowles, T. P. J., Vendruscolo, M. & Dobson, C. M. The amyloid state and its association with protein misfolding diseases. *Nat Rev Mol Cell Biol* **15**, 384-396, doi:10.1038/nrm3810 (2014).
- 28 Fändrich, M. & Dobson, C. M. The behaviour of polyamino acids reveals an inverse side chain effect in amyloid structure formation. *The EMBO Journal* **21**, 5682-5690, doi:10.1093/emboj/cdf573 (2002).
- 29 Lührs, T. *et al.* 3D structure of Alzheimer's amyloid- β (1-42) fibrils. *Proceedings of the National Academy of Sciences of the United States of America* **102**, 17342-17347, doi:10.1073/pnas.0506723102 (2005).
- 30 Petkova, A. T. *et al.* A structural model for Alzheimer's β -amyloid fibrils based on experimental constraints from solid state NMR. *Proceedings of the National Academy of Sciences* **99**, 16742-16747, doi:10.1073/pnas.262663499 (2002).
- 31 Chiti, F. *et al.* Designing conditions for in vitro formation of amyloid protofilaments and fibrils. *Proceedings of the National Academy of Sciences of the United States of America* **96**, 3590-3594 (1999).
- 32 Auer, S., Meersman, F., Dobson, C. M. & Vendruscolo, M. A Generic Mechanism of Emergence of Amyloid Protofilaments from Disordered Oligomeric Aggregates. *PLoS Comput Biol* **4**, e1000222, doi:10.1371/journal.pcbi.1000222 (2008).
- 33 Khurana, R. *et al.* A General Model for Amyloid Fibril Assembly Based on Morphological Studies Using Atomic Force Microscopy. *Biophysical Journal* **85**, 1135-1144, doi:[http://dx.doi.org/10.1016/S0006-3495\(03\)74550-0](http://dx.doi.org/10.1016/S0006-3495(03)74550-0) (2003).
- 34 Fändrich, M., Meinhardt, J. & Grigorieff, N. Structural polymorphism of Alzheimer Abeta and other amyloid fibrils. *Prion* **3**, 89-93 (2009).
- 35 Volpatti, L. R., Vendruscolo, M., Dobson, C. M. & Knowles, T. P. J. A Clear View of Polymorphism, Twist, and Chirality in Amyloid Fibril Formation. *ACS Nano* **7**, 10443-10448, doi:10.1021/nn406121w (2013).
- 36 Adamcik, J. *et al.* Understanding amyloid aggregation by statistical analysis of atomic force microscopy images. *Nat Nanotechnol* **5**, 423-428, doi:10.1038/nnano.2010.59 (2010).
- 37 Usov, I., Adamcik, J. & Mezzenga, R. Polymorphism Complexity and Handedness Inversion in Serum Albumin Amyloid Fibrils. *ACS Nano* **7**, 10465-10474, doi:10.1021/nn404886k (2013).
- 38 Usov, I. & Mezzenga, R. Correlation between Nanomechanics and Polymorphic Conformations in Amyloid Fibrils. *Acs Nano* **8**, 11035-11041, doi:10.1021/nn503530a (2014).
- 39 Usov, I., Adamcik, J. & Mezzenga, R. Polymorphism in bovine serum albumin fibrils: morphology and statistical analysis. *Faraday Discussions* **166**, 151-162, doi:10.1039/c3fd00083d (2013).
- 40 Pedersen, J. S., Andersen, C. B. & Otzen, D. E. Amyloid structure - one but not the same: the many levels of fibrillar polymorphism. *FEBS Journal* **277**, 4591-4601 (2010).
- 41 Anfinsen, C. B. Principles that govern the folding of protein chains. *Science* **181**, 223-230 (1973).
- 42 Dobson, C. M. Protein folding and misfolding. *Nature* **426**, 884-890 (2003).

- 43 Dunker, A. K., Cortese, M. S., Romero, P., Iakoucheva, L. M. & Uversky, V. N. Flexible nets - The roles of intrinsic disorder in protein interaction networks. *Febs Journal* **272**, 5129-5148, doi:10.1111/j.1742-4658.2005.04948.x (2005).
- 44 Uversky, N. V. Natively unfolded proteins: A point where biology waits for physics. *Protein Science* **11**, 739-756 (2002).
- 45 Uversky, V. N., Gillespie, J. R. & Fink, A. L. Why are "natively unfolded" proteins unstructured under physiologic conditions? *Proteins* **41**, 415-427 (2000).
- 46 Uversky, V. N., Li, J. & Fink, A. L. Evidence for a partially folded intermediate in alpha-synuclein fibril formation. *J Biol Chem* **276**, 10737-10744, doi:10.1074/jbc.M010907200 (2001).
- 47 Lara & Horwich, A. Protein aggregation in disease: a role for folding intermediates forming specific multimeric interactions. *Journal of Clinical Investigation* **110**, 1221-1232 (2002).
- 48 Turoverov, K. K., Kuznetsova, I. M. & Uversky, V. N. The protein kingdom extended: Ordered and intrinsically disordered proteins, their folding, supramolecular complex formation, and aggregation. *Progress in Biophysics and Molecular Biology* **102**, 73-84 (2010).
- 49 Onuchic, J. N., Luthey-Schulten, Z. & Wolynes, P. G. THEORY OF PROTEIN FOLDING: The Energy Landscape Perspective. *Annual Review of Physical Chemistry* **48**, 545-600, doi:10.1146/annurev.physchem.48.1.545 (1997).
- 50 Baldwin, A. J. *et al.* Metastability of native proteins and the phenomenon of amyloid formation. *Journal of the American Chemical Society* **133**, 14160-14163 (2011).
- 51 Fändrich, M. *et al.* Myoglobin forms amyloid fibrils by association of unfolded polypeptide segments. *Proceedings of the National Academy of Sciences of the United States of America* **100**, 15463-15468, doi:10.1073/pnas.0303758100 (2003).
- 52 Santambrogio, C. *et al.* The role of the central flexible region on the aggregation and conformational properties of human ataxin-3. *FEBS Journal* **279**, 451-463, doi:10.1111/j.1742-4658.2011.08438.x (2012).
- 53 Neupert, W. & Herrmann, J. M. Translocation of Proteins into Mitochondria. *Annual Review of Biochemistry* **76**, 723-749, doi:10.1146/annurev.biochem.76.052705.163409 (2007).
- 54 Goers, J. *et al.* Nuclear Localization of α -Synuclein and Its Interaction with Histones. *Biochemistry* **42**, 8465-8471 (2003).
- 55 Chua, C. E. L., Chua, C. E. & Tang, B. L. Rabs, SNAREs and α -synuclein — Membrane trafficking defects in synucleinopathies. *Brain Research Reviews* **67**, 268-281 (2011).
- 56 Stefani, M. & Dobson, C. M. Protein aggregation and aggregate toxicity: new insights into protein folding, misfolding diseases and biological evolution. *Journal of Molecular Medicine* **81**, 678-699 (2003).
- 57 Soto, C. Unfolding the role of protein misfolding in neurodegenerative diseases. *Nature Reviews Neuroscience* **4**, 49-60 (2003).
- 58 Dobson, C. M. Protein misfolding, evolution and disease. *Trends in Biochemical Sciences* **24**, 329-332, doi:[http://dx.doi.org/10.1016/S0968-0004\(99\)01445-0](http://dx.doi.org/10.1016/S0968-0004(99)01445-0) (1999).
- 59 Jahn, T. R. & Radford, S. E. Folding versus aggregation: Polypeptide conformations on competing pathways. *Archives of Biochemistry and Biophysics* **469**, 100-117, doi:10.1016/j.abb.2007.05.015 (2008).
- 60 White, D. A., Buell, A. K., Knowles, T. P., Welland, M. E. & Dobson, C. M. Protein Aggregation in Crowded Environments. *Journal of the American Chemical Society* **132**, 5170-5175 (2010).
- 61 Gillam, J. E. & MacPhee, C. E. Modelling amyloid fibril formation kinetics: mechanisms of nucleation and growth. *Journal of Physics: Condensed Matter* **25**, 373101 (2013).
- 62 Nayak, A., Sorci, M., Krueger, S. & Belfort, G. A universal pathway for amyloid nucleus and precursor formation for insulin. *Proteins: Structure, Function, and Bioinformatics* **74**, 556-565 (2009).
- 63 Militello, V. *et al.* Aggregation kinetics of bovine serum albumin studied by FTIR spectroscopy and light scattering. *Biophysical Chemistry* **107**, 175-187 (2004).

- 64 Sarroukh, R., Goormaghtigh, E., Ruyschaert, J.-M. & Raussens, V. ATR-FTIR: A “rejuvenated” tool to investigate amyloid proteins. *Biochimica et Biophysica Acta (BBA) - Biomembranes* **1828**, 2328-2338, doi:<http://dx.doi.org/10.1016/j.bbamem.2013.04.012> (2013).
- 65 Jeong, J. S., Ansaloni, A., Mezzenga, R., Lashuel, H. A. & Dietler, G. Novel Mechanistic Insight into the Molecular Basis of Amyloid Polymorphism and Secondary Nucleation during Amyloid Formation. *Journal of Molecular Biology* **425**, 1765-1781, doi:10.1016/j.jmb.2013.02.005 (2013).
- 66 Cohen, S. I. A. *et al.* From Macroscopic Measurements to Microscopic Mechanisms of Protein Aggregation. *Journal of Molecular Biology* **421**, 160-171 (2012).
- 67 Michaels, T. C. T. & Knowles, T. P. J. Mean-field master equation formalism for biofilament growth. *American Journal of Physics* **82**, 476-483, doi:10.1119/1.4870004 (2014).
- 68 Knowles, T. P. *et al.* An analytical solution to the kinetics of breakable filament assembly. *Science* **326**, 1533-1537, doi:10.1126/science.1178250 (2009).
- 69 Cohen, S. I. A. *et al.* Proliferation of amyloid- β 42 aggregates occurs through a secondary nucleation mechanism. *Proceedings of the National Academy of Sciences* **110**, 9758-9763, doi:10.1073/pnas.1218402110 (2013).
- 70 Chayen, N. E. Methods for separating nucleation and growth in protein crystallisation. *Prog. Biophys. Mol. Biol.* **88**, 329-337, doi:10.1016/j.pbiomolbio.2004.07.007 (2005).
- 71 Bouchard, M., Zurdo, J., Nettleton, E. J., Dobson, C. M. & Robinson, C. V. Formation of insulin amyloid fibrils followed by FTIR simultaneously with CD and electron microscopy. *Protein science : a publication of the Protein Society* **9**, 1960-1967, doi:10.1110/ps.9.10.1960 (2000).
- 72 Chow, M. K. M., Ellisdon, A. M., Cabrita, L. D. & Bottomley, S. P. Polyglutamine Expansion in Ataxin-3 Does Not Affect Protein Stability: IMPLICATIONS FOR MISFOLDING AND DISEASE. *Journal of Biological Chemistry* **279**, 47643-47651, doi:10.1074/jbc.M405799200 (2004).
- 73 Buell, A. K. *et al.* Detailed Analysis of the Energy Barriers for Amyloid Fibril Growth. *Angewandte Chemie International Edition* **51**, 5247-5251 (2012).
- 74 Knowles, T. P. *et al.* Kinetics and thermodynamics of amyloid formation from direct measurements of fluctuations in fibril mass. *Proceedings of the National Academy of Sciences* **104**, 10016-10021 (2007).
- 75 White, D. A. *et al.* Biosensor-based label-free assays of amyloid growth. *FEBS Letters* **583**, 2587-2592 (2009).
- 76 Buell, A. K., Dobson, C. M. & Knowles, T. P. The physical chemistry of the amyloid phenomenon: thermodynamics and kinetics of filamentous protein aggregation. *Essays in biochemistry* **56**, 11-39, doi:10.1042/bse0560011 (2014).
- 77 Gales, L. *et al.* Towards a Structural Understanding of the Fibrillization Pathway in Machado-Joseph's Disease: Trapping Early Oligomers of Non-expanded Ataxin-3. *Journal of Molecular Biology* **353**, 642-654, doi:<http://dx.doi.org/10.1016/j.jmb.2005.08.061> (2005).
- 78 Hinault, M.-. *et al.* Stable α -Synuclein Oligomers Strongly Inhibit Chaperone Activity of the Hsp70 System by Weak Interactions with J-domain Co-chaperones. *Journal of Biological Chemistry* **285**, 38173-38182 (2010).
- 79 Hong, D., Han, S., Fink, A. L. & Uversky, V. N. Characterization of the non-fibrillar α -synuclein oligomers. *Protein and peptide letters* **18**, 230-240 (2011).
- 80 McLean, P., Kawamata, H. & Shariff, S. TorsinA and heat shock proteins act as molecular chaperones: suppression of α -synuclein aggregation. *of neurochemistry* (2002).
- 81 Muchowski, P. J. Protein misfolding, amyloid formation, and neurodegeneration: a critical role for molecular chaperones? *Neuron* **35**, 9-12 (2002).
- 82 Sherman, M. Y. & Goldberg, A. L. Cellular defenses against unfolded proteins: a cell biologist thinks about neurodegenerative diseases. *Neuron* **29**, 15-32 (2001).
- 83 x, Lansbury, P. T. & Lashuel, H. A. A century-old debate on protein aggregation and neurodegeneration enters the clinic. *Nature* **443**, 774-779 (2006).
- 84 Granel, B. *et al.* Lysozyme amyloidosis: report of 4 cases and a review of the literature. *Medicine* **85**, 66-73, doi:10.1097/01.md.0000200467.51816.6d (2006).

- 85 Jaikaran, E. T. A. S. & Clark, A. Islet amyloid and type 2 diabetes: from molecular misfolding to islet pathophysiology. *Biochimica et Biophysica Acta (BBA) - Molecular Basis of Disease* **1537**, 179-203, doi:[http://dx.doi.org/10.1016/S0925-4439\(01\)00078-3](http://dx.doi.org/10.1016/S0925-4439(01)00078-3) (2001).
- 86 Hull, R. L., Westermark, G. T., Westermark, P. & Kahn, S. E. Islet Amyloid: A Critical Entity in the Pathogenesis of Type 2 Diabetes. *The Journal of Clinical Endocrinology & Metabolism* **89**, 3629-3643, doi:doi:10.1210/jc.2004-0405 (2004).
- 87 Meetoo, D., McGovern, P. & Safadi, R. An epidemiological overview of diabetes across the world. *British journal of nursing (Mark Allen Publishing)* **16**, 1002-1007, doi:10.12968/bjon.2007.16.16.27079 (2007).
- 88 Lashuel, H. A. & Lansbury, P. T. Are amyloid diseases caused by protein aggregates that mimic bacterial pore-forming toxins? *Quarterly Reviews of Biophysics* **39**, 167 (2006).
- 89 Uversky, V. & Eliezer, D. Biophysics of Parkinsons Disease: Structure and Aggregation of-Synuclein. *Current Protein and Peptide Science* (2009).
- 90 Lashuel, H. A., Overk, C. R., Oueslati, A. & Masliah, E. The many faces of α -synuclein: from structure and toxicity to therapeutic target. *Nature Reviews Neuroscience* **14**, 38-48 (2012).
- 91 Lashuel, H. A., Hartley, D., Petre, B. M., Walz, T. & Lansbury, P. T. Neurodegenerative disease - Amyloid pores from pathogenic mutations. *Nature* **418**, 291-291, doi:10.1038/418291a (2002).
- 92 Ballard, C. *et al.* Alzheimer's disease. *The Lancet* **377**, 1019-1031, doi:[http://dx.doi.org/10.1016/S0140-6736\(10\)61349-9](http://dx.doi.org/10.1016/S0140-6736(10)61349-9).
- 93 Selkoe, D. J. Amyloid protein and Alzheimer's disease. *Scientific American* **265**, 68-71, 74-66, 78 (1991).
- 94 Masters, C. L. *et al.* Amyloid plaque core protein in Alzheimer disease and Down syndrome. *Proc Natl Acad Sci U S A* **82**, 4245-4249 (1985).
- 95 Glenner, G. G. & Wong, C. W. Alzheimer's disease: initial report of the purification and characterization of a novel cerebrovascular amyloid protein. *Biochem Biophys Res Commun* **120**, 885-890 (1984).
- 96 Busciglio, J., Gabuzda, D. H., Matsudaira, P. & Yankner, B. A. Generation of beta-amyloid in the secretory pathway in neuronal and nonneuronal cells. *Proceedings of the National Academy of Sciences* **90**, 2092-2096, doi:10.1073/pnas.90.5.2092 (1993).
- 97 Palop, J. J. & Mucke, L. Amyloid-[beta]-induced neuronal dysfunction in Alzheimer's disease: from synapses toward neural networks. *Nat Neurosci* **13**, 812-818 (2010).
- 98 Hardy, J. & Higgins, G. Alzheimer's disease: the amyloid cascade hypothesis. *Science* **256**, 184-185, doi:10.1126/science.1566067 (1992).
- 99 Lemere, C. A. *et al.* Sequence of deposition of heterogeneous amyloid beta-peptides and APO E in Down syndrome: implications for initial events in amyloid plaque formation. *Neurobiology of disease* **3**, 16-32, doi:10.1006/nbdi.1996.0003 (1996).
- 100 Terry, R. D. *et al.* PHYSICAL BASIS OF COGNITIVE ALTERATIONS IN ALZHEIMERS-DISEASE - SYNAPSE LOSS IS THE MAJOR CORRELATE OF COGNITIVE IMPAIRMENT. *Ann. Neurol.* **30**, 572-580, doi:10.1002/ana.410300410 (1991).
- 101 Hasegawa, K., Yamaguchi, I., Omata, S., Gejyo, F. & Naiki, H. Interaction between A beta(1-42) and A beta(1-40) in Alzheimer's beta-amyloid fibril formation in vitro. *Biochemistry* **38**, 15514-15521 (1999).
- 102 Iwatsubo, T. *et al.* Visualization of A β 42(43) and A β 40 in senile plaques with end-specific A β monoclonals: Evidence that an initially deposited species is A β 42(43). *Neuron* **13**, 45-53, doi:10.1016/0896-6273(94)90458-8.
- 103 Jan, A., Gokce, O., Luthi-Carter, R. & Lashuel, H. A. The ratio of monomeric to aggregated forms of A beta 40 and A beta 42 is an important determinant of amyloid-beta aggregation, fibrillogenesis, and toxicity. *Journal of Biological Chemistry* **283**, 28176-28189, doi:10.1074/jbc.M803159200 (2008).
- 104 Hsia, A. Y. *et al.* Plaque-independent disruption of neural circuits in Alzheimer's disease mouse models. *Proc Natl Acad Sci U S A* **96**, 3228-3233 (1999).

- 105 Chapman, P. F. *et al.* Impaired synaptic plasticity and learning in aged amyloid precursor protein transgenic mice. *Nat Neurosci* **2**, 271-276, doi:10.1038/6374 (1999).
- 106 Walsh, D. M. *et al.* Naturally secreted oligomers of amyloid beta protein potently inhibit hippocampal long-term potentiation in vivo. *Nature* **416**, 535-539, doi:10.1038/416535a (2002).
- 107 Lansbury, P. T. & Lanshuel, H. A. A century-old debate on protein aggregation and neurodegeneration enters the clinic. *Nature* **443**, 774-779, doi:10.1038/nature05290 (2006).
- 108 Jan, A. *et al.* A beta 42 Neurotoxicity Is Mediated by Ongoing Nucleated Polymerization Process Rather than by Discrete A beta 42 Species. *Journal of Biological Chemistry* **286**, 8585-8596, doi:10.1074/jbc.M110.172411 (2011).
- 109 Goedert, M. Alpha-synuclein and neurodegenerative diseases. *Nature reviews. Neuroscience* **2**, 492-501 (2001).
- 110 Conway, K. A., Harper, J. D. & Lansbury, P. T. Accelerated in vitro fibril formation by a mutant alpha-synuclein linked to early-onset Parkinson disease. *Nature medicine* **4**, 1318-1320 (1998).
- 111 Khalaf, O. *et al.* The H50Q mutation enhances alpha-synuclein aggregation, secretion, and toxicity. *J Biol Chem* **289**, 21856-21876, doi:10.1074/jbc.M114.553297 (2014).
- 112 Wood, S. J. *et al.* alpha-synuclein fibrillogenesis is nucleation-dependent. Implications for the pathogenesis of Parkinson's disease. *The Journal of biological chemistry* **274**, 19509-19512 (1999).
- 113 Giehm, L., Lorenzen, N. & Otzen, D. E. Assays for α -synuclein aggregation. *Methods* **53**, 295-305 (2011).
- 114 Simone *et al.* Secondary Structure of α -Synuclein Oligomers: Characterization by Raman and Atomic Force Microscopy. *Journal of Molecular Biology* **355**, 63-71 (2006).
- 115 Davidson, W., Jonas, A. & Clayton, D. Stabilization of α -synuclein secondary structure upon binding to synthetic membranes. *of Biological Chemistry* (1998).
- 116 McLean, P. J., Kawamata, H., Ribich, S. & Hyman, B. T. Membrane association and protein conformation of alpha-synuclein in intact neurons. Effect of Parkinson's disease-linked mutations. *The Journal of biological chemistry* **275**, 8812-8816 (2000).
- 117 Eliezer, D., Kutluay, E., Bussell, R. & Browne, G. Conformational properties of alpha-synuclein in its free and lipid-associated states. *Journal of Molecular Biology* **307**, 1061-1073 (2001).
- 118 Vamvaca, K., Volles, M. J. & Lansbury, P. T. The First N-terminal Amino Acids of α -Synuclein Are Essential for α -Helical Structure Formation In Vitro and Membrane Binding in Yeast. *Journal of Molecular Biology* **389**, 413-424 (2009).
- 119 Butterfield, S. & Lanshuel, H. Amyloidogenic Protein-Membrane Interactions: Mechanistic Insight from Model Systems. *Angewandte Chemie International Edition* **49**, 5628-5654 (2010).
- 120 Ruipérez, V., Darios, F. & Davletov, B. Alpha-synuclein, lipids and Parkinson's disease. *Progress in Lipid Research* **49**, 420-428 (2010).
- 121 Hsu, L. J. *et al.* alpha-synuclein promotes mitochondrial deficit and oxidative stress. *Am J Pathol* **157**, 401-410 (2000).
- 122 Hashimoto, M. *et al.* The Role of alpha-synuclein assembly and metabolism in the pathogenesis of Lewy body disease. *J Mol Neurosci* **24**, 343-352, doi:10.1385/jmn:24:3:343 (2004).
- 123 Alim, M. A. *et al.* Demonstration of a role for alpha-synuclein as a functional microtubule-associated protein. *Journal of Alzheimer's disease : JAD* **6**, 435-442; discussion 443-439 (2004).
- 124 Lanshuel, H. A., Overk, C. R., Oueslati, A. & Masliah, E. The many faces of [alpha]-synuclein: from structure and toxicity to therapeutic target. *Nat Rev Neurosci* **14**, 38-48 (2013).
- 125 Oueslati, A., Paleologou, K. E., Schneider, B. L., Aebischer, P. & Lanshuel, H. A. Mimicking phosphorylation at serine 87 inhibits the aggregation of human alpha-synuclein and protects

- against its toxicity in a rat model of Parkinson's disease. *J Neurosci* **32**, 1536-1544, doi:10.1523/jneurosci.3784-11.2012 (2012).
- 126 Taschenberger, G. *et al.* Aggregation of alphaSynuclein promotes progressive in vivo neurotoxicity in adult rat dopaminergic neurons. *Acta neuropathologica* **123**, 671-683, doi:10.1007/s00401-011-0926-8 (2012).
- 127 Orr, H. T. & Zoghbi, H. Y. in *Annual Review of Neuroscience* Vol. 30 *Annual Review of Neuroscience* 575-621 (Annual Reviews, 2007).
- 128 Trottier, Y. *et al.* POLYGLUTAMINE EXPANSION AS A PATHOLOGICAL EPITOPE IN HUNTINGTONS-DISEASE AND 4 DOMINANT CEREBELLAR ATAXIAS. *Nature* **378**, 403-406, doi:10.1038/378403a0 (1995).
- 129 Saunders, H. M. & Bottomley, S. P. Multi-domain misfolding: understanding the aggregation pathway of polyglutamine proteins. *Protein engineering, design & selection : PEDS* **22**, 447-451, doi:10.1093/protein/gzp033 (2009).
- 130 Landles, C. & Bates, G. P. Huntingtin and the molecular pathogenesis of Huntington's disease. Fourth in molecular medicine review series. *EMBO reports* **5**, 958-963, doi:10.1038/sj.embor.7400250 (2004).
- 131 MacDonald, M. E., Gines, S., Gusella, J. F. & Wheeler, V. C. Huntington's disease. *Neuromolecular Med* **4**, 7-20, doi:10.1385/nmm:4:1-2:7 (2003).
- 132 Li, S. & Li, X. J. Multiple pathways contribute to the pathogenesis of Huntington disease. *Mol Neurodegener* **1**, 19, doi:10.1186/1750-1326-1-19 (2006).
- 133 Rigamonti, D. *et al.* Wild-type huntingtin protects from apoptosis upstream of caspase-3. *J Neurosci* **20**, 3705-3713 (2000).
- 134 Leavitt, B. R. *et al.* Wild-type huntingtin protects neurons from excitotoxicity. *Journal of Neurochemistry* **96**, 1121-1129, doi:10.1111/j.1471-4159.2005.03605.x (2006).
- 135 Kim, Y. J. *et al.* Caspase 3-cleaved N-terminal fragments of wild-type and mutant huntingtin are present in normal and Huntington's disease brains, associate with membranes, and undergo calpain-dependent proteolysis. *Proceedings of the National Academy of Sciences of the United States of America* **98**, 12784-12789, doi:10.1073/pnas.221451398 (2001).
- 136 Ansaloni, A. *et al.* One-Pot Semisynthesis of Exon 1 of the Huntingtin Protein: New Tools for Elucidating the Role of Posttranslational Modifications in the Pathogenesis of Huntington's Disease. *Angewandte Chemie-International Edition* **53**, 1928-1933, doi:10.1002/anie.201307510 (2014).
- 137 Mangiarini, L. *et al.* Exon 1 of the HD gene with an expanded CAG repeat is sufficient to cause a progressive neurological phenotype in transgenic mice. *Cell* **87**, 493-506 (1996).
- 138 Scherzinger, E. *et al.* Self-assembly of polyglutamine-containing huntingtin fragments into amyloid-like fibrils: Implications for Huntington's disease pathology. *Proceedings of the National Academy of Sciences* **96**, 4604-4609, doi:10.1073/pnas.96.8.4604 (1999).
- 139 Lakhani, V. V., Ding, F. & Dokholyan, N. V. Polyglutamine Induced Misfolding of Huntingtin Exon1 is Modulated by the Flanking Sequences. *PLoS Computational Biology* **6**, e1000772, doi:10.1371/journal.pcbi.1000772 (2010).
- 140 Chen, S., Berthelie, V., Yang, W. & Wetzel, R. Polyglutamine aggregation behavior in vitro supports a recruitment mechanism of cytotoxicity. *Journal of Molecular Biology* **311**, 173-182 (2001).
- 141 Thakur, A. K. *et al.* Polyglutamine disruption of the huntingtin exon 1 N terminus triggers a complex aggregation mechanism. *Nature structural & molecular biology* **16**, 380-389, doi:10.1038/nsmb.1570 (2009).
- 142 Sivanandam, V. N. *et al.* The aggregation-enhancing huntingtin N-terminus is helical in amyloid fibrils. *J Am Chem Soc* **133**, 4558-4566, doi:10.1021/ja110715f (2011).
- 143 Jayaraman, M. *et al.* Kinetically competing huntingtin aggregation pathways control amyloid polymorphism and properties. *Biochemistry* **51**, 2706-2716, doi:10.1021/bi3000929 (2012).
- 144 Ross, C. A. & Poirier, M. A. Protein aggregation and neurodegenerative disease. *Nature Medicine* **10**, S10-S17, doi:10.1038/nm1066 (2004).

- 145 Ross, C. A. & Tabrizi, S. J. Huntington's disease: from molecular pathogenesis to clinical
treatment. *The Lancet. Neurology* **10**, 83-98, doi:10.1016/s1474-4422(10)70245-3 (2011).
- 146 Hoffner, G. & Djian, P. Monomeric, Oligomeric and Polymeric Proteins in Huntington Disease
and Other Diseases of Polyglutamine Expansion. *Brain Sciences* **4**, 91-122 (2014).
- 147 Schols, L., Bauer, P., Schmidt, T., Schulte, T. & Riess, O. Autosomal dominant cerebellar
ataxias: clinical features, genetics, and pathogenesis. *Lancet Neurol.* **3**, 291-304,
doi:10.1016/s1474-4422(04)00737-9 (2004).
- 148 Maciel, P. *et al.* Correlation between CAG repeat length and clinical features in Machado-
Joseph disease. *American journal of human genetics* **57**, 54-61 (1995).
- 149 Scarff, C. A. *et al.* A tale of a tail: Structural insights into the conformational properties of the
polyglutamine protein ataxin-3. *International Journal of Mass Spectrometry* **345–347**, 63-70,
doi:<http://dx.doi.org/10.1016/j.ijms.2012.08.032> (2013).
- 150 Evers, M. M., Toonen, L. J. & van Roon-Mom, W. M. Ataxin-3 protein and RNA toxicity in
spinocerebellar ataxia type 3: current insights and emerging therapeutic strategies.
Molecular neurobiology **49**, 1513-1531, doi:10.1007/s12035-013-8596-2 (2014).
- 151 Ellisdon, A. M., Thomas, B. & Bottomley, S. P. The two-stage pathway of ataxin-3
fibrillogenesis involves a polyglutamine-independent step. *J Biol Chem* **281**, 16888-16896,
doi:10.1074/jbc.M601470200 (2006).
- 152 Ellisdon, A. M., Pearce, M. C. & Bottomley, S. P. Mechanisms of ataxin-3 misfolding and fibril
formation: kinetic analysis of a disease-associated polyglutamine protein. *J Mol Biol* **368**, 595-
605, doi:10.1016/j.jmb.2007.02.058 (2007).
- 153 Masino, L. *et al.* The Josephin Domain Determines the Morphological and Mechanical
Properties of Ataxin-3 Fibrils. *Biophysical Journal* **100**, 2033-2042 (2011).
- 154 Nicastro, G. *et al.* The solution structure of the Josephin domain of ataxin-3: Structural
determinants for molecular recognition. *Proceedings of the National Academy of Sciences*
102, 10493-10498, doi:10.1073/pnas.0501732102 (2005).
- 155 Paulson, H. L. *et al.* Intranuclear inclusions of expanded polyglutamine protein in
spinocerebellar ataxia type 3. *Neuron* **19**, 333-344 (1997).
- 156 Haacke, A. *et al.* Proteolytic cleavage of polyglutamine-expanded ataxin-3 is critical for
aggregation and sequestration of non-expanded ataxin-3. *Hum Mol Genet* **15**, 555-568,
doi:10.1093/hmg/ddi472 (2006).
- 157 Hubener, J. *et al.* Calpain-mediated ataxin-3 cleavage in the molecular pathogenesis of
spinocerebellar ataxia type 3 (SCA3). *Hum Mol Genet* **22**, 508-518, doi:10.1093/hmg/dds449
(2013).
- 158 Fowler, D. M., Koulov, A. V., Balch, W. E. & Kelly, J. W. Functional amyloid--from bacteria to
humans. *Trends Biochem Sci* **32**, 217-224, doi:10.1016/j.tibs.2007.03.003 (2007).
- 159 Maji, S. K. *et al.* Functional amyloids as natural storage of peptide hormones in pituitary
secretory granules. *Science* **325**, 328-332, doi:10.1126/science.1173155 (2009).
- 160 Garcia-Osta, A. & Alberini, C. M. Amyloid beta mediates memory formation. *Learning &
Memory* **16**, 267-272, doi:10.1101/lm.1310209 (2009).
- 161 Hauser, C. A. E., Maurer-Stroh, S. & Martins, I. C. Amyloid-based nanosensors and
nanodevices. *Chemical Society Reviews* **43**, 5326-5345, doi:10.1039/c4cs00082j (2014).
- 162 Cherny, I. & Gazit, E. Amyloids: Not Only Pathological Agents but Also Ordered
Nanomaterials. *Angewandte Chemie International Edition* **47**, 4062-4069,
doi:10.1002/anie.200703133 (2008).
- 163 Adamcik, J. *et al.* Measurement of intrinsic properties of amyloid fibrils by the peak force
QNM method. *Nanoscale* **4**, 4426 (2012).
- 164 Knowles, T. P., Oppenheim, T. W., Buell, A. K., Chirgadze, D. Y. & Welland, M. E.
Nanostructured films from hierarchical self-assembly of amyloidogenic proteins. *Nat
Nanotechnol* **5**, 204-207, doi:10.1038/nnano.2010.26 (2010).
- 165 Li, C. & Mezzenga, R. The interplay between carbon nanomaterials and amyloid fibrils in bio-
nanotechnology. *Nanoscale* **5**, 6207-6218, doi:10.1039/C3NR01644G (2013).

- 166 Ling, S. *et al.* Modulating Materials by Orthogonally Oriented β -Strands: Composites of Amyloid and Silk Fibroin Fibrils. *Advanced Materials* **26**, 4569-4574, doi:10.1002/adma.201400730 (2014).
- 167 Reynolds, N. P., Charnley, M., Mezzenga, R. & Hartley, P. G. Engineered Lysozyme Amyloid Fibril Networks Support Cellular Growth and Spreading. *Biomacromolecules* **15**, 599-608, doi:10.1021/bm401646x (2014).
- 168 Maji, S. K. *et al.* Amyloid as a Depot for the Formulation of Long-Acting Drugs. *PLoS Biol* **6**, e17, doi:10.1371/journal.pbio.0060017 (2008).
- 169 Pertinhez, T. A. *et al.* Reversible self-assembly: a key feature for a new class of autodelivering therapeutic peptides. *Molecular pharmaceuticals* **6**, 1036-1039, doi:10.1021/mp900024z (2009).
- 170 Li, C. & Mezzenga, R. Functionalization of Multiwalled Carbon Nanotubes and Their pH-Responsive Hydrogels with Amyloid Fibrils. *Langmuir* **28**, 10142-10146, doi:10.1021/la301541d (2012).
- 171 Li, C., Bolisetty, S., Chaitanya, K., Adamcik, J. & Mezzenga, R. Tunable Carbon Nanotube/Protein Core-Shell Nanoparticles with NIR- and Enzymatic-Responsive Cytotoxicity. *Advanced Materials* **25**, 1010-1015, doi:10.1002/adma.201203382 (2013).
- 172 Li, C., Adamcik, J. & Mezzenga, R. Biodegradable nanocomposites of amyloid fibrils and graphene with shape-memory and enzyme-sensing properties. *Nat Nano* **7**, 421-427, doi:<http://www.nature.com/nnano/journal/v7/n7/abs/nnano.2012.62.html#supplementary-information> (2012).
- 173 Krebs, M. R. H., Bromley, E. H. C. & Donald, A. M. The binding of thioflavin-T to amyloid fibrils: localisation and implications. *Journal of Structural Biology* **149**, 30-37, doi:<http://dx.doi.org/10.1016/j.jsb.2004.08.002> (2005).
- 174 Biancalana, M. & Koide, S. Molecular mechanism of Thioflavin-T binding to amyloid fibrils. *Biochimica et Biophysica Acta (BBA) - Proteins and Proteomics* **1804**, 1405-1412, doi:<http://dx.doi.org/10.1016/j.bbapap.2010.04.001> (2010).
- 175 Wolfe, L. S. *et al.* Protein-induced photophysical changes to the amyloid indicator dye thioflavin T. *Proceedings of the National Academy of Sciences of the United States of America* **107**, 16863-16868, doi:10.1073/pnas.1002867107 (2010).
- 176 LeVine Iii, H. in *Methods in Enzymology* Vol. Volume 309 (ed Wetzel Ronald) 274-284 (Academic Press, 1999).
- 177 Martin, S. R. & Schilstra, M. J. in *Methods in Cell Biology* Vol. Volume 84 (eds J. Correia Dr. John & Dr. H. William Detrich, III) 263-293 (Academic Press, 2008).
- 178 Kelly, S. M., Jess, T. J. & Price, N. C. How to study proteins by circular dichroism. *Biochimica et Biophysica Acta (BBA) - Proteins and Proteomics* **1751**, 119-139, doi:<http://dx.doi.org/10.1016/j.bbapap.2005.06.005> (2005).
- 179 Whitmore, L. & Wallace, B. A. Protein secondary structure analyses from circular dichroism spectroscopy: Methods and reference databases. *Biopolymers* **89**, 392-400, doi:10.1002/bip.20853 (2008).
- 180 Calero, M. & Gasset, M. Featuring amyloids with Fourier transform infrared and circular dichroism spectroscopies. *Methods in molecular biology (Clifton, N.J.)* **849**, 53-68, doi:10.1007/978-1-61779-551-0_5 (2012).
- 181 Kumosinski, T. F. & Unruh, J. J. Quantitation of the global secondary structure of globular proteins by FTIR spectroscopy: Comparison with X-ray crystallographic structure. *Talanta* **43**, 199-219, doi:10.1016/0039-9140(95)01726-7 (1996).
- 182 Barth, A. Infrared spectroscopy of proteins. *Biochimica et Biophysica Acta (BBA) - Bioenergetics* **1767**, 1073-1101, doi:10.1016/j.bbapap.2007.06.004 (2007).
- 183 Sassi, P. *et al.* Unfolding and aggregation of lysozyme: A thermodynamic and kinetic study by FTIR spectroscopy. *Biophysical Chemistry* **158**, 46-53 (2011).
- 184 Kong, J. & Yu, S. Fourier transform infrared spectroscopic analysis of protein secondary structures. *Acta biochimica et biophysica Sinica* **39**, 549-559 (2007).

- 185 Haris, P. & Severcan, F. FTIR spectroscopic characterization of protein structure in aqueous
and non-aqueous media. *Journal of Molecular Catalysis B: Enzymatic* (1999).
- 186 Shivu, B. *et al.* Distinct β -Sheet Structure in Protein Aggregates Determined by ATR-FTIR
Spectroscopy. *Biochemistry* **52**, 5176-5183, doi:10.1021/bi400625v (2013).
- 187 Khurana, R. & Fink, A. L. Do Parallel β -Helix Proteins Have a Unique Fourier Transform
Infrared Spectrum? *Biophysical Journal* **78**, 994-1000, doi:[http://dx.doi.org/10.1016/S0006-3495\(00\)76657-4](http://dx.doi.org/10.1016/S0006-3495(00)76657-4) (2000).
- 188 Stuart, B. H. *Infrared Spectroscopy: Fundamentals and Applications*. 1-208 (2005).
- 189 Born, M. & Wolf, E. *Principles of optics: electromagnetic theory of propagation, interference
and diffraction of light*. (Cambridge university press, 1999).
- 190 Binnig, G. & Rohrer, H. Scanning tunneling microscopy. *IBM Journal of research and
development* **44**, 279-293 (2000).
- 191 Allison, D. P., Mortensen, N. P., Sullivan, C. J. & Doktycz, M. J. Atomic force microscopy of
biological samples. *Wiley Interdiscip. Rev.-Nanomed. Nanobiotechnol.* **2**, 618-634,
doi:10.1002/wnan.104 (2010).
- 192 Cappella, B. & Dietler, G. Force-distance curves by atomic force microscopy. *Surf. Sci. Rep.* **34**,
1-104, doi:[http://dx.doi.org/10.1016/S0167-5729\(99\)00003-5](http://dx.doi.org/10.1016/S0167-5729(99)00003-5) (1999).
- 193 Hendrik, H. in *Dynamic Force Spectroscopy and Biomolecular Recognition* 51-91 (CRC Press,
2012).
- 194 Garcia, R. & Perez, R. Dynamic atomic force microscopy methods. *Surf. Sci. Rep.* **47**, 197-301,
doi:10.1016/s0167-5729(02)00077-8 (2002).
- 195 de Pablo, P. J. & Carrion-Vazquez, M. Imaging biological samples with atomic force
microscopy. *Cold Spring Harbor protocols* **2014**, 167-177, doi:10.1101/pdb.top080473 (2014).
- 196 Kuznetsov, Y. G. & McPherson, A. Atomic Force Microscopy in Imaging of Viruses and Virus-
Infected Cells. *Microbiology and Molecular Biology Reviews* **75**, 268-285,
doi:10.1128/mubr.00041-10 (2011).
- 197 Adamcik, J. & Mezzenga, R. Study of amyloid fibrils via atomic force microscopy. *Current
Opinion in Colloid & Interface Science* **17**, 369-376 (2012).
- 198 Volpatti, L. R. & Knowles, T. P. J. Polymer Physics Inspired Approaches for the Study of the
Mechanical Properties of Amyloid Fibrils. *J. Polym. Sci. Pt. B-Polym. Phys.* **52**, 281-292,
doi:10.1002/polb.23428 (2014).
- 199 Gittes, F., Mickey, B., Nettleton, J. & Howard, J. Flexural rigidity of microtubules and actin
filaments measured from thermal fluctuations in shape. *J Cell Biol* **120**, 923-934 (1993).
- 200 Florin, E. L. *et al.* Sensing specific molecular interactions with the atomic force microscope.
Biosensors and Bioelectronics **10**, 895-901, doi:[http://dx.doi.org/10.1016/0956-5663\(95\)99227-C](http://dx.doi.org/10.1016/0956-5663(95)99227-C) (1995).
- 201 McConney, M. E., Singamaneni, S. & Tsukruk, V. V. Probing Soft Matter with the Atomic Force
Microscopies: Imaging and Force Spectroscopy. *Polym. Rev.* **50**, 235-286,
doi:10.1080/15583724.2010.493255 (2010).
- 202 Sweers, K., Werf, K., Bennink, M., Subramaniam, V. & Werf, K. Nanomechanical properties of
 α -synuclein amyloid fibrils: a comparative study by nanoindentation, harmonic force
microscopy, and Peakforce QNM. *Nanoscale Research Letters* **6**, 270 (2011).
- 203 Ramos, J. R., Pabijan, J., Garcia, R. & Lekka, M. The softening of human bladder cancer cells
happens at an early stage of the malignancy process. *Beilstein Journal of Nanotechnology* **5**,
447-457, doi:10.3762/bjnano.5.52 (2014).
- 204 Kellermayer, M. S. *et al.* Reversible mechanical unzipping of amyloid beta-fibrils. *J Biol Chem*
280, 8464-8470, doi:10.1074/jbc.M411556200 (2005).
- 205 Karsai, A. *et al.* Mechanical manipulation of Alzheimer's amyloid beta 1-42 fibrils. *Journal of
Structural Biology* **155**, 316-326, doi:10.1016/j.jsb.2005.12.015 (2006).
- 206 Dunstan, D. E., Hamilton-Brown, P., Asimakis, P., Ducker, W. & Bertolini, J. Shear-induced
structure and mechanics of [small beta]-lactoglobulin amyloid fibrils. *Soft Matter* **5**, 5020-
5028, doi:10.1039/B914089A (2009).

- 207 Kasas, S., Longo, G. & Dietler, G. Mechanical properties of biological specimens explored by atomic force microscopy. *Journal of Physics D-Applied Physics* **46**, doi:10.1088/0022-3727/46/13/133001 (2013).
- 208 Adamcik, J., Berquand, A. & Mezzenga, R. Single-step direct measurement of amyloid fibrils stiffness by peak force quantitative nanomechanical atomic force microscopy. *Applied Physics Letters* **98**, 193701, doi:Artn 193701
Doi 10.1063/1.3589369 (2011).
- 209 Jackson, M. & Mantsch, H. The use and misuse of FTIR spectroscopy in the determination of protein structure. *Critical Reviews in Biochemistry* (1995).
- 210 Dazzi, A. *et al.* AFM-IR: combining atomic force microscopy and infrared spectroscopy for nanoscale chemical characterization. *Appl. Spectrosc.* **66**, 1365-1384, doi:10.1366/12-06804 (2012).
- 211 Dazzi, A., Glotin, F. & Carminati, R. Theory of infrared nanospectroscopy by photothermal induced resonance. *Journal of Applied Physics* **107**, doi:10.1063/1.3429214 (2010).
- 212 Dazzi, A. *et al.* AFM-IR: Combining Atomic Force Microscopy and Infrared Spectroscopy for Nanoscale Chemical Characterization. *Appl. Spectrosc.* **66**, 1365-1384 (2012).
- 213 Carr, G. L. Resolution limits for infrared microspectroscopy explored with synchrotron radiation. *Review of Scientific Instruments* **72**, 1613-1619, doi:doi:<http://dx.doi.org/10.1063/1.1347965> (2001).
- 214 Janik, E. *et al.* Molecular Architecture of Plant Thylakoids under Physiological and Light Stress Conditions: A Study of Lipid-Light-Harvesting Complex II Model Membranes. *Plant Cell* **25**, 2155-2170, doi:10.1105/tpc.113.113076 (2013).
- 215 Knowles, T. P. J., Vendruscolo, M. & Dobson, C. M. The amyloid state and its association with protein misfolding diseases. *Nat Rev Mol Cell Biol* **15**, 496-496, doi:10.1038/nrm3826 (2014).
- 216 Fredenburg, R. A. *et al.* The impact of the E46K mutation on the properties of alpha-synuclein in its monomeric and oligomeric states. *Biochemistry* **46**, 7107-7118 (2007).
- 217 Li, J., Uversky, V. N. & Fink, A. L. Effect of Familial Parkinson's Disease Point Mutations A30P and A53T on the Structural Properties, Aggregation, and Fibrillation of Human α -Synuclein. *Biochemistry* **40**, 11604-11613 (2001).
- 218 Fauvet, B., Butterfield, S. M., Fuks, J., Brik, A. & Lashuel, H. A. One-pot total chemical synthesis of human [small alpha]-synuclein. *Chemical Communications* **49**, 9254-9256, doi:10.1039/C3CC45353G (2013).
- 219 Mikhaylov, A., Sekatskii, S. K. & Dietler, G. DNA Trace: A Comprehensive Software for Polymer Image Processing. *Journal of Advanced Microscopy Research* **8**, 241-245, doi:10.1166/jamr.2013.1164 (2013).
- 220 Sweers, K. K., Segers-Nolten, I. M., Bennink, M. L. & Subramaniam, V. Structural model for α -synuclein fibrils derived from high resolution imaging and nanomechanical studies using atomic force microscopy. *Soft Matter* **8**, 7215 (2012).
- 221 Adamcik, J. & Mezzenga, R. Proteins Fibrils from a Polymer Physics Perspective. *Macromolecules* **45**, 1137-1150, doi:10.1021/ma202157h (2011).
- 222 Cerreta, A. *et al.* FM-AFM constant height imaging and force curves: high resolution study of DNA-tip interactions. *Journal of molecular recognition : JMR* **25**, 486-493, doi:10.1002/jmr.2212 (2012).
- 223 Dedmon, M. M., Lindorff-Larsen, K., Christodoulou, J., Vendruscolo, M. & Dobson, C. M. Mapping Long-Range Interactions in α -Synuclein using Spin-Label NMR and Ensemble Molecular Dynamics Simulations. *Journal of the American Chemical Society* **127**, 476-477 (2005).
- 224 Watson, J. D. & Crick, F. H. C. Molecular Structure of Nucleic Acids: A Structure for Deoxyribose Nucleic Acid. *Nature* **171**, 737-738 (1953).
- 225 Fändrich, M., Meinhardt, J. & Grigorieff, N. Structural polymorphism of Alzheimer Abeta and other amyloid fibrils. *Prion* **3**, 89-93 (2009).

- 226 Sandal, M., Benedetti, F., Brucale, M., Gomez-Casado, A. & Samori, B. Hooke: an open software platform for force spectroscopy. *Bioinformatics (Oxford, England)* **25**, 1428-1430, doi:10.1093/bioinformatics/btp180 (2009).
- 227 Deng, Z. *et al.* A Close Look at Proteins: Submolecular Resolution of Two- and Three-Dimensionally Folded Cytochrome c at Surfaces. *Nano Letters* **12**, 2452-2458 (2012).
- 228 Santos, S., Stefancich, M., Hernandez, H., Chiesa, M. & Thomson, N. H. Hydrophilicity of a Single DNA Molecule. *The Journal of Physical Chemistry C* **116**, 2807-2818, doi:10.1021/jp211326c (2012).
- 229 Santos, S., Barcons, V., Christenson, H. K., Font, J. & Thomson, N. H. The intrinsic resolution limit in the atomic force microscope: implications for heights of nano-scale features. *PLoS One* **6**, e23821, doi:10.1371/journal.pone.0023821 (2011).
- 230 Rief, M., Gautel, M., Oesterhelt, F., Fernandez, J. M. & Gaub, H. E. Reversible Unfolding of Individual Titin Immunoglobulin Domains by AFM. *Science* **276**, 1109-1112, doi:10.1126/science.276.5315.1109 (1997).
- 231 Benedetti, F., Micheletti, C., Bussi, G., Sekatskii, S. K. & Dietler, G. Nonkinetic Modeling of the Mechanical Unfolding of Multimodular Proteins: Theory and Experiments. *Biophysical Journal* **101**, 1504-1512 (2011).
- 232 Friedsam, C., Wehle, A., Kuhner, F. & Gaub, H. Dynamic single-molecule force spectroscopy: bond rupture analysis with variable spacer length. *Journal of Physics: Condensed Matter* **15**, S1709-S1723, doi:citeulike-article-id:943619 (2003).
- 233 Bustamante, C., Marko, J. F., Siggia, E. D. & Smith, S. ENTROPIC ELASTICITY OF LAMBDA-PHAGE DNA. *Science* **265**, 1599-1600, doi:10.1126/science.8079175 (1994).
- 234 Zinober, R. C. *et al.* Mechanically unfolding proteins: the effect of unfolding history and the supramolecular scaffold. *Protein Sci* **11**, 2759-2765, doi:10.1110/ps.0224602 (2002).
- 235 Caughey, B. & Lansbury, P. T. Protofibrils, pores, fibrils, and neurodegeneration: separating the responsible protein aggregates from the innocent bystanders. *Annu Rev Neurosci* **26**, 267-298, doi:10.1146/annurev.neuro.26.010302.081142 (2003).
- 236 Eisenberg, D. *et al.* The Structural Biology of Protein Aggregation Diseases: Fundamental Questions and Some Answers. *Accounts of Chemical Research* **39**, 568-575 (2006).
- 237 Lara, C., Gourdin-Bertin, S., Adamcik, J., Bolisetty, S. & Mezzenga, R. Self-Assembly of Ovalbumin into Amyloid and Non-Amyloid Fibrils. *Biomacromolecules*, 121106145514000 (2012).
- 238 Paparcone, R., Cranford, S. W. & Buehler, M. J. Self-folding and aggregation of amyloid nanofibrils. *Nanoscale* **3**, 1748-1755, doi:10.1039/c0nr00840k (2011).
- 239 Paparcone, R. & Buehler, M. J. Microscale structural model of Alzheimer A beta(1-40) amyloid fibril. *Applied Physics Letters* **94**, doi:10.1063/1.3148641 (2009).
- 240 Paparcone, R., Keten, S. & Buehler, M. J. Atomistic simulation of nanomechanical properties of Alzheimer's A beta(1-40) amyloid fibrils under compressive and tensile loading. *J. Biomech.* **43**, 1196-1201, doi:10.1016/j.jbiomech.2009.11.026 (2010).
- 241 Xu, Z. P., Paparcone, R. & Buehler, M. J. Alzheimer's A beta(1-40) Amyloid Fibrils Feature Size-Dependent Mechanical Properties. *Biophysical Journal* **98**, 2053-2062, doi:10.1016/j.bpj.2009.12.4317 (2010).
- 242 Fink, A. L. The Aggregation and Fibrillation of α -Synuclein. *Accounts of Chemical Research* **39**, 628-634 (2006).
- 243 Haass, C., & Selkoe, D. J. Soluble protein oligomers in neurodegeneration: lessons from the Alzheimer's amyloid β -peptide. *Nat. Rev. Mol. Cell Biol.* **8**, 101-112, doi:10.1038/nrm2101 (2007).
- 244 Serpell, L. C., Berriman, J., Jakes, R., Goedert, M. & Crowther, R. A. Fiber diffraction of synthetic alpha-synuclein filaments shows amyloid-like cross-beta conformation. *Proceedings of the National Academy of Sciences of the United States of America* **97**, 4897-4902 (2000).

- 245 Dokukin, M. E. & Sokolov, I. Quantitative Mapping of the Elastic Modulus of Soft Materials with HarmoniX and PeakForce QNM AFM Modes. *Langmuir* **28**, 16060-16071, doi:10.1021/la302706b (2012).
- 246 Dittrich, P. S., Jahnz, M. & Schwille, P. A New Embedded Process for Compartmentalized Cell-Free Protein Expression and On-line Detection in Microfluidic Devices. *ChemBioChem* **6**, 811-814, doi:10.1002/cbic.200400321 (2005).
- 247 Courtois, F. *et al.* An Integrated Device for Monitoring Time-Dependent in vitro Expression From Single Genes in Picolitre Droplets. *ChemBioChem* **9**, 439-446, doi:10.1002/cbic.200700536 (2008).
- 248 Agresti, J. J. *et al.* Ultrahigh-throughput screening in drop-based microfluidics for directed evolution. *Proceedings of the National Academy of Sciences* **107**, 4004-4009, doi:10.1073/pnas.0910781107 (2010).
- 249 Hatakeyama, T., Chen, D. L. & Ismagilov, R. F. Microgram-Scale Testing of Reaction Conditions in Solution Using Nanoliter Plugs in Microfluidics with Detection by MALDI-MS. *Journal of the American Chemical Society* **128**, 2518-2519, doi:10.1021/ja057720w (2006).
- 250 Hong, J., Edel, J. B. & deMello, A. J. Micro- and nanofluidic systems for high-throughput biological screening. *Drug Discovery Today* **14**, 134-146, doi:<http://dx.doi.org/10.1016/j.drudis.2008.10.001> (2009).
- 251 Brouzes, E. *et al.* Droplet microfluidic technology for single-cell high-throughput screening. *Proceedings of the National Academy of Sciences* **106**, 14195-14200, doi:10.1073/pnas.0903542106 (2009).
- 252 Shah, R. K. *et al.* Designer emulsions using microfluidics. *Materials Today* **11**, 18-27, doi:10.1016/s1369-7021(08)70053-1 (2008).
- 253 Shah, R. K., Kim, J.-W., Agresti, J. J., Weitz, D. A. & Chu, L.-Y. Fabrication of monodisperse thermosensitive microgels and gel capsules in microfluidic devices. *Soft Matter* **4**, 2303-2309, doi:10.1039/b808653m (2008).
- 254 Meier, M. *et al.* Plug-Based Microfluidics with Defined Surface Chemistry to Miniaturize and Control Aggregation of Amyloidogenic Peptides. *Angewandte Chemie-International Edition* **48**, 1487-1489, doi:10.1002/anie.200805225 (2009).
- 255 Knowles, T. P. J. *et al.* Observation of spatial propagation of amyloid assembly from single nuclei. *Proceedings of the National Academy of Sciences* **108**, 14746-14751, doi:10.1073/pnas.1105555108 (2011).
- 256 Song, H., Chen, D. L. & Ismagilov, R. F. Reactions in droplets in microfluidic channels. *Angewandte Chemie-International Edition* **45**, 7336-7356, doi:10.1002/anie.200601554 (2006).
- 257 Theberge, A. B. *et al.* Microdroplets in Microfluidics: An Evolving Platform for Discoveries in Chemistry and Biology. *Angewandte Chemie-International Edition* **49**, 5846-5868, doi:10.1002/anie.200906653 (2010).
- 258 Gielen, F. *et al.* A Fully Unsupervised Compartment-on-Demand Platform for Precise Nanoliter Assays of Time-Dependent Steady-State Enzyme Kinetics and Inhibition. *Analytical Chemistry* **85**, 4761-4769, doi:10.1021/ac400480z (2013).
- 259 Luo, C. *et al.* Picoliter-volume aqueous droplets in oil: Electrochemical detection and yeast cell electroporation. *ELECTROPHORESIS* **27**, 1977-1983, doi:10.1002/elps.200500665 (2006).
- 260 Liu, S. *et al.* The electrochemical detection of droplets in microfluidic devices. *Lab on a Chip* **8**, 1937-1942, doi:10.1039/B809744E (2008).
- 261 Roman, G. T., Wang, M., Shultz, K. N., Jennings, C. & Kennedy, R. T. Sampling and Electrophoretic Analysis of Segmented Flow Streams Using Virtual Walls in a Microfluidic Device. *Analytical Chemistry* **80**, 8231-8238, doi:10.1021/ac801317t (2008).
- 262 Fidalgo, L. M. *et al.* Coupling Microdroplet Microreactors with Mass Spectrometry: Reading the Contents of Single Droplets Online. *Angewandte Chemie-International Edition* **48**, 3665-3668, doi:10.1002/anie.200806103 (2009).

- 263 Pei, J., Li, Q., Lee, M. S., Valaskovic, G. A. & Kennedy, R. T. Analysis of Samples Stored as Individual Plugs in a Capillary by Electrospray Ionization Mass Spectrometry. *Analytical Chemistry* **81**, 6558-6561, doi:10.1021/ac901172a (2009).
- 264 Cristobal, G. *et al.* On-line laser Raman spectroscopic probing of droplets engineered in microfluidic devices. *Lab on a Chip* **6**, 1140-1146, doi:10.1039/b602702d (2006).
- 265 Barnes, S. E., Cygan, Z. T., Yates, J. K., Beers, K. L. & Amis, E. J. Raman spectroscopic monitoring of droplet polymerization in a microfluidic device. *Analyst* **131**, 1027-1033, doi:10.1039/b603693g (2006).
- 266 Pan, T., Kelly, R. T., Asplund, M. C. & Woolley, A. T. Fabrication of calcium fluoride capillary electrophoresis microdevices for on-chip infrared detection. *Journal of Chromatography A* **1027**, 231-235, doi:10.1016/s0021-9673(03)01300-1 (2004).
- 267 Chan, K. L. A., Gulati, S., Edel, J. B., de Mello, A. J. & Kazarian, S. G. Chemical imaging of microfluidic flows using ATR-FTIR spectroscopy. *Lab on a Chip* **9**, 2909-2913, doi:10.1039/b909573j (2009).
- 268 Kjoller, K., Felts, J. R., Cook, D., Prater, C. B. & King, W. P. High-sensitivity nanometer-scale infrared spectroscopy using a contact mode microcantilever with an internal resonator paddle. *Nanotechnology* **21**, doi:10.1088/0957-4484/21/18/185705 (2010).
- 269 Marcott, C. *et al.* Nanoscale infrared (IR) spectroscopy and imaging of structural lipids in human stratum corneum using an atomic force microscope to directly detect absorbed light from a tunable IR laser source. *Experimental Dermatology* **22**, 419-421, doi:10.1111/exd.12144 (2013).
- 270 Ahn, K. *et al.* Dielectrophoretic manipulation of drops for high-speed microfluidic sorting devices. *Applied Physics Letters* **88**, doi:10.1063/1.2164911 (2006).
- 271 Baroud, C. N., de Saint Vincent, M. R. & Delville, J.-P. An optical toolbox for total control of droplet microfluidics. *Lab on a Chip* **7**, 1029-1033, doi:10.1039/b702472j (2007).
- 272 Yap, Y.-F. *et al.* Thermally mediated control of liquid microdroplets at a bifurcation. *Journal of Physics D-Applied Physics* **42**, doi:10.1088/0022-3727/42/6/065503 (2009).
- 273 Franke, T., Abate, A. R., Weitz, D. A. & Wixforth, A. Surface acoustic wave (SAW) directed droplet flow in microfluidics for PDMS devices. *Lab on a Chip* **9**, 2625-2627, doi:10.1039/b906819h (2009).
- 274 Zhang, K. *et al.* On-chip manipulation of continuous picoliter-volume superparamagnetic droplets using a magnetic force. *Lab on a Chip* **9**, 2992-2999, doi:10.1039/b906229g (2009).
- 275 McDonald, J. C. & Whitesides, G. M. Poly(dimethylsiloxane) as a material for fabricating microfluidic devices. *Accounts of Chemical Research* **35**, 491-499, doi:10.1021/ar010110q (2002).
- 276 Blake, C. C. F. *et al.* Structure of Hen Egg-White Lysozyme: A Three-dimensional Fourier Synthesis at 2 [angst] Resolution. *Nature* **206**, 757-761 (1965).
- 277 Zandomenighi, G., Krebs, M. R., McCammon, M. G. & Fändrich, M. FTIR reveals structural differences between native β -sheet proteins and amyloid fibrils. *Protein Science* **13**, 3314-3321 (2004).
- 278 Diamond, R. Real-space refinement of the structure of hen egg-white lysozyme. *Journal of Molecular Biology* **82**, 371-391, doi:[http://dx.doi.org/10.1016/0022-2836\(74\)90598-1](http://dx.doi.org/10.1016/0022-2836(74)90598-1) (1974).
- 279 Jimenez, J. L., Tennent, G., Pepys, M. & Saibil, H. R. Structural diversity of ex vivo amyloid fibrils studied by cryo-electron microscopy. *Journal of Molecular Biology* **311**, 241-247, doi:10.1006/jmbi.2001.4863 (2001).
- 280 Srisa-Art, M., deMello, A. J. & Edel, J. B. High-throughput DNA droplet assays using picoliter reactor volumes. *Analytical Chemistry* **79**, 6682-6689, doi:10.1021/ac070987o (2007).
- 281 Guo, F. *et al.* A Droplet-Based, Optofluidic Device for High-Throughput, Quantitative Bioanalysis. *Analytical Chemistry* **84**, 10745-10749, doi:10.1021/ac302623z (2012).
- 282 Muller, T. *et al.* Nanoscale spatially resolved infrared spectra from single microdroplets. *Lab on a Chip* **14**, 1315-1319, doi:10.1039/C3LC51219C (2014).

- 283 Masino, L. *et al.* Characterization of the Structure and the Amyloidogenic Properties of the Josephin Domain of the Polyglutamine-containing Protein Ataxin-3. *Journal of Molecular Biology* **344**, 1021-1035, doi:<http://dx.doi.org/10.1016/j.jmb.2004.09.065> (2004).
- 284 Nasse, M. J. *et al.* High-resolution Fourier-transform infrared chemical imaging with multiple synchrotron beams. *Nat Meth* **8**, 413-416, doi:<http://www.nature.com/nmeth/journal/v8/n5/abs/nmeth.1585.html#supplementary-information> (2011).
- 285 Dazzi, A., Glotin, F. & Carminati, R. Theory of infrared nanospectroscopy by photothermal induced resonance. *Journal of Applied Physics* **107**, -, doi:<http://dx.doi.org/10.1063/1.3429214> (2010).
- 286 Dazzi, A. *et al.* Chemical mapping of the distribution of viruses into infected bacteria with a photothermal method. *Ultramicroscopy* **108**, 635-641, doi:<http://dx.doi.org/10.1016/j.ultramic.2007.10.008> (2008).
- 287 Ridgley, D. M. & Barone, J. R. Evolution of the Amyloid Fiber over Multiple Length Scales. *ACS Nano* **7**, 1006-1015, doi:10.1021/nn303489a (2013).
- 288 Hong, D., Fink, A. L. & Uversky, V. N. Structural Characteristics of α -Synuclein Oligomers Stabilized by the Flavonoid Baicalein. *Journal of Molecular Biology* **383**, 214-223 (2008).
- 289 Nicastro, G., Habeck, M., Masino, L., Svergun, D. I. & Pastore, A. Structure validation of the Josephin domain of ataxin-3: Conclusive evidence for an open conformation. *Journal of Biomolecular Nmr* **36**, 267-277, doi:10.1007/s10858-006-9092-z (2006).
- 290 Barth, A. The infrared absorption of amino acid side chains. *Progress in Biophysics and Molecular Biology* **74**, 141-173 (2000).
- 291 Ruggeri, F. S. *et al.* Influence of the beta-Sheet Content on the Mechanical Properties of Aggregates during Amyloid Fibrillization. *Angew Chem Int Ed Engl*, n/a-n/a, doi:10.1002/anie.201409050 (2015).
- 292 Masino, L., Nicastro, G., Calder, L., Vendruscolo, M. & Pastore, A. Functional interactions as a survival strategy against abnormal aggregation. *Faseb Journal* **25**, 45-54, doi:10.1096/fj.10-161208 (2011).
- 293 Bemporad, F. & Chiti, F. "Native-like aggregation" of the acylphosphatase from *Sulfolobus solfataricus* and its biological implications. *Febs Letters* **583**, 2630-2638, doi:10.1016/j.febslet.2009.07.013 (2009).